Quantum Control over a Low Frequency Mechanical Oscillator Using a Superconducting Qubit

by

Xizheng Ma

B.S., William Marsh Rice University, 2013

M.S., University of Colorado, 2017

A thesis submitted to the

Faculty of the Graduate School of the

University of Colorado in partial fulfillment

of the requirements for the degree of

Doctor of Philosophy

Department of Physics

2020

This thesis entitled:
Quantum Control over a Low Frequency Mechanical Oscillator Using a Superconducting Qubit
written by Xizheng Ma
has been approved for the Department of Physics

_____

Prof. Konrad W. Lehnert

_____

Prof. John D. Teufel

Date _____

The final copy of this thesis has been examined by the signatories, and we find that both the content and the form meet acceptable presentation standards of scholarly work in the above mentioned discipline.

Ma, Xizheng (Ph.D., Physics)

Quantum Control over a Low Frequency Mechanical Oscillator Using a Superconducting Qubit

Thesis directed by Prof. Konrad W. Lehnert

The ability to access a broad range of quantum states with mechanical oscillators has many applications and is an enduring ambition in the fields of opto- and electromechanics. However, as mechanical oscillators are linear at the quantum scale, arbitrary quantum control over them requires an extrinsic nonlinearity. In this thesis, I aim to provide this extrinsic nonlinearity and establish quantum control over the motion of a suspended aluminum disk by coupling it strongly to a superconducting qubit. To this end, I design and fabricate a device, when operated at its maximum coupling strength, could enable phonon-number-resolved measurements and arbitrary quantum control over the mechanical motion. However, limited by unclear reasons that break the qubit readout, I operate at approximately a quarter of the maximum coupling strength.

Nevertheless, at this smaller coupling strength, I demonstrate the preparation of a non-Gaussian nonclassical state of motion. Because of the large coupling achieved in this work, the sideband transitions are phonon-number-sensitive, selectively altering the phonon populations in only a few Fock states. Using these phonon-number-sensitive sideband transitions, I dissipatively stabilize the mechanical oscillator into a highly-energized sub-Poissonian state, where its energy fluctuations are below the classical limit. This result represents a major step toward the long-time ambition of accessing a broad range of nonclassical states with macroscopic mechanical oscillators. Moreover, requiring neither number-resolution nor coherent control of the qubit, the dissipative stabilization technique demonstrated in this work also provides an accessible path toward preparing nonclassical states in other harmonic oscillators coupled to qubits.

Dedication

In Loving Memory of My Grandfather, Zhitian Ma

Acknowledgements

I would like to thank everyone who has helped, supported, and advised me throughout my years at CU Boulder. I cannot imagine finishing this journey without any of you. However, to properly acknowledge everyone would be take far too many pages than is allotted here. Instead, I make a meager attempt to highlight just a few:

To start, I must express my gratitude to Jérémie Viennot. You showed me on a daily basis what a true experimental physicist should be like. It was great fun and honor to have worked so closely with you for four years, and I shall be forever indebted to you for the great many things you have taught me.

I am extremely lucky to have worked alongside many talented physicists during the past years. In particular, I would like to thank my collaborator Shlomi Kotler for the many enlightening discussions that always propelled the project forward; Will Kindel for showing me how qubits and JPA work; Daniel Palken for teaching me all about statistics; and Lucas Sletten and Robert Delaney for bearing with my countless "dumb questions". More broadly, I would like to thank every member of the Lehnert lab, you have all helped and supported me in one way or another, making this journey not just rewarding but also fun.

Of course, this journey would have been possible without the support from my advisor Konrad Lehnert. I could not ask for a better mentor. I am always amazed by your ability to provide brilliant insights on all facets of physics, from experimental details to profound physical meanings. More importantly, you are always available to your students. It must have taken an incredible amount of dedication.

Finally, I would like to thank my friends and family for sharing all my frustration and elation of the past seven years. To my parents, thank you for your support and encouragement. To my wife, Sylvia Bao, your love and sweetness drove me to finish this thesis.

Contents

Chapter

Tables

Table

Figures

Figure

Chapter 1

Introduction

Throughout history, mechanical systems have proved useful as tools that advanced our understanding of the physical world. In 1851, the procession of a Foucault pendulum succinctly demonstrated the rotation of the earth. For a long time, torsional oscillators were the most sensitive force detectors: in 1798, they were used in the Cavendish experiment [1] to achieve the first measurement of the gravitational constant. In 1909, their inability to measure a force in the Eötvös experiment demonstrated the equivalence of inertial mass and gravitational mass; even today, they are still used to test the validity of Newtonian gravity at the microscopic scale [2]. For centuries, mechanical oscillators have also provided the most reliable methods to measure time: pendulums were used as reliable clocks since the mid-17th century, while spring-loaded mechanical oscillators allowed for the creation of portable watches and chronometers. More recently, modern forms of mechanical oscillators, such as quartz tuning forks, have become the standard in both keeping time and sensing forces. Perhaps the most salient example of the importance of mechanical systems in physics was the experimental observation of gravitational waves in 2015 [3]. By continuously monitoring the separation between freely suspended test masses, LIGO was able to observe a minute relative motion (with an amplitude less than $1/10^{21}$ of the initial separation) at frequencies around 100 Hz induced by the gravitational strain and detect the merger of a binary system of black-holes a billion light-years away.

Necessitated by such minute effects, the development of gravitational wave detectors motivated the understanding of quantum effects on measurements. The famous Heisenberg uncertainty

principle states that a completely accurate measurement of an oscillator's position will kick it with a completely random force such that it's position at a later time would be impossible to predict. Although pioneers in quantum physics understood this compromise between measurement and disturbance as early as 1925 [4], prior experiments with macroscopic objects neither required nor achieved precision at the quantum scale. However by the 1970s, this was no longer the case with the development of gravitational wave detectors. This development evolved around two different paths, where the oscillator's position is detected using either electricity or light. Early experimental efforts envisioned that a gravitational strain will drive motion in a massive bar-resonator [5, 6, 7], whose motion can be converted into electrical signals using either piezo-electricity [6] or capacitive transducers [8]; on the other hand, LIGO [9, 10] uses laser interferometry to detect the relative motion between two freely suspended masses. As experiments steadily improved detector sensitivity, both paths — despite their different approaches — were equally confronted with hard questions: when will quantum effects limit the sensitivity of the detector? Is it possible to leverage quantum mechanics and build detectors beyond the classical limit? To answer these fundamental physics questions, from the two approaches to build gravitational wave detectors emerged the parallel fields of circuit electromechanics [11, 12] and cavity optomechanics [13].

The first answers to these questions came in 1980, when two theoretical papers [14, 15] discussed the limitation on the sensitivity of continuous position measurement using electromagnetic fields. Later known as the standard quantum limit, this limitation arises because the quantum fluctuations in the field also create fluctuating forces on the oscillator, and is consistent with the Heisenberg uncertainty principle. Moreover, the authors pointed to a way to surpass such limitations — by preparing the mechanical oscillator in nonclassical states of motion.

The experimental progress of coaxing mechanical oscillators into nonclassical states is much slower. The majority of electro- and optomechanical experiments use the radiation-pressure interaction between the mechanical motion and the energy of an ancillary electrical or optical cavity. As demonstrated in the pioneering experiment of 1970 [16], this interaction can provide an additional damping or anti-damping to the oscillator's motion to change its dynamical behavior. It

was envisioned that this phenomena, termed "dynamical backaction", can be leveraged to control the mechanical motion and prepare it into nonclassical states [17, 18]. However, to reach this goal took a concerted experimental effort. A major obstacle is cooling the mechanical oscillator to its ground state using the radiation-pressure interaction. Because the mechanical oscillators in these experiments often have low resonant frequencies (< 100 MHz) [13], even at the base temperatures of dilution refrigerators (~ 25 mK), they have high thermal occupations that can obscure quantum signatures. Using electricity [19] and light [20], two experiments in 2011 finally achieved the active cooling of macroscopic mechanical oscillators to their ground state. Since then, mechanical oscillators have been prepared into quadrature squeezed states [21, 22, 23], where the uncertainty in one quadrature is below vacuum fluctuation. Entanglement has also been created between mechanical oscillators and other systems, such as microwave [24] or optical [25] fields or a separate macroscopic mechanical oscillator [26, 27, 28], allowing for the construction of highly sensitive force detectors beyond the classical limit [29, 30, 31].

In addition to building highly sensitive detectors, the prospect of preparing nonclassical states of motion inspired new applications for macroscopic mechanical oscillators. However, to fully exploit their potential, one needs access to a broad range of nonclassical states. States characterized by sub-Poissonian energy distributions, such as Fock states, have been analyzed for their ability to improve the sensitivity of gravitational wave detectors [15, 14]. Macroscopically distinguishable superposition states of motion [32, 33] are envisioned to test wavefunction collapse models [34]. Mechanical oscillators are also versatile tools in quantum information, for the construction of quantum computers and quantum networks. Because of their long coherence times, mechanical oscillators can be used as quantum memories [35, 36]. Because they couple easily to both electrical and optical systems, they can be used as quantum transducers between different frequency domains [37]. Furthermore, they can be used as amplifiers for the quantum information stored in its own motion [38], or in a propagating field [24]. Although Gaussian nonclassical states such as quadrature squeezed states can be useful in certain tasks [39], any process that only involves Gaussian states can be efficiently simulated using classical computers [40]. Instead, many advanced quantum protocols, such

as entanglement distillation [41, 42, 43] and Shor's algorithm [44], explicitly call for non-Gaussian resources.

Because macroscopic mechanical oscillators are generally linear at the quantum scale, accessing such non-Gaussian states requires an extrinsic nonlinearity such as a nonlinear source [45] or detector [25, 46]. In standard opto- and electromechanical systems based on the radiation-pressure interaction, driving the system at the difference frequency of the ancillary-cavity and mechanical resonances initiates a beam-splitter interaction that coherently exchanges the mechanical phonons with the cavity photons [35]. This linear interaction is leveraged in the 2017 experiment [45] to capture and store a propagating superposition state of zero and one photons in the motion of a macroscopic mechanical oscillator, creating a non-Gaussian mechanical state using a nonlinear source. Instead of a nonlinear source, a nonlinear detector such as a photon counter [47, 48] can also create non-Gaussian nonclassical states in the mechanical oscillator using the "heralding" technique: the detection of a single photon in a correlated photon-phonon pair heralds the presence of a single phonon in the mechanical oscillator [25, 46]. Such correlated phonon-photon pairs can be created in opto- and electromechancial systems by driving at the sum frequency of the mechanical oscillator and ancillary cavity [24]. Alternatively, the extrinsic nonlinearity can also be a strong nonlinear interaction.

The radiation-pressure interaction is inherently nonlinear, and can in theory [49, 50, 51] create non-Gaussian nonclassical states in the mechanical oscillator. Such proposals call for an extremely large coupling such that the radiation-pressure force from a single cavity photon will displace the mechanical oscillator by more than its zero-point fluctuation x_{zp}. To reach this so-called "single-photon strong-coupling" regime requires the single-photon coupling rate g_0 to be larger than both the mechanical frequency $\omega_{\rm m}$ and the cavity decoherence rate κ. However, the nature of the radiation-pressure interaction dictates that g_0 is intrinsically small. To illustrate this, I consider a standard electromechanical system, where the mechanical motion $\hat{x}$ alters the microwave resonance frequency ω_c of a LC-circuit by changing the separation between the two electrodes of the capacitor. The mechanical modulation of the small single photon energy $\hbar\omega_c$

stored in the circuit creates a parametric coupling of rate $g_0 = (d\omega_c/dx)x_{zp} \approx \omega_c(x_{zp}/x_0)$, where x_0 is the static separation between the capacitor electrodes. Limited by physical constraints such as the Casmir force, the ratio x_{zp}/x_0 is typically small ($\sim 10^{-7}$) [52], and consequently in most experiments $g_0 \ll \kappa \ll \omega_\mathrm{m}$. Despite a variety of proposals and efforts to enhance g_0, such as mediating it through a qubit [53, 54] or modulating it at ω_m [55], no experiment so far has come close to reaching the single-photon strong-coupling regime. Instead, most experiments operate with a large cavity drive, enhancing the coupling strength but yielding a linear interaction [56, 57] between the mechanical position and cavity field.

However, the drive-enhanced coupling can remain nonlinear if the cavity energy is coupled to the position-squared, instead of just position, of the oscillator motion [58, 59]. This "quadratic coupling" can be generated using the electromechancial setup [14] of Fig. 1.1: two identical LC resonators are coupled by a common inductance L_c at rate $J = \omega_c L_c/2L$ and their resonant frequencies $\omega_{R,L}$ are modulated with opposite phase by the anti-symmetric motion of the mechanical oscillator $x_{zp}d\omega_{R,L}/dx = \pm g_0$. Consequently, the normal modes of this circuit anti-cross at $x = 0$ with a splitting $2J$, and sense the square of the mechanical displacement with quadratic coupling strength $x_{zp}^2 d^2\omega_\pm/dx^2 \approx \pm g_0^2/2J$. By selecting on the measured mechanical position squared, an experiment in 2016 [60] was able to generate non-Gaussian, albeit classical, bimodal states of motion in a nanostring. Accessing non-Gaussian nonclassical states of motion, however, is prevented because a residual linear coupling emerges under a large cavity drive, and causes accelerated mechanical decoherence [61, 60]. Despite early doubts [61], this limitation can be overcome by active feedback [62, 60] or better designs [63, 64, 65] without requiring the single-photon strong-coupling regime. Yet, quadratic coupling schemes for opto- and electromechanics have not yielded nonclassical states in mechanical oscillators.

A strong nonlinear coupling can also be created by replacing the harmonic cavity with an anharmonic device, such as a superconducting qubit. These superconducting qubits have propelled progress in quantum science, such as preparing arbitrary quantum states in microwave cavities [66, 67], and their integration with mechanical oscillators was heavily anticipated for the prospects of

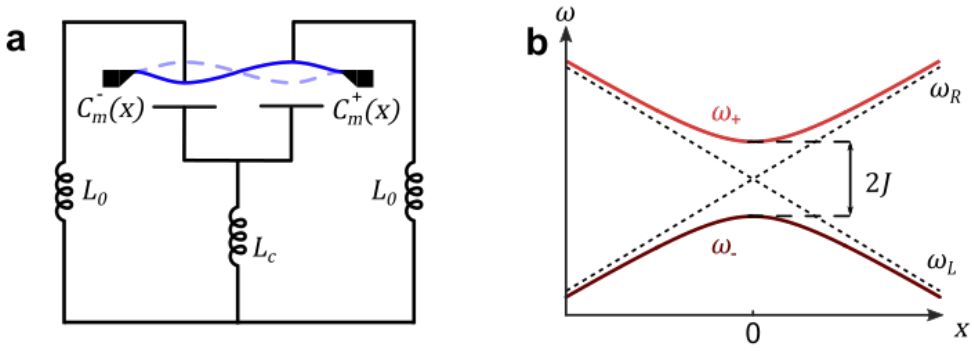

Figure 1.1: Quadratic electromechanical coupling
a, The capacitance of two mechanically compliant capacitors, $C_{\mathrm{m}}^{\pm}(x)$, are modulated with opposite phase by the anti-symmetric motion of the mechanical oscillator (blue). The two separate LC resonators are coupled by a common inductance L_c at a rate $J = \omega_c L_c/2L_0$. b, The resonant frequencies of the uncoupled LC resonators (dashed) depend linearly on mechanical displacement x with opposite phase, $x_{zp} d\omega_{R,L}/dx = \pm g_0$, where x_{zp} is the zero-point displacement of the mechanical oscillator. The normal modes of the circuit (solid), however, anti-cross at $x = 0$ with splitting $2J$ and sense the square of mechanical displacement with quadratic coupling strength $x_{zp}^2 d^2\omega_{\pm}/dx^2 \approx \pm g_0^2/2J$.

creating a broad range of nonclassical states of motion [68, 69, 70, 71, 72, 73, 74]. However, it has been experimentally challenging to create a coupling strength large enough to achieve this goal.

One strategy to strongly couple mechanical motion to qubits involves piezo-electricity: when motion deforms the crystal lattice of a piezoelectric material, such as quartz or AlN, accumulated charges in the material create an electric field that drives the qubit and vice versa. In order to increase the strength of this electric field, piezoelectric materials often have high stiffness, and create mechanical oscillations at high frequencies from hundreds of megahertz to many gigahertz. This approach was first demonstrated in a 2010 experiment, where the high-frequency 6 GHz dilational-mode of a bulk-acoustic resonator was resonantly coupled to a tunable superconducting qubit. During the years of my Ph.D., this approach experienced tremendous success and has developed into a distinctive field known as "quantum acoustics". Through resonant coupling, the preparation of phonon Fock states has been demonstrated using both surface-acoustic-wave [75] and bulk-acoustic-wave resonators [36]. In the dispersive coupling limit, where the qubit and mechanical frequencies are far apart, phonon-number-resolved measurements have also been reported on both surface-acoustic-wave resonators [76] and phononic-crystal defect resonators [77], but the preparation of phonon Fock state is prevented by a limited mechanical decoherence rate. In these experiments, the investigated mechanical motion are confined to a small class of elastic waves in stiff piezoelectric material. Although such mechanical oscillators can be useful for special tasks in quantum computing, they are much less general-purpose compared to the more conventional mechanical oscillators. For example, because of the high stiffness, they are not sensitive force detectors; because of their typically small zero-point motions ($\sim 10^{-16}$ m) [78], they are less macroscopic and thus less useful for testing wave-function collapse models [34].

Without using piezo-electricity, conventional, center-of-mass motions of low-frequency macroscopic mechanical oscillators can be coupled to qubits using the schematic shown in Fig. 1.2 . Instead of leveraging the particular material properties to transduce mechanical motion to electrical signals, a dc-voltage V_{dc} can transduce the motion of a macroscopic mechanical oscillator to a position-dependent charge-source by embedding the oscillator in a mechanically compliant capacitor. When

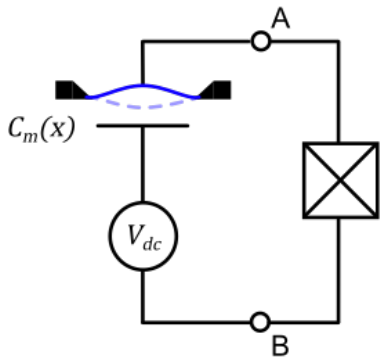

Figure 1.2: Qubit-mechanics coupling
The dc-voltage V_{dc} transduces the mechanical motion (blue) into a position-dependent charge-source ac cross open terminals A and B. This charge-source controls the electrostatic energy of a charge-sensitive qubit and couples the mechancial motion to the qubit energy.

this charge-source drives a charge-sensitive qubit, such as a Cooper-pair box (CPB) qubit [79, 80], it couples the mechanical position to the qubit energy with a strength controlled by V_{dc}.

However, the experimental progress in creating nonclassical states of motion using this coupling scheme has been slow. Using a nano-beam resonator, a 2009 experiment [81] first created this type of qubit-mechanics coupling and observed a shift in mechanical frequency when the qubit frequency is changed — an entirely classical effect. Limited by a large qubit decoherence rate, the experiment is unable to control the mechanical motion using the qubit. To combat this problem, later experiments [82, 83] attempted to reduce the qubit's charge-sensitivity by going toward the transmon limit [84], which reduces the qubit decoherence due to charge-noise but also reduces the qubit-mechanics coupling rate. In 2013, the phonon-number-dependent Stark shift of the qubit frequency was first observed [82]. However, because of the small coupling rate, this effect is only visible at very large phonon numbers and cannot distinguish the quantization of mechanical energy. In the same experiment, motional sidebands that simultaneously excite the qubit and change the phonon occupation were also observed. However, these sidebands are only observable at large phonon numbers where their effects on the motion are insignificant. Moverover, the small qubit-mechanics coupling rate impedes the selective manipulation of the phonon occupation in each Fock state. Instead, driving these sideband transitions at a particular frequency would indistinguishably

address hundreds of phonon Fock states. Despite the progress made in these early demonstrates, it remains an experimental challenge to prepare nonclassical states of motion in macroscopic mechanical oscillators using qubits.

In this thesis, I aim to pursue the coupling scheme shown in Fig. 1.2, and establish quantum control over the motion of a suspended aluminum disk using a superconducting qubit. Instead of exchanging coupling strength for improvements in the coherence time, I aim to create a stronger coupling between the qubit and mechanical oscillator by using a CPB qubit. I design and fabricate a device, when operated at the maximum dc-voltage, could enable phonon-number-resolved measurements and arbitrary quantum control over the mechanical motion. However, limited by unclear reasons that break the qubit readout, I operate at approximately a quarter of the maximum dc-voltage.

Nevertheless, at this smaller coupling strength, I demonstrate the preparation of a non-Gaussian nonclassical state of motion [85]. Because of the large coupling achieved in this work, the sideband transitions are phonon-number-sensitive, selectively altering the phonon populations in only a few Fock states. This phonon-number-sensitivity can be observed by either cooling the mechanical oscillator close to its ground state using a red sideband transition that removes phonons from the mechanical oscillator, or by preparing a highly non-thermal phonon distribution using blue sideband transitions that add excitations to the oscillator [86]. Using these phonon-number-sensitive sideband transitions, I dissipatively stabilize the mechanical oscillator into a highly-energized sub-Poissonian state [85], where its energy fluctuations are below the classical limit [87]. This result represents a major step toward the long-time ambition of accessing a broad range of nonclassical states with macroscopic mechanical oscillators by strongly coupling it to a superconducting qubit. Moreover, requiring neither number-resolution nor coherent control of the qubit, the dissipative stabilization technique demonstrated in this work also provides an accessible path toward preparing nonclassical states in other harmonic oscillators coupled to qubits.

1.1 Thesis contents

Chapter 2 introduces both the mechanical oscillator and the superconducting qubit, and provides a theoretical description of the coupled qubit-mechanics system. Chapter 3 details the designing of the hybrid system, and explains the reasoning behind many design choices, such as using a CPB qubit. It also introduces a microwave resonator that couples only to the qubit, allowing for its control and readout. Chapter 4 demonstrates the control and readout of the qubit using the microwave resonator, and provides an initial experimental characterization of the coupled qubit-mechanics system by measuring the qubit-mechanics coupling rate. It also shows the break down of the qubit readout at large V_{dc} and provides a plausible explanation for this limitation. Chapter 5 describes the extraction of mechanical energy distributions from measured qubit spectra, and demonstrates the procedure on thermal and displaced-thermal mechanical states. Chapter 6 shows the manipulation of phonon population using motional sideband transitions. It demonstrates the phonon-number-sensitivity of these sideband transitions and provides a theoretical model to predict their effects. Using these sideband transitions, it also demonstrates the dissipative stabilization technique, capable of simultaneously adding energy to and extracting entropy from a massive mechanical oscillator. Finally, Chapter 7 uses the this technique to create a non-Gaussian nonclassical state of motion whose uncertainty in energy is below the classical limit. Chapter 8 looks to future experiments and advancements that could follow the work of this thesis.

Chapter 2

Theory of a mechanical oscillator coupled to a qubit

In order to provide a consistent mathematical language and theoretical background for the rest of this thesis, this chapter theoretically describes the interaction between a mechanical oscillator and a superconducting qubit. Sec.2.1 begins by providing a quantum description for mechanical oscillators. Sec.2.2 introduces the superconducting qubit, which is an anharmonic oscillator formed by a nonlinear circuit. Finally, Sec.2.3 describes the interaction between the two systems when a coupling is created using the schematic shown in Fig. 1.2.

2.1 Mechanical oscillators

Mechanical oscillators are perhaps the most tangible examples of harmonic oscillators. In classical mechanics, the oscillator motion is described by its position and momentum $\{x, p\}$, which can be simultaneously specified. Canonically depicted as a mass m attached to a spring of constant k, the oscillator is subject to a restoring force $F = -kx$ when displaced from its equilibrium position by a distance x. The evolution of this system is specified by the classical Hamiltonian,

$$H_{\mathrm{m}} = \frac{p^2}{2m} + \frac{1}{2}kx^2. \tag{2.1}$$

With an initial displacement of x_i, the position of the mass oscillates around the equilibrium position according to $x(t) = x_i \cos(\omega_{\mathrm{m}} t)$, where $\omega_{\mathrm{m}} = \sqrt{k/m}$ is the resonant angular frequency of the mechanical oscillator.

Quantum mechanically, the state of the mechanical oscillator is more naturally described by its energy. The dynamical variables from classical mechanics are replaced by quantum operators

$\hat{x}$ and $\hat{p}$, which obey the commutation relation $[\hat{x}, \hat{p}] = i\hbar$. They can be expressed in terms of the phonon creation $\hat{a}^\dagger$ and annihilation operators $\hat{a}$,

$$\hat{x} = x_{zp}(\hat{a}^\dagger + \hat{a}), \tag{2.2}$$

$$\hat{p} = im\omega_{\rm m} x_{zp}(\hat{a}^\dagger - \hat{a}). \tag{2.3}$$

Here, the zero-point motion $x_{zp} = \sqrt{\hbar/2m\omega_{\rm m}}$ corresponds to the magnitude of position fluctuation when the mechanical oscillator is in its energy ground state, $\langle 0|\, \hat{x}^2\, |0\rangle = x_{zp}^2$. Written with phonon operators, the quantum Hamiltonian analogous to Eqn.(2.1) is

$$H_{\rm m} = \frac{\hat{p}^2}{2m} + \frac{1}{2}k\hat{x}^2 = \hbar\omega_{\rm m}(\hat{n} + \frac{1}{2}), \tag{2.4}$$

where $\hat{n} = \hat{a}^\dagger\hat{a}$ is the phonon number operator. The eigenstates of the Hamiltonian are phonon Fock states $|n\rangle$, with evenly spaced energies $E_n = \hbar\omega_{\rm m}(n + 1/2)$ such that all transitions between adjacent phonon states are degenerate.

This degeneracy prevents the access to individual Fock states with a classical drive. Instead, classically driving a mechanical oscillator addresses all energy levels at the same time, and prepares it into a classical state — a coherent state. Such a state is denoted by $|\alpha\rangle$ and satisfies $\hat{a}\,|\alpha\rangle = \alpha\,|\alpha\rangle$, where α is a complex number that describes the strength of the classical drive. In the Fock basis, a coherent state is described by a Poisson distribution,

$$|\alpha\rangle = e^{-\frac{|\alpha|^2}{2}} \sum_{n=0}^{\infty} \frac{\alpha}{\sqrt{n!}} |n\rangle\,, \tag{2.5}$$

with equal mean and variance in energy or phonon number, $\mathrm{var}(n) = \langle n\rangle = |\alpha|^2$.

Over time, the energy stored in a damped mechanical oscillator by the external drive will slowly decay into an external bath at a rate $\gamma_{\rm m}$. The external bath can be thought of as a large collection of harmonic oscillators at various frequencies, which can exchange energy with the mechanical oscillator. Because we do not keep track of the bath states, energy appears as lost when it flows from the mechanical oscillator into the bath. To model this disspative process, I write the master equation of the mechanical oscillator in the Lindblad form [88],

$$\frac{d\rho}{dt} = -i[H_{\rm m}, \rho] + \mathcal{L}_{\rm m}(\rho), \tag{2.6}$$

where $\rho = \sum_{m,n} \rho_{mn} |m\rangle \langle n|$ is the density matrix of the oscillator, and $\mathcal{L}_\mathrm{m}$ is the Lindbladian. For a thermal bath at temperature T,

$$\mathcal{L}_\mathrm{m}(\rho) = \gamma_\mathrm{m}(n_b + 1)D[\hat{a}](\rho) + \gamma_\mathrm{m} n_b D[\hat{a}^\dagger](\rho), \tag{2.7}$$

where $n_b = [\exp(\hbar\omega_\mathrm{m}/k_B T) - 1]^{-1}$ is the bath-photon number at the mechanical frequency ω_m, and $D[\hat{O}](\rho) = \frac{1}{2}\left(2\hat{O}\rho\hat{O}^\dagger - \rho\hat{O}^\dagger\hat{O} - \hat{O}^\dagger\hat{O}\rho\right)$ is the Lindblad superoperator. Starting from any statistical mixture of phonon Fock states, the initial density matrix is diagonal and commutes with H_m. Subsequently, because Eqn.(2.7) couples diagonal elements only among themselves and not to off-diagonal elements, this initial state evolves according to,

$$\frac{1}{\gamma_\mathrm{m}}\frac{d}{dt}P(n) = n_b n P(n-1) + (n_b+1)(n+1)P(n+1) - [n_b(n+1) + (n_b+1)n]\,P(n), \tag{2.8}$$

where $P(n) = \rho_{nn} = \langle n|\,\rho\,|n\rangle$ is the probability of having n phonons in the mechanical oscillator. In steady state where the mechanical oscillator reaches equilibrium with the thermal bath, its phonon distribution is described by a thermal distribution,

$$P_\mathrm{th}(n_\mathrm{th}, n) = \frac{n_\mathrm{th}^n}{(n_\mathrm{th}+1)^{n+1}}, \tag{2.9}$$

where,

$$n_\mathrm{th} = \langle n \rangle = n_b = [\exp(\hbar\omega_\mathrm{m}/k_B T) - 1]^{-1}, \tag{2.10}$$

is the mean phonon occupation number. In this work, I use a mechanical oscillator with $\omega_\mathrm{m} = 2\pi \times 25$ MHz. Operating in a dilution refrigerator with a typical temperature of 25 mK ($k_B T/\hbar \approx 2\pi \times 0.5$ GHz), its thermal occupation is $n_\mathrm{th} \approx 20$ phonons.

2.2 Superconducting qubits

A superconducting qubit is an LC-circuit with a strong nonlinearity. Similar to a mechanical oscillator, a linear LC-circuit also behaves like a harmonic oscillator with an evenly spaced photon energy E_n. However, by replacing the inductor with a nonlinear element, an anharmonicity is introduced that lifts the degeneracy of neighboring-photon transitions. When this anharmonicity

is large enough, the nonlinear circuit can be treated as an effective two-level system, also known as a quantum bit (qubit).

2.2.1 Josephson junction

The nonlinear inductors in such circuits are provided by Josephson junctions. A Josephson junction consists of two superconducting electrodes separated by an insulating layer (Fig. 2.1). In each superconducting electrode, charges bind together to form Cooper-pairs of charge $2e$. All Cooper-pairs in one electrode form a common quantum state characterized by its quantum phase. Because the wavefunctions of macroscopic quantum states from the two superconducting electrodes overlap in the Josephson junction, Cooper-pairs can tunnel across the insulating layer. This tunneling of discreet Cooper-pairs creates a periodic current across the junction,

$$I(t) = I_c \sin \phi(t), \tag{2.11}$$

where ϕ is the phase difference between the two electrodes. The critical current I_c is the maximum superconducting current that can flow through the junction, given by the Ambegaokar-Baratoff relation [89],

$$I_c = \frac{\pi \Delta}{2eR_N} \tanh\left(\frac{\Delta}{2k_B T}\right), \tag{2.12}$$

where R_N is the normal state resistance of the tunnel junction, and Δ is the superconducting gap of the electrodes. The tunneling Cooper-pairs also create a voltage potential,

$$V(t) = \frac{\Phi_0}{2\pi} \frac{d}{dt} \phi(t), \tag{2.13}$$

where $\Phi_0 = h/2e$ is the superconducting flux quantum. Taken together, this Josephson effect creates an nonlinear, phase-dependent inductance

$$L_J(\phi) = \left(\frac{1}{V(t)} \frac{d}{dt} I(t)\right)^{-1} = L_{J0}/\cos\phi, \tag{2.14}$$

where $L_{J0} = \Phi_0/2\pi I_c$ is the characteristic Josephson inductance. The tunneling Cooper-pairs also store energy in the junction,

$$E(\phi) = \int dt' V(t') I(t') = E_J \cos\phi, \tag{2.15}$$

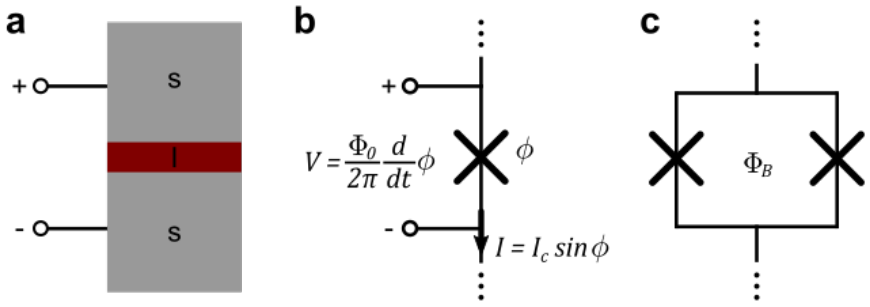

Figure 2.1: Josephson junctions
a, A Josephson junction is created by connecting two superconducting electrodes (grey) with an insulating layer (red). **b,** The Josephson junction can be schematically represented by the symbol "X". The junction is characterized by the phase difference ϕ across the two electrodes: the instantaneous current I flowing through the junction is related to $\sin\phi$ by the critical current I_c; and the voltage drop V across the junction is proportional to the time derivative of ϕ. Together, they store an energy $E_J \cos\phi$, where E_J is the Josephson energy. **c,** To provide in-situ control over this Josephson energy, a Josephson junction is often split in two, such that an external magnetic flux Φ_B piercing the superconducting loop can change E_J according to Eqn.(2.18).

where $E_J = I_c\Phi_0/2\pi$ is the Josephson energy. Quantum mechanically, this corresponds to a Hamiltonian [90],

$$H_J = E_J \cos\hat{\phi}, \tag{2.16}$$

where $\hat{\phi}$ is the quantum operator for the phase difference across the junction.

Alternatively, the tunneling of Cooper-pairs can be understood phenomenologically in the charge basis $|\mathbf{n}\rangle$ [1] , associated with $\hat{\mathbf{n}}$ number of Cooper-pairs having crossed the junction. In this basis, the tunneling connects adjacent charge states with a Hamiltonian [79],

$$H_J = \frac{E_J}{2}\sum_{\mathbf{n}\in\mathbb{Z}} \left(|\mathbf{n}\rangle\langle\mathbf{n+1}| + |\mathbf{n+1}\rangle\langle\mathbf{n}|\right). \tag{2.17}$$

Evidently, the Josephson energy characterizes the amount of overlap between wavefunctions of adjacent charge states within the junction.

To provide in-situ control over the Josephson energy, a Josephson junction is often split in two as shown in Fig. 2.1(c). The energy of the split Josephson junction can be controlled by an external magnetic flux piercing the superconducting loop Φ_B. Assuming identical junctions each characterized by a Josephson energy $E_J/2$, the overall Josephson energy is given by [80],

$$E_J(\Phi_B) = E_J \cos\left(\pi\frac{\Phi_B}{\Phi_0}\right). \tag{2.18}$$

2.2.2 A charge-sensitive qubit

By embedding the nonlinear Josephson junction in the circuit as shown in Fig. 2.2(a), one creates a qubit [79, 80]. The circuit consists of a superconducting island suspended from ground by a total capacitance $C_\Sigma = C_J + C_g$, where C_g is the gate-capacitance, and C_J is the stray capacitance between the two superconducting islands of the Josephson junction. The biasing gate-voltage V_g sets a preferred amount of excess gate-charge on the island, $n_g = C_g V_g/2e$ in units of Cooper-pairs. However, the actual excess charge on the island is a quantized, integer number of Cooper-pairs $\hat{\mathbf{n}}$. This gives rise to an electrostatic energy stored on the island by the gate-voltage,

$$H_{\text{el}} = 4E_c(\hat{\mathbf{n}} - n_g)^2, \tag{2.19}$$

[1] bold to differentiate from phonon Fock states in mechanical oscillators

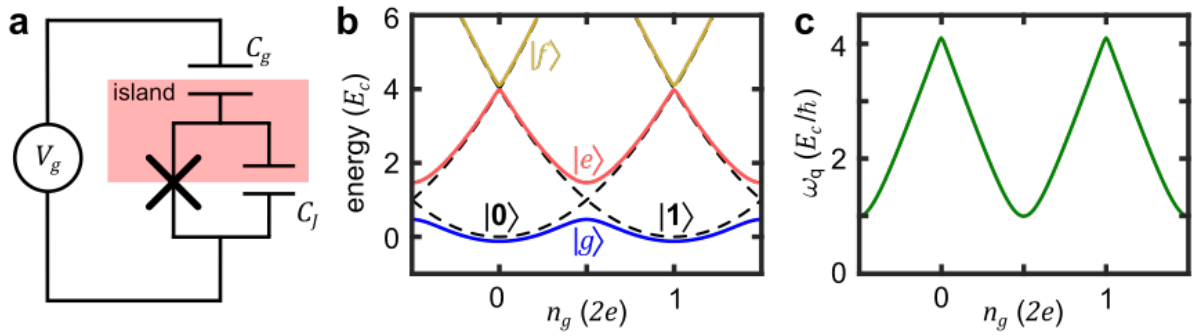

Figure 2.2: A Cooper-pair box qubit
a, A Cooper-pair box (CPB) qubit is created by connecting a suspended superconducting island (red shaded box) to a superconducting reservoir through a Josephson junction. The biasing gate-voltage V_g sets a preferred amount of excess gate-charge on the island, $n_g = C_g V_g/2e$ in units of Cooper-pairs, where C_g is the gate capacitance. However, the actual number of charges $\hat{\mathbf{n}}$ on the island is a quantized, integer number of Cooper-pairs. The gate voltage thus stores an electrostatic energy on the island, proportional to the CPB charging energy E_c and $(\hat{\mathbf{n}} - n_g)^2$. **b,** As a function of n_g, the electrostatic energy for a charge state $|\mathbf{n}\rangle$ (i.e., $\mathbf{n}$ Cooper-pairs on the island) is described by a parabola (dashed black lines). Because the Josephson junction allows Cooper-pairs to tunnel across the junction, it couples adjacent charge states at rate $E_J/\hbar$, where E_J is the Josephson energy. This coupling lifts the energy degeneracy at the charge degeneracy points $n_g = 1/2$, and results in discrete energy levels (solid lines). In this figure, I assume $E_c = E_J$. The CPB qubit is formed by the lowest two energy levels $|g\rangle$ (blue) and $|e\rangle$ (red). At $n_g = 1/2$, the qubit states are given by a superposition of charge states $|e(g)\rangle = (|\mathbf{0}\rangle \pm |\mathbf{1}\rangle)/\sqrt{2}$. **c,** The qubit frequency is given by the difference in the ground and excited state energies, and is highly dependent on the gate-charge (Eqn.(2.24)).

where $E_c = e^2/2C_\Sigma$ is the electrostatic charging energy to add a single electron to the island. In the absence of the Josephson junction, this system is described by a family of parabolas corresponding to the energy of a capacitor with a fixed number of charges on it (dashed lines in Fig. 2.2(b)). By allowing Cooper-pairs to tunnel across the junction and reach ground, the Josephson junction couples adjacent charge states. This coupling results in discrete energy levels as shown with solid lines in Fig. 2.2(b) that are highly anharmonic.

In the so called "Cooper-pair box (CPB) regime" where $E_J \lesssim E_c$, the high level of anharmonicity allows the nonlinear circuit to be treated as an effective two-level system, acting as a qubit. In this limit, the lowest two energy eigenstates of the circuit belong to the subspace spanned by charge states $\{|\mathbf{0}\rangle, |\mathbf{1}\rangle\}$. At the point of charge degeneracy $n_g = 1/2$, the degeneracy between the two charge states is lifted by the Josephson energy. Consequently, the ground $|g\rangle$ and the excited $|e\rangle$ energy eigenstates of the qubit are given by the charge superposition states $\big(|\mathbf{0}\rangle \pm |\mathbf{1}\rangle\big)/\sqrt{2}$.

This effective two-level system is most conveniently described in the language of a spin-1/2 particle. Working around the charge degeneracy point in the CPB regime, the Pauli operators can be approximately written as,

$$\begin{aligned} \hat{\sigma}'_z &= 2(\hat{\mathbf{n}} - 1) \\ \hat{\sigma}'_x &= |\mathbf{n}\rangle \langle \mathbf{n{+}1}| + |\mathbf{n{+}1}\rangle \langle \mathbf{n}| \,. \end{aligned} \tag{2.20}$$

After removing the constant terms, the Hamiltonian of this charge-sensitive qubit is given by

$$H_{\mathrm{CPB}} = H_{\mathrm{el}} + H_J = \frac{1}{2}\left[4E_c(1-2n_g)\hat{\sigma}'_z + E_J\hat{\sigma}'_x\right]. \tag{2.21}$$

This resembles the Hamiltonian of a spin with dipole moment $\mu = 1$ subject to a fictitious magnetic field of $\vec{B} = E_J\hat{x}' + 4E_c(1-2n_g)\hat{z}'$ (Fig. 2.3). The quantization of energy happens along the net magnetic field axis $\hat{z}$, rotated about $\hat{y}'$ axis by an mixing angle

$$\theta_0 = \arctan\left(\frac{E_J}{4E_c(1-2n_g)}\right). \tag{2.22}$$

In this new coordinate system, the Hamiltonian of the qubit is simply

$$H_{\mathrm{q}} = \frac{1}{2}\hbar\omega_{\mathrm{q}}\hat{\sigma}_z, \tag{2.23}$$

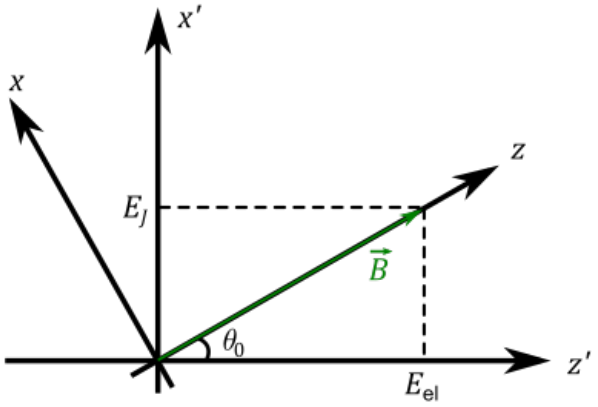

Figure 2.3: Fictitious field picture
The qubit Hamiltonian H_{CPB} resembles that of a spin with dipole moment $\mu = 1$ subject to a fictitious magnetic field of $\vec{B} = E_J\hat{x}' + E_{\mathrm{el}}\hat{z}'$, where the electrostatic energy $E_{\mathrm{el}} = 4E_c(1 - 2n_g)$. The quantization of energy happens along the net magnetic field axis $\hat{z}$ rotated about $\hat{y}'$ axis by an mixing angle θ_0.

where

$$\omega_{\mathrm{q}} = \frac{1}{\hbar}\sqrt{[4Ec(1-2n_g)]^2 + E_J^2} \tag{2.24}$$

is the qubit frequency. The eigenstates of this two-level system are

$$\begin{aligned} \hat{\sigma}_z \left|g\right\rangle &= -\left|g\right\rangle, \\ \hat{\sigma}_z \left|e\right\rangle &= \left|e\right\rangle. \end{aligned} \tag{2.25}$$

2.2.3 Qubit decoherence

When the qubit is coupled to the outside world, a variety of factors in its environment will degrade its performance. These can be characterized in two categories: relaxation and dephasing. Relaxation is the process in which the qubit state is changed by its interaction with the environment, whereas dephasing doesn't involve a change in the qubit's excitation. Instead, dephasing causes noise in the relative phase between different quantum states such that a superposition state will lose its quantum coherence. Both decoherence processes can be modeled by writing its Lindbladian [91]

$$\mathcal{L}_{\mathrm{q}}(\rho) = \Gamma_{\downarrow} D[\hat{\sigma}_-](\rho) + \Gamma_{\uparrow} D[\hat{\sigma}_+](\rho) + \frac{\Gamma_{\phi}}{2} D[\hat{\sigma}_z](\rho), \tag{2.26}$$

where $\rho = \sum_{i,j=g,e} \rho_{ij} |i\rangle \langle j|$ is the density matrix of the qubit, $\Gamma_{\uparrow\downarrow}$ is the environmental excitation or relaxation rate of the qubit, and Γ_ϕ is the qubit's pure dephasing rate.

2.2.3.1 Relaxation

Random fluctuations in a coupled environmental parameter can cause qubit relaxation when they are resonant with the qubit frequency. For example, to control the gate voltage of a CPB qubit, we connect the qubit to an external voltage source. In this process, the qubit is also introduced to an outside electrical environmental impedance $Z(\omega)$, as shown in Fig. 2.4. Given by the Johnson-Nyquist formula, the voltage noise δV from the impedance is characterized by a two-sided noise spectral density

$$S_v(\omega) = \frac{2\hbar\omega}{1 - e^{-\hbar\omega/k_B T}} \mathrm{Re}\left[Z(\omega)\right], \tag{2.27}$$

and is related to a noise in the gate charge by $\delta n_g = C_g \delta V / 2e$. When resonant with the qubit transition, this noise can excite ($\uparrow$) or relax ($\downarrow$) the qubit at rates [92]

$$\Gamma^v_{\uparrow\downarrow} = \left(\frac{4E_c C_g}{e\hbar}\right)^2 \left|\langle g| \hat{\mathbf{n}} |e\rangle\right|^2 S_v(\mp\omega_\mathrm{q}). \tag{2.28}$$

In steady state, the qubit will be polarized with a mean excitation

$$P_e^{\mathrm{ss}} = \frac{\Gamma^v_\uparrow}{\Gamma^v_\uparrow + \Gamma^v_\downarrow}. \tag{2.29}$$

Consequently, to have a qubit naturally relax to its ground state in a dilution refrigerator at 25 mK, it is desirable to work with qubit frequencies $\omega_\mathrm{q} > 2\pi \times 3$ GHz, such that $\hbar\omega_\mathrm{q} \gg k_B T$. In this work, I use a qubit at frequency $\omega_\mathrm{q} \approx 2\pi \times 3.9$ GHz. In this limit, the voltage noise from the impedance would not excite the qubit ($\Gamma^v_\uparrow = 0$), and an excited qubit relaxes to its ground state at rate

$$\Gamma^v_\downarrow = 2\hbar\omega_\mathrm{q} \mathrm{Re}\big[Z(\omega_\mathrm{q})\big] \left(\frac{4E_c C_g}{e\hbar}\right)^2 \left|\langle g| \hat{\mathbf{n}} |e\rangle\right|^2. \tag{2.30}$$

This voltage-noise-induced qubit relaxation can be generalized to any circuit capacitively coupled to any type of qubits [93]. Specifically, in the case of a qubit coupled to a single-mode electrical cavity, this leads to the well-known Purcell effect [94], where the qubit relaxes through

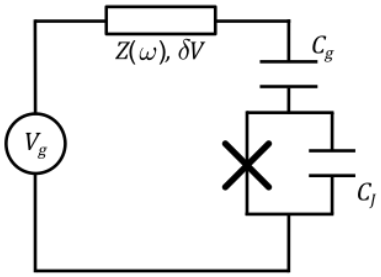

Figure 2.4: Voltage-noise-induced qubit relaxation
By connecting it to an external voltage source V_g, the qubit is also introduced to an outside electrical environmental impedance $Z(\omega)$. The voltage noise δV arising from the impedance can drive qubit transitions, and cause qubit relaxation.

the cavity at rate,

$$\Gamma_{\downarrow}^{\kappa} = \left(\frac{g_c}{\omega_{\mathrm{q}} - \omega_c}\right)^2 \kappa, \tag{2.31}$$

where g_c is the qubit-cavity coupling rate, ω_c is the cavity frequency, and κ is the coupling rate of the cavity to the outside world.

Another source of qubit relaxation is dielectric loss. When the electric field of the qubit passes through the dielectric materials surrounding it, such as the substrate material or the insulating layer between the junctions, energy can be lost in the process. The resulting loss rate is proportional to the loss tangent of the dielectric material. When the electric field passes through multiple materials, the contribution to the dielectric relaxation rate from each material is weighted by their participation ratios.

The overall qubit relaxation rate [92]

$$\Gamma_1 = \Gamma_{\uparrow} + \Gamma_{\downarrow}$$

sums over all sources of relaxation, and corresponds to the rate for the qubit to return to its thermal equilibrium. For a gigahertz-frequency qubit thermalized to the base temperature of a dilution refrigerator, $\Gamma_{\uparrow} \approx 0$, and $\Gamma_1 \approx \Gamma_{\downarrow}$.

2.2.3.2 Dephasing

The qubit dephasing is generally understood as fluctuations of the qubit frequency, which causes the qubit to accumulate a random phase. Qubit relaxations will dephase the qubit at a rate $\Gamma_1/2$ [91]. In addition, there can be fluctuations in the qubit frequency during the the course of one qubit relaxation, labeled as pure dephasing rate Γ_ϕ. This is typically caused by noise at frequencies much lower than the qubit frequency. Finally, if the fluctuations occur at even longer timescales, varying from experiment to experiment, they create an ensemble dephasing rate Γ_ϕ^*. Because they are not intrinsic to a single experiment, this last type of ensemble dephasing can be reduced by certain experimental techniques, such as using spin-echo protocols or post-selecting on the qubit frequency. The overall qubit dephasing rate is given by the sum of all these rates,

$$\frac{\Gamma_2}{2} = \frac{\Gamma_1}{2} + \Gamma_\phi + \Gamma_\phi^*. \tag{2.32}$$

A major source of dephasing for a CPB qubit is charge noise. Because of the strong dependence of qubit frequency on gate-charge (Eqn.(2.24)), a small fluctuation in n_g or V_g can lead to large changes in ω_q and dephase the qubit. To reduce this detrimental effect, a CPB qubit is often operated at the charge degeneracy point, where the qubit energy become first-order insensitive to charge. Nevertheless at this "sweet-spot", charge noise leads to a dephasing rate Γ_ϕ through the curvature of the charge-dispersion [84],

$$\Gamma_\phi \propto \partial^2\omega_\mathrm{q}/\partial {n_g}^2\Big|_{n_g=1/2} = (8E_c)^2/E_J. \tag{2.33}$$

A more devastating source of dephasing comes from quasiparticles. These are single-electron-like excitations residing in a superconductor, created by either thermal excitations or other non-equilibrium processes such as the absorption of electromagnetic irradiation from cosmic rays or higher-temperature environments [95]. At the base temperature of a dilution refrigerator, the quasiparticle population is dominated by the non-equilibrium processes. In aluminum-based superconducting qubits, the quasiparticle density is typically found to be within the range of 0.1 – 10 μm^{-3} [70, 96, 97]. When a single quasiparticle tunnels across the Josephson junction, it will

change the gate charge by one electron. For a CPB qubit operating at the charge degeneracy, the tunnelling of a quasiparticle with bring the qubit to $n_g = 1$, and drastically change the qubit frequency from $E_J/\hbar$ to $4E_c/\hbar$. One solution to alleviate this problem is to reduce the probability of these tunneling events by reducing the number of available quasiparticles. This can be achieved by simply limiting the size of the junction electrodes. Alternatively, the quasiparticle density can be reduced by using quasiparticle traps composed of either normal metal [98, 99] or magnetic vortices [97, 100, 101].

2.2.4 The transmon limit

Going toward the transmon regime (i.e., $E_J \gg E_c$) [84] offers another solution to the problems of both quasiparticle and charge-noise-induced qubit dephasing. In this limit, the normal mode energies of the nonlinear circuit become increasingly insensitive to charge. Instead of being the super-position of charge states $|\mathbf{n}\rangle$, the eigenstates of the circuit in this transmon regime are better described by the quantum phase $\hat{\phi}$ of the superconducting island, and their wavefunctions are given by Mathieu functions [102].

However, the decreased charge-sensitivity comes at the cost of a reduced anharmonicity. Instead of a simple two-level system, the nonlinear circuit in the transmon regime is often approximated as a weakly anharmonic oscillator,

$$H = \sqrt{8E_cE_J}(\hat{b}^\dagger\hat{b} + \frac{1}{2}) - \frac{E_c}{12}(\hat{b} + \hat{b}^\dagger)^4, \tag{2.34}$$

where $\hat{b}$, $\hat{b}^\dagger$ are the annihilation and creation operator for the harmonic oscillator approximating the circuit, and are related to the original phase and Cooper-pair operators according to [103],

$$\begin{aligned} \hat{\mathbf{n}} &= \left(\frac{E_J}{8E_c}\right)^{1/4} \frac{1}{\sqrt{2}}(\hat{b}^\dagger - \hat{b}), \\ \hat{\phi} &= i\left(\frac{8E_c}{E_J}\right)^{1/4} \frac{1}{\sqrt{2}}(\hat{b}^\dagger + \hat{b}). \end{aligned} \tag{2.35}$$

In this limit, the transition frequency $\omega_{j,j+1}$ between neighboring eigenstates of the oscillator $|j\rangle \leftrightarrow$

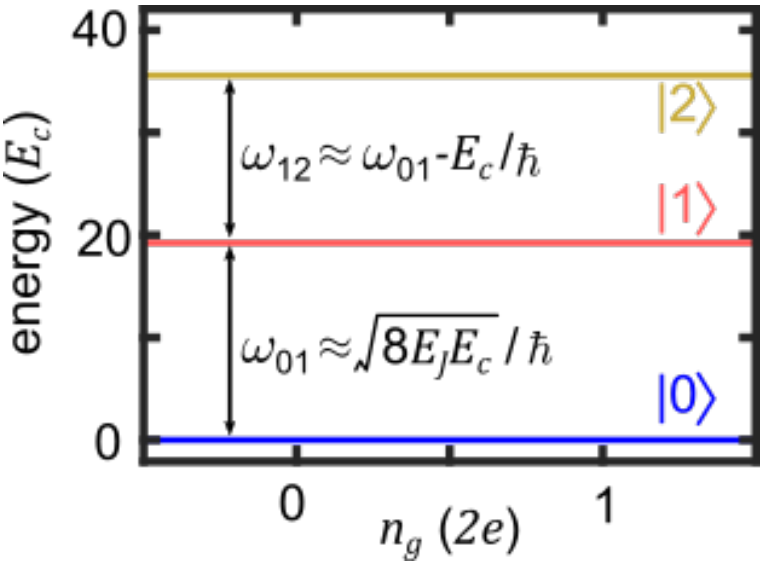

Figure 2.5: A transmon qubit
By making $E_J \gg E_c$, the qubit enters the transmon regime, and its energy becomes effectively insensitive to the gate-charge. Here, I plot the energy landscape of a transmon qubit with $E_J = 100E_c$ as a function of n_g. The energy is normalized to E_c, and chosen such that the lowest energy state $|0\rangle$ has energy $E_0 = 0$ at $n_g = 0$. The lowest two energy levels can be treated as a qubit, with a qubit frequency $\omega_q = \omega_{01} \approx \sqrt{8E_JE_c}/\hbar$. However, the insensitivity to gate-charge comes at the cost of a lowered anharmonicity, $\omega_{12} - \omega_{01} \approx E_c/\hbar$, small compared to ω_{01}.

$|j+1\rangle$ is different from $\omega_{j+1,j+2}$ by a weak anharmonicity,

$$\omega_{j+1,j+2} - \omega_{j,j+1} = \frac{E_c}{\hbar} \ll \omega_{01} = \frac{1}{\hbar}\sqrt{8E_cE_J}. \tag{2.36}$$

Nevertheless, when this anharmonicity is larger than the spectral width of an external drive resonant with ω_{01}, the nonlinear circuit can be treated as an effective two-level system consisting only of the lowest two energy levels, with a qubit frequency given by

$$\omega_{\mathrm{q}} = \omega_{01} = \frac{1}{\hbar}\sqrt{8E_cE_J}. \tag{2.37}$$

Because the charge-sensitivity decreases faster than anharmonicity [84], nonlinear circuits in the transmon regime can become effectively insensitive to charge fluctuations while remaining anharmonic enough to be considered a qubit.

It is important to note here that being insensitive to charge does not mean the qubit cannot be coupled to charge. Indeed, numerous experiments [47, 67, 45] have demonstrated the coupling between transmon qubits and electric fields that drive the gate-voltage V_g. Similarly, transmon qubits can also be coupled to mechanical oscillators through charge, as I show in the next section.

2.3 Qubit-mechanics interaction

Having introduced both building blocks, I now discuss a coupled system between a superconducting qubit and a mechanical oscillator. By altering the separation between two electrodes, the mechanical motion can modulate n_g of a charge-sensitive qubit through a position-dependent gate-capacitance,

$$C_g = C_{\mathrm{m}}(x) = \frac{C_{\mathrm{m}}^0}{1 + x/x_0}, \tag{2.38}$$

where x is the position of the oscillator, x_0 is the static separation between the electrodes, and $C_{\mathrm{m}}^0 = C_{\mathrm{m}}(0)$ is the static gate-capacitance. Consequently, the motion alters the qubit energy to created a coupled qubit-mechanical system. In this section, I explore theoretically the effects of this coupling.

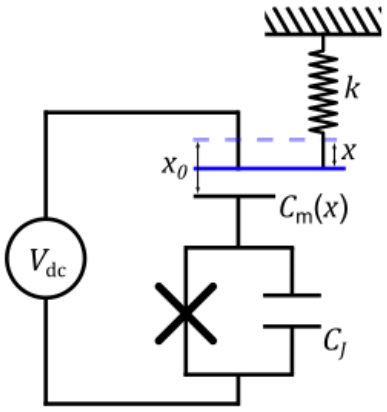

Figure 2.6: A coupled qubit-mechanical system
A mechanical oscillator (blue) held by a spring of constant k is suspended above another electrode to create a capacitor. When the oscillator is displaced from its static position x_0 by an amount x, it changes the separation between the two capacitor electrodes, and creates a position-dependent capacitance $C_{\mathrm{m}}(x)$. When this capacitance is used as the gate capacitance of a charge-sensitive qubit, an applied dc-voltage V_{dc} converts the mechanical motion into a modulation on the qubit's gate-charge n_g. Consequently, this motion-induced n_g modulation couples the mechanical motion to the qubit's electrostatic energy.

2.3.1 Coupling a mechanical oscillator to a charge-sensitive qubit

To start, I find the Hamiltonian for a coupled system when the qubit is in the CPB regime. By applying a dc-voltage $V_{\rm dc}$, the motion of the mechanical oscillator is converted into a position-dependent gate-charge, $n_g(x) = V_{\rm dc} \times C_{\rm m}(x)/2e$. This creates an interaction,

$$H_I = \hat{x}\frac{\partial}{\partial x}H = 8E_c\frac{\partial n_g(x)}{\partial x}x_{zp}(\hat{a}+\hat{a}^\dagger)(\hat{\mathbf{n}}-n_g), \tag{2.39}$$

where the mechanical position $\hat{x} = x_{zp}(\hat{a}+\hat{a}^\dagger)$ is coupled to the Cooper-pair number operator $\hat{\mathbf{n}}$. For small motional amplitudes such that the charge modulation is smaller than a single Cooper-pair, the CPB charge basis can be restricted to two adjacent charge states $\{|\mathbf{0}\rangle, |\mathbf{1}\rangle\}$. Because a qubit in the CPB regime has a strong anharmonicity, it can be considered as an effective two-level system formed by the lowest two energy levels. Defining $\hat{\sigma}_z$ to align with the its energy quantization axis (Eqn.(2.20)-(2.23)), I find an interaction Hamiltonian,

$$\begin{aligned} H_I = \hat{x}\frac{\partial}{\partial x}H &= 4E_c\frac{\partial n_g(x)}{\partial x}x_{zp}(\hat{a}+\hat{a}^\dagger)\big(\hat{\sigma}_z\cos\theta_0 - \hat{\sigma}_x\sin\theta_0\big) \\ &= \hbar g_{\rm m}\big(\hat{a}+\hat{a}^\dagger\big)\big(\hat{\sigma}_z\cos\theta_0 - \hat{\sigma}_x\sin\theta_0\big), \end{aligned} \tag{2.40}$$

where $\theta_0 = \arctan[E_J/4E_c(1-2n_g)]$ is the mixing angle between the charging energy and Josephson energy, and

$$g_{\rm m} = \frac{1}{\hbar}4E_c\frac{\partial n_g(x)}{\partial x}x_{zp} = \frac{4E_c}{2e\hbar}C_{\rm m}^0\frac{x_{zp}}{x_0}V_{\rm dc} \tag{2.41}$$

is the single-phonon qubit-mechanics coupling rate.

Within this Hamiltonian, there are two types of couplings: longitudinal and transverse, as shown in Fig. 2.7. Away from the charge degeneracy, the longitudinal coupling

$$\hbar g_{\rm m}\cos\theta_0\big(\hat{a}+\hat{a}^\dagger\big)\hat{\sigma}_z, \tag{2.42}$$

where mechanical motion changes the qubit energy with a coupling rate $g_{\rm m}^z = g_{\rm m}\cos\theta_0$ dominates. As expected from the qubit energy's charge dispersion (Fig. 2.2), this coupling changes sign at every half-integer gate-charge. Because a positive mechanical displacement x increases the separation between the electrodes and decreases the gate capacitance, it reduces the gate-charge n_g.

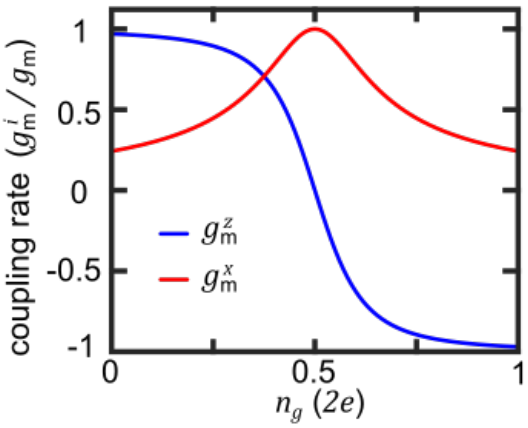

Figure 2.7: Longitudinal vs. transverse coupling
There are two types of qubit-mechanics coupling in a CPB qubit: longitudinal (g_{m}^z, blue) and transversal (g_{m}^x, red). Away from the charge degeneracy point, the longitudinal coupling, where mechanical motion changes the qubit energy, dominates with coupling rate g_m^z. Because a positive displacement reduces the gate charge, g_{m}^z is positive between $0 < n_g < 1/2$ and negative between $1/2 < n_g < 1$. At the charge degeneracy, the qubit energy becomes first-order insensitive to gate-charge, and g_{m}^z vanishes. Instead, the coupling rotates entirely to a transversal coupling, where the mechanical motion drives the qubit excitation.

Consequently, the smaller n_g leads to a higher qubit energy between $0 < n_g < 1/2$ and a positive g_{m}^z, and vice versa between $1/2 < n_g < 1$. However, at the charge degeneracy, the qubit energy become in first order insensitive to gate-charge, and the longitudinal coupling vanishes. Instead, the coupling rotates entirely to a transversal coupling, where the mechanical motion drives the qubit excitation at rate g_{m}.

Similarly, the charge insensitivity of a transmon qubit does not prevent it from being coupled to mechanical motion, but merely rotates the coupling to a transversal one that drives qubit excitation. To see this, I begin by rewriting Eqn.(2.39) in the uncoupled qubit eigenbasis,

$$\begin{aligned} H_I &= 2\hbar g_{\mathrm{m}}(\hat{a}+\hat{a}^\dagger)(\hat{\mathbf{n}}-n_g) \\ &= 2\hbar \sum_{i,j} g_{i,j}\,|i\rangle_b\,{}_b\langle j|(\hat{a}+\hat{a}^\dagger), \end{aligned} \tag{2.43}$$

where $|i\rangle_b$ is the i-th eigenstate of the uncoupled nonlinear oscillator that acts as a qubit, g_{m} is given by Eqn.(2.41), and the matrix element

$$g_{i,j} = g_{\mathrm{m}}\,{}_b\langle i|\hat{\mathbf{n}}\,|j\rangle_b\,. \tag{2.44}$$

Approximating the transmon qubit as a weakly anharmonic oscillator according to Eqn.(2.34), the above matrix elements are, to first-order,

$$\begin{aligned} g_{j,j} &= 0, \\ g_{j,j+1} = g_{j+1,j} &= g_{\mathrm{m}}\left(\frac{E_J}{8E_c}\right)^{1/4}\sqrt{\frac{j+1}{2}}, \\ g_{j,j+l} &\approx 0 \quad \forall \quad |l|>1, \end{aligned} \tag{2.45}$$

showing that the mechanical motion couples to a transmon qubit only transversely, driving excitations between adjacent qubit states. For clarity in this chapter, I restrict the qubit to the lowest two energy states, and write the transmon-mechanics interaction using Pauli matrices as

$$H_I = \hbar g_{\mathrm{m}}^x(\hat{a}+\hat{a}^\dagger)\hat{\sigma}_x, \tag{2.46}$$

where

$$g_{\mathrm{m}}^x = g_{01} = \left(\frac{E_J}{32E_c}\right)^{1/4}\frac{4E_c}{2e\hbar}C_{\mathrm{m}}^0\frac{x_{zp}}{x_0}V_{\mathrm{dc}} \tag{2.47}$$

However, because a transmon qubit is only weakly anharmonic, it is highly inaccurate to ignore the mechanical coupling to higher-level qubit states. Indeed, as I will discuss in the next chapter (Sec.3.1), these couplings can strongly diminish the observable effects of a transmon-mechanics interaction.

2.3.2 The Rabi Hamiltonian

The coupled qubit-mechanical system is described by a Rabi Hamiltonian either by using a transmon qubit or by working at the sweet-spot of a CPB qubit,

$$H_{\text{Rabi}}/\hbar = \frac{1}{2}\omega_{\text{q}}\hat{\sigma}_z + \omega_{\text{m}}\hat{a}^\dagger\hat{a} + g_{\text{m}}^x\hat{\sigma}_x(\hat{a}^\dagger + \hat{a}), \tag{2.48}$$

where g_{m}^x is given by either Eqn.(2.41) for a CPB qubit or Eqn.(2.47) for a transmon qubit. If the qubit and the mechanical oscillator were resonant, the energy would slosh between the two at rate g_{m}^x. However, because we work with gigahertz-frequency qubits and megahertz-frequency mechanical oscillators, the large difference in their resonant frequencies impedes the spontaneous transfer of energy.

2.3.3 Dispersive limit and an effective quadratic interaction

Instead, the qubit energy become sensitive to the square of the mechanical displacement, creating an effective quadratic coupling. To see this, I apply an unitary transformation [104],

$$\hat{U}_{\text{disp}} = \exp\left[\frac{g_{\text{m}}^x}{\Delta}(\hat{a}\hat{\sigma}_+ - \hat{a}^\dagger\hat{\sigma}_-) + \frac{g_{\text{m}}^x}{\Sigma}(\hat{a}^\dagger\hat{\sigma}_+ - \hat{a}\hat{\sigma}_-)\right], \tag{2.49}$$

with $\Delta = \omega_{\text{q}} - \omega_{\text{m}}$, and $\Sigma = \omega_{\text{q}} + \omega_{\text{m}}$, to remove the effects of spontaneous energy exchange. Contrary to the standard dispersive transformations employed in circuit quantum-electrodynamics (cQED) [47, 105, 106, 107], Eqn.(2.49) accounts for the counter-rotating terms $\hat{a}^\dagger\hat{\sigma}_+$ and $\hat{a}\hat{\sigma}_-$ in the Rabi Hamiltonian because $\omega_{\text{m}} \ll \omega_{\text{q}}$. Keeping to the first order of g_{m}/Δ and g_{m}/Σ, I find,

$$H_{\text{disp}} = \hbar\omega_{\text{m}}\hat{a}^\dagger\hat{a} + \frac{1}{2}\hbar\omega_{\text{q}}\hat{\sigma}_z + \frac{1}{2}\hbar\chi_{\text{m}}\hat{\sigma}_z(\hat{a} + \hat{a}^\dagger)^2, \tag{2.50}$$

where

$$\chi_{\mathrm{m}} = \frac{(g_{\mathrm{m}}^{x})^2}{\Delta} + \frac{(g_{\mathrm{m}}^{x})^2}{\Sigma} \tag{2.51}$$

includes the Block-Siegert shift [108]. For large qubit frequencies such that $\omega_{\mathrm{q}} \gg g_{\mathrm{m}}^{x}$, performing this dispersive transformation doesn't alter the eigenstate of the coupled system [109]. Because a qubit excitation is much faster than the mechanical dynamics, the position can be regarded as stationary under a sudden qubit excitation. The physics is clear if the Hamiltonian is written as

$$H_{\mathrm{eff}} = \frac{1}{2}\hbar\omega_{\mathrm{q}}\hat{\sigma}_z + \frac{\hat{p}^2}{2m} + \frac{1}{2}k\hat{x}^2 + \frac{1}{2}k\left(\frac{2\chi_{\mathrm{m}}}{\omega_{\mathrm{m}}}\right)\hat{\sigma}_z\hat{x}^2, \tag{2.52}$$

where ω_{m} and ω_{q} are the uncoupled mechanical and qubit frequency, m and k are the mass and the spring constant of the mechanical oscillator, and $\hat{x} = x_{zp}(\hat{a}^\dagger + \hat{a})$, and $\hat{p} = im\omega_{\mathrm{m}}x_{zp}(\hat{a}^\dagger - \hat{a})$ are the oscillator's position and momentum operators respectively.

The quadratic coupling can be understood as a qubit-state controlled mechanical spring constant,

$$k(\hat{\sigma}_z) = k\left(1 + \frac{2\chi_{\mathrm{m}}}{\omega_{\mathrm{m}}}\hat{\sigma}_z\right). \tag{2.53}$$

A change in qubit state simultaneously alters both the mechanical frequency

$$\omega_{\mathrm{m}}(\hat{\sigma}_z) = \sqrt{k(\hat{\sigma}_z)/m} \tag{2.54}$$

and the mechanical impedance

$$Z_{\mathrm{m}}(\hat{\sigma}_z) = \sqrt{k(\hat{\sigma}_z)m}. \tag{2.55}$$

These two changes corresponds to two different physical phenomena.

First, the dispersive shift of the mechanical frequency leads to a phonon-number-dependent Stark-shift of the qubit resonance,

$$\omega_{\mathrm{q}}^{|n\rangle} = (\omega_{\mathrm{q}} + \chi_{\mathrm{m}}) + 2\chi_{\mathrm{m}}n, \tag{2.56}$$

where n is the number of phonons in the mechanical oscillator. When this dispersive shift is large enough, one can address individual phonon numbers using the qubit, as I will discuss in Sec.2.3.4.

Second, the impedance determines the spatial scale of the mechanical wavefunction. This changing impedance allows for prominent sideband transitions, where a qubit excitation also causes the creation or annihilation of mechanical phonons. To understand this effect, I introduce the Frank-Condon description.

2.3.3.1 Frank-Condon description

As shown in Fig. 2.8, the mechanical spatial wavefunction for a phonon Fock state $|n\rangle$ is given by [110],

$$\psi(x,n,\sigma_z) = \frac{1}{\sqrt{2^n n!}} \left(\frac{Z_{\mathrm{m}}^{\pm}}{\pi\hbar}\right)^{\frac{1}{4}} e^{Z_{\mathrm{m}}^{\pm}x^2/2\hbar} H_n\left(x\sqrt{\frac{Z_{\mathrm{m}}^{\pm}}{\hbar}}\right), \tag{2.57}$$

where $\sigma_z = \pm 1$ is the qubit state, $Z_{\mathrm{m}}^{\pm} = \sqrt{k(\pm 1)m}$ is the qubit-state-dependent mechanical impedance, and the functions $H_n(z)$ are Hermite polynomials.

As such, a qubit excitation can connect otherwise orthogonal mechanical states, according to the Frank-Condon principle [111, 112]. The probability of such a transition is given by the overlap in the spatial wavefunctions,

$$P_{n,m} \propto \int_{-\infty}^{\infty} \psi^*(x,n,-1)\psi(x,m,1)dx, \tag{2.58}$$

where $P_{n,m}$ is the probability of observing transition $|g,n\rangle \rightarrow |e,m\rangle$. Because of the symmetry in the mechanical potential, only transitions that change the phonon occupation by an even number are expected. When $m = n$, the qubit transition preserves the mechanical phonon number. However, when $m > n$, a blue sideband transition is realized, where phonons are added while exciting the qubit. Vice versa when $m < n$, a red sideband transition is realized, which cools the mechanical oscillator while exciting the qubit.

2.3.3.2 System eigenstates

To provide a quantitative understanding of the interaction and be able to make predictions, I directly diagonalize the Hamiltonian of Eqn.(2.50) to find the system eigenstates. To do this, I

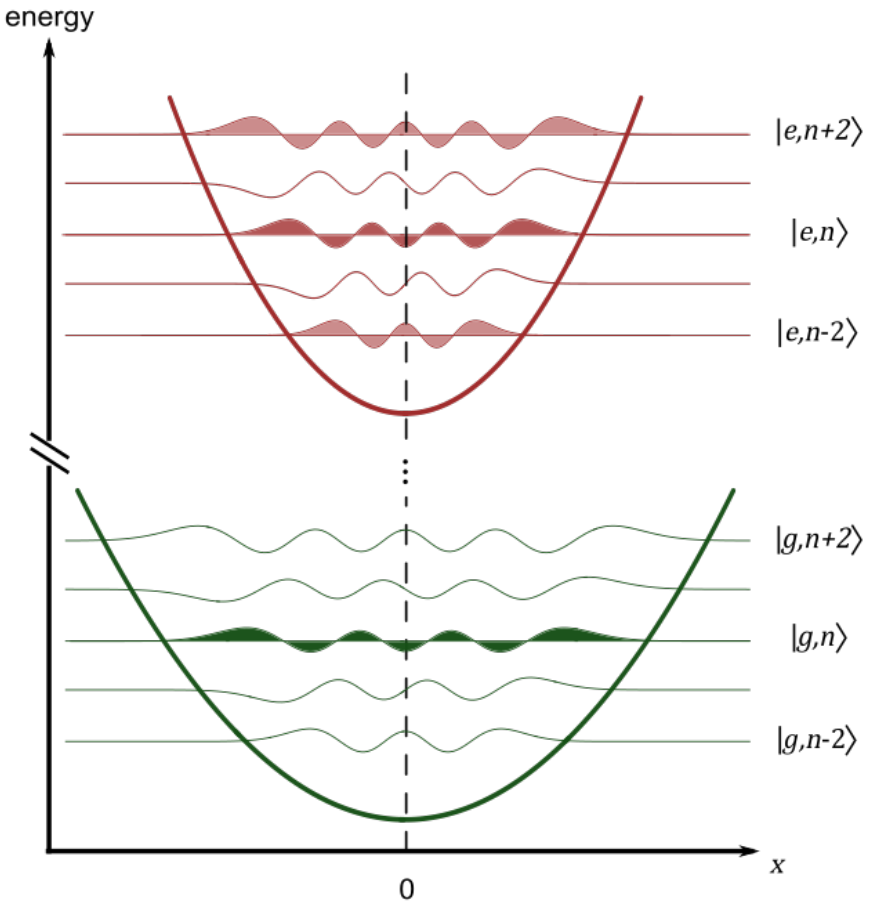

Figure 2.8: Frank-Condon description
A qubit excitation causes a sudden change of the mechanical potential (parabolas) and a non-zero overlap between spatial wavefunctions (lines) of different mechanical states. Because of symmetry, this process only connects an initial state $|n, g\rangle$ (shaded green) with states of the same mechanical parity $|n, e\rangle$ (shaded red), creating or annihilating phonons by pairs.

introduce an unitary transformation [113, 114],

$$\hat{S}\left(\imath(\hat{\sigma}_z)\right) = \exp\left[\frac{1}{2}\imath(\hat{\sigma}_z)(\hat{a}^2 - \hat{a}^{\dagger 2})\right], \tag{2.59}$$

where for a small dispersive shift $\chi_\mathrm{m} \ll \omega_\mathrm{m}$ [2] ,

$$\imath(\hat{\sigma}_z) = \frac{1}{2}\mathrm{arctanh}\left(\frac{\chi_\mathrm{m}\hat{\sigma}_z}{\omega_\mathrm{m} + \chi_\mathrm{m}\hat{\sigma}_z}\right) \approx \frac{\chi_\mathrm{m}}{2\omega_\mathrm{m}}\hat{\sigma}_z \equiv r\hat{\sigma}_z. \tag{2.60}$$

Because $\hat{S}^\dagger(r)\hat{S}(r) = \hat{S}(-r)\hat{S}(r) = \hat{1}$, $\hat{S}^\dagger(r) = \hat{S}(-r)$. This unitary transformation diagonalizes the Hamiltonian to,

$$H_{sq} = \hbar\sum_n \left\{\omega_n^- \left|g\right\rangle_b \left|n\right\rangle_b {}_b\!\left\langle n\right| {}_b\!\left\langle g\right| + \omega_n^+ \left|e\right\rangle_b \left|n\right\rangle_b {}_b\!\left\langle n\right| {}_b\!\left\langle e\right|\right\} \tag{2.61}$$

where $\left|g\right\rangle_b$, $\left|e\right\rangle_b$, and $\left|n\right\rangle_b$ are the eigenstates of the uncoupled qubit and mechanical oscillator respectively. The eigenvalues are given by

$$\omega_n^\pm = n\omega_\mathrm{m} \pm \frac{1}{2}(\omega_\mathrm{q} + 2\chi_\mathrm{m} n) = n\omega_\mathrm{m} \pm \frac{1}{2}\omega_\mathrm{q}^{|n\rangle}, \tag{2.62}$$

where $\omega_\mathrm{q}^{|n\rangle}$ is the phonon-number-dependent qubit frequency given by Eqn.(2.56). The eigenstates of the diagonalized Hamiltonian $\left|g\right\rangle_b \left|n\right\rangle_b$ and $\left|e\right\rangle_b \left|n\right\rangle_b$ are related to the the eigenstates of the original Rabi Hamiltonian Eqn.(2.50) through the unitary transformation $\hat{S}\left(\imath(\hat{\sigma}_z)\right)$,

$$\begin{aligned} \left|g,n\right\rangle &= \hat{S}(r\hat{\sigma}_z)\left|g\right\rangle_b \left|n\right\rangle_b = \left|g\right\rangle_b \hat{S}(-r)\left|n\right\rangle_b, \\ \left|e,n\right\rangle &= \hat{S}(r\hat{\sigma}_z)\left|e\right\rangle_b \left|n\right\rangle_b = \left|e\right\rangle_b \hat{S}(r)\left|n\right\rangle_b. \end{aligned} \tag{2.63}$$

Compared to the uncoupled mechanical oscillator, the excited-state qubit stiffens the mechanical spring, and squeezes the oscillator energy along its position axis. Similarly, the qubit ground state loosens the mechanical spring, and anti-squeezes the oscillator energy along its position axis.

2.3.4 System dynamics

Having diagonalized the Hamiltonian, I now proceed to describe the time evolution of the coupled qubit-mechanical system. This is given by the master equation,

$$\frac{d}{dt}\rho = -i[H,\rho] + \mathcal{L}_\mathrm{qm}\rho, \tag{2.64}$$

[2] In this work, I explore a qubit-mechanical system with a maximum coupling rate $g_\mathrm{m} \approx 2\pi\times 80$ MHz (see Sec.4.2.2). Before this work, no experiment [81, 82, 83] has come close to such a large coupling rate value. Nevertheless, with a qubit frequency $\omega_\mathrm{q} \approx 2\pi \times 3.8$ GHz, this large coupling rate only corresponds to a dispersive shift $\chi_\mathrm{m} \approx 2\pi \times 3.2$ MHz, much less than $\omega_\mathrm{m} \approx 2\pi \times 25$ MHz.

where $\rho = \sum_{i,j} \rho_{ij} |i\rangle \langle j|$ is the density matrix, with eigenstates $|i\rangle$ and $|j\rangle$ given by Eqn.(2.63). $H = H_{\text{Rabi}} + H_d$ is the overall system Hamiltonian, containing the Rabi Hamiltonian of Eqn.(2.48) and contributions from any external drive H_d. Although this master equation contains all dynamics of the coupled system, it provides little insight. Instead, in this section, I attempt to achieve a more intuitive understanding by analyzing three extreme cases. Based on these understandings, in Sec.6.3.1, I will write a simplified master equation more suitable for simulating the experiments in this work.

2.3.4.1 Dissipative dynamics

First, I consider a system without any external drives to explore the dissipative dynamics. Because H_{Rabi} commutes with ρ, time evolution only arises from the system's interaction with its environmental bath, illustrated in Fig. 2.9 and described by the Lindbladian $\mathcal{L}_{\text{qm}}$ [115],

$$\mathcal{L}_{\text{qm}}(\rho) = \sum_i \frac{\Gamma_\phi}{2} D\Big[|i\rangle \langle i| \Big](\rho) + \sum_{i,j>i} \Gamma_{\text{q}}^{ij} D\Big[|i\rangle \langle j| \Big](\rho) + \sum_{i,j>i} \Gamma_{\text{m}}^{ij} D\Big[|i\rangle \langle j| \Big](\rho) + \sum_{i,j<i} \Gamma_{\text{m}}^{ij} D\Big[|j\rangle \langle i| \Big](\rho). \tag{2.65}$$

The first term describes the dephasing of the qubit, but is decoupled from the mechanical oscillator.

The second terms describes the system relaxation through the qubit channel,

$$\Gamma_{\text{q}}^{ij} = \Gamma_1 \left| \langle i| \hat{\sigma}_x |j\rangle \right|^2, \tag{2.66}$$

where Γ_1 is the qubit decay rate. Because $k_B T \ll \hbar\omega_{\text{q}}$, the qubit contains no thermal excitation, and the system can only relax from a higher-energy eigenstate $|j\rangle$ to a lower-energy state $|i\rangle$ $(j > i)$. Given the much larger qubit frequency ($\omega_{\text{q}} \gg \omega_{\text{m}}$), this relaxation process is dominated by the relaxation of the qubit state accompanied by a possible change of phonon number, $|e, n\rangle \mapsto |g, m\rangle$. Because $\hat{\sigma}_x$ operates on the uncoupled qubit eigenbasis $|g\rangle_b$ and $|e\rangle_b$, the relaxation rates can be further evaluated using Eqn.(2.63),

$$\Gamma_{\text{q}}^{ij} = \Gamma_1 |\alpha_{mn}^*|^2, \tag{2.67}$$

where $|i\rangle = |g, n\rangle$, $|j\rangle = |e, m\rangle$, and

$$\alpha_{mn}^* \equiv \langle g, m| \hat{\sigma}_x |e, n\rangle = {}_b\langle m| \hat{S}^\dagger(-2r) |n\rangle_b \tag{2.68}$$

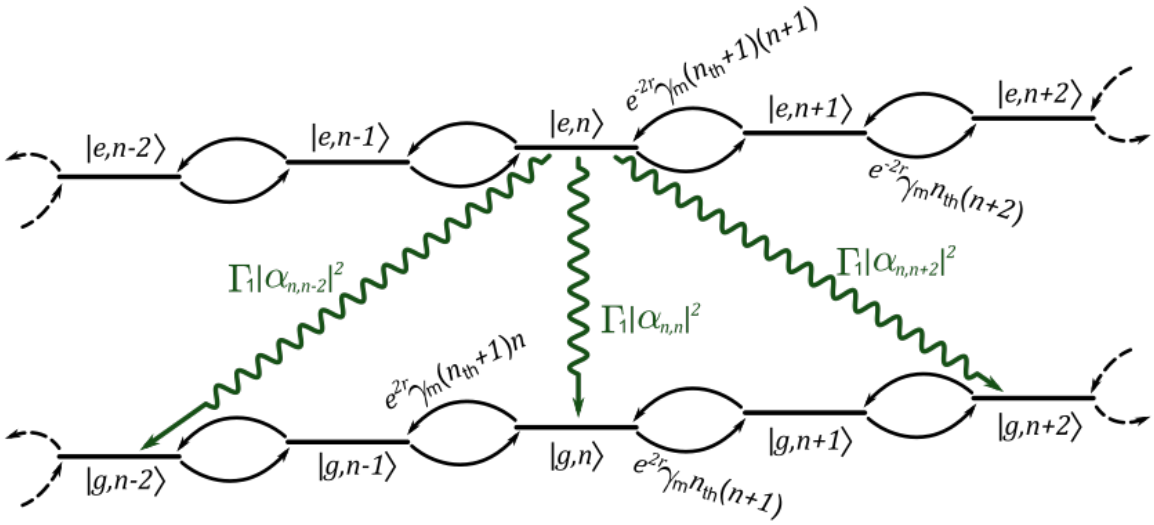

Figure 2.9: Decoherence of the qubit-mechanical system
A qubit in its excited state relaxes to the ground state at rate Γ_1. In the coupled qubit-mechanical system, because a decaying qubit causes a sudden change of mechanical spring constant, it can connect different mechanical states at rates $\Gamma_1|\alpha_{m,n}|^2$, proportional to the overlap between mechanical spatial wavefunctions of $|e,m\rangle$ and $|g,n\rangle$ (see Similar to Sec.2.3.3.1). Because of symmetry, this rate is only non-zero between states with phonon numbers that differ by an even value. The qubit-mechanics interaction also alters the mechanical relaxation, such that the mechanical decay rate becomes qubit-state dependent $\gamma_{\mathrm{m}}(\hat{\sigma}_z) = e^{-2\hat{\sigma}_z}\gamma_{\mathrm{m}}$. This relaxation process connects adjacent mechanical states of the same qubit excitation. Finally, all states also experience qubit dephasing, which is unaffected by the qubit-mechanics interaction. This dephasing process is not illustrated in this figure.

is the same overlap in spatial wavefunctions between different mechanical states as discussed in Sec.2.3.3.1, $|\alpha^*_{mn}|^2 = \int_{-\infty}^{\infty} \psi^*(x,m,1)\psi(x,n,-1)dx$. Consequently, a qubit relaxation can also change the phonon occupation by an even number.

Finally, the last two terms describe the dissipative dynamics from the mechanical channel. In addition to relaxation, the environmental bath can also excite the qubit-mechanical system by adding thermal phonons into the mechanical oscillator (because $k_B T \gg \hbar\omega_{\mathrm{m}}$). The rates of these processes are given by,

$$\Gamma_{\mathrm{m}}^{ij} = \begin{cases} \gamma_{\mathrm{m}}(n_{\mathrm{th}}+1)\left|\langle i|\,\hat{X}\,|j\rangle\right|^2 & j > i \text{ (relaxation)} \\ \gamma_{\mathrm{m}} n_{\mathrm{th}}\left|\langle j|\,\hat{X}\,|i\rangle\right|^2 & i > j \text{ (excitation)} \end{cases}, \tag{2.69}$$

where $\hat{X} = \hat{a}+\hat{a}^\dagger$, and n_{th} is given by Eqn.(2.10). Because $\hat{X}$ operates on the uncoupled mechanical eigenstates $|n\rangle_b$, the inner product in the above equation can be evaluated,

$$\begin{aligned} \langle g,n|\,\hat{X}\,|g,m\rangle &= e^{2r}\left(\sqrt{m}\delta_{m,n+1} + \sqrt{m+1}\delta_{m,n-1}\right), \\ \langle e,n|\,\hat{X}\,|e,m\rangle &= e^{-2r}\left(\sqrt{m}\delta_{m,n+1} + \sqrt{m+1}\delta_{m,n-1}\right), \end{aligned} \tag{2.70}$$

where $\delta_{m,n}$ is the Kronecker delta. Thus, this last term in the Lindbladian connects adjacent mechanical states under the same qubit excitation with a qubit-state dependent mechanical decay rate $\gamma_{\mathrm{m}}(\hat{\sigma}_z) = e^{-2\hat{\sigma}_z}\gamma_{\mathrm{m}}$.

2.3.4.2 Driven dynamics without dissipation

Next, I consider the dynamics of the system without any dissipation, but driven by a coherent signal applied to the qubit. The coherent qubit drive can be characterized by the Hamiltonian,

$$H_d(t) = 2\hbar\Omega_R\hat{\sigma}_x\cos(\omega_d t), \tag{2.71}$$

where Ω_R is the Rabi rate due to the external drive, and ω_d is the drive frequency. Instead of directly solving the master equation, I go into the interaction picture with

$$H_{\mathrm{Rabi}} = \hbar\sum_n \left(\omega_n^-\,|g,n\rangle\langle g,n| + \omega_n^+\,|e,n\rangle\langle e,n|\right), \tag{2.72}$$

where $\omega_n^{\pm}$ are the eigenenergies given by Eqn.(2.62). The resulting interaction Hamiltonian is

$$\begin{aligned}\mathcal{V}(t) &= e^{-iH_0t/\hbar}H_d(t)e^{iH_0t/\hbar} \\ &= \hbar\Omega_R\sum_{n,m}\left(\alpha^*_{mn}e^{-i\Delta^d_{mn}t}\left|g,n\right\rangle\left\langle e,m\right| + \alpha_{mn}e^{i\Delta^d_{mn}t}\left|e,m\right\rangle\left\langle g,n\right|\right),\end{aligned} \tag{2.73}$$

where $\alpha_{mn} = {}_b\langle m|\hat{S}(-2r)\left|n\right\rangle_b$ is the overlap between different motional states under a qubit flip (Eqn.(2.68)), and

$$\Delta^d_{mn} = \omega^+_{\mathrm{m}} - \omega^-_n - \omega_d = \omega_{\mathrm{q}}^{|n\rangle} + (m-n)(\omega_{\mathrm{m}} + \chi_{\mathrm{m}}) - \omega_d \tag{2.74}$$

is the detuning between the qubit drive and transition $|g,n\rangle \leftrightarrow |e,m\rangle$.

Assuming an initial state $|g,n\rangle$, the interaction Hamiltonian of Eqn.(2.73) identifies two types of resonant conditions. First, when

$$\omega_d = \omega_{\mathrm{q}}^{|n\rangle}, \tag{2.75}$$

the system will oscillate between states $|g,n\rangle \leftrightarrow |e,n\rangle$ at a rate

$$\Omega_{n,0} = \Omega_R|\alpha_{nn}| = \Omega_R\left|{}_b\langle n|\hat{S}(-2r)\left|n\right\rangle_b\right|, \tag{2.76}$$

exciting the qubit while preserving the mechanical phonon number. A second type of resonance corresponds to sideband transitions. When

$$\omega_d = \omega_{\mathrm{q}}^{|n\rangle} + 2l(\omega_{\mathrm{m}} + \chi_{\mathrm{m}}) \qquad (l \in \mathbb{Z}^{\neq}) \tag{2.77}$$

the system oscillates between states $|g,n\rangle \leftrightarrow |g,n+2l\rangle$ at a sideband rate of

$$\Omega_{n,2l} = \Omega_R|\alpha_{n+2l,n}| = \Omega_R\left|{}_b\langle n+2l|\hat{S}(-2r)\left|n\right\rangle_b\right|, \tag{2.78}$$

adding $2l$ phonons into the mechanical oscillator while exciting the qubit.

An interesting figure of merit in the above driven response of the qubit-mechanical system is the ratio $\chi_{\mathrm{m}}n/\omega_{\mathrm{m}}$. A change in the qubit excitation alters the mean mechanical energy by

$$\frac{1}{2}\delta k\langle\hat{x}^2\rangle = 2\hbar\chi_{\mathrm{m}}n, \tag{2.79}$$

where n is the initial phonon number. When this value is larger than the energy of two phonons $2\hbar\omega_{\mathrm{m}}$, a qubit transition is likely to alter the phonon number $|\alpha_{nn}|^2 \lesssim 0.5$. Thus, the limiting condition

$$\frac{\chi_{\mathrm{m}}}{\omega_{\mathrm{m}}} n \gtrsim 1 \tag{2.80}$$

signifies the entry into a regime where sideband transitions become dominant. In contrast to standard cQED systems [47, 105, 106, 107] where the large cavity frequency suppresses these sideband transitions, the small ω_{m} means that a qubit-mechanical system can display prominent sideband transitions even at a small phonon number, as I observe in Chapter 5.

2.3.4.3 A driven dissipative system

Finally, I consider the effect of the same coherent drive in a dissipative system. In particular, I am interested in the probability of finding the qubit in the excited state as a function of ω_d. These qubit spectra $P_e(\omega_d)$ are extremely useful monitors of the mechanical phonon distribution.

For simplicity, here I only consider the simple case of $r = \chi_{\mathrm{m}}/\omega_{\mathrm{m}} \approx 0$ such that $\alpha_{mn} = \delta_{mn}$. In this limit, the qubit dynamics become decoupled from the mechanical dynamics, and their interaction appears only as shifts in ω_{q} and ω_{m}. With exactly n phonons in the mechanical oscillator, the driven qubit-mechanical system oscillates between states $|g,n\rangle$ and $|e,n\rangle$ at rate Ω_R. For a weak qubit spectroscopic drive ($\Omega_R \ll \Gamma_1, \Gamma_2$), the effective two-level system spanned by states $\{|g,n\rangle, |e,n\rangle\}$ (Fig. 2.10(a)) reaches steady state with a characteristic time scale given by the qubit lifetime $T_1 = 1/\Gamma_1$. Because mechanical relaxation typically occurs at a much slower rate compared to the qubit decay $\gamma_{\mathrm{m}} \ll \Gamma_1$, the driven two-level system can reach steady-state before the phonon number changes. This steady-state qubit spectrum with exactly n phonons in the mechanical oscillator is described by a Lorentzian,

$$\begin{aligned} P_e^{|n\rangle}(\omega_d) &= \frac{\Omega_R^2 \Gamma_2/4\Gamma_1}{\Delta_n^2 + (\Gamma_2/2)^2 + \Omega_R^2 \Gamma_2/2\Gamma_1} \\ &= \frac{1}{2} \frac{(A\Gamma_2/2)^2}{\Delta_n^2 + (\Gamma_2/2)^2(1+A^2)}, \end{aligned} \tag{2.81}$$

where $\Delta_n = \omega_{\mathrm{q}}^{|n\rangle} - \omega_d$ is the detuning between the drive frequency and the qubit resonance, and

$$A = \Omega_R \sqrt{\frac{2}{\Gamma_1 \Gamma_2}} \tag{2.82}$$

is an unitless parameter describing the transition rate. This Lorentzian is centered at frequency $\omega_{\mathrm{q}}^{|n\rangle}$ with a maximum probability of finding the qubit excited state

$$P_e^{\mathrm{res}} = \frac{1}{2} \frac{A^2}{1 + A^2}, \tag{2.83}$$

and a full-width at half-maximum (FWHM) broadened by the drive power,

$$W_{\mathrm{spec}} = \Gamma_2 \sqrt{1 + A^2}. \tag{2.84}$$

When $r \neq 0$, the qubit excitation and relaxation can both change phonon numbers in the mechanical oscillator, which complicates the qubit spectrum significantly. I defer a more detailed discussion on this topic to a later chapter (see Sec.5.2.2). Nevertheless, from Sec.2.3.4.2, I can predict that the qubit spectrum will contain excitation peaks not only at the qubit resonance, but also at the sideband transition frequencies given by Eqn.(2.77).

Regardless of the value of r and the specific shape of the qubit spectrum $P_e^{|n\rangle}(\omega)$ for phonon Fock state $|n\rangle$, because the qubit resonance $\omega_{\mathrm{q}}^{|n\rangle}$ is phonon-number-dependent (Eqn.(2.56)), each phonon in the mechanical oscillator will shift its corresponding spectrum by an amount $2\chi_{\mathrm{m}} n$. Consequently for a statistical mixture of phonon Fock states in the mechanical oscillator, the overall qubit spectrum is given by a convolution between the phonon distribution $P(n)$ and $P_e^{|n\rangle}(\omega)$,

$$P_e(\omega) = \sum_n P(n) \times P_e^{|n\rangle}(\omega). \tag{2.85}$$

When $\Gamma_2 < 2\chi_{\mathrm{m}}$, the qubit spectrum produced by a weak spectroscopic drive becomes phonon-number-resolved, where $P_e^{|n\rangle}(\omega)$ from adjacent photon numbers are individually resolvable (Fig. 2.10(c)). In other words, this phonon-number-resolved regime allows a weak qubit drive to address transitions corresponding to individual phonon Fock states. Conversely, when $\Gamma_2 \geq 2\chi_{\mathrm{m}}$, individual photon peaks cannot be resolved directly in the qubit spectrum. Nevertheless, because of $\omega_{\mathrm{q}}^{|n\rangle}$,

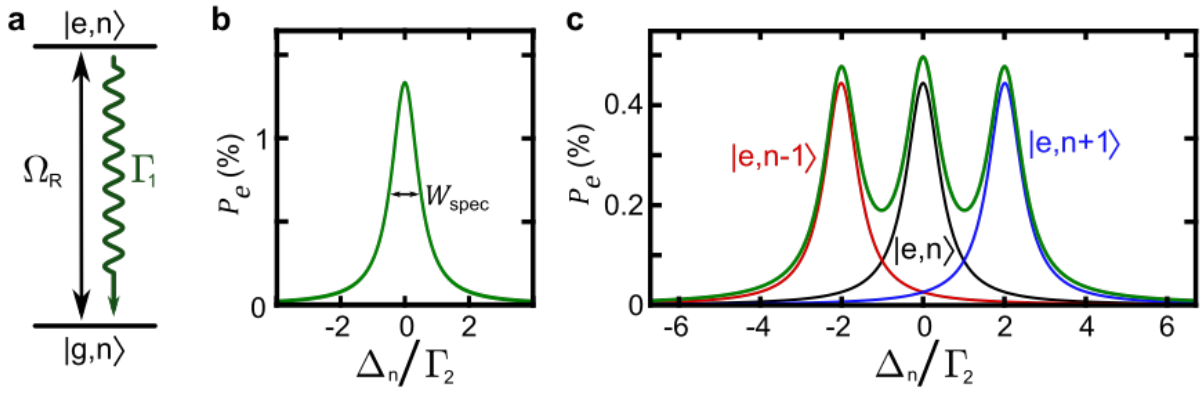

Figure 2.10: Spectrum of a simple driven dissipative system at $r = 0$
a, In the simple case of $r = 0$, the driven qubit-mechanical system can be simply modeled by a sum over many effective two-level systems spanned by $\{|g,n\rangle, |e,n\rangle\}$, each at frequency $\omega_q^{|n\rangle}$ given by Eqn.(2.56). A resonant qubit drive excites this effective two-level system at rate Ω_R. The qubit decays to its ground state at rate Γ_1, and dephases at rate $\Gamma_2/2$ **b,** Starting with an initial state $|g,n\rangle$, the steady-state qubit spectrum is given by a Lorentzian centered at detunning $\Delta_n = \omega_q^{|n\rangle} - \omega_d$, with a FWHM W_{spec} broadened by the drive strength Ω_R according to Eqn.(2.84). To plot this spectrum, I assumed the following parameters: $\Omega_R = 0.1\Gamma_1$, $\Gamma_2 = 3\Gamma_1$, and the qubit detuning is normalized to the minimum qubit FWHM Γ_2. **c,** When the mechanical state is composed by a statistical mixture of Fock states, the overall qubit spectrum is given by a convolution between the qubit spectra of different phonon Fock states and the phonon distribution. As an example, here I plot the overall qubit spectrum (green) for a mechanical state with $P(n-1) = P(n) = P(n+1) = 1/3$, with the same parameters in **b** and $2\chi_{\text{m}} = 2\Gamma_2$. In this phonon-resolved-regime, individual phonon Fock states result in distinct qubit excitation peaks, and are easily resolvable.

both phonon-conserving transitions (Eqn.2.75) and sideband transitions (Eqn.2.77) are phonon-number-sensitive. In this limit, the phonon distribution in the mechanical oscillator can be extracted through a deconvolution procedure with knowledge of both $P_e(\omega)$ and $P_e^{|n\rangle}(\omega)$, as will be discussed in Chapter 5. Moreover, a qubit drive can address a section of the phonon population with a characteristic width of

$$W = 2\chi_{\mathrm{m}}/\Gamma_2 \tag{2.86}$$

phonons. The power of the resulting phonon-number-sensitive sideband transitions will be explored in Chapter 6 & 7.

2.3.5 Beyond the Rabi Hamiltonian

Finally, I consider what happens when the gate-charge deviates from the sweet-spot of a CPB qubit. Although it is desirable to operate at the charge degeneracy point when working with a CPB qubit, charge noise — arising either from noise on the voltage bias or impurities in the material — can lead to deviations in the gate-charge δn_g. This introduces a residual $\hat{\sigma}_z$ coupling between the qubit energy and mechanical oscillator position. According to Eqn.(2.40), the overall Hamiltonian at $n_g = 1/2 + \delta n_g$ is

$$H_0^{\mathrm{rsd}} = \omega_{\mathrm{m}}\hat{a}^\dagger\hat{a} + \frac{1}{2}\omega_q\hat{\sigma}_z + g_{\mathrm{m}}^x\hat{\sigma}_x(\hat{a}+\hat{a}^\dagger) + g_{\mathrm{m}}^z\hat{\sigma}_z(\hat{a}+\hat{a}^\dagger). \tag{2.87}$$

where

$$\begin{aligned} g_{\mathrm{m}}^x &= g_{\mathrm{m}}\sin\theta_0, \\ g_{\mathrm{m}}^z &= g_{\mathrm{m}}\cos\theta_0, \end{aligned} \tag{2.88}$$

with θ_0 given by Eqn.(2.22).

The residual $\hat{\sigma}_z$ coupling can have important effects because it describes the coupling between qubit energy and mechanical position at the first order; whereas the $\hat{\sigma}_x$ coupling discussed above describes the second order coupling of position to energy. Thus, even a small coupling rate can significantly alter the qubit-mechanical system. To quantify its effect, I apply consecutively the following unitary transformations to diagonalize the Hamiltonian under the assumption of a small

deviation from the charge degeneracy point, $g_{\rm m}^z \ll g_{\rm m}^x \approx g_{\rm m}$,

$$H_{\rm diag}^{\rm rsd} = \hat{S}^\dagger\Big(\imath(\hat{\sigma}_z)\Big)\hat{\mathcal{D}}^\dagger\Big(\alpha(\hat{\sigma}_z)\Big)\hat{R}^\dagger\Big(\theta(\hat{X})\Big)\hat{U}_{\rm disp}^\dagger H_0^{\rm rsd}\hat{U}_{\rm disp}\hat{\mathcal{D}}\Big(\alpha(\hat{\sigma}_z)\Big)\hat{R}\Big(\theta(\hat{X})\Big)\hat{S}\Big(\imath(\hat{\sigma}_z)\Big), \quad (2.89)$$

where

$$\hat{R}\Big(\theta(\hat{X})\Big) = \exp\Big[-i\frac{1}{2}\hat{\sigma}_y \arctan\Big(\frac{\chi_{\rm m}^z\hat{X}^2}{\omega_q/2 + g_{\rm m}^z\hat{X} + \chi_{\rm m}\hat{X}^2}\Big)\Big] \approx \hat{\mathbb{1}} \quad (2.90)$$

is the qubit rotation operator with $\hat{X} = \hat{a} + \hat{a}^\dagger$, $\chi_{\rm m}^z = g_{\rm m}^x g_{\rm m}^z\big(\frac{1}{\Delta} + \frac{1}{\Sigma}\big) \ll \chi_{\rm m}$, and

$$\begin{aligned}\hat{\mathcal{D}}\Big(\alpha(\hat{\sigma}_z)\Big) &= \exp\Big[\alpha(\hat{\sigma}_z)\hat{a}^\dagger - \alpha^*(\hat{\sigma}_z)\hat{a}\Big],\\ \alpha(\hat{\sigma}_z) &= -\frac{g_{\rm m}^z\hat{\sigma}_z}{\omega_{\rm m} + 4\chi_{\rm m}\hat{\sigma}_z} \approx -\frac{g_{\rm m}^z}{\omega_{\rm m}}\hat{\sigma}_z \equiv \beta\hat{\sigma}_z\end{aligned} \quad (2.91)$$

is the qubit-state-dependent displacement operator. Similar to Eqn.(2.63), the eigenstate of $H_0^{\rm rsd}$ are given by,

$$\begin{aligned}|g,n\rangle &= \hat{S}(r\hat{\sigma}_z)\hat{\mathcal{D}}(\beta\hat{\sigma}_z)\,|g\rangle_b\,|n\rangle_b = |g\rangle_b\,\hat{S}(-r)\hat{\mathcal{D}}(-\beta)\,|n\rangle_b\,,\\ |e,n\rangle &= \hat{S}(r\hat{\sigma}_z)\hat{\mathcal{D}}(\beta\hat{\sigma}_z)\,|e\rangle_b\,|n\rangle_b = |e\rangle_b\,\hat{S}(r)\hat{\mathcal{D}}(\beta)\,|n\rangle_b\,.\end{aligned} \quad (2.92)$$

Consequently, the overlap between different mechanical states under a qubit transition is given by

$$\alpha_{mn}^{\rm rsd} = \langle e,m|\,\hat{\sigma}_+\,|g,n\rangle = {}_b\langle m|\hat{\mathcal{D}}^\dagger(\beta)\hat{S}(-2r)\hat{\mathcal{D}}(-\beta)\,|n\rangle_b\,. \quad (2.93)$$

Therefore, as the residual $\hat{\sigma}_z$ coupling breaks the symmetry in the system, a qubit excitation can connect all mechanical states. Starting from state $|g,n\rangle$, the coherent qubit drive of Eqn.(2.71) will drive oscillations between the initial state and state $|e,n+l\rangle$ at frequencies

$$\omega_d = \omega_{\rm q}^{|n\rangle} + l(\omega_{\rm m} + \chi_{\rm m}) \qquad (l \in \mathbb{Z}) \quad (2.94)$$

with transition rates

$$\Omega_{n,l} = \Omega_R|\alpha_{n+l,n}^{\rm rsd}|. \quad (2.95)$$

Chapter 3

Hybrid system design

In pursuit of reaching the phonon-number-resolved regime, I choose to use a CPB qubit to couple strongly to an anti-symmetric mode of a mechanical oscillator. In this chapter, I explain the reasons behind this choice, as well as other design considerations. In Sec.3.1, I explain the choice of a CPB qubit over a transmon as the better candidate for reaching a strong dispersive coupling rate χ_{m} larger than the qubit dephasing rate $\Gamma_2/2$. However, because the qubit-mechanics coupling arises from an external dc-voltage V_{dc} applied across the mechanically compliant capacitor, the maximum qubit-mechanics coupling rate is limited by a maximum dc-voltage V_{max}, beyond which the capacitor plates collapse under an electrostatic instability. This limitation is explained in Sec.3.2, and improved upon in Sec.3.3 by introducing an additional capacitance in series with the mechanically compliant capacitor. In Sec.3.4, I discuss another complication because of the applied dc-voltage: voltage fluctuations on V_{dc}, composed of both thermal and quantum fluctuation, can drive motion in the mechanical oscillator, and cause an increased mechanical relaxation. By coupling the qubit to the anti-symmetric, second mode of the mechanical oscillator, I create a symmetry that protects the mechanical motion from noise on the dc-voltage. In addition to the mechanical oscillator, in Sec.3.5, the qubit is coupled capacitively to a microwave resonator to allow for its control and readout. Taken together, these choices allow me to design a series of qubit-mechanical systems in Sec.3.6 that, when operated at the maximum voltage, could reach the phonon-number-resolved regime.

3.1 Choosing a CPB qubit

In this work, I choose to use a CPB qubit instead of a transmon because the transmon can only be coupled effectively to mechanical oscillators that have a resonant frequency ω_{m} close to the qubit frequency ω_{q}. Consequently with the low-frequency mechanical oscillators ($\omega_{\mathrm{m}} \ll \omega_{\mathrm{q}}$) that I'm interested in, a transmon-mechanics system will have a very small dispersive coupling rate χ_{m}. At its core, the reason for the vanishing χ_{m} lies with the weak anharmonicity of a transmon qubit. Because of this weak anharmonicity, it is inaccurate to simplify a transmon qubit to consist of only the lowest two energy levels as I did in the previous chapter (see Sec.2.2.4 & 2.3.3). Instead, the coupling between the mechanical oscillator and higher transmon levels will contribute to diminish the resulting dispersive shift χ_{m}.

Indeed, it can be shown [116] that a coupled transmon-mechanics system has a dispersive shift χ_{m} that approaches zero in the limit of $\omega_{\mathrm{m}}/\omega_{\mathrm{q}} \to 0$. By modeling the transmon qubit as a weakly anharmonic oscillator, the effects of mechanical coupling to higher transmon levels can be captured by writing the overall Hamiltonian,

$$H/\hbar = \omega_{\mathrm{q}}(\hat{b}^\dagger\hat{b} + \frac{1}{2}) - \frac{E_c}{12\hbar}(\hat{b} + \hat{b}^\dagger)^4 + \omega_{\mathrm{m}}(\hat{a}^\dagger\hat{a} + \frac{1}{2}) + g_{\mathrm{m}}^x(\hat{a}^\dagger + \hat{a})(\hat{b}^\dagger + \hat{b}). \tag{3.1}$$

In this equation, the first two terms describes the weakly anharmonic oscillator that is the transmon (Sec.2.2.4) with a qubit frequency $\omega_{\mathrm{q}} = \sqrt{8E_J E_c}/\hbar$ and anharmonicity $E_c/\hbar \ll \omega_{\mathrm{q}}$. The third term is the mechanical oscillator, with frequency ω_{m}. Finally, the last term corresponds to the transmon-mechanics coupling with coupling rate (see Sec.2.3.1)

$$g_{\mathrm{m}}^x = \left(\frac{E_J}{32E_c}\right)^{1/4} g_{\mathrm{m}}, \tag{3.2}$$

where

$$g_{\mathrm{m}} = \frac{1}{\hbar} 4E_c \frac{\partial n_g(x)}{\partial x} x_{zp}. \tag{3.3}$$

Without the second, anharmonic term in Eqn.(3.1), the Hamiltonian simply describes two coupled harmonic oscillators, whose normal modes can be found through direct diagonalization. Treating the anharmonic term as a perturbation (because $E_c/\hbar \ll \omega_{\mathrm{q}}$) and rewriting it in the basis of

these normal modes [117, 116], a phonon-number-dependent frequency shift on the transmon-mode (cross-Kerr) can be identified, which corresponds to the dispersive shift $\chi_{\rm m}$. Assuming a small mechanical frequency $\omega_{\rm m} \ll \omega_{\rm q}$ and keeping to the second-order in $g_{\rm m}^x/\omega_{\rm q}$, this dispersive shift is found to be [116]

$$\chi_{\rm m} \approx 4\frac{E_c}{\hbar}(g_{\rm m}^x)^2\frac{\omega_{\rm m}^2}{\Delta^2\Sigma^2} \approx 4\frac{E_c}{\hbar\omega_{\rm q}}\frac{(g_{\rm m}^x)^2}{\omega_{\rm q}}\left(\frac{\omega_{\rm m}}{\omega_{\rm q}}\right)^2 = 2\frac{(g_{\rm m}^x)^2}{\omega_{\rm q}}\sqrt{\frac{E_c}{2E_J}}\left(\frac{\omega_{\rm m}}{\omega_{\rm q}}\right)^2 \tag{3.4}$$

where $E_c \ll E_J$, and I approximate $\Delta = \omega_{\rm q} - \omega_{\rm m} \approx \omega_{\rm q}$ and $\Sigma = \omega_{\rm q} + \omega_{\rm m} \approx \omega_{\rm q}$. Comparing this result to the dispersive shift found when I only keep the lowest two energy levels of the transmon qubit (Eqn.(2.51)),

$$\chi_{\rm m} = \frac{(g_{\rm m}^x)^2}{\Delta} + \frac{(g_{\rm m}^x)^2}{\Sigma} \approx 2\frac{(g_{\rm m}^x)^2}{\omega_{\rm q}}, \tag{3.5}$$

the detrimental effect of the mechanical coupling to higher transmon levels is clear. This detrimental effect can be alleviated by increasing the qubit's anharmonicity.

To this end, it is beneficial to use a CPB qubit, whose strong anharmonicity makes it valid to keep only the lowest two qubit energy levels. In this limit, the CPB-mechanics coupling rate $g_{\rm m}$ is given by Eqn.(3.3), and the resulting dispersive shift

$$\chi_{\rm m} = \frac{g_{\rm m}^2}{\Delta} + \frac{g_{\rm m}^2}{\Sigma}, \tag{3.6}$$

is no longer diminished by the small mechanical frequency $\omega_{\rm m}$.

3.2 Collapse voltage and maximum coupling rate

Although $g_{\rm m}$ seems to be linearly enhanced by increasing the external dc-voltage $V_{\rm dc}$ (see, for example, Eqn.(2.41)), it is not possible to reach an arbitrarily large coupling rate by simply increasing $V_{\rm dc}$. Instead, the coupling rate is limited by a maximum dc-voltage $V_{\rm max}$, beyond which the capacitor plates collapse under an electrostatic instability.

To understand this instability, consider with the simple picture as shown in Fig. 3.1(a): $V_{\rm dc}$ is applied across a mechanically compliant vacuum-gap capacitor with capacitance $C_{\rm m}^0$ and separation x_0 between the two capacitor plates at $V_{\rm dc} = 0$ V. This voltage creates an electrostatic force that

pulls the two plates closer, but is impeded by a restoring force from the spring. To find the static separation x_v under dc-voltage $V_{\rm dc}$, I write the potential energy of the suspended electrode at any separation x_s,

$$U(x_s) = -\frac{1}{2}\left(C_{\rm m}^0 \frac{x_0}{x_s}\right) V_{\rm dc}^2 + \frac{1}{2}k(x_0 - x_s)^2, \tag{3.7}$$

where the first term is the electrostatic energy $E_{\rm el}$ stored in the capacitor, and the second term is the potential energy E_k stored in the spring. The static separation x_v is found when the total force experienced by the suspended plate is zero,

$$F(x_v) = -\frac{\partial}{\partial x_s} U(x_s)\Big|_{x_s = x_v} = 0. \tag{3.8}$$

However, as Fig. 3.1(b,c) shows, when $V_{\rm dc}$ is increased beyond a maximum voltage

$$V_{\rm max} = \left(\frac{2}{3}\right)^{3/2} x_0 \sqrt{\frac{k}{C_{\rm m}^0}}, \tag{3.9}$$

the above equation has no real-positive solution, and the capacitor plates collapse.

This maximum voltage therefore leads to a maximum qubit-mechanics coupling rate $g_{\rm max}$ for the basic coupled-system discussed in Sec.2.3.1 (reproduced in Fig.3.1(d)), where a Josephson junction is inserted in series between the mechanically compliant capacitor and ground. Although there can be a small voltage-drop on the order of $e/C_{\rm m}^0$ across the Josephson junction because of the quantized nature of Cooper-pairs, the large dc-voltage $V_{\rm dc} \gg e/C_{\rm m}^0$ drops almost entirely across the mechanically compliant capacitor [79]. Thus, the maximum voltage $V_{\rm max}$ and the static separation x_v found above remain accurate with the addition of the Josephson junction. Small displacement x of the suspended electrode around its static position x_v alters the CPB gate-capacitance according to

$$C_g(x) = C_{\rm m}(x_v, x) = C_{\rm m}^0 \frac{x_0}{x_v} \frac{1}{1 + x/x_v} = C_{\rm m}^v \frac{1}{1 + x/x_v}, \tag{3.10}$$

where $C_{\rm m}^v = C_{\rm m}^0 x_0/x_v$ is the static capacitance at dc-voltage $V_{\rm dc}$. This position-dependent capacitance is then converted into a position-dependent gate-charge to create a qubit-mechanics coupling of rate

$$g_{\rm m}(V_{\rm dc}) = \frac{4E_c}{2e\hbar} x_{zp} V_{\rm dc} \frac{d}{dx} C_{\rm m}(x_v, x) = \frac{e}{\hbar} \frac{C_{\rm m}^v}{C_\Sigma} \frac{x_{zp}}{x_v} V_{\rm dc}, \tag{3.11}$$

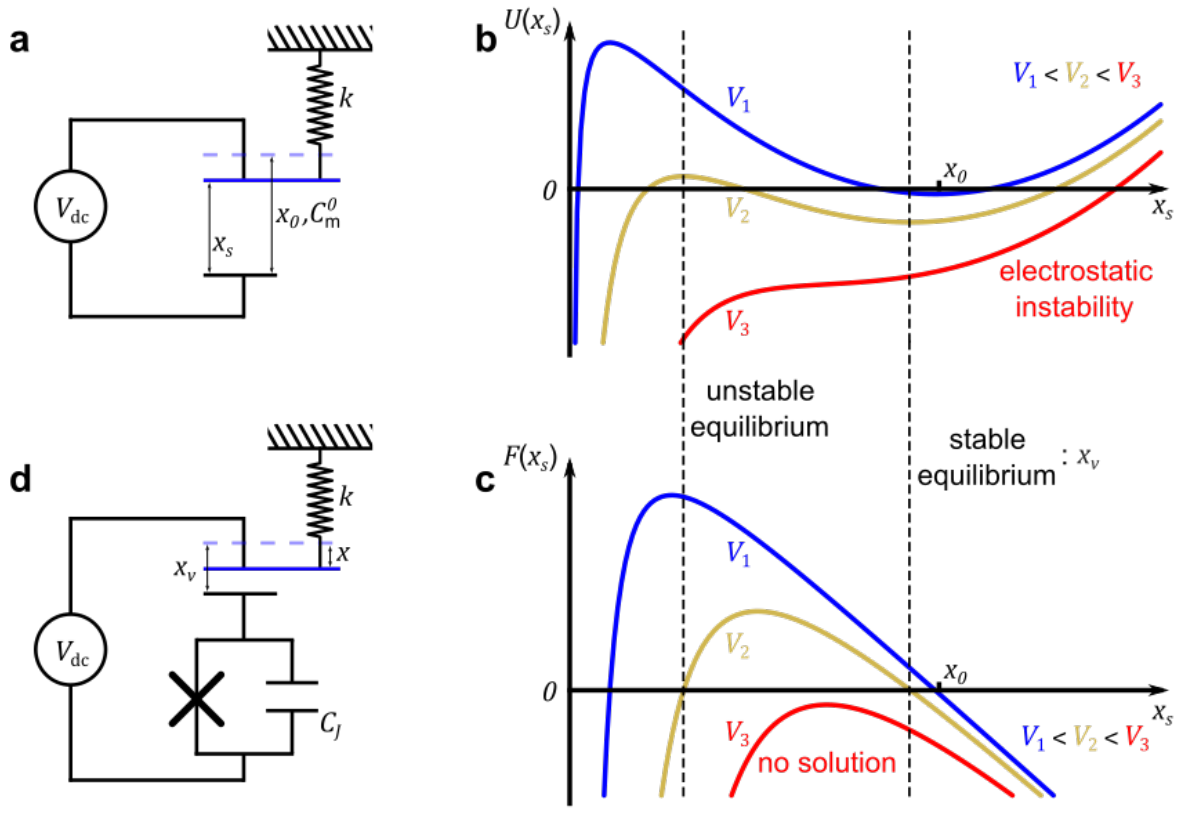

Figure 3.1: Electrostatic instability
a, A mechanically compliant vacuum-gap capacitor C_{m}^{0} is created by suspending a top plate with a spring constant k at a distance x_0 above a bottom electrode. A dc-voltage V_{dc} applied across this capacitor creates an electrostatic force that pulls the two plates together, but is resisted by the restoring force from the spring. **b,** As a function of the plate separation x_s, the potential energy of the suspended plate is plotted for three values of V_{dc}. **c,** The overall force experienced by the plate is in turn given by the slope of these potentials. For a small voltage $V_{\mathrm{dc}} = V_2$ (mustard line), two equilibrium positions can be identified at the dashed lines where the overall force is zero. At this voltage, the static separation between the plates x_v is found at the stable equilibrium position. However, when V_{dc} is further increased beyond a threshold $V_3 > V_{\mathrm{max}}$ (red line), no equilibrium position can be found, and the electrostatic instability in the potential causes the suspended plate to collapse. **d,** A CPB qubit can be created by placing a Josephson junction in series between the mechanically compliant capacitor and the ground. In such a device, V_{dc} couples the mechanical motion x around the static separation x_v to the qubit energy. The maximum coupling rate g_{max} is found at the maximum voltage $V_{\mathrm{dc}} = V_{\mathrm{max}}$

where both x_v and $C_{\rm m}^v$ dependents on $V_{\rm dc}$, and $C_\Sigma = C_{\rm m}^v + C_J$. At the point of collapse ($V_{\rm dc} = V_{\rm max}$), the static separation x_v reaches its minimum value of

$$x_{\rm min} = \frac{2}{3} x_0. \tag{3.12}$$

Using the expression for both $V_{\rm max}$ and $x_{\rm min}$ and assuming a small stray capacitance $C_J \ll C_{\rm m}^v$, the maximum qubit-mechanics coupling rate for this simple system is given by,

$$g_{\rm max} = \frac{e}{\hbar}\left(\frac{3C_{\rm m}^0}{3C_{\rm m}^0 + 2C_J}\right) x_{zp}\sqrt{\frac{2k}{3C_{\rm m}^0}} \approx \frac{e}{\hbar} x_{zp}\sqrt{\frac{2k}{3C_{\rm m}^0}}. \tag{3.13}$$

Because the capacitance $C_{\rm m}^0$ is linearly dependent on the area of the capacitor plate, this equation shows that to maximize the qubit-mechanical coupling rate, it is beneficial to use a smaller mechanical oscillator (i.e., smaller plate area) to reduce $C_{\rm m}^0$ until C_J becomes non-negligible. However, this increased coupling rate comes at the cost of a larger charge-noise-induced qubit dephasing, and may be counter-productive to reaching the strong-dispersive limit, as I will discuss in Sec.3.6.

3.3 Improving the maximum coupling rate with a series capacitance

Beyond reducing the size of the mechanical oscillator, inserting a static capacitance C_0 in series between the dc-voltage and the mechanically compliant capacitor (Fig. 3.2) can also increase the maximum coupling rate $g_{\rm max}$. At first glance, this may seem counter-productive because the addition of C_0 reduces the participation ratio of the mechanically compliant capacitor in the CPB gate-capacitance, and therefore reduces the qubit-mechanics coupling rate $g_{\rm m}$ per external dc-voltage. However, by converting the dc-voltage source into an effective charge source, this static capacitance can greatly delay the onset of the electrostatic instability and increase the maximum coupling rate $g_{\rm max}$ by (at best) a factor of approximately two.

To demonstrate the improvement of adding C_0, I start by quantifying the effect of diluting the mechanical participation ratio in the CPB gate-capacitance. In this new system, the gate-capacitance $C_g(x)$ is position-dependent and given by the series capacitance of C_0 and the

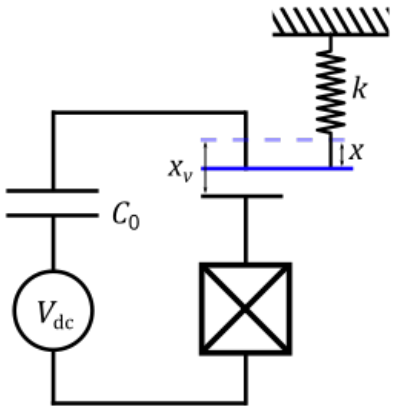

Figure 3.2: Improving the maximum qubit-mechanics coupling rate with a series capacitance
By inserting a static capacitance C_0 in series between the dc-voltage and the mechanically compliant capacitor, I increase the maximum coupling rate $g_{\max}$ by increasing the maximum voltage $V_{\max}$ that can be applied before the mechanically compliant capacitor collapses.

mechanically compliant capacitor $C_{\rm m}$,

$$C_g(x) = \frac{C_{\rm m}(x_v, x)C_0}{C_{\rm m}(x_v, x) + C_0} \approx \frac{C_{\rm m}^v C_0}{C_{\rm m}^v + C_0} + \frac{C_{\rm m}^v C_0^2}{\left(C_{\rm m}^v + C_0\right)^2}\frac{x}{x_v} + \mathcal{O}\left(\frac{x}{x_v}\right)^2, \tag{3.14}$$

where I have expanded around a small motional amplitude $x \ll x_v$. Because the CPB gate-voltage is simply $V_{\rm dc}$, the coupling rate is found using Eqn.(3.3),

$$g_{\rm m}(V_{\rm dc}) = \frac{4E_c}{2e\hbar}x_{zp}V_{\rm dc}\frac{d}{dx}C_g(x) \approx \frac{e}{\hbar}\frac{C_0}{C_{\rm m}^v + C_0}\frac{x_{zp}}{x_v}V_{\rm dc}, \tag{3.15}$$

where I have again assumed a small stray capacitance C_J such that

$$C_\Sigma = C_J + \frac{C_{\rm m}(x_v, x)C_0}{C_{\rm m}(x_v, x) + C_0} \approx \frac{C_{\rm m}^v C_0}{C_{\rm m}^v + C_0}. \tag{3.16}$$

Comparing Eqn.(3.15) and Eqn.(3.11), it is clear that adding C_0 reduces the qubit-mechanics coupling rate per external dc-voltage.

However, C_0 can also delay the onset of the electrostatic instability, and greatly increase the maximum voltage $V_{\rm max}$ that can be applied. As discussed above, for a large $V_{\rm dc} \gg e/C_g$, very little voltage will be dropped across the Josephson junction. Ignoring the junction, I again write the potential energy of the circuit when the motional electrode is suspended x_s above the bottom one,

$$U(x_s) = -\frac{1}{2}\frac{x_0 C_{\rm m}^0 C_0}{x_0 C_{\rm m}^0 + x_s C_0}V_{\rm dc}^2 + \frac{1}{2}k(x_0 - x_s)^2. \tag{3.17}$$

From this potential, the static separation x_v can be found for any dc-voltage. When this separation is reduced to a minimum value of

$$x_{\rm min} = \frac{1}{3}\left(2 - \frac{C_{\rm m}^0}{C_0}\right)x_0, \tag{3.18}$$

$V_{\rm dc}$ reaches its maximum value

$$V_{\rm max} = \left[\frac{2}{3}\left(\frac{C_{\rm m}^0}{C_0} + 1\right)\right]^{3/2} x_0\sqrt{\frac{k}{C_{\rm m}^0}} \tag{3.19}$$

beyond which the instability in the potential will collapse the mechanically compliant capacitor. Interestingly when $C_{\rm m}^0 \geq 2C_0$, $x_{\rm min}$ can become negative! Physically, this means the vacuum-gap

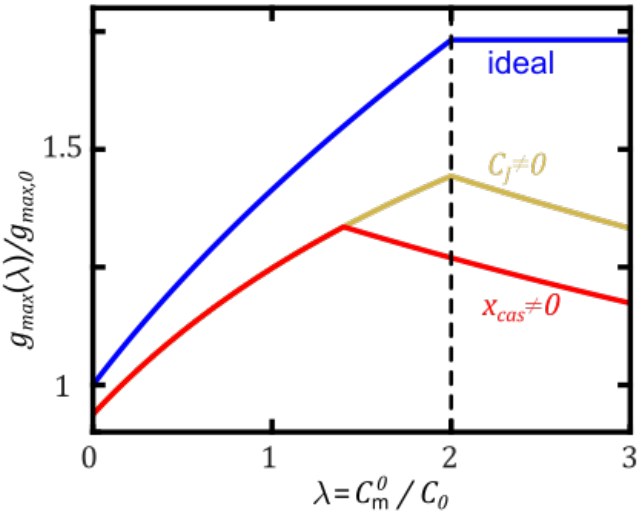

Figure 3.3: The series capacitance improves the maximum qubit-mechanics coupling rate
The maximum achievable qubit-mechanics coupling rate $g_{\max}(\lambda)$ is plotted as a function of the capacitor ratio $\lambda = C_{\mathrm{m}}^0/C_0$, normalized to $g_{\mathrm{m}}(0)$. Assuming an ideal case (blue line) where the stray capacitance $C_J = 0$, $g_{\max}$ monotonically increases until the two capacitor plates can be statically brought into contact at $\lambda = 2$ (dashed black line), giving a maximum enhancement on $g_{\max}$ by a factor of $\sqrt{3}$. However, this maximum enhancement is diminished by a nonzero C_J that reduces the CPB charging energy E_c (mustard line for $C_J = 0.1C_{\mathrm{m}}^0$). Additionally, the maximum enhancement is further reduced if the capacitor plates cannot be brought into contact, but instead collapse at a minimum separation x_{cas} because of other factors such as the Casimir force (red line assumes $C_J = 0.1C_{\mathrm{m}}^0$, and $x_{\mathrm{cas}} = 10$ nm with an initial separation of $x_0 = 50$ nm).

of the mechanically compliant capacitor can be statically reduced until its two plates come into contact at a final voltage

$$V_{\text{touch}} = \sqrt{2}\left(\frac{C_{\text{m}}^0}{C_0}\right) x_0 \sqrt{\frac{k}{C_{\text{m}}^0}}. \tag{3.20}$$

To find the maximum achievable qubit-mechanics coupling rate g_{max}, I substitute V_{dc} in Eqn.(3.15) by the expression of V_{max} (Eqn.(3.19)) if there exists an electrostatic instability, or by the expression of V_{touch} (Eqn.(3.20)) if the plates can smoothly come into contact. Expressed as a function of the capacitance ratio $\lambda = C_{\text{m}}^0/C_0$,

$$g_{\text{max}}(\lambda) = \begin{cases} \sqrt{1+\lambda}\, g_{\text{max},0} & \lambda \leq 2 \\ \sqrt{3}\, g_{\text{max},0} & \lambda > 2 \end{cases}, \tag{3.21}$$

where $g_{\text{max},0} = g_{\text{max}}(0)$ is the maximum coupling rate without adding C_0 found in the previous section, Eqn.(3.13). This equation shows the optimal $\lambda = 2$ can result in a maximum improvement on g_{max} by a factor of $\sqrt{3}$, and a maximum improvement of χ_{max} by a factor of 3. In reality, however, this improvement is limited by other factors such as a non-negligible stray capacitance C_J, as I show in Fig. 3.3. Moreover, although C_0 can prevent the mechanically compliant capacitor from collapsing from the electrostatic instability, it offers no protection against the Casimir force collapse at a minimum separation $x_{\text{cas}} \sim 10$ nm [52]. Consequently, the optimal λ appears at a smaller value, and the maximum coupling rate is reduced accordingly. More details on the modeling of the Casimir force is discussed in Sec.3.6.

3.4 Using symmetry to protect against the noise on the dc-line

Although the large external dc-voltage is crucial for creating a strong qubit-mechanics interaction, it also makes the mechanical oscillator more susceptible to noise on this dc-line. This noise, composed of both thermal and quantum fluctuation, can drive motion in the mechanical oscillator and cause an increased mechanical relaxation. To combat this problem, I use the anti-symmetric, second mode of the suspended capacitor plate as the mechanical oscillator, and couple it to a CPB

qubit. This symmetric arrangement (Fig. 3.4) has the benefit of simultaneously allowing for a large qubit-mechanics coupling rate, and protecting the oscillator from noise on the dc-voltage.

To understand this design choice, I first quantify the effect of noise on the mechanical oscillator when an external dc-voltage $V_{\rm dc}$ is applied [118]. The Johnson-Nyquist noise caused by the impedance $Z(\omega)$ of the dc-line not only drives random motion on the oscillator, but also induces an extra source of damping. In thermal equilibrium, these two effects are related through the quantum fluctuation-dissipation theorem (i.e., detailed balance), and can be expressed as a function of $Z(\omega)$. To see this, I consider the simple picture discussed in Sec.3.2, and write the overall noisy voltage applied on the suspended capacitor plate as,

$$V_{\rm tot} = V_{\rm dc} + V_n, \tag{3.22}$$

where V_n is a small fluctuation on the applied dc-voltage $V_{\rm dc}$, with a random phase and an amplitude characterized by the double-sided noise power spectrum (see Sec.2.2.3)

$$S_v(\omega) = \frac{2\hbar\omega}{1-e^{-\hbar\omega/k_BT}}\mathrm{Re}\left[Z(\omega)\right]. \tag{3.23}$$

This voltage fluctuation V_n exerts a noisy force

$$F_v = \frac{C_{\rm m}^v}{x_v}V_{\rm dc}V_n + \mathcal{O}(V_n^2) \tag{3.24}$$

on the oscillator, whose double-sided power spectrum is

$$S_F(\omega) = \left(\frac{C_{\rm m}^2}{x_v}V_{\rm dc}\right)^2 S_v(\omega). \tag{3.25}$$

When this noisy force is resonant with the oscillator frequency $\omega_{\rm m}$, it can add (Γ_+) or remove (Γ_-) phonons from the oscillator's motion at rates

$$\Gamma_\pm = \frac{1}{2m\hbar\omega_{\rm m}}S_F(\mp\omega_{\rm m}), \tag{3.26}$$

where m is the mass of the oscillator. In thermal equilibrium at temperature T, these noise-induced transition rates obey detailed balance, which determines the oscillator's thermal distribution as discussed in Sec.2.1 and dictates the relationship

$$S_F(\omega_{\rm m}) = \exp\left(\frac{\hbar\omega_{\rm m}}{k_BT}\right)S_F(-\omega_{\rm m}). \tag{3.27}$$

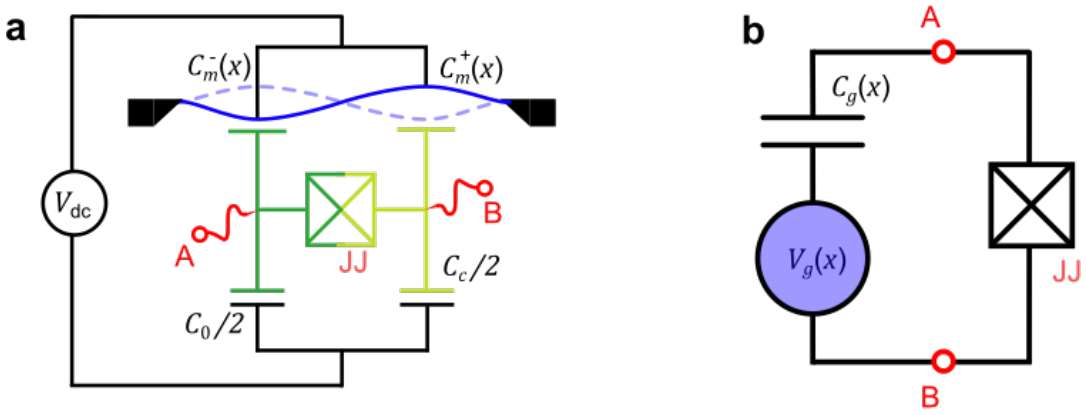

Figure 3.4: Creating strong qubit-mechanics coupling with a symmetric arrangement
a, Using the anti-symmetric, second mode of the suspended capacitor plate as the mechanical oscillator, I create a symmetry in the qubit-mechanics device that protects the oscillator against noise on the dc-line. Meanwhile, this arrangement allows for the creation of a strong qubit-mechanics coupling rate: a voltage $V_{\rm dc}$ converts the anti-symmetric motion of the oscillator into a voltage $V_g(x)$ across the open terminals A and B. **b,** The Thevenin equivalent representation of the circuit seen by the junctions is a Cooper-pair box qubit, with a mechanical-position dependent gate charge $n_g(x) = V_g(x) \times C_g/2e$.

Moreover, because the noise-induced force is more likely to remove phonons (because $S_F(\omega_\mathrm{m}) > S_F(-\omega_\mathrm{m})$), it damps the oscillator's motion at rate

$$\gamma_v = \frac{1}{2m\hbar\omega_\mathrm{m}}\left[S_F(\omega_\mathrm{m}) - S_F(-\omega_\mathrm{m})\right]. \tag{3.28}$$

Using Eqn.(3.25), Eqn.(3.27), and assuming $\hbar\omega_\mathrm{m} \ll k_B T$, the damping rate can be related to the environmental impedance $Z(\omega)$ according to,

$$\gamma_v = \left(\frac{C_\mathrm{m}^v}{x_v}V_\mathrm{dc}\right)^2 \frac{S_v(\omega_\mathrm{m}) + S_v(-\omega_\mathrm{m})}{4k_B T m} = \left(\frac{C_\mathrm{m}^v}{x_v}V_\mathrm{dc}\right)^2 \frac{\mathrm{Re}\left[Z(\omega_\mathrm{m})\right]}{m}. \tag{3.29}$$

This voltage-noise-induced damping rate contributes to the overall mechanical relaxation rate,

$$\gamma_\mathrm{m} = \gamma_v + \gamma_0, \tag{3.30}$$

where γ_0 is the intrinsic mechanical relaxation rate associated with the material, geometry and tension [119] of the mechanical oscillator.

In order for γ_v to not significantly increase the overall mechanical relaxation rate, a stringent requirement is placed on the allowed resistive impedance $\mathrm{Re}\left[Z(\omega_\mathrm{m})\right]$ on the dc-line. To give sense of scale, consider a typical circular mechanically compliant vacuum-gap capacitor [57, 19] of 15 μm diameter, 48 pg mass with an initial separation $x_0 \approx 50$ nm, and spring constant $k \approx 190$ N/m. Using the results from Sec.3.2, I can estimate the initial capacitance $C_\mathrm{m}^0 \approx 31$ fF is increased to approximately $C_\mathrm{m}^v \approx 46$ fF at the maximum voltage $V_\mathrm{max} \approx 2.1$ V. According to Eqn.(3.29), in order for γ_v to be much smaller than the intrinsic damping rate of approximately $\gamma_0 = 2\pi \times 32$ Hz [19] when operating at the maximum voltage, the resistive impedance at the mechanical frequency needs to be much smaller than 1 Ω[3] ! Although this can be achieved using a carefully designed filter, it is a rather demanding design.

A better way to protect the mechanical oscillator from noise on the dc-voltage is to engineer a symmetry that naturally reduces the random force it experiences. To this end, instead of the fundamental mode of the suspended plate, the mechanical oscillator corresponds to the second, anti-symmetric mode, where motion displaces two halves of the suspended plate in opposite directions

[3] I have also optimistically assumed that the voltage noise is well thermalized to its environment. Any out-of-equilibrium voltage noise will only make this worse

away from the static position x_v to create two position-dependent capacitances,

$$C_{\rm m}^{v,\pm}(x) = \frac{C_{\rm m}^v/2}{1 \pm x/x_v}. \tag{3.31}$$

As shown in Fig. 3.4(a), each half of the mechanically compliant capacitor is connected to ground by a series capacitance $C_0/2$ or $C_c/2$. The Josephson junction connects the two legs of the circuit in a Wheatstone-bridge manner, and as I will show shortly, creates a CPB qubit that couples to motion in the anti-symmetric mode. Intuitively, the protection offered by symmetry can be deduced by realizing that when the suspended plate is stationary at static separation x_v, the symmetry from $C_0 = C_c$ means the voltage drops across the two halves of the plate are identical, and cannot drive the oscillator with opposite phase.

To go beyond this intuition, I start by finding the noisy force the drum experiences at static separation x_v and dc-voltage $V_{\rm dc}$ for any values of C_0 and C_c. This can be achieved by finding the Thevenin equivalent circuit seen by the Josephson junction as shown in Fig. 3.4(b). For small motion $x \ll x_v$, the equivalent voltage $V_g(x)$ is the voltage difference between open terminals A and B,

$$V_g(x) = \frac{(C_0 - C_c)C_{\rm m}^v}{(C_0 + C_{\rm m}^v)(C_c + C_{\rm m}^v)} V_{\rm tot} + \left[\frac{C_0 C_{\rm m}^v}{(C_0 + C_{\rm m}^v)^2} + \frac{C_c C_{\rm m}^v}{(C_c + C_{\rm m}^v)^2}\right] \frac{x}{x_v} V_{\rm tot} + \mathcal{O}\left(\frac{x}{x_v}\right)^2, \tag{3.32}$$

where $V_{\rm tot} = V_{\rm dc} + V_n$ is the noisy voltage applied on the device. Similarly, the equivalent capacitance is found by replacing the voltage source with a short circuit,

$$C_g(x) = \frac{(C_0 + C_{\rm m}^v)(C_c + C_{\rm m}^v)}{2(C_0 + C_c + 2C_{\rm m}^v)} + \frac{(C_0 - C_c)C_{\rm m}^v}{2(C_0 + C_c + 2C_{\rm m}^v)} \frac{x}{x_v} + \mathcal{O}\left(\frac{x}{x_v}\right)^2. \tag{3.33}$$

Ignoring the effect of the Josephson junction, when the mechanical oscillator is stationary ($x = 0$) at static separation x_v, it experiences a noisy force of amplitude

$$F_v = \frac{(C_0 - C_c)(C_{\rm m}^v)^2(2C_0C_c + C_0C_{\rm m}^v + C_cC_{\rm m}^v)}{2(C_0 + C_{\rm m}^v)^2(C_c + C_{\rm m}^v)^2 x_v} V_{\rm dc} V_n + \mathcal{O}(V_n^2) \tag{3.34}$$

Similar to Eqn.(3.29), this noisy force results in a mechanical damping of rate

$$\begin{aligned}\gamma_v &= \left[\frac{(C_0-C_c)(C_{\rm m}^v)^2(2C_0C_c+C_0C_{\rm m}^v+C_cC_{\rm m}^v)}{2(C_0+C_{\rm m}^v)^2(C_c+C_{\rm m}^v)^2x_v}V_{\rm dc}\right]^2\frac{{\rm Re}\left[Z(\omega_{\rm m})\right]}{m}\\ &= \frac{1}{4}\left\{\frac{1}{(1+C_{\rm m}^v/C_0)^2}-\frac{1}{\left[1+(1+\Lambda)C_{\rm m}^v/C_0\right]^2}\right\}^2\left(\frac{C_{\rm m}^v}{x_v}V_{\rm dc}\right)^2\frac{{\rm Re}\left[Z(\omega_{\rm m})\right]}{m}\\ &\approx \left[\frac{C_{\rm m}^v/C_0}{(1+C_{\rm m}^v/C_0)^3}\Lambda+\mathcal{O}(\Lambda^2)\right]^2\left(\frac{C_{\rm m}^v}{x_v}V_{\rm dc}\right)^2\frac{{\rm Re}\left[Z(\omega_{\rm m})\right]}{m},\end{aligned} \tag{3.35}$$

where I expanded to the first order in the asymmetry between the two arms

$$\Lambda=\frac{C_0-C_c}{C_c}. \tag{3.36}$$

Clearly, when $\Lambda = 0$, the random force vanishes, and fluctuations on $V_{\rm dc}$ has no effect on the oscillator. In reality, I intentionally preserve a small asymmetry of approximately $\Lambda \approx -0.09$ to allow for coherent driving of the mechanical oscillator using the combination of $V_{\rm dc}$ and an ac-signal at $\omega_{\rm m}$, both applied on the dc-line (see Sec.4.2.2, Sec.5.4 and Appendix.B). Nevertheless, assuming $C_{\rm m}^0/C_0 = 2$, $\Lambda = -0.09$, and the same oscillator parameters as discussed above, the quasi-symmetry of the circuit reduces the voltage-noise induced mechanical damping by more than three orders of magnitude at the point of collapse[4] .

This symmetric design not only protectes the mechanical oscillator against voltage fluctuations on $V_{\rm dc}$, but also has the additional benefit of further increasing the maximum qubit-mechanics coupling rate $g_{\rm max}$ achieved in the previous section. When the two-halves of the capacitor plate oscillate in opposite phase around the static position x_v, the changing capacitance pushes the charges — deposited on them by $V_{\rm dc}$ — across the Josephson junction to create a qubit-mechanics coupling. The rate of this coupling can be found from the position-dependent gate-charge $n_g(x) = C_g(x)V_g(x)/2e$, where $V_g(x)$ and $C_g(x)$ are given by Eqn.(3.32) and Eqn.(3.33) respectively. For the simple case of $C_c = C_0$, I find the qubit-mechanics coupling rate to be,

$$\begin{aligned}g_{\rm m}(V_{\rm dc}) &= \frac{4E_c}{\hbar}x_{zp}\frac{\partial}{\partial x}n_g(x)\\ &= \frac{e}{\hbar}\frac{C_0C_{\rm m}^v}{C_\Sigma(C_0+C_{\rm m}^v)}\frac{x_{zp}}{x_v}V_{\rm dc}\approx\frac{e}{\hbar}\frac{2C_0C_{\rm m}^v}{(C_0+C_{\rm m}^v)^2}\frac{x_{zp}}{x_v}V_{\rm dc},\end{aligned} \tag{3.37}$$

[4] Because $C_{\rm m}^0/C_0 = 2$, there is no electrostatic instability. Instead, I assume the mechanically compliant capacitor will collapse under the Casimir force at separation $x_{\rm cas} \approx 10$ nm, which corresponds to a dc-voltage of $V_{\rm dc} \approx 11$ V (see footnote 5). To reach $\gamma_v = 2\pi \times 32$ Hz with the same oscillator parameters ($C_{\rm m}^0 = 31$ fF and initial separation $x_0 = 50$ nm), I find ${\rm Re}\left[Z(\omega_{\rm m})\right] \approx 2.3$ kΩ, more than three-orders of magnitude larger than the 1 Ω found above.

where I have assumed a small stay capacitance C_J such that

$$C_\Sigma = C_g(x) + C_J \approx \frac{1}{2}(C_0 + C_\mathrm{m}^0). \tag{3.38}$$

One should take care when comparing this qubit-mechanics coupling rate to the ones found in previous sections (such as Eqn.(3.15)): because this symmetric arrangement uses a higher frequency mode, the zero-point motion $x_{zp} \propto 1/\sqrt{\omega_\mathrm{m}}$ is reduced accordingly. Compared to using the fundamental mode of a circular plate, using its second, anti-symmetric mode increases ω_m by a factor of 1.59 [120], and reduces the x_{zp} by a factor of 0.8. Nevertheless, accounting for this reduction in x_{zp}, the symmetric arrangement can still create a larger maximum coupling rate than that found in Sec.3.3. Using the expression for x_min and V_max found previously[5] , I find the maximum achievable qubit-mechanics coupling rate in this arrangement as a function of the capacitance ratio $\lambda = C_\mathrm{m}^0/C_0$,

$$g_\mathrm{max}(\lambda) = \begin{cases} 0.8 \times \frac{3\lambda}{\sqrt{1+\lambda}} g_{\mathrm{max},0} & \lambda \leq 2 \\ 0.8 \times 2\sqrt{2} g_{\mathrm{max},0} & \lambda > 2 \end{cases}, \tag{3.39}$$

where $g_{\mathrm{max},0}$ is given by Eqn.(3.13) assuming $C_J = 0$, and the factor of 0.8 comes from the reduced x_{zp} discussed above. At $\lambda = 0$, the Josephson junction is shorted to ground on both nodes through the series capacitance $C_0/2$, and the coupling rate vanishes. Similar to the discussion in Sec.3.3, the maximum improvement on the coupling rate is limited by other factors such as the presence of a stray capacitance C_J or the capacitor collapse because of Casimir force, as shown in Fig. 3.5.

3.5 Coupling the qubit to a readout cavity

To control and read out the qubit state, it is coupled capacitively to a microwave resonator (henceforth referred to as the cavity to avoid possible confusion with the mechanical oscillator) in the dispersive limit. In Sec.3.5.1, I introduce the cavity, which is formed by a transmission

[5] The static position x_v and the collapse voltage V_max can be found by treating the Josephson junction as a short circuit. This treatment is valid because very little voltage drops across the Josephson junction when the plate is stationary. In doing so, I find a similar circuit to the one discussed in the previous section, but with C_0 in Fig. 3.2 replaced by $(C_0 + C_c)/2$. Thus with this replacement, expressions for x_v, x_min and V_max found in Eqn.(3.17 – Eqn.(3.20)) remains accurate.

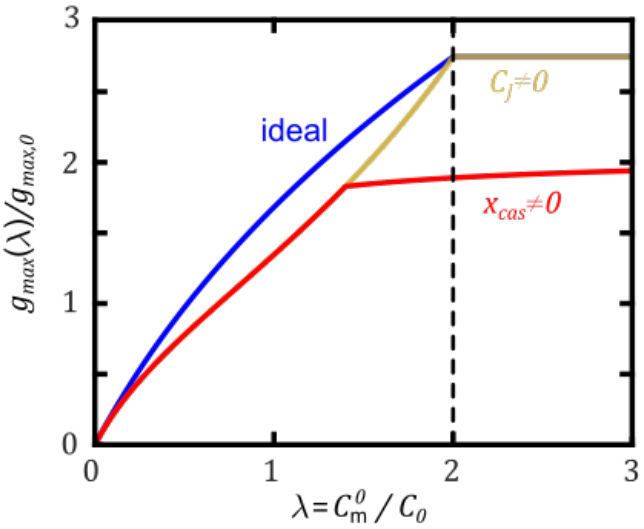

Figure 3.5: Maximum achievable qubit-mechanics coupling rate in the symmetric arrangement
The maximum coupling rate $g_{\max}(\lambda)$ achievable with the symmetric arrangement is plotted as a function of the capacitance ratio $\lambda = C_{\mathrm{m}}^0/C_0$ assuming $C_0 = C_c$. This coupling rate is normalized to $g_{\max,0}$ achieved with the basic arrangement discussed in Sec.3.2. In both the ideal case (blue line) and $C_J \neq 0$ (mustard line for $C_J = 0.1C_{\mathrm{m}}^0$), the maximum enhancement on $g_{\max}$ is achieved when the mechanically compliant capacitor can be statically brought into contact at $\lambda = 2$ (dashed black line), with a maximum enhancement of approximately 3. However, this maximum enhancement is diminished of the capacitor plates collapse at a minimum separation x_{cas} because of factors other than the electrostatic instability, such as the Casimir force (red line assumes $C_J = 0.1C_{\mathrm{m}}^0$, and $x_{\mathrm{cas}} = 10$ nm with an initial separation of $x_0 = 50$ nm).

line resonator and behaves like a harmonic oscillator. By placing this cavity in series between the capacitance $C_c/2$ and the electrical ground (Fig. 3.6), a qubit-cavity coupling is created as explained in Sec.3.5.2. However, there is a trade-off between having a large qubit-cavity coupling rate g_c and having a large qubit-mechanics coupling rate g_{m}. Thus, in Sec.3.5.3, I optimize the qubit readout in the dispersive limit such that I minimize g_c while allowing for single-shot qubit readout with one cavity photon.

3.5.1 Cavity formed by a microwave resonator

The cavity is formed by a half-wave co-planer waveguide (CPW) resonator. Designed to have a fundamental frequency of $\omega_c = 2\pi \times 5$ GHz and a characteristic impedance $Z_0 = 50\ \Omega$, the resonator[6] has a total length $\xi = 12.76$ mm and can be characterized by a distributed model with capacitance per unit-length $C_\xi = 153$ pF/m and inductance per unit-length $L_\xi = 394$ nH/m. Although this CPB resonator consists of many modes, here I'm interested only in its fundamental mode, which behaves like a harmonic oscillator with Hamiltonian

$$H_c = \hbar\omega_c \hat{c}^\dagger \hat{c}, \tag{3.40}$$

where $\hat{c}^\dagger$ and $\hat{c}$ are the cavity's photon creation and annihilation operators. Similar to how a mechanical oscillator's phonon operators $\hat{a}^\dagger$ and $\hat{a}$ relate to its position $\hat{x}$ (see Sec.2.1), these photon operator are related to the resonators voltage according to

$$\hat{V} = V_{zp}(\hat{c}^\dagger + \hat{c}), \tag{3.41}$$

where [103]

$$V_{zp} = \sqrt{\frac{\hbar\omega_c}{\xi C_\xi}} \tag{3.42}$$

is the zero-point voltage fluctuation.

Access to the electromagnetic environment of the cavity is provided by two ports on either side of it. From these ports, energy can enter of leave the cavity at rates κ_{in} or κ_{out}, determined

[6] The CPW resonator is formed by a 10 μm wide center conductor, which is separated from the lateral ground planes by a gap 5 μm wide. These patterns are created by depositing 100 nm thick aluminum on a sapphire substrate.

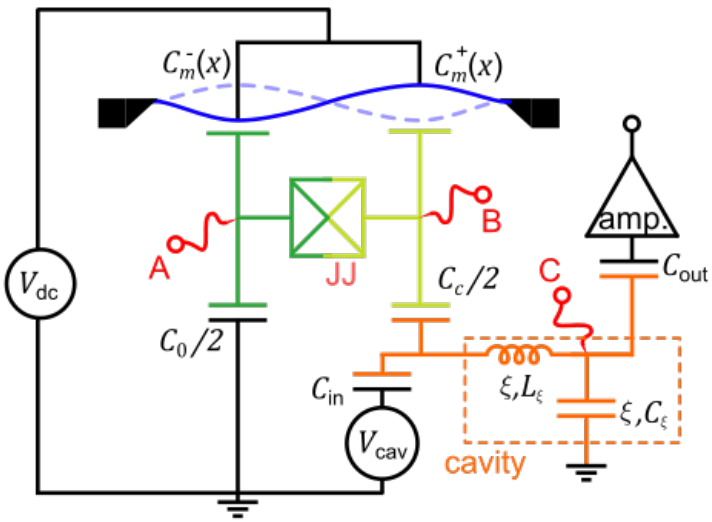

Figure 3.6: Adding a microwave cavity to the qubit-mechanics device
To control and read out the state of the qubit, it is coupled capacitively to a microwave resonator (orange), placed in series between the capacitance $C_c/2$ and the ground, in the dispersive limit. The resonator is formed by a half-wave co-planer waveguide (CPW) resonator with a total length ξ and represented as a distributed LC circuit with capacitance per unit-length C_ξ and inductance per unit-length L_ξ. Control and readout of the qubit state is achieved with a voltage V_{cav} applied to the resonator's center conductor through an input-port defined by capacitance C_{in}. Finally, the resonator is connected to the amplifier chain through its output-port defined by C_{out}.

by the capacitance values of the coupling capacitors $C_{\rm in}$ and $C_{\rm out}$ respectively [121]. In Sec.3.5.3, I explain how these coupling rates are chosen. In addition to these ports, energy in the cavity can also leak to the environment at a rate $\kappa_{\rm loss}$. Thus, the overall rate at which energy leaves the cavity is

$$\kappa = \kappa_{\rm in} + \kappa_{\rm out} + \kappa_{\rm loss}. \tag{3.43}$$

3.5.2 Qubit-cavity interaction

The cavity is placed in series between the capacitance $C_c/2$ and the electrical ground as shown in Fig. 3.6. While this arrangement allows for a strong qubit-cavity interaction as I show shortly, the addition of the cavity doesn't change the qubit-mechanics interaction. At frequencies close to dc or $\omega_{\rm m}$, the cavity appears as a large shunt capacitance $C_{\rm shunt} = \xi C_\xi \approx 2$ pF to ground. Because this capacitance is much larger than any reasonable choice of C_c (a few femto-Farads), node C in Fig. 3.6 can be treated as if it were grounded, and I recover Fig. 3.4(a) discussed in the previous section.

To understand the qubit-cavity coupling, I treat the cavity as a voltage source [103], defined by the voltage difference V_c between its center-pin and the ground plane. This voltage is composed of a classical dc-voltage $V_{\rm set}$ set by the dc-component of $V_{\rm cav}$[7] , and a quantum voltage $\hat{V}$ due to the photons inside the cavity,

$$V_c = V_{\rm set} + \hat{V}. \tag{3.44}$$

I then find the Thevenin equivalent circuit seen by the Josephson junction. Ignoring the mechanical motion ($x = 0$), the equivalent gate-voltage V_g is the voltage difference between open terminals A and B,

$$V_g = V_{\rm dc}\frac{C_{\rm m}^v(C_0 - C_c)}{(C_{\rm m}^v + C_c)(C_{\rm m}^v + C_0)} + \left(V_{\rm set} + \hat{V}\right)\frac{C_c}{C_c + C_{\rm m}^v}. \tag{3.45}$$

Here I find that, in addition to the dc-voltage applied on the mechanical oscillator $V_{\rm dc}$, the dc-voltage on the cavity $V_{\rm set}$ can also be used to bias the CPB gate-voltage. Indeed as discussed in

[7] $V_{\rm set} = V_{\rm cav}^{\rm dc} C_{\rm in}/(C_{\rm in} + C_{\rm shunt})$, where $V_{\rm cav}^{\rm dc}$ is the dc-component of $V_{\rm cav}$

Sec.4.1.2, $V_{\rm set}$ is used experimentally to reset the CPB gate-charge to the sweet-spot before each experiment. In the rest of this section, I consider the simple case of $C_c = C_0$, and simplifies the above equation to,

$$V_g = \left(V_{\rm set} + \hat{V}\right) \frac{C_0}{C_0 + C_{\rm m}^v}. \tag{3.46}$$

Similarly, the equivalent capacitance is found by replacing both voltage sources with short circuits,

$$C_g = \frac{1}{4}(C_0 + C_{\rm m}^v). \tag{3.47}$$

Combining these two equations, I find the electrostatic energy of this CPB qubit (Eqn.(2.19)),

$$\begin{aligned} H_{\rm el} &= 4E_c \left(\hat{\mathbf{n}} - \frac{C_g V_g}{2e}\right)^2 \\ &= 4E_c \left[\left(\hat{\mathbf{n}} - \frac{C_0 V_{\rm set}}{8e}\right)^2 + \left(\frac{C_0}{8e}\right)^2 \hat{V}\left(2V_{\rm set} + \hat{V}\right) + \frac{C_0}{4e}\hat{\mathbf{n}}\hat{V}\right], \end{aligned} \tag{3.48}$$

where $\hat{\mathbf{n}}$ is the Cooper-pair number operator. In this equation, the first term is the original electrostatic Hamiltonian under a classical dc-voltage. The second term corresponds to the extra electrostatic energy stored in the qubit capacitor by the cavity photon, independent of the qubit state. Finally, the third term couples the electrostatic energy of the qubit to the cavity field. Transforming $\hat{\mathbf{n}}$ to qubit Pauli operators $\hat{\sigma}_z$ and $\hat{\sigma}_x$ (see Sec.2.2.2), I find the qubit-cavity interaction Hamiltonian,

$$H_{\rm int} = \hbar g_{\rm c}\left(\hat{c} + \hat{c}^\dagger\right)\left(\cos\theta_0 \hat{\sigma}_z - \sin\theta_0 \hat{\sigma}_x\right), \tag{3.49}$$

where $\theta_0 = \arctan[E_J/4E_c(1-2n_g)]$ is the mixing angle between the charging energy and Josephson energy (Eqn.(2.22)),

$$g_c = \frac{4E_c}{2\hbar e} V_{zp} C_0 = \frac{C_0}{C_J + (C_0 + C_{\rm m}^v)/4} \frac{e}{\hbar} V_{zp} \approx \frac{4C_0}{C_0 + C_{\rm m}^v} g_{c0} \tag{3.50}$$

is the qubit-cavity coupling rate, and $g_{c0} = eV_{zp}/\hbar \approx 2\pi \times 315$ MHz according to Eqn.(3.42). For the rest of this chapter, I assume that the CPB qubit is operated at the charge-degeneracy point $n_g = 1/2$ so that $\theta_0 = 0$.

There is a trade-off between having a large qubit-cavity coupling rate g_c and having a large qubit-mechanics coupling rate $g_{\rm m}$. While increasing $g_{\rm m}$ corresponds to increasing $V_{\rm dc}$ applied on

the mechanical oscillator and thereby reducing the vacuum-gap x_v of the mechanically compliant capacitor, doing so simultaneously increases C_{m}^{v} and decreases g_c. Thus, the question arises: what is the minimum g_c, such that I can maximize g_{m} while still able to read out the qubit? To answer this question, I calculate the measurement rate of the qubit state via the cavity.

3.5.3 Qubit readout through the cavity

To read out the qubit, the qubit-cavity system is operated in the dispersive limit, with a coupling rate g_c much smaller than the qubit-cavity detunning $\Delta_c = \omega_{\mathrm{q}} - \omega_c$ such that energy will not spontaneously transfer between the two. This type of interaction is already discussed in the context of qubit-mechanics interaction in Sec.2.3.3, but can be greatly simplified here due to the large ω_c. Because $\Sigma_c = \omega_{\mathrm{q}} + \omega_c \gg \Delta_c$, the qubit-cavity dispersive shift is approximately,

$$\chi_c = \frac{g_c^2}{\Delta_c} + \frac{g_c^2}{\Sigma_c} \approx \frac{g_c^2}{\Delta_c}. \tag{3.51}$$

Furthermore, because the large ω_c strongly suppresses the sideband transitions at small cavity photon number n_c (see discussion around Eqn.(2.80)), the qubit-state-dependent cavity-impedance has little effect (see Eqn.(2.55)). Consequently, the qubit-cavity interaction merely causes a qubit-state-dependent cavity frequency

$$\omega_c'(\hat{\sigma}_z) = \omega_c + \chi_c \hat{\sigma}_z. \tag{3.52}$$

By determining the frequency of the cavity, the state of the qubit is measured.

The frequency of the cavity is determined by measuring the transmission phase φ_c of a microwave signal at frequency ω_c. Applied on the cavity input-port with a field strength ϵ_c (corresponds to the ac-component of V_{cav} in Fig. 3.6), the probe signal enters the cavity at rate κ_{in} and populates it with a coherent state characterized by a mean photon number [88],

$$\langle n_c \rangle = \frac{\kappa_{\mathrm{in}} \epsilon_c^2}{\chi_c^2 + (\kappa/2)^2}. \tag{3.53}$$

Because of the qubit-cavity interaction, the coherent state acquires a phase shift

$$\varphi_c(\hat{\sigma}_z) = \arctan\left(\frac{2\chi_c \hat{\sigma}_z}{\kappa}\right), \tag{3.54}$$

dependent on the qubit state. Carrying this information, the coherent state then leaves the cavity from the output-port with a probability $\kappa_{\text{out}}/\kappa$, and become amplified and recorded. As such, I acquire information on the qubit state at rate [122],

$$\Gamma_{\text{meas}} = \frac{2\langle n_c \rangle \chi_c^2 \kappa_{\text{out}}}{\chi_c^2 + (\kappa/2)^2}. \tag{3.55}$$

Depending on the type of measurement [123], the qubit state is determined after a time

$$t_{\text{meas}} \geq \frac{1}{\eta_{\text{meas}}} \frac{1}{\Gamma_{\text{meas}}} \tag{3.56}$$

for a two-quadrature measurement, and

$$t_{\text{meas}} \geq \frac{1}{\eta_{\text{meas}}} \frac{1}{2\Gamma_{\text{meas}}} \tag{3.57}$$

for a single-quadrature measurement, where η_{meas} is the measurement efficiency.

With this understanding, I can now design the qubit-cavity system to achieve efficient qubit readout while maintaining a large qubit-mechanics coupling rate. First, the energy in the cavity should predominantly leave from the output-port at rate $\kappa_{\text{out}} \gg \kappa_{\text{in}}, \kappa_{\text{loss}}$. Next, for a given phonon number $\langle n_c \rangle$ and dispersive shift χ_c, the measurement rate is maximized when $\kappa = 2\chi_c$. Finally, I desire to achieve single-shot readout of the qubit state, meaning t_{meas} should be smaller than the qubit decay time $T_1 = 1/\Gamma_1$. Assuming a two-quadrature readout scheme, a near perfect measurement efficiency ($\eta \approx 1$) and taking $\kappa = 2\chi_c$, this requires

$$\Gamma_{\text{meas}} = \langle n_c \rangle \kappa_{\text{out}} \geq \Gamma_1. \tag{3.58}$$

With these in mind, I now minimize the qubit-cavity coupling rate. Assuming a qubit decay rate $\Gamma_1 \approx 2\pi \times 1$ MHz (see next section) and $\langle n_c \rangle \approx 1$, I design the cavity with an output coupling rate $\kappa_{\text{out}} = 2\pi \times 1.55$ MHz ($C_{\text{out}} \approx 13.9$ fF), and an input coupling rate $\kappa_{\text{in}} \approx 2\pi \times 171$ kHz $\ll \kappa_{\text{out}}$ ($C_{\text{in}} \approx 4.6$ fF). Assuming a small environmental coupling rate κ_{loss} on the order of $2\pi \times 10$ kHz for the superconducting aluminum CPW resonator [124], the overall cavity loss rate $\kappa \approx 2\pi \times 1.58$ MHz determines the optimal qubit-cavity dispersive shift $\chi_c = 2\pi \times 0.79$ MHz. Choosing a

qubit frequency at the charge degeneracy point $\omega_{\mathrm{q}}^{b} = E_J/\hbar = 2\pi \times 4$ GHz, the minimum qubit-cavity coupling rate needed to achieve single-photon qubit readout with $\langle n_c \rangle = 1$ is therefore $g_c = \sqrt{\chi_c(\omega_c - \omega_{\mathrm{q}}^{b})} = 2\pi \times 28.1$ MHz.

3.6 Design choices for the fabricated device and expected performance

From the preceding discussions, I have arrived at a circuit schematics of the mechanics-qubit-cavity hybrid system as shown in Fig. 3.6 (reproduced in Fig. 3.7(a)). To implement this circuit, the device is laid out as shown in Fig. 3.7(b). The mechanical oscillator is formed by an aluminum drumhead (blue), similar to those used in previous electromechanical experiments [19]. It is suspended above two aluminum electrodes (green and yellow) to realize two mechanically compliant capacitors. These electrodes then extend out and are connected by the Josephson junctions. This device is finally embedded between the center-pin (orange) and one ground plane (grey) of the CPW resonator. In this section, I decide on the exact geometry of this device.

3.6.1 Choosing a drum size

The first question is: how large should the drumhead be? In Sec.3.2, I have shown that it is beneficial to reduce the size of the suspended plate in order to increase the maximum voltage V_{max} and thereby increase the maximum qubit-mechanics coupling rate. However, the reduction of the plate size causes a larger charge-noise-induced qubit dephasing rate Γ_ϕ, which, as a function of the plate size, increases faster than χ_{max}. Consequently, because I aim to reach a strong dispersive qubit-mechanics interaction, where χ_{m} is larger than the overall qubit dephasing rate $\Gamma_2/2 = \Gamma_1/2 + \Gamma_\phi$, I should reduce the drumhead size to increase χ_{m} until Γ_ϕ becomes the dominant source of qubit dephasing.

To see this, I assume the suspended plate has an area A. This area is related linearly to the mechanically compliant capacitance $C_{\mathrm{m}}^{0} \propto A$. Additionally, assuming a constant plate thickness,

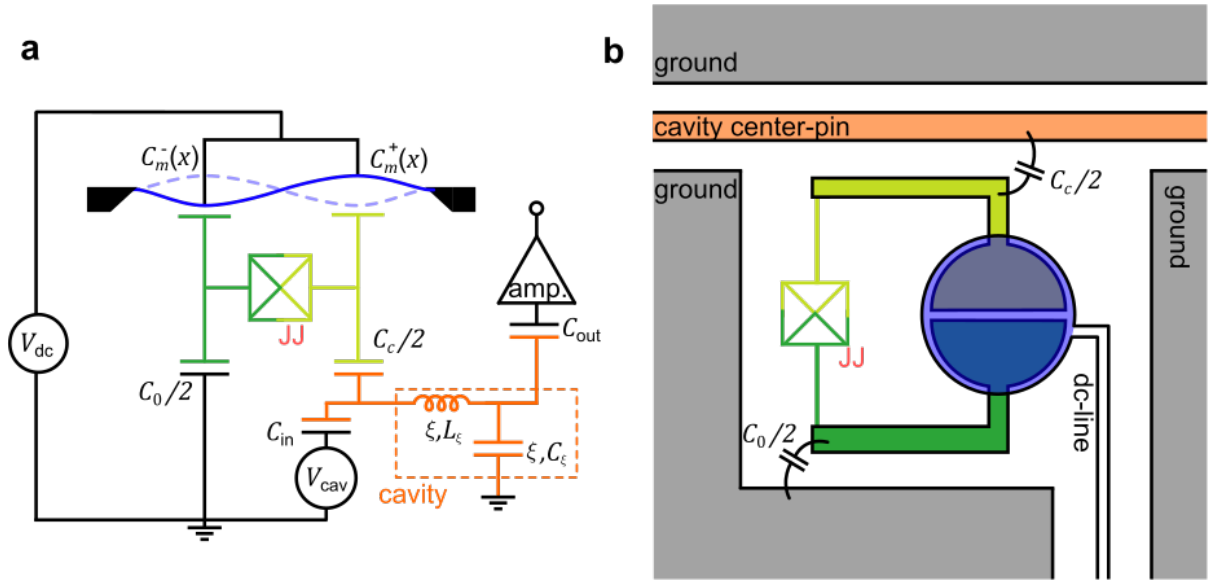

Figure 3.7: Layout of the device
To implement the circuit schematic of **a** (identical to Fig. 3.6), the device is laid out as shown in **b**. The mechanical oscillator is formed by an aluminum drumhead (blue). It is suspended above two aluminum electrodes (green and yellow) underneath to realize two mechanically compliant capacitors. These electrodes then extends out, and are connected by the Josephson junctions. This device is finally embedded in between the center-pin (orange) and one ground plane (grey) of the CPW resonator to form capacitors $C_0/2$ and $C_c/2$.

the plate area also changes the mass of the mechanical oscillator and therefore its zero-point motion,

$$x_{zp} = \sqrt{\frac{\hbar}{2m\omega_{\mathrm{m}}}} = \sqrt{\frac{\hbar}{2\sqrt{mk}}} \propto \sqrt[4]{\frac{1}{A}}, \tag{3.59}$$

where k is the spring constant of the mechanical oscillator. Combined, χ_{m} at V_{max} and at the charge degeneracy point depends on this area according to (see Eqn.(3.13)),

$$\chi_{\mathrm{max}} \approx 2\frac{\hbar g_{\mathrm{max}}^2}{E_J} \propto \frac{x_{zp}^2}{C_{\mathrm{m}}^0} \propto A^{-3/2}. \tag{3.60}$$

On the other hand, assuming a small stray capacitance C_J from the junctions, the CPB charging energy depends inversely to A because,

$$E_c = \frac{e^2}{C_\Sigma} \propto \frac{1}{C_{\mathrm{m}}^0} \propto \frac{1}{A}. \tag{3.61}$$

Recalling from Sec.2.2.3 that the dephasing rate of a CPB qubit because of charge noise is proportional to E_c^2 (Eqn.(2.33)),

$$\Gamma_\phi \propto (8E_c)^2 / E_J \propto \frac{1}{A^2}, \tag{3.62}$$

I find

$$\frac{\chi_{\mathrm{max}}}{\Gamma_\phi} \propto \sqrt{A}. \tag{3.63}$$

Indeed, once the overall qubit dephasing rate $\Gamma_2/2$ is dominated by Γ_ϕ, I should stop further reducing the plate area A, because its detrimental effect (i.e., increased Γ_ϕ because of charge noise) exceeds its benefit (i.e., increased χ_{m}).

Thus, to determine the size of the plate, I compare the expected qubit relaxation rate Γ_1 to the expected Γ_ϕ because of charge noise. The qubit relaxation is likely dominated by the dielectric loss on the dirty surfaces of the mechanically compliant capacitors: because of the fabrication process used to create the suspended drumhead, residuals of silicon nitride are likely to be left on the surfaces between the plates of the mechanically compliant capacitor (see Appendix.A). Indeed in a previous electromechanical experiment [46], where a linear LC-circuit is coupled to a similar drumhead, this dielectric loss is identified as the dominant source of internal loss for the LC circuit, and is observed to happen at a rate of approximately $2\pi \times 1$ MHz when one photon is inside the

LC-circuit. Assuming a similar level of cleanness on the capacitor surfaces, I therefore estimate the qubit relaxation rate will be approximately $\Gamma_1 \approx 2\pi \times 1$ MHz. In comparison, assuming a typical charge noise intensity of $10^{-3} - 10^{-4}\ e/\sqrt{\text{Hz}}$ at 10 Hz [125] and $E_J = E_c$, the charge-noise-induced qubit dephasing is estimated to be a few hundred kilohertz [84], comparable to $\Gamma_1/2$.

In the end, because I cannot exactly predict Γ_ϕ and Γ_1, I choose three different sizes of the drum, each with diameter 6 μm, 7.6 μm and 9.5 μm. Assuming a static separation $x_0 =$ 50 nm at $V_{\text{dc}} = 0$ V, these sizes each have a C_{m}^0 value of approximately 5 fF, 8 fF, and 12.4 fF respectively. These capacitance values are chosen such that when operated at their maximum voltage (see next sub-section), they would each correspond to a E_J/E_c ratio of approximately 1, 1.5, and 2 respectively. In other words, while the 6 μm drumhead device can create the largest χ_{m}, the 9 μm drumhead device will have the smallest Γ_ϕ.

3.6.2 Parasitic capacitance

Having decided on the size of the drumhead, I can now specify the rest of the device geometry. For example, by specifying the shape and size of the upper arm connecting the Josephson junction to one bottom drumhead electrode (yellow in Fig. 3.7), as well as the distance from this arm to the center-pin of the cavity, the capacitance $C_c/2$ is determined. However, in addition to this desired capacitance, this upper arm also creates other parasitic capacitances as illustrated in Fig. 3.8(a), which include a parasitic capacitance to the ground C_{ct}, a parasitic capacitance to the other arm C_t, and a stationary capacitance C_r to the suspended drumhead. By simulating in *Sonnet*, I can find these capacitance values for different geometries.

Including these parasitic capacitances in the circuit schematic as shown in Fig. 3.8, I can realistically predict the performance of a given device. The stray capacitance C_J from the Josephson junction is estimated to be approximately 1 fF for a typical junction area of 0.01 μm^2 [126]. Following similar procedures discussed in previous sections, the qubit-mechanics and qubit-cavity coupling rates can be found by finding the Thevenin equivalent circuit seen by the Josephson junction.

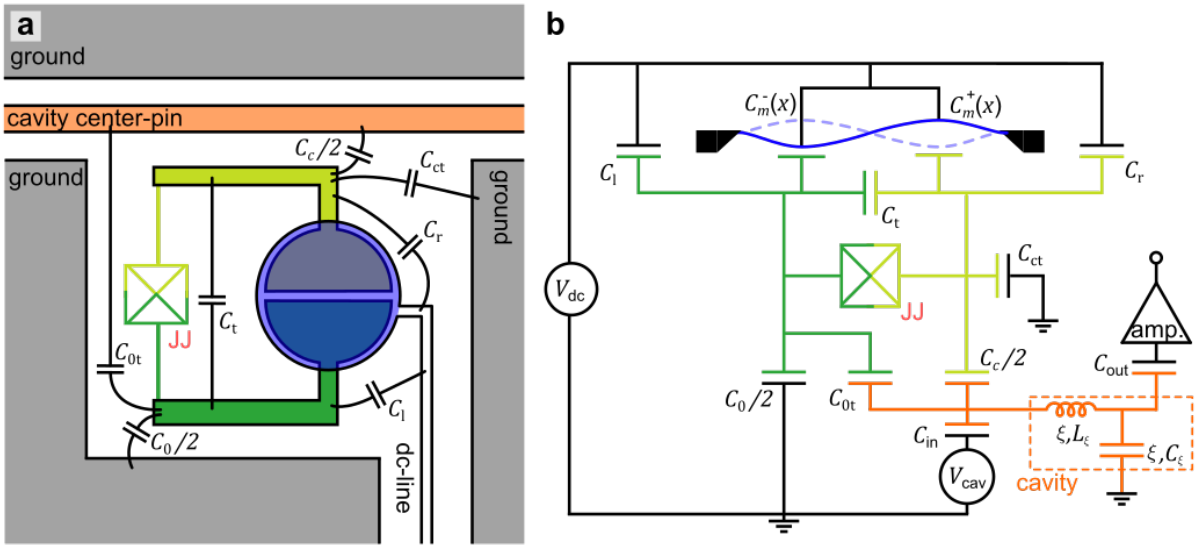

Figure 3.8: Parasitic capacitance
To realistically predict the performance of the designed device, I need to consider the effects of the parasitic capacitances. For example, in the layout of **a**, one arm of the CPB qubit (yellow) is connected to other components of the device through the following capacitances: an intentional $C_c/2$ to the center-pin of the cavity (orange), an intentional motional capacitance $C^{+}_{\mathrm{m}}(x)$ to the top plate (not represented), a parasitic C_r to the dc-line, a parasitic C_{ct} to the ground plane (grey), and a parasitic C_t to the other CPB arm (green). This device is represented by the circuit schematic of **b**.

3.6.3 Estimating the maximum voltage

Finally, I find the dependence of the vacuum-gap x_v on the external dc-voltage $V_{\rm dc}$ in the presence of the parasitic capacitances. Similar to previous discussions, I treat the Josephson junction as a short circuit and write down the potential energy $U(x_s)$ in the circuit when the top drumhead plate is suspended x_s above the bottom electrodes. To compute this separation in a realistic manner, I also include the Casimir force potential [127],

$$U_{\rm cas}(x_s) = -\frac{1}{3}\frac{\hbar c \pi^2 A}{240 x_s^3}, \tag{3.64}$$

where c is the speed of light and A is the plate area. Numerically, I can find x_v for any $V_{\rm dc}$ by solving,

$$F(x_v) = -\frac{\partial}{\partial x_s}\left[U(x_s) + U_{\rm cas}(xs)\right]\Big|_{x_s=x_v} = 0. \tag{3.65}$$

To find the point of collapse, I look at how $V_{\rm dc}$ softens the effective spring constant $k_{\rm eff}$ at the static position x_v. To do this, I approximate the potential around x_v as a second order polynomial, whose coefficient corresponds to $k_{\rm eff}/2$. From previous electromechanical experiments using similar drumhead devices [19, 57], I estimate an initial effective mechanical spring constant $k_0 = 190$ N/m at $V_{\rm dc} = 0$ V. The instability sets in when $k_{\rm eff}$ approaches zero as $V_{\rm dc}$ is increased. In this work, I estimate the maximum voltage $V_{\rm max}$ and the minimum vacuum-gap separation $x_{\rm min}$ by choosing an arbitrary, but pessimistic, value of minimum spring constant $k_{\rm min} = 120$ N/m. Once $k_{\rm eff}$ reaches $k_{\rm min}$, I consider the drumhead to be at the verge of collapse, and assign the applied $V_{\rm dc}$ to be $V_{\rm max}$.

3.6.4 Final designs

For each drum size, I optimize the geometry of the device such that when operated at the maximum voltage $V_{\rm dc}$, the qubit-mechanics coupling rate $g_{\rm m}$ is maximized while the qubit-cavity coupling rate is approximately $g_c \approx 2\pi \times 31.5$ MHz. The estimated essential performance parameters for the final designs are presented in Table 3.1. Assuming a qubit relaxation rate $\Gamma_1 \approx 2\pi \times 1$ MHz, and a qubit dephasing rate because of charge noise $\Gamma_\phi \approx 2\pi \times 1$ MHz, the overall qubit dephasing

rate is approximately $\Gamma_2/2 = \Gamma_1/2 + \Gamma_\phi \approx 2\pi \times 1.5$ MHz. Indeed, when operated at $V_{\max}$, the final designs should allow the device to reach the strong dispersive limit, where $\chi_{\mathrm{m}} > \Gamma_2/2$.

For the rest of this work, I will be working with the device with a drum diameter of 7.6 μm. Pictures of this device is shown in Fig. 3.9.

drum diameter	6 μm	7.6 μm	9.5 μm
maximum voltage, $V_{\max}$	22.1 V	20.5 V	18.7 V
maximum qubit-mechanics coupling rate, $g_{\max}/2\pi$	133.2 MHz	120.3 MHz	100.7 MHz
maximum qubit-mechanics dispersive shift $\chi_{\max}/2\pi$[8]	8.9 MHz	7.2 MHz	5.1 MHz
qubit-cavity coupling rate at $V_{\max}$, $g_c/2\pi$	31.7 MHz	32.6 MHz	32.4 MHz

Table 3.1: Estimated essential performance parameters of the final designs

[8] Evaluated at the point of charge degeneracy assuming $E_J/\hbar = 2\pi \times 4$ GHz

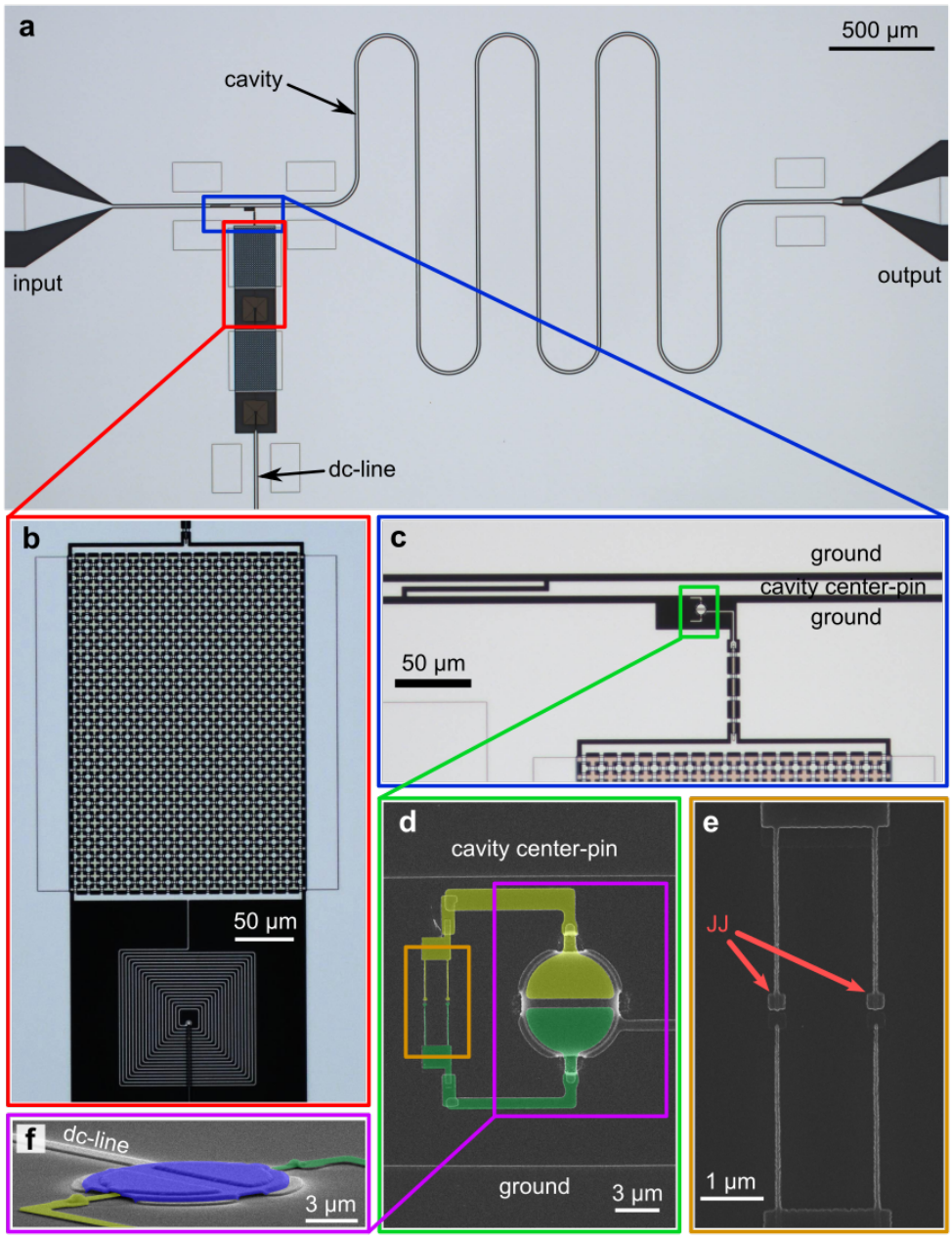

Figure 3.9: The physical device used in this work
a, Optical micrograph of the device chip, showing the cavity (a CPW resonator), input and output ports and the dc-line. **b,** One stage of the on-chip LC filter, composed of an inductance in series and a waffled capacitance to ground (see Appendix.B). **c,** Zoom on the area where the qubit and mechanical oscillator are embedded. The input coupling capacitance of the resonator is visible on the left. **d,** Scanning electron micrograph of the oscillator and the qubit. The center pin and ground of the cavity are also visible. **e,** Zoom on the Josephson junctions (JJ). The split junction allows for in-situ tuning of E_J using an external magnetic flux, and the long and skinny wires connecting the junction to the rest of the circuit could contribute to a long parity-switching time (see Sec.4.1.3). **f,** Viewed at an angle, the mechanical oscillator (blue) is suspended above the two bottom electrodes (green and yellow) to form the mechanically compliant capacitor.

Chapter 4

Characterizing the hybrid system

Having explained the theory and design of the hybrid system, I now start discussing the experimental aspects of this work. In this chapter, I describe the basic characterization of the hybrid system. With the mechanical oscillator decoupled from the qubit at $V_{\rm dc} = 0$ V, I explain in Sec.4.1 how control and readout of qubit state is achieved experimentally using the microwave cavity (i.e., the CPW resonator). With this ability, in Sec.4.2, I increase $V_{\rm dc}$ to 6 V to observe the first indication of having achieved a strong qubit-mechanics interaction, and extract the corresponding dispersive coupling rate $\chi_{\rm m}$. Although this device could reach the strong dispersive limit ($2\chi_{\rm m} > \Gamma_2$) if it were operated at its designed maximum dc-voltage of 21 V, a breakdown of the qubit readout occurs when $V_{\rm dc}$ is increased beyond 6 V. This breakdown is explained in Sec.4.2.3. Consequently, the reminder of this work will be performed at $V_{\rm dc} = 6$ V, where the dispersive shift $2\chi_{\rm m}$ is smaller than, but a significant fraction of, Γ_2. For reasons that will become clear in later chapters, I name this regime the "phonon-number-sensitive regime".

4.1 Cavity-enabled qubit readout

The ability to control and read out the qubit state is integral to all experiments in this work. Theoretically discussed in Sec.3.5, this ability is enabled by a microwave cavity that is dispersively coupled to the qubit. In this section, I experimentally demonstrate this. In Sec.4.1.1, I infer the qubit state from the cavity transmission phase, measured at the bare cavity frequency ω_c. In Sec.4.1.2, I describe using a dc-voltage applied on the cavity to set the CPB qubit to its

sweet-spot (i.e., charge degeneracy point) in order to minimize the charge-noise-induced dephasing (see Sec.2.2.3). Despite this effort, a jump in the qubit's charge-number parity, caused by the tunneling of a quasiparticle across the junction, will bring the qubit far away from its sweet-spot with devastating effects. To ensure the qubit remains at the sweet-spot throughout each experiment, I perform post-selection on the qubit parity as I explain in Sec.4.1.3. Finally in Sec.4.1.4, I characterize the qubit coherence in both time and frequency domains. For clarity, I work at $V_{\rm dc} = 0$ V to decouple the qubit from the mechanical oscillator in this section. However, all techniques described in this section remain unchanged for all values of $V_{\rm dc}$.

4.1.1 Inferring the qubit state

The qubit state is inferred from the phase shift φ_c acquired by a coherent signal transmitting through the cavity. As discussed in Sec.3.5.3, the cavity is dispersively coupled to the qubit, where its bare frequency ω_c is pulled by the state of the qubit according to

$$\omega_c'(\hat{\sigma}_z) = \omega_c + \chi_c \hat{\sigma}_z, \tag{4.1}$$

where χ_c is the dispersive qubit-cavity coupling rate. Driven at frequency ω_c, the coherent signal populates the cavity with a coherent state of mean photon number $\langle n_c \rangle$, and acquires a phase shift φ_c approximately given by [128]

$$\varphi_c \approx \frac{2}{\kappa} \mathrm{Re}(\chi_c) \langle \hat{\sigma}_z \rangle, \tag{4.2}$$

where κ is the overall energy loss rate of the cavity, and

$$\chi_c = \frac{g_c^2}{-i\Gamma_2 + \omega_{\rm q} - \omega_c}, \tag{4.3}$$

is modified by the qubit dephasing rate $\Gamma_2/2$. Experimentally, I determine $\omega_c \approx 2\pi \times 4.76$ GHz and $\kappa \approx 2\pi \times 2.3$ MHz. In Fig. 4.1, I measure this phase as a function of the gate-charge n_g when the qubit is in its ground state, $\langle \hat{\sigma}_z \rangle = -1$. This response can be understood with the help of Fig. 4.1(a): close to the charge degeneracy where $\omega_{\rm q} < \omega_c$, $\chi_c < 0$ and the coherent signal acquires a positive phase shift $\varphi_c > 0$. When the qubit frequency crosses the cavity resonance at $n_g = 0.38$

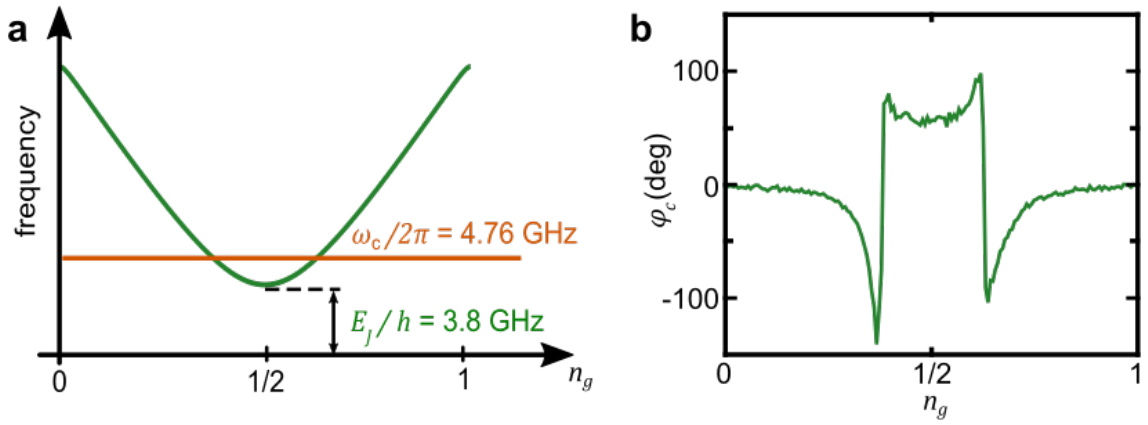

Figure 4.1: Cavity phase shift as a function of gate charge
a, The qubit frequency (green) is strongly dependent on the gate charge n_g, and would cross the cavity (orange) at $n_g = 0.38$ and 0.62 if they were uncoupled. **b**, Because they are coupled, the qubit state alters the cavity frequency and shifts its transmission phase φ_c. Here, φ_c is measured when driving at the uncoupled cavity frequency ω_c with the qubit in its ground state, but would have the opposite sign if the qubit is excited. This measurement of φ_c vs. n_g allows the determination of the sweet-spot. Moreover at a fixed n_g, measurement of φ_c enables qubit readout. This figure is reproduced from reference [85].

and 0.62, φ_c changes sign as can be observed in Fig. 4.1(b). When the qubit is in its excited state, the phase response in this figure has the opposite sign. If this phase can be measured with enough accuracy to determine the qubit state within one qubit lifetime T_1, I would achieve single-shot qubit readout. However, despite the design considerations (see Sec.3.5.3), such single-shot capability remains ellusive in this experiment because of both the limited measurement efficiency ($\eta_{\rm meas} \leq 0.67$ because $\kappa_{\rm out}/\kappa \approx 0.67$) and the need to measure with a small cavity photon number ($\langle n_c \rangle \approx 0.6$, see Sec.4.2.3).

Instead, I adopt an incoherent measurement technique [129, 86, 85], and infer the average occupation of the qubit $\langle \hat{\sigma}_z \rangle$ from the measured phase φ_c. Working at the charge degeneracy point, the qubit excited state probability is approximately

$$P_e = \frac{1}{2}\left(1 + \langle \hat{\sigma}_z \rangle\right) \approx \frac{1}{2} - \varphi_c / 2\varphi^{|g\rangle}_{n_g=0.5}, \tag{4.4}$$

where $\varphi^{|g\rangle}_{n_g=0.5} \approx 58.5$ (deg) is the phase measured at $n_g = 0.5$ with the qubit in its ground state.

4.1.2 Setting the qubit to its sweet-spot

Because there is typically $1/f$ noise on the gate-charge parameter n_g, all experiments have a routine running in the background that automatically reset it every one or two seconds to ensure the qubit is always operated close to its sweet spot. The gate-charge is partly controlled by a dc-voltage applied on the cavity input-port (see Sec.3.5.2 and Appendix.B). Fig.4.1 shows the cavity phase shift φ_c measured as a function of this dc-voltage. Using this measurement, the dc-voltage is set to the charge degeneracy point, identified at the point of symmetry in the φ_c response [86].

4.1.3 Selecting the qubit parity

In addition to the $1/f$ noise, n_g is also displaced from the sweet-spot in a sudden and discontinuous way when a quasiparticle tunnels across the junction. As discussed in Sec.2.2.3, quasiparticles are single-electron-like excitations that reside in superconductors. When a quasiparticle tunnels across the junction, it causes a jump in the qubit parity, changing n_g by 1/2. For a qubit

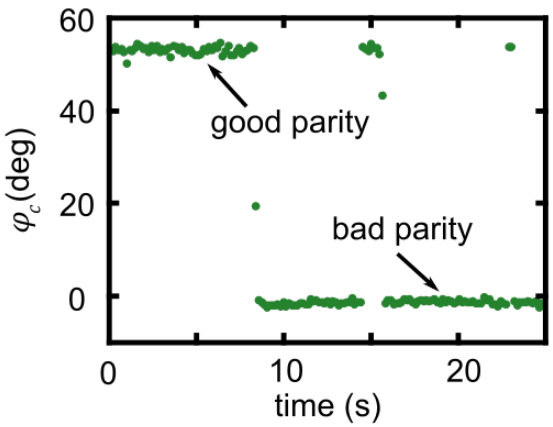

Figure 4.2: Qubit parity jumps
The qubit parity jumps can be observed by measuring φ_c in time with the qubit in its ground state at the sweet-spot. I observe no preferred parity, and the qubit is found in either parity positions in approximately 50% of the time. Conditioned on the parity being in the "good parity" position, I post-select the data to ensure all experiments are conducted at the sweet-spot. This figure is reproduced from reference [86].

operated at $n_g = 1/2$, a parity jump takes it to the furthest point away from the sweet-spot, and drastically changes both the qubit-mechanics (if $V_{\rm dc} \neq 0$) and qubit-cavity interactions. In Fig. 4.2, I observe such parity jumps by measuring φ_c in time with the qubit in its ground state.

From similar measurements, I estimate a characteristic parity-switching time of $1 \sim 10$ s [86]. This relatively long [130] switching time is likely determined by the special geometry around the Josephson junctions. As shown in Fig. 3.9(e), the junctions are defined by small aluminum pads of approximate dimensions $300 \times 300 \times 100$ nm^3, which are only connected to the rest of the superconducting device via wires that are 4 μm long and 60 nm wide. These small volumes ensure that less than a single quasiparticle (see Sec.2.2.3) resides in the immediate surroundings of the junctions to cause parity jumps. Although large number of quasiparticles reside in the rest of the device, they will need to diffuse across the long and skinny wires to reach the junction, making them less likely to cause parity jumps.

Because of this long switching time, the qubit parity can be determined in a "single-shot" manner as already demonstrated in Fig. 4.2. Leveraging this, I henceforth determine the qubit parity at the end of every experiment. Conditioned on observing the "good parity" position, I post-select the data to ensure all experiments are conducted at the sweet-spot.

4.1.4 Qubit characterization

With the qubit correctly initialized to its sweet-spot, I now characterize it in both time and frequency domains [86].

To start, I demonstrate the manipulation of qubit state with a large qubit-drive at frequency $\omega_{\rm q}^b \approx 2\pi \times 3.8$ GHz by inducing Rabi oscillations as shown in Fig. 4.3(a). Keeping the drive strength constant, I vary its duration T_d and measure the cavity transmission phase, which detects the qubit excited state probability P_e according to Eqn.(4.4). As discussed in Sec.2.3.4.3, the qubit oscillates between the ground and excited state at a rate $\Omega_R \approx 2\pi \times 160$ MHz, determined by the drive strength, before reaching a steady-state excitation at longer time. In this figure, the maximum excited state probability is low because the qubit decays quickly to ground state during the time

I measure. Nevertheless, at $t_\pi \approx 12$ ns, the qubit-drive realizes a "π-pulse", swapping the qubit state from $|g\rangle$ to $|e\rangle$.

Using this calibrated qubit-drive, I now measure the qubit lifetime T_1 and decoherence time T_2. To measure T_1, I excite the qubit with a π-pulse and wait a variable delay τ before measuring the cavity transmission phase, as shown in Fig. 4.3(b). Because P_e decays according to,

$$P_e(\tau) = P_e(0)e^{-\tau/T_1}, \tag{4.5}$$

a fit reveals $T_1 = 1/\Gamma_1 \approx 260$ ns. To measure the qubit decoherence, the variable delay τ is instead inserted between two consecutive "$\pi/2$-pulses". As a function of the qubit-drive detunning from the qubit resonance $\Delta_{\mathrm{d,q}}$, P_e oscillates according to

$$P_e(\tau) \propto \cos(\Delta_{\mathrm{d,q}}\tau)e^{-\tau/T_2}. \tag{4.6}$$

Fitting the data presented in Fig.4.3(c) using this equation, I find $T_2 \approx 85$ ns.

Finally, I measure the steady-state qubit spectrum, where the probability of exciting the qubit is measured as a function of the frequency of a weak qubit-drive signal as shown in Fig. 4.4. This type of spectroscopic measurement will be used extensively in the rest of this work. To ensure the spectrum is measured in steady-state, the qubit drive is applied 1 μs ($\approx 4T_1$) before the start of cavity phase measurement. Evident from the small maximum P_e ($\sim 1\%$), I use a very weak qubit drive to to minimize the power broadening of the qubit lineshape (see Sec.2.3.4.3). Fitting this measured qubit spectrum with a Lorentzian lineshape, I find a FWHM $\Gamma_2 = 2/T_2 \approx 2\pi \times 3.7$ MHz, consistent with the time-domain measurement of $T_2 \approx 85$ ns. Because of low-frequency noise on the gate-charge, an asymmetry can be observed in this qubit spectrum, where a tail extends toward higher frequency. This effect will be explored in more detail in Sec.5.2.4.

4.2 Turning on the qubit-mechanics coupling

Having demonstrated the ability to control and read out the qubit state, I now turn on the qubit-mechanics interaction by increasing V_{dc} to 6 V. In Sec.4.2.1, I observe the first indication

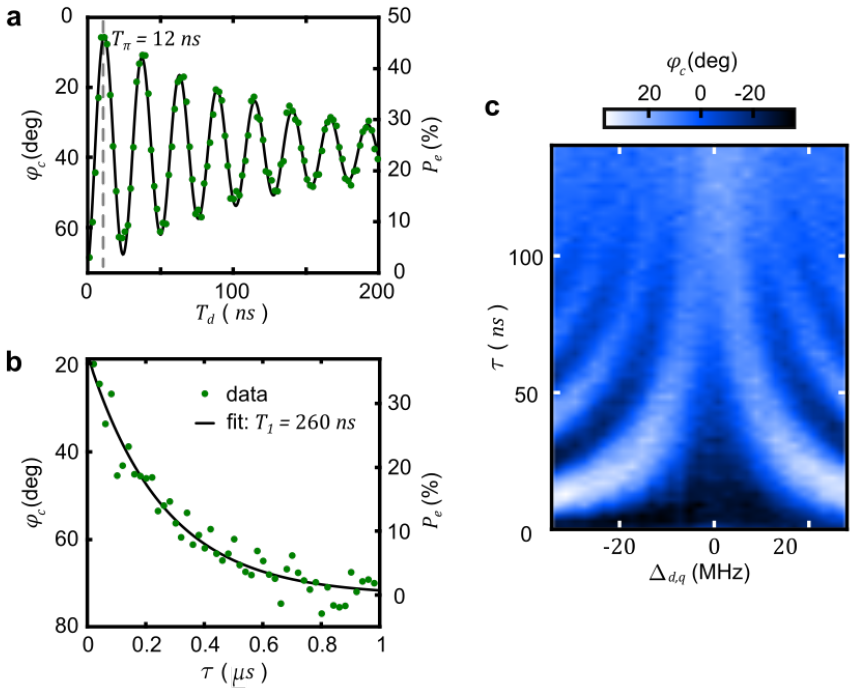

Figure 4.3: Time-domain qubit characterization
a, I observe the qubit Rabi oscillation (green dots) by varying the duration T_d (x-axis) of a strong excitation signal driven at the qubit's resonant frequency and measuring the cavity transmission phase φ_c (left-axis). This phase is related to the qubit excited state probability P_e (right-axis) according to Eqn.(4.4). Because of its short lifetime T_1, the qubit decays quickly from $|e\rangle$ to $|g\rangle$ during the measurement, resulting in a reduced maximum P_e. At the vertical dashed line, I identify the duration for a $\pi-$pulse $T_\pi \approx 12$ ns. **b**, After exciting the qubit with a π-pulse, I wait for different delays τ before measuring φ_c (green dots). Fitting this result acording to Eqn.(4.5), I find $T_1 \approx 260$ ns (black line). **c**, To quantify the qubit decoherence, I vary the detunning $\Delta_{d,q}$ between the qubit excitation signal and ω_q^0 (x-axis), and measure φ_c (color-scale) as a function of the delay time τ between two consecutive $\pi/2$-pulses. Using Eqn.(4.6), I find a characteristic qubit decoherence time $T_2 \approx 85$ ns.

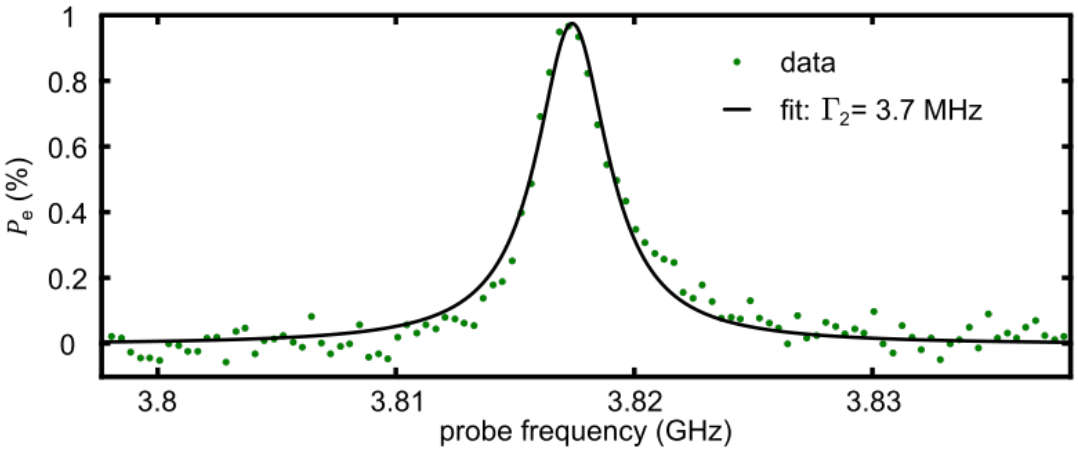

Figure 4.4: Steady-state qubit spectrum
Sweeping the frequency of a weak qubit drive, I measure the qubit spectrum (green dots) at $V_{\rm dc} = 0$ V. The reported P_e (y-axis) is inferred from the measured cavity transmission phase φ_c according to Eqn.(4.4). Fitting the qubit spectrum with a Lorentzian lineshape (black line), I find a FWHM $\Gamma_2 = 2/T_2 \approx 2\pi \times 3.7$ MHz, consistent with the time-domain measurement of T_2. The asymmetric qubit lineshape is caused by noise on the gate-charge (see Sec.5.2.4).

of having achieved a strong qubit-mechanics interaction: the qubit spectrum is broadened by the thermal motion of the mechanical oscillator. To begin understanding this motion-broadened qubit spectrum, I find the qubit-mechanics dispersive shift $\chi_{\rm m} \approx 2\pi \times 0.26$ kHz [86] in Sec.4.2.2. This shows that, if this device could be operated at its maximum voltage around 21 V, it could reach the strong dispersive limit ($2\chi_{\rm m} > \Gamma_2$). However, as I explain in Sec.4.2.3, attempt to further increase $V_{\rm dc}$ beyond 6 V is impeded by a break-down of the qubit readout.

4.2.1 Motion induced qubit spectrum broadening

In Fig. 4.5, I measure the qubit spectrum (orange dots) at $V_{\rm dc} = 6$ V. Compared to that measured at $V_{\rm dc} = 0$ V (green dots), the 6 V qubit spectrum has a pronounced tail that extends toward higher frequencies. Because each mechanical phonon would shift the qubit frequency by $2\chi_{\rm m} > 0$ (see Sec.2.3.3), this tail in the qubit spectrum is consistent with the expected qubit response to a mechanical thermal state, and indicates the presence of a strong qubit-mechanics interaction. Indeed, as I will show in Sec.5.4, this qubit spectrum reveals a thermal phonon distribution characterized by its mean phonon number $\langle n \rangle = n_{\rm th} \approx 17.7$, consistent with the base temperature of the fridge. However, although much information on the mechanical phonon distribution is contained in the qubit spectrum, extracting it requires that I determine the dispersive qubit-mechanics coupling rate $\chi_{\rm m}$.

4.2.2 Determining the qubit-mechanics coupling rate

To determine $\chi_{\rm m}$, I measure how the mechanical oscillator's resonant frequency is pulled by its interaction with the ground state qubit as a function of the gate-charge n_g. Because n_g controls both the uncoupled qubit frequency $\omega_{\rm q}$ and the mixing angle θ_0 between the $\hat{\sigma}_x$ and $\hat{\sigma}_z$ qubit-mechanics coupling (see Sec.2.3.1), it strongly influences the oscillator's dispersive shift,

$$\chi_{\rm m} = \frac{g_{\rm m}^2 \sin^2\theta_0}{\omega_{\rm q} - \omega_{\rm m}} + \frac{g_{\rm m}^2 \sin^2\theta_0}{\omega_{\rm q} + \omega_{\rm m}}, \tag{4.7}$$

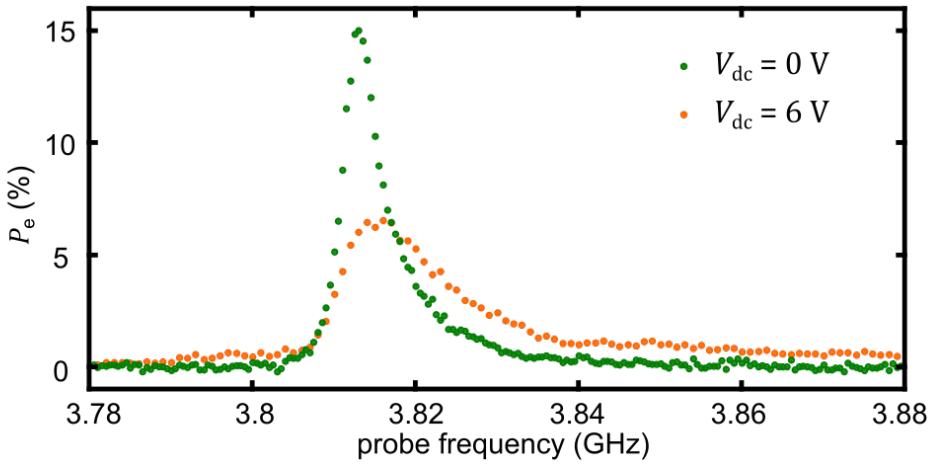

Figure 4.5: Motion-induced broadening of the qubit spectrum
At $V_{dc} = 6$ V, I measure the qubit spectrum (orange dots). Compared to the spectrum measured at $V_{dc} = 0$ V with the same qubit drive power (green dots), the 6 V spectrum has a pronounced tail extending toward higher frequencies, indicating a strong qubit-mechanics interaction.

where $\omega_{\rm m}$ is the uncoupled mechanical frequency. Thus, by measuring the oscillator's resonant frequency as a function of n_g, one can determine $g_{\rm m}$ and therefore $\chi_{\rm m}$. Such a measurement was first performed in an experiment [81] that coupled a CPB qubit to a silicon nitride beam oscillator. However, in contrast to that experiment, the mechanical oscillator cannot be independently measured in this work. Instead, I use the qubit qubit-cavity system to infer the mechanical resonance while coherently driving motion on the oscillator [86].

The coherent motion is driven by the product of $V_{\rm dc}$ and a resonant ac-voltage (i.e., coherent mechanical drive) applied on the same port, as discussed in Sec.3.4. Once the mechanical drive is turned off, the oscillator's coherent motion survives for a characteristic time scale $1/\gamma_{\rm m} \approx 1.7$ ms (see Appendix.D). During this time, the qubit frequency is Stark shifted by the coherent motion. Leveraging this effect, I detect the mechanical resonance via the qubit spectrum as shown in Fig. 4.6. Although this measurement works well at the charge degeneracy point where the qubit FWHM is small, it fails at other values of n_g because of a large charge-noise-induced qubit dephasing.

Instead, I determine the mechanical frequency by observing a motion-induced rectification of φ_c while keeping the qubit in its ground state. Indeed, the coherent mechanical motion can be treated as a sinusoidal modulation of n_g (see Sec.5.2). This modulation not only causes a Stark shift on the qubit frequency, but also, in turn, rectifies the cavity phase. This can be intuitively understood by considering the effect of a n_g modulation on the phase signal in Fig. 4.1. With a sufficiently large coherent mechanical motion, I can observe the rectified φ_c as shown in Fig.4.7 with $V_{\rm dc} = 6$ V. At $n_g = 1/2$, I observe a mechanical resonance at around 25.078 MHz (selecting on the correct parity). Meanwhile at $n_g = 1/4$, I observe a mechanical resonance at around 25.294 MHz (both parities are degenerate at this n_g position, and I do not select parity). However, close to $n_g = 0$ (or 1), I cannot measure a motion-induced phase rectification with a reasonable number of phonons because the curvature of the phase signal is very small. Nevertheless, with these two data points and using Eqn.(4.7), I calculate that, at $V_{\rm dc} = 6$ V, $g_{\rm m} \approx 2\pi \times 22$ MHz[9] , which corresponds

[9] The coherent motion has approximately 200 phonons, much less than the critical phonon number $\omega_{\rm q}/4\chi_{\rm m}^2 \approx 1.4 \times 10^4$ [122] at the charge degeneracy point.

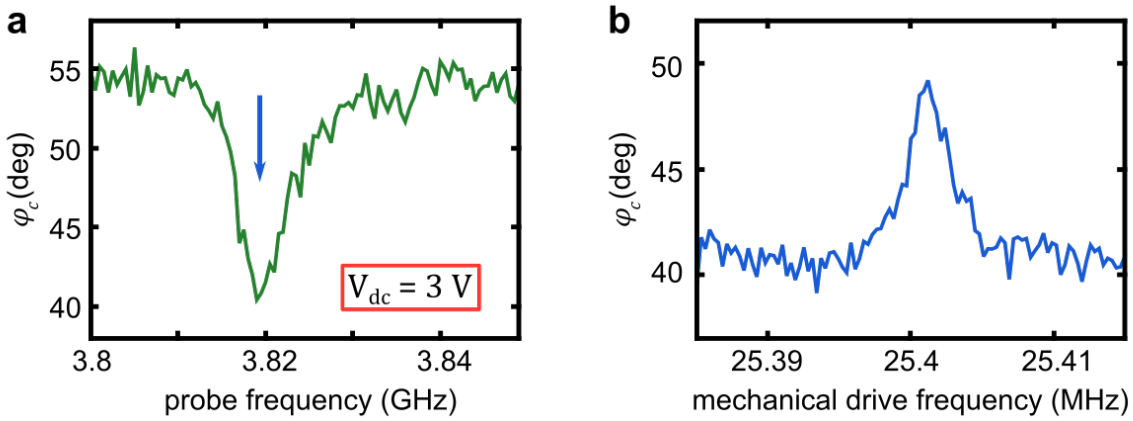

Figure 4.6: Detecting the mechanical resonance via qubit spectrum
a, At $V_{\mathrm{dc}} = 3$ V and $n_g = 1/2$, I measure the qubit spectrum with the coherent mechanical drive off. **b**, Parking the qubit drive at the frequency highlighted by the vertical arrow in **a**, I measure the cavity phase φ_c as a function of the frequency of the coherent mechanical drive. When this mechanical drive resonates with the oscillator, its drives coherent motion on the oscillator that Stark shifts the qubit and causes the qubit drive to become off-resonant. Consequently, φ_c goes back to the value corresponding to the qubit in the ground state, hence the observed contrast. The observed width of the mechanical resonance is broadened by the short duration of the coherent drive. This figure is reproduced from reference [86].

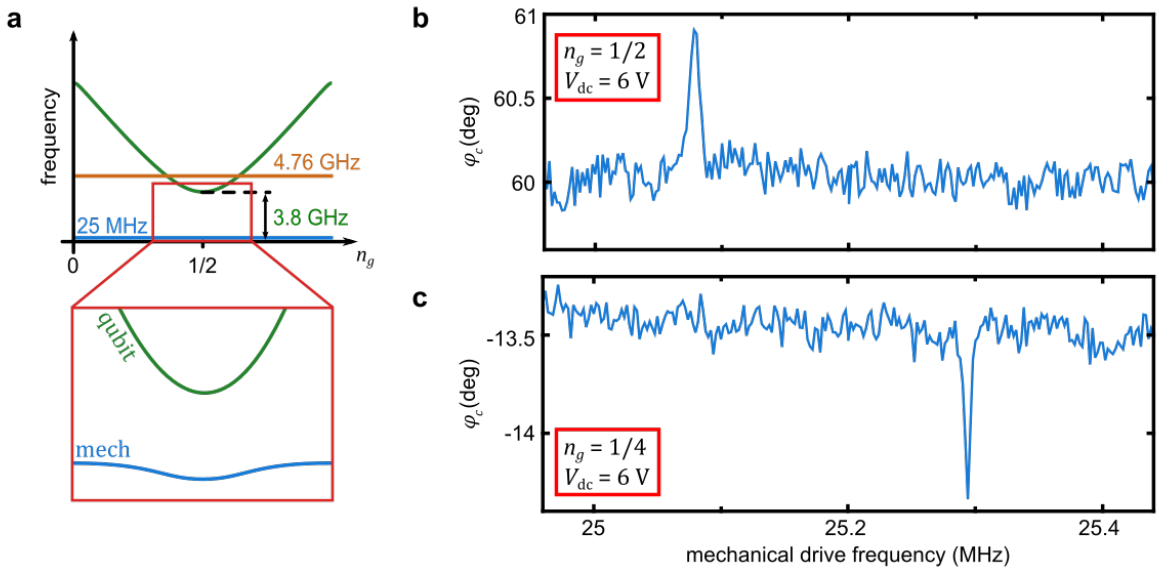

Figure 4.7: Measuring χ_m
a, Because the qubit frequency (green) is strongly dependent on the gate-charge n_g, the ground state qubit pulls the mechanical resonance by different amounts. Consequently, measuring the mechanical resonance as a function of n_g can reveal the qubit-mechanics coupling rate g_m and in turn the dispersive shift χ_m. **b**, At $V_{dc} = 6$ V and $n_g = 1/2$, I measure the cavity phase φ_c after a 10 μs mechanical drive at varying frequencies. When the mechanical drive comes in resonance with the oscillator, the resulting coherent motion rectifies the phase signal in Fig. 4.1 and allows for detecting the mechanical resonance at frequency 25.078 MHz. **c**, Same as **b** but measured at $n_g = 1/4$, showing a significantly less shifted mechanical resonance at frequency 25.294 MHz. This figure is reproduced from reference [86].

to a dispersive coupling rate $\chi_m \approx 2\pi \times 0.26$ MHz at the charge degeneracy point.

Because $\chi_m \propto V_{dc}^2$, if the device were operated at its maximum voltage of 21 V, I expect a maximum dispersive coupling rate $\chi_m^{max} \approx 2\pi \times 3.2$ MHz. Compared to the measured value of $\Gamma_2 \approx 2\pi \times 3.7$ MHz, this would place the device in the strong dispersive limit ($2\chi_m > \Gamma_2$).

4.2.3 Break-down of the qubit readout at large dc-voltage

However, further increasing V_{dc} is impeded by a breakdown of the qubit readout: the cavity phase response becomes bi-stable at the charge degeneracy point for $V_{dc} \gtrsim 8$ V. This bi-stability can be observed in Fig. 4.8 using a parity measurement similar to that used in Fig. 4.2, but shows a 3rd stable parity position. From similar measurements, I observe that, while the qubit is in the bad parity position for approximately 50% of the time, the probability of finding the qubit in the good parity position is reduced.

In Fig.4.9, I further investigate this bi-stability of the cavity phase by plotting the histogram of parity measurements as a function of n_g. The 3rd parity position first appears at charge positions where the uncoupled qubit frequency approaches the cavity frequency. As I enhance either the qubit-mechanics interaction by increasing V_{dc} (Fig.4.9(a)) or the qubit-cavity interaction by increasing the cavity photon number $\langle n_c \rangle$ (Fig.4.9(b)), I observe both a broadening of the region over which the 3rd parity position persists, and a reduction in the probability of finding the good parity. Thus, I speculate the bi-stability of the cavity phase arises because of a strong three-body interaction that first arises when the frequency detuning between the qubit and the cavity comes in resonance with the mechanical frequency. This speculation is partly justified by Fig. 4.9(c), which shows the 3rd parity position does not appear when the qubit frequency is always sufficiently larger than the cavity frequency. Unfortunately, the maximum $E_J/\hbar$ of this device is approximately $2\pi \times 5.1$ GHz, too close to ω_c to allow for dispersive qubit readout. Instead, I operate the qubit below the cavity at $E_J/\hbar \approx 2\pi \times 3.8$ GHz.

In order to avoid observing this bi-stability of the cavity phase, for the reminder of this work, I operate the device at $V_{dc} = 6$ V and measure φ_c with a small mean photon number $\langle n_c \rangle \approx 0.6$.

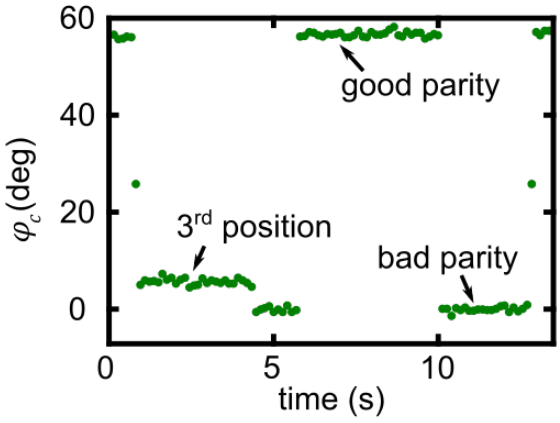

Figure 4.8: Observing a 3$^{\text{rd}}$ parity position
At $V_{\text{dc}} = 10$ V and $n_g = 1/2$, I perform a parity measurement similar to that in Fig. 4.2. In addition to the usual parity positions, I observe a 3$^{\text{rd}}$ stable parity position at $\varphi_c \approx 5$ deg. Similar measurements show that the bad parity position still appears at approximately 50% of the time, demonstrating this 3$^{\text{rd}}$ position arise from a φ_c bi-stability at $n_g = 1/2$.

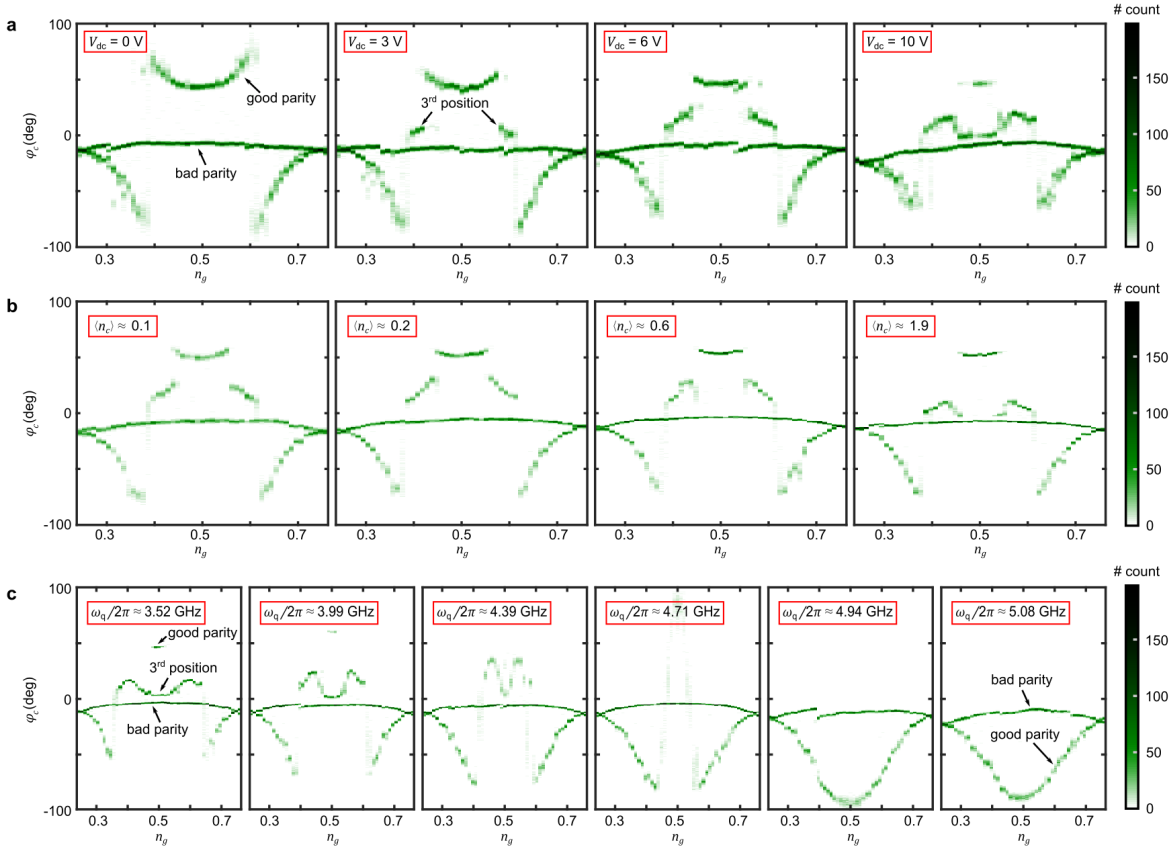

Figure 4.9: Investigating the 3rd parity position
a, I plot the histogram of parity measurements (color-scale vs. y-axis) as a function of n_g (x-axis) for different values of $V_{\rm dc}$. The cavity phase is measured at $\langle n_c \rangle \approx 0.6$. At $V_{\rm dc} = 0$ V, only two parity positions can be observed. However, at $V_{\rm dc} = 3$ V, the 3rd parity position first appears at charge positions where the uncoupled qubit frequency approaches the cavity frequency. Further increasing $V_{\rm dc}$ broadens the region over which the 3rd parity position is observed. At $V_{\rm dc} = 10$ V, the 3rd parity position can be observed even at $n_g = 1/2$. **b**, Same as **a**, but keeping $V_{\rm dc} = 6$ V while changing $\langle n_c \rangle$. Beyond $\langle n_c \rangle \approx 0.6$, I start to observe a broadening of the region over which the 3rd parity position is observed, similar to the effect observed in **a** by increasing $V_{\rm dc}$. **c**, At $V_{\rm dc} = 10$ V and $\langle n_c \rangle \approx 0.6$, I plot the parity histogram while changing the minimum qubit frequency $\omega_{\rm q} = E_J/\hbar$ using an external magnetic flux (see Sec.2.2.1 and Fig. 3.9(e)). When the minimum qubit frequency is sufficiently larger than the cavity frequency ($\omega_{\rm q} \approx 2\pi \times 5.08$ GHz), the 3rd parity position do not appear.

For clarity, I summarize the important performance parameters of this device when operated at this V_{dc} in Table 4.1. Although $2\chi_{\mathrm{m}} \approx 2\pi \times 0.52$ MHz is smaller than Γ_2, it is nevertheless a significant fraction of it with $\Gamma_2/2\chi_{\mathrm{m}} \approx 7.1$. Using this fact, I will show the extraction of the phonon population from the measurement qubit spectrum (Chapter 5) and the manipulation of a small section of the phonon population with a characteristic width of approximately 7.1 phonons (Chapter 6) in the following chapters.

Parameter	Value
qubit Josephson energy	$E_J/\hbar \approx 2\pi \times 3.8$ GHz
qubit charging energy	$E_c/\hbar \approx 2\pi \times 2.9$ GHz
qubit lifetime	$T_1 \approx 0.26\mu$s
qubit decoherence time	$T_2 \approx 0.08\mu$s
mechanical frequency	$\omega_{\mathrm{m}} \approx 2\pi \times 25$ MHz
mechanical thermal occupation	$n_{th} = 13 \sim 20$
mechanical damping rate	$\gamma_{\mathrm{m}} \approx 2\pi \times 93$ Hz
cavity frequency	$\omega_c \approx 2\pi \times 4.76$ GHz
cavity loss rate	$\kappa \approx 2\pi \times 2.3$ MHz
qubit-mechanics coupling rate	$g_{\mathrm{m}} \approx 2\pi \times 22$ MHz
single-phonon Stark shift	$2\chi_{\mathrm{m}} \approx 2\pi \times 0.52$ MHz (at $n_g = 1/2$)
qubit-cavity coupling rate	$g_c \approx 2\pi \times 37$ MHz

Table 4.1: Essential performance parameters of the device at $V_{\mathrm{dc}} = 6$ V

Chapter 5

Extracting phonon distribution from qubit spectrum

Being able to measure and understand the phonon distribution is the foundation to any meaningful manipulation of the phonon state. In this chapter, I discuss how the phonon distribution can be reconstructed from the measured qubit spectrum. In Sec.5.1, I introduce the idea of using deconvolution to extract the phonon distribution. However, this procedure requires an accurate description for the expected qubit spectrum $P_e^{|n\rangle}(\omega)$ when there is exactly n phonons in the mechanical oscillator. In Sec.5.2, I determine $P_e^{|n\rangle}(\omega)$ by simulating the mechanical motion with a classical modulation on the qubit gate-charge. In Sec.5.3, I describe the Lucy-Richardson deconvolution procedure used in this work. Finally in Sec.5.4, I validate both the experimentally determined $P_e^{|n\rangle}(\omega)$ and the deconvolution procedure by extracting the phonon populations of thermal and displaced thermal states.

5.1 Understanding the mechanical state using the qubit spectrum

The qubit can be leveraged as a meter for measuring and extracting the phonon distribution in the mechanical oscillator. This is achieved by measuring the qubit spectrum $P_e(\omega)$, whereby I measure the probability of successfully driving the qubit to its excited-state as a function of the frequency of a weak coherent drive. Recalling the discussion of Sec.2.3.4.3, a statistical mixture of phonon Fock states in the mechanical oscillator will cause an overall qubit spectrum,

$$P_e(\omega) = \sum_n P(n) \times P_e^{|n\rangle}(\omega), \tag{5.1}$$

given by the convolution between the phonon distribution $P(n)$ and $P_e^{|n\rangle}(\omega)$. Because $P_e^{|n\rangle}(\omega)$ is different for different phonon numbers n, a deconvolution procedure can be used to invert this equation and extract the phonon distribution $P(n)$.

Clearly, an accurate extraction of the phonon distribution requires an accurate description of $P_e^{|n\rangle}(\omega)$. However, this is not easily achieved because of the small mechanical frequency. In contrast to the simple Lorentzian lineshape discussed in Sec.2.3.4.3, the small $\omega_{\rm m}$ significantly complicates $P_e^{|n\rangle}(\omega)$ with sideband transitions. In addition to being close to the qubit frequency, these sidebands can also be highly prominent even at a relatively small number of phonons $n \sim 100$ (because of the relatively large ratio of $\chi_{\rm m}/\omega_{\rm m} \approx 0.01$, see discussion around Eqn.(2.80)). Moreover, because of these sideband transitions, the measurement of the qubit spectrum is not a quantum-nondemolition (QND) measurement of the phonon number. Instead, as I discuss in Sec.5.2.2, measuring the qubit spectrum can alter the phonon number, further complicating the issue of finding an accurate description of $P_e^{|n\rangle}(\omega)$. Without the ability to prepare arbitrary phonon Fock state (because $\chi_{\rm m} < \Gamma_2^*$), I cannot determine $P_e^{|n\rangle}(\omega)$ directly.

5.2 Simulating quantized motion with classical gate-charge modulation

Instead, I experimentally determine $P_e^{|n\rangle}(\omega)$ by using a classical modulation of the qubit gate-charge at frequency $\omega_{\rm m}$ to simulate the effect of motion. Because the qubit-mechanical coupling originates from a oscillator-position dependent gate-charge $n_g(x)$ (Sec.2.3.1), the effect of the motion, when treated classically, is identical to a classical gate-charge modulation in time,

$$n_g(t) = \frac{1}{2} + \delta n_g + n_x \cos(\omega_{\rm m} t), \tag{5.2}$$

where n_x is the modulation amplitude, and δn_g is an offset from the charge degeneracy point. This classical modulation is achieved by setting $V_{\rm dc} = 0$ V and driving an ac-voltage on the dc-bias line, which is weakly coupled to the qubit. Varying the amplitude of the ac-voltage, I measure the qubit response as shown in Fig. 5.1. In this section, I demonstrate this measured qubit response to be in close correspondence with the qubit response expected from quantized motion (Sec.5.2.3), allowing

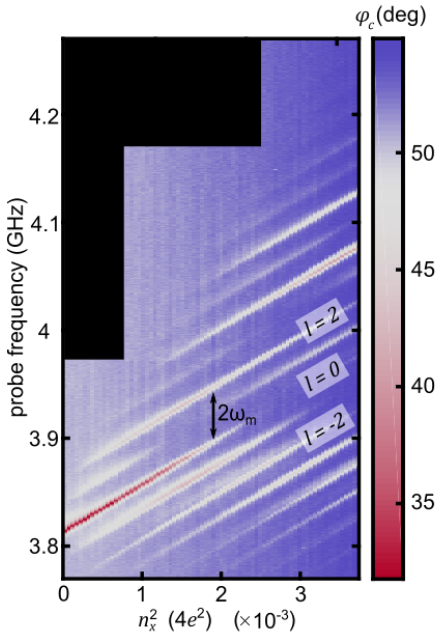

Figure 5.1: Measured qubit response under classical classical gate-charge modulation
At $V_{\rm dc} = 0$ V, I sweep the frequency of a weak qubit-excitation probe signal (y-axis) and measure the cavity transmission phase φ_c (color-scale) as a function of the classical modulation amplitude squared n_x^2 (x-axis). The qubit excitations appear as dips in φ_c. In addition to a qubit frequency shift that is linearly dependent on n_x^2, the gate-charge modulation at frequency $\omega_{\rm m}$ also causes the appearance of sideband ($l \neq 0$) peaks. The background phase increases at larger n_x because the gate-charge modulation around $n_g = 1/2$ rectifies the cavity phase response of Fig. 4.1 (see Sec.4.1.1). Data is not collected in the black region because no feature is expected.

me to extract $P_e^{|n\rangle}(\omega)$ (Sec.5.2.5). This section (except Sec.5.2.2) closely follows publication [85].

5.2.1 Qubit spectrum under classical gate-charge modulation

To demonstrate this close correspondence, I first find the expected qubit spectrum for a classical gate charge modulation according to Eqn.(5.2). I will show that, working around the charge degeneracy point ($\delta n_g = 0$), the driven modulated-qubit can be viewed as a sum of many two-level systems, each located at frequencies,

$$\begin{aligned}\omega_{x,2l}(n_x) &= \frac{1}{\hbar}\left[E_J + \frac{(4E_c)^2}{E_J} n_x^2\right] + 2l\omega_{\mathrm{m}} \\ &= \omega_{\mathrm{q}}^b + \delta\omega_{\mathrm{q}}^x(n_x) + 2l\omega_{\mathrm{m}} \qquad (l \in \mathbb{Z}),\end{aligned} \tag{5.3}$$

and oscillates at rates given by the Bessel function of the first kind,

$$\Omega_{x,2l}(n_x) = \Omega_R J_l\left(\frac{\delta\omega_{\mathrm{q}}^x(n_x)}{2\omega_{\mathrm{m}}}\right). \tag{5.4}$$

Consequently, the qubit spectrum in steady state is a sum of Lorentzians, each given by Eqn.(2.81).

To derive the above equations, I start by expanding the qubit frequency (Eqn.(2.24)) around small modulation amplitude,

$$\begin{aligned}\hbar\omega_{\mathrm{q}}(t) &= \sqrt{E_J^2 + (4E_c)^2(1-2n_g(t))^2} \\ &= E_J + 2\frac{(4E_c)^2}{E_J} n_x^2 \cos^2(\omega_{\mathrm{m}} t) + \mathcal{O}(n_x^4) \\ &\approx E_J + \frac{(4E_c)^2}{E_J} n_x^2 + \frac{(4E_c)^2}{E_J} n_x^2 \cos(2\omega_{\mathrm{m}} t).\end{aligned} \tag{5.5}$$

Here, the first term corresponds to the bare (i.e., without modulation) qubit frequency at the charge degeneracy point, $\omega_{\mathrm{q}}^b = E_J/\hbar$. The second term is a static frequency shift of the qubit

$$\delta\omega_{\mathrm{q}}^x(n_x) = \omega_{\mathrm{q}}^x(n_x) - \omega_{\mathrm{q}}^b = \frac{(4E_c)^2}{\hbar E_J} n_x^2 \tag{5.6}$$

that is proportional to the energy in the classical drive. This frequency shift is analogous to the ac-Stark shift proportional to phonon numbers (Eqn.(2.56)). Finally, the last term in the above equation is a frequency modulation of the qubit frequency at $2\omega_{\mathrm{m}}$.

Without decoherence, the time evolution of the modulated qubit under a coherent qubit drive is clear in the interaction picture. I begin with the bare Hamiltonian

$$H_0^c = \frac{1}{2}\hbar\omega_q(t)\hat{\sigma}_z, \tag{5.7}$$

whose time evolution operator is

$$\hat{U}_0^c(t) = \hat{\mathcal{T}}\left(\exp\left[-\frac{i}{\hbar}\int_0^t H_0^c(\tau)d\tau\right]\right) = \exp\left[-\frac{i}{2}\phi(t)\hat{\sigma}_z\right], \tag{5.8}$$

where the time ordering operator $\hat{\mathcal{T}}$ is dropped because the Hamiltonian commutes at any time ($[H_0^c(t_1), H_0^c(t_2)] = 0$), and

$$\phi(t) = \int_0^t \omega_q(\tau)d\tau = \left[\omega_q^b + \delta\omega_q^x(n_x)\right]t + \frac{\delta\omega_q^x(n_x)}{2\omega_m}\sin(2\omega_m t). \tag{5.9}$$

In the interaction picture, the coherent qubit drive of Eqn.(2.71) is transformed to an interaction Hamiltonian,

$$\begin{aligned}\mathcal{V}^c(t) &= \hat{U}_0^{c\dagger}(t)H_d(t)\hat{U}_0^c(t)\\ &= \hbar\Omega_R\left(\hat{\sigma}_+ e^{i[\phi(t)-\omega_d t]} + \hat{\sigma}_- e^{-i[\phi(t)-\omega_d t]}\right)\\ &= \hbar\sum_{l=-\infty}^{\infty}\Omega_{x,2l}(n_x)\left[\hat{\sigma}_+ e^{i\Delta_{x,2l}t} + \hat{\sigma}_- e^{-i\Delta_{x,2l}t}\right]\end{aligned} \tag{5.10}$$

where I have invoked the Jacobi-Anger expansion to find $\Omega_{x,2l}(n_x)$ given by Eqn.(5.4), and

$$\Delta_{x,2l} = \omega_{x,2l}(n_x) - \omega_d. \tag{5.11}$$

Thus, when the qubit drive is resonant with this $2l$-th transition frequency, the state of the qubit will oscillate at rate $\Omega_{x,2l}(n_x)$. Similar to Eqn.(2.73), these qubit transitions are separated by $2\omega_m$ because of symmetric gate-charge modulation.

Finally, the dissipation can be added to find the expected qubit spectrum [131, 132]. For a weak qubit drive $\Omega_R < \omega_m$ close to the $2l$-th transition frequency $\omega_{x,2l}(n_x)$, Eqn.(5.10) can be simplified to contain only the near-resonant terms. Furthermore, because $\omega_m \gg \Gamma_2$, the qubit spectrum from each resonance is easily resolvable and can be calculated separately. The overall steady-state qubit spectrum is given by the sum,

$$P_e^{n_x}(\omega_d) = \frac{1}{2}\sum_{l=-\infty}^{\infty}\frac{(A_{x,2l}\Gamma_2/2)^2}{\Delta_{x,2l}^2(\omega_d) + (\Gamma_2/2)^2\left(1 + A_{x,2l}^2\right)}, \tag{5.12}$$

where

$$A_{x,2l} = \Omega_{x,2l}\left(n_x\right)\sqrt{\frac{2}{\Gamma_1\Gamma_2}}. \tag{5.13}$$

A comparison between the above equations and Eqn.(2.81) shows that the driven modulated qubit resembles a sum over many effective two-level systems, each of which is located at frequency $\omega_{x,2l}(n_x)$ and oscillates at rate $\Omega_{x,2l}(n_x)$.

5.2.2 Qubit spectrum for a phonon Fock state

In comparison to the classical case discussed above, I now calculate the qubit spectrum for an initial Fock state $|g,n\rangle$. Although this can in general be accomplished by solving the master equation in Eqn.(2.64), it is extremely calculation intensive and provides little insight. Instead, I consider three cases for different phonon-number-sensitivities. For simplicity, I will ignore the mechanical relaxation process, $\gamma_{\mathrm{m}} = 0$.

In addition to providing a basis of comparison, this calculation also highlights the fact that measuring the qubit spectrum can alter the phonon number. For the rest of this thesis, I refer to this phenomena of qubit-measurement-induced change in phonon number as measurement backaction. This measurement backaction happens through either driving sideband transitions $|g,n\rangle \leftrightarrow |e,m\rangle$ or phonon-altering qubit decay processes $|e,n\rangle \mapsto |g,m\rangle$ $(m \neq n)$. Because of the large ratio $\chi_{\mathrm{m}}/\omega_{\mathrm{m}} \approx 0.01$, the phonon-altering qubit decay can have significant impacts even at a small phonon number (see Eqn.(2.67) and Sec.2.3.4.2). Consequently, in contrast to standard cQED systems [47, 105, 106, 107], measuring only the qubit spectrum from phonon-conserving transitions can still demolish the initial state (i.e., it is not a QND measurement of the phonon number).

5.2.2.1 phonon-number-resolved

First, I consider the qubit-mechanical system in the phonon-number-resolved regime ($2\chi_{\mathrm{m}} > \Gamma_2$). In this limit, a weak qubit drive close to frequency

$$\omega_{n,2l} = \omega_{\mathrm{q}}^{|n\rangle} + 2l\omega_{\mathrm{m}} \tag{5.14}$$

can only excite the transition $|g,n\rangle \leftrightarrow |e,n+2l\rangle$ with rate

$$\Omega_{n,2l} = \Omega_R |\alpha_{n+2l,n}|, \tag{5.15}$$

but not any other transitions $|g,m\rangle \leftrightarrow |e,m+2l\rangle$ for $m \neq n$. However, the decaying qubit can alter the phonon number to create a final state inaccessible to the qubit drive. These driven dynamics can be modeled by a three-level system as shown in Fig. 5.2(a), where $|\text{dark}\rangle$ represents all states $|g,m\rangle$ ($m \neq n$) that are inaccessible to the qubit drive. According to Sec.2.3.4.1, state $|e,n+2l\rangle$ decays to $|g,n\rangle$ at rate $\Gamma_1|\alpha_{n+2l,n}|^2$ and decays to $|\text{dark}\rangle$ at rate $\Gamma_1(1-|\alpha_{n+2l,n}|^2)$. The master equation of this three-level system can be solved numerically for different values of $|\alpha_{n+2l,n}|^2$. Driven at frequency ω_n^{2l}, the time evolution of the probability $P_{|e,n+2l\rangle}$ for finding state $|e,n+2l\rangle$ and probability P_{dark} for finding state $|\text{dark}\rangle$ is plotted in Fig. 5.3.

Inspired by the discussion above (Sec.5.2.1), I compare these dynamics to the driven response of a two-level system located at frequency $\omega_{n,2l}$, which oscillates between states $|\uparrow\rangle$ and $|\downarrow\rangle$ at rate $\Omega_{n,2l}$ (Fig. 5.2(b)). Depending on the strength of $\Omega_{n,2l}$, the evolution of $P_{|e,n+2l\rangle}$ is well approximated by the evolution of $P_\uparrow$ over a time scale of a few T_1. However, this approximation fails at larger times as the population slowly accumulates in the dark state $|\text{dark}\rangle$, and becomes inaccessible to the qubit drive. Thus, my attempt to measure the initial state $|g,n\rangle$ using qubit spectroscopy ends up driving it to a different state $|g,m\rangle$. This measurement backaction prevents the measurement from being QND even in the case of driving phonon-conserving transitions ($l=0$) when $|\alpha_{n,n}|^2 \neq 1$.

Nevertheless, at a drive time $T_d > T_1$ but before the effect of measurement backaction becomes clear ($P_{\text{dark}} \ll 1$), the qubit spectrum around frequencies $\omega_{n,2l}$ is well approximated by the steady-state spectrum of the effective two-level system. Generalizing this result to all l, the overall qubit spectrum $P_e^{|n\rangle}(\omega_d)$ of the initial state $|g,n\rangle$ can be approximated by a sum over steady-state qubit spectra of the effective two-level systems

$$P_e^{|n\rangle}(\omega_d) \approx \frac{1}{2}\sum_{l=-\infty}^{\infty} \frac{(A_{n,2l}\Gamma_2/2)^2}{\Delta_{n,2l}^2(\omega_d) + (\Gamma_2/2)^2\left(1+A_{n,2l}^2\right)}, \tag{5.16}$$

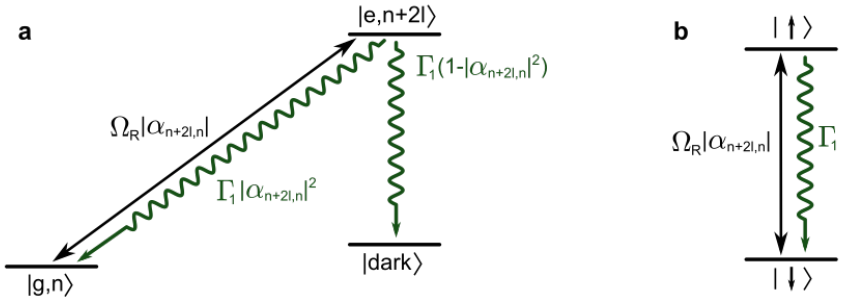

Figure 5.2: Driving a phonon-number-resolved system
a, In the phonon-number-resolved regime, the driven qubit-mechanical system can be modelled by a three-level system. A qubit drive close to frequency $\omega_{n,2l} = \omega_{\mathrm{q}}^{|n\rangle} + 2l\omega_{\mathrm{m}}$ can only excite transition $|g,n\rangle \leftrightarrow |e,n+2l\rangle$ at rate $\Omega_R|\alpha_{n+2l,n}|$. Thus, all other states $|g,m\rangle$ with $m \neq n$ appear as dark states to the qubit drive, and are labeled as $|\mathrm{dark}\rangle$. When the qubit decays from $|e,n+2l\rangle$, it can either decay to the original state $|g,n\rangle$ at rate $\Gamma_1|\alpha_{n+2l,n}|^2$, or to the dark states $|\mathrm{dark}\rangle$ at rate $\Gamma_1\left(1-|\alpha_{n+2l,n}|^2\right)$. **b,** It can be shown that at small driving time T_d such that the population P_{dark} in the dark state is small, the three-level system in **a** can be approximated by an effective two-level system at frequency $\omega_{n,2l}$. In this effective system, the drive excites transitions $|\downarrow\rangle \leftrightarrow |\uparrow\rangle$ at rate $\Omega_R|\alpha_{n+2l,n}|$, and $|\uparrow\rangle$ decays to $|\downarrow\rangle$ at rate Γ_1. For both **a** and **b**, the qubit also experiences a dephasing at rate $\Gamma_2/2$, which is not shown in the figure.

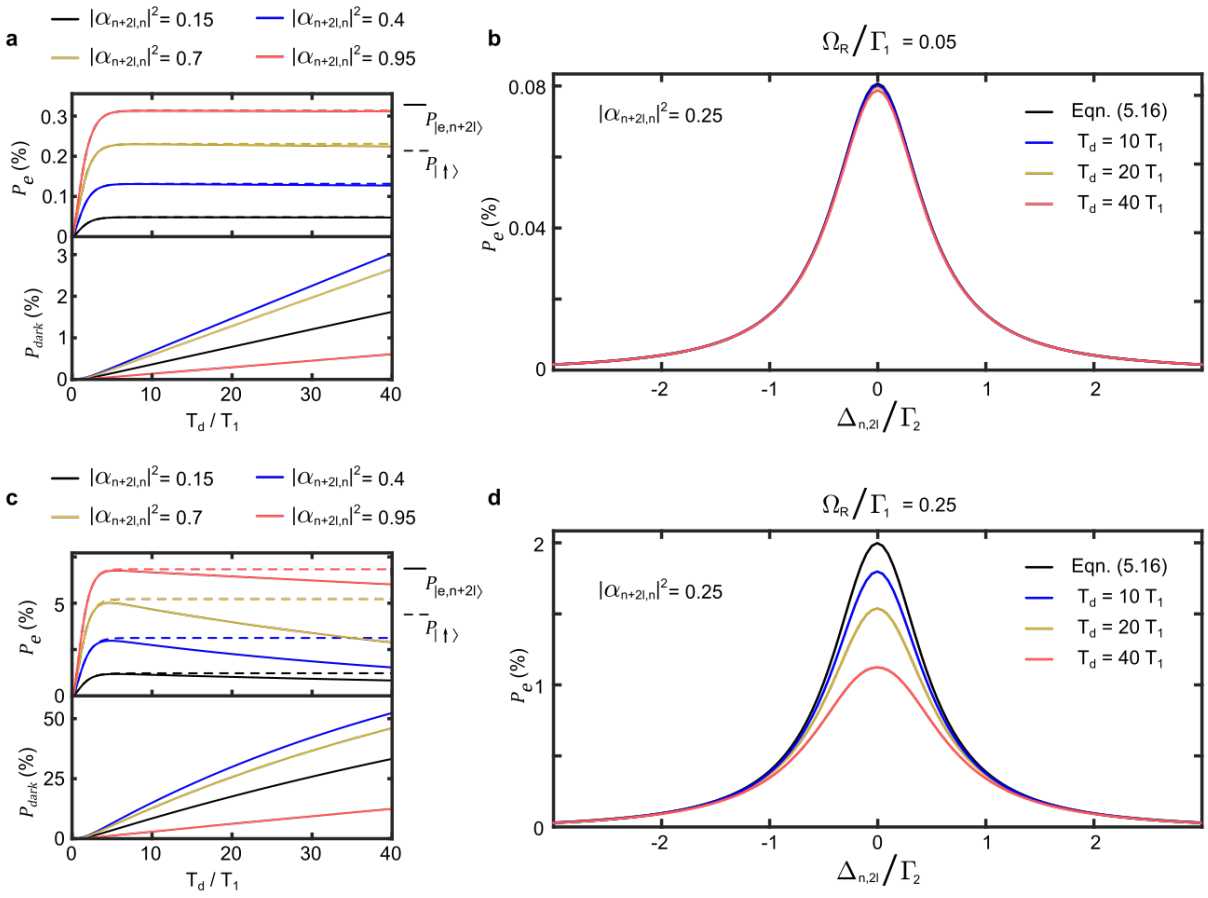

Figure 5.3: Dynamics in the phonon-number-resolved regime
a, Under a resonant drive $\Delta_{n,2l} = \omega_{n,2l} - \omega_d = 0$, I solve the master equation for both driven dissipative systems in Fig. 5.2 assuming an initial state $|g, n\rangle$ and the following parameters: $\Omega_R = 0.05\Gamma_1$, $\Gamma_2 = 3\Gamma_1$. For different values of $|\alpha_{n+2l,n}|$ (different colors), I plot the time evolution of the states $|e, n + 2l\rangle$ (top panel, solid lines), $|\uparrow\rangle$ (top panel, dashed lines), and $|\text{dark}\rangle$ (bottom panel, solid lines). The driving time T_d is normalized to the qubit lifetime $T_1 = 1/\Gamma_1$. Up to $T_d = 40T_1$, very little population escapes to the dark state at this weak drive strength, and the dynamics of the qubit-mechanical system is well approximated by the simple effective two-level system of Fig. 5.2(b).
b, Solving the master equation of the qubit-mechanical system at all values of driving frequency, I find the qubit spectrum $P_{|e,n+2l\rangle}(\omega_d)$ after different driving times $T_d = 10T_1$ (blue), $T_d = 20T_1$ (mustard), $T_d = 40T_1$ (red). Here, I assume $|\alpha_{n+2l,n}|^2 = 0.25$, and normalize the drive detuning $\Delta_{n,2l}$ to the qubit spectrum's minimum FWHM Γ_2 (see Sec.2.3.4.3). For reference, I also plot the steady-state spectrum for the effective two-level system (black) according to Eqn.(5.16). Indeed, because the qubit-mechanical system has experienced little measurement backaction (i.e. P_{dark} is small) in these cases, the qubit spectrum is well approximated by Eqn.(5.16). Similar calculations can be repeated for a larger drive strength $\Omega_R = 0.25\Gamma_1$, and the resulting time evolution (**c**) and qubit spectrum (**d**) are plotted. Because the qubit-mechanical system experiences significant backaction, the resulting qubit spectrum is not well approximated by Eqn.(5.16), with worse quality of the approximation at larger measurement backaction (i.e., larger T_d).

where

$$A_{n,2l} = \Omega_{n,2l}\sqrt{\frac{2}{\Gamma_1\Gamma_2}}, \tag{5.17}$$

and

$$\Delta_{n,2l}(\omega_d) = \omega_{n,2l} - \omega_d. \tag{5.18}$$

5.2.2.2 phonon-number-sensitive

To further demonstrate the effect of measurement backaction, I now consider a phonon-number-sensitive qubit-mechanical system, where a qubit drive can address the same type of transitions over a section of the phonon population. As an example, I start from an initial state $|g, n\rangle$ and consider the effect of a qubit drive of strength Ω_R close to its two-phonon blue sideband transition $|g, n\rangle \leftrightarrow |e, n+2\rangle$ in the hypothetical scenario shown in Fig. 5.4. When it is resonant with frequency $\omega_{n,2}$, the qubit drive will excite the transition with rate $\Omega_{n,2} = \Omega_R|\alpha_{n+2,n}|$. Furthermore, the qubit drive can also excite transition $|g, n+2\rangle \leftrightarrow |e, n+4\rangle$ at frequency $\omega_{n+2,2} = \omega_{n,2} + 4\chi_{\mathrm{m}}$ with transition rate $\Omega_{n+2,2} = \Omega_R|\alpha_{n+4,n+2}|$. All other states $|g, m\rangle$ with $m \neq \{n, n+2\}$ are inaccessible to the qubit drive, and labeled as $|\mathrm{dark}\rangle$. A decaying qubit connects state $|e, n+2\rangle$ to $|g, n\rangle$ at rate $\Gamma_1|\alpha_{n+2,n}|^2$ and to $|g, n+2\rangle$ at rate $\Gamma_1(1 - |\alpha_{n+2,n}|^2)$. Similarly, decays $|e, n+4\rangle \mapsto |g, n+2\rangle$ happens at rate $\Gamma_1|\alpha_{n+4,n+2}|^2$ and $|e, n+4\rangle \mapsto |\mathrm{dark}\rangle$ happens at rate $\Gamma_1(1 - |\alpha_{n+4,n+2}|^2)$. I solve the master equation of this driven dynamics numerically. Approximating $|\alpha_{n+2,n}| \approx |\alpha_{n+4,n+2}|$, I plot the resulting qubit spectrum at different T_d in Fig. 5.5.

When the detuning between the two sideband transitions $\omega_{n+2,2} - \omega_{n,2} = 4\chi_{\mathrm{m}}$ is larger than Γ_2, $|g, n+2\rangle$ becomes effectively part of the dark state $|\mathrm{dark}\rangle$, and I recover the phonon-number-resolved regime as discussed above. This identifies a characteristic width

$$W = \Gamma_2/2\chi_{\mathrm{m}} \qquad [\mathrm{phonons}] \tag{5.19}$$

over which the qubit drive is effective. In other words, a qubit drive at frequency $\omega_{n,2l}$ can excite the transition $|g, m\rangle \leftrightarrow |e, m+2l\rangle$ effectively for $|m - n| < W/2$, but does little for transitions further

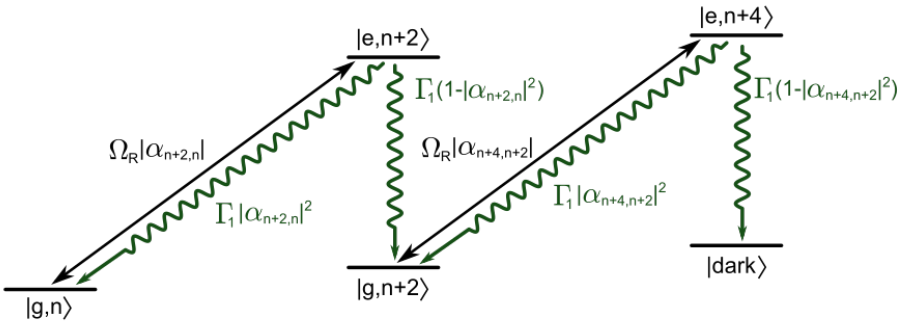

Figure 5.4: Driving blue sideband transitions in a phonon-number-sensitive system
Starting from an initial state $|g, n\rangle$, I consider a qubit drive that can only access two transitions. At frequency $\omega_{n,2}$, the qubit drive can excite transition $|g, n\rangle \leftrightarrow |e, n+2\rangle$ at rate $\Omega_R|\alpha_{n+2,n}|$; and at frequency $\omega_{n+2,2} = \omega_{n,2} + 4\chi_{\mathrm{m}}$, the qubit drive can excite transition $|g, n+2\rangle \leftrightarrow |e, n+4\rangle$ at rate $\Omega_R|\alpha_{n+4,n+2}|$. All other states appear as dark states to the qubit drive and are labeled as $|\mathrm{dark}\rangle$. For simplicity, I assume $|e, n+2\rangle$ can only decay to states $|g, n\rangle$ and $|g, n+2\rangle$ at rates $\Gamma_1|\alpha_{n+2,n}|^2$ and $\Gamma_1(1-|\alpha_{n+2,n}|^2)$ respectively. Similarly, state $|e, n+4\rangle$ only decays to either $|g, n+2\rangle$ at rate $\Gamma_1|\alpha_{n+4,n+2}|^2$ or $|\mathrm{dark}\rangle$ at rate $\Gamma_1(1-|\alpha_{n+4,n+2}|^2)$. All states also experiences a qubit dephasing at rate $\Gamma_2/2$, which is not plotted. I also assume no mechanical relaxation.

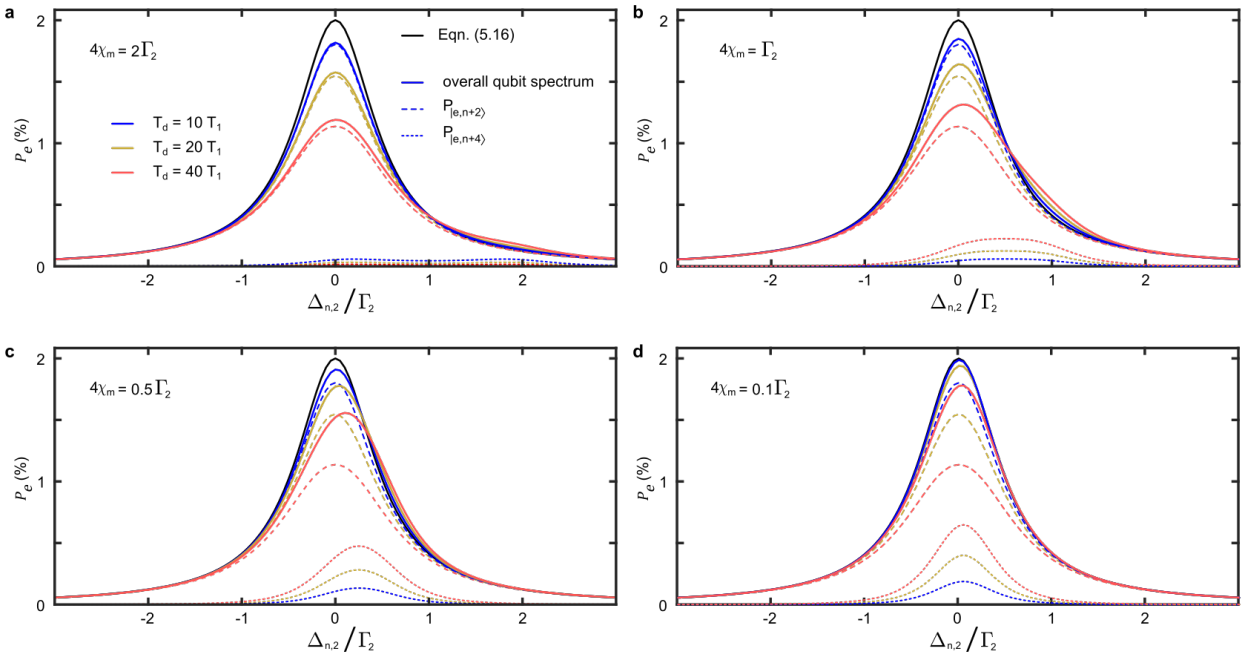

Figure 5.5: Sideband spectrum in a phonon-number-sensitive system
a, I solve the master equation for the driven dissipative system in Fig. 5.4 assuming the following parameters: $|\alpha_{n+2,n}|^2 = |\alpha_{n+4,n+2}| = 0.25$, $\Omega_R = 0.25\Gamma_1$, $\Gamma_2 = 3\Gamma_1$, and $4\chi_{\rm m} = 2\Gamma_2$. Normalizing the drive detunning ($\Delta_{n,2} = \omega_{n,2} - \omega_d$) to the minimum qubit FWHM Γ_2, I then plot the expected overall qubit spectrum (solid lines) after different values of drive time, $T_d = 10T_1$ (blue), $T_d = 20T_1$ (mustard), $T_d = 40T_1$ (red). For comparison, I also plot the expected spectrum according to Eqn.(5.1) (black line). The overall qubit spectrum $P_e(\omega_d)$ has two contributions $P_{|e,n+2\rangle}(\omega_d)$ (dashed lines) and $P_{|e,n+4\rangle}(\omega_d)$ (dotted lines). At this small $W = \Gamma_2/2\chi_{\rm m} = 1$, the qubit drive has little effect on the population in $|g, n+2\rangle$, which appear as if it were part of the dark state $|\text{dark}\rangle$. Consequently, the resulting spectrum resembles that found in the phonon-number-resolved regime (Fig. 5.3(d)). I repeat the same calculation for different values of $W = \Gamma_2/2\chi_{\rm m}$ and plot the resulting qubit spectrum: $W = 2$ (**b**), $W = 4$ (**c**), and $W = 20$ (**d**). In these cases, the qubit drive can excite transition $|g, n+2\rangle \leftrightarrow |e, n+4\rangle$ effectively, and the measurement backaction appear as a broadening of the overall qubit spectrum accompanied by a shift toward higher frequency.

away. In the next chapter, I will explore the effects of such phonon-number-sensitive sideband drives in more detail.

On the other hand for $4\chi_{\mathrm{m}} < \Gamma_2$, the qubit drive can simultaneously excite both sideband transitions. At small T_d, the population is mostly confined in the sub-space $\{|g,n\rangle, |e,n+2\rangle\}$, and the overall qubit spectrum (solid lines) is dominated by the probability of finding state $|e,n+2\rangle$ (dashed lines). However, at larger T_d, the population slowly escapes the sub-space through the decaying qubit, and can be further excited to state $|e,n+4\rangle$ (dotted lines). Consequently, because the measurement increases the phonon number and $\chi_{\mathrm{m}} > 0$, the overall qubit spectrum broadens and shifts toward a higher frequency. Conversely, if the measurement causes a reduction of the phonon number by driving the red sideband transitions, the overall qubit spectrum will shift toward a lower frequency. These effects are experimentally observed in Sec.7.1.1, and are used to quantify the amount of measurement backaction the qubit-mechanical system has experienced. Nevertheless, before such effects become prominent, the overall qubit spectrum can be well approximated by Eqn.(5.16).

5.2.2.3 phonon-number-insensitive

Finally, I consider a qubit-mechanical system that is entirely phonon-number-insensitive ($W \to \infty$), such that a qubit drive does not differentiate between different phonon numbers. This can be understood as an extremely weak coupling between the qubit and the mechanical oscillator. In this limit, the motion of the mechanical oscillator can be treated classically as was done in Sec.5.2.1, and Eqn.(5.16) becomes exact. This trend can also be observed in Fig. 5.5 by imagining the effect of reducing χ_{m}.

5.2.3 Classical vs. quantum

From the above discussions, I find the qubit spectrum for a phonon Fock state can be well approximated by the qubit spectrum (Eqn.(5.12)) under a classical gate-charge modulation when two conditions are simultaneously satisfied:

- The spectroscopic drive time T_d needs to be sufficiently short such that the effect of measurement backaction is negligible.

- Under the same resonant condition $\omega_{n,2l} = \omega_{x,2l}$, the effective transition rates should be almost equal

$$\Omega_{n,2l} \approx \Omega_{x,2l}, \tag{5.20}$$

  such that the difference between the spectra according to Eqn.(5.12) and Eqn.(5.16) is negligible.

In Sec.7.1.1, I will experimentally determine the appropriate T_d to satisfy the first condition. Here, I demonstrate the second condition can also be satisfied given the achieved $\chi_{\mathrm{m}}/\omega_{\mathrm{m}} \approx 0.01$ in this work.

In general, the effective transition rates in a quantum system are not the same as those under a classical gate-charge modulation. Specifically, under a classical modulation, the transition rates are symmetric around the center qubit peak, $\Omega_{x,2l} = \Omega_{x,-2l}$ (Eqn.(5.4)). With quantized motion, however, the transition rates are asymmetric around the phonon-conserving transition $l = 0$. A simple example is the case of an initial state $|g, 0\rangle$. While phonons can be added into the mechanical oscillator through blue sideband transitions, no phonon can be extracted from the mechanical ground state with a red sideband transition.

In this work, however, the qubit response to quantized motion is well approximated by the qubit response to classical modulation. When the sideband transitions become prominent features in the qubit spectrum at $n \gtrsim 100$, the asymmetry between the blue and red sideband transitions is small enough to be neglected. Conversely, when the asymmetry is strong at small phonon numbers, the qubit spectrum is dominated by the phonon-conserving transition and the sidebands can be all together ignored. To provide an intuition for this, I calculate the asymmetry by expanding the sideband rate $\Omega_{n,\pm 2}$ connecting states $|g, n\rangle$ and $|g, n \pm 2\rangle$ to first order in $\chi_{\mathrm{m}}/\omega_{\mathrm{m}}$ (Eqn.(2.78)),

$$\frac{\Omega_{n,-2}}{\Omega_{n,2}} \approx \sqrt{\frac{n(n-1)}{(n+1)(n+2)}} \approx 1 - \frac{2}{n} + \mathcal{O}(\frac{1}{n^2}). \tag{5.21}$$

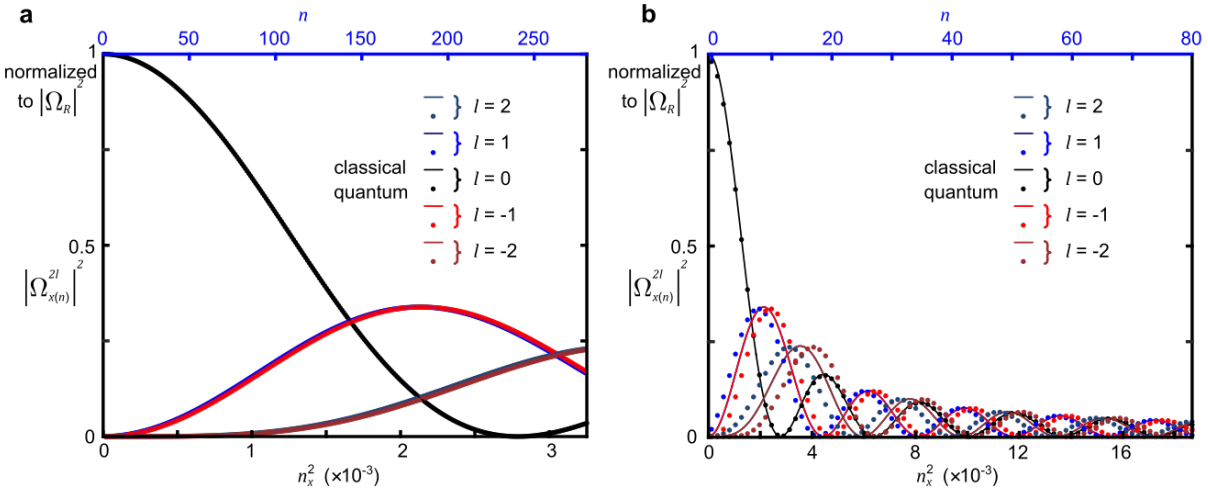

Figure 5.6: Transition rates under classical modulation vs. quantized motion
The solid lines correspond to transition rates squared $|\Omega_{x,2l}|^2$ as functions of the n_g modulation amplitude squared n_x^2 (bottom-axis) according to Eqn.(5.4). The dots correspond to transition rates squared $|\Omega_{n,2l}|^2$ for a given initial phonon number n (top-axis) according to Eqn.(2.78). For a given ratio of $\chi_\mathrm{m}/\omega_\mathrm{m}$ $\left(\mathbf{a},\ \chi_\mathrm{m}/\omega_\mathrm{m} = 0.01 \text{ and } \mathbf{b},\ \chi_\mathrm{m}/\omega_\mathrm{m} = 0.2\right)$, n_x^2 is related to n by enforcing the same qubit-frequency shift according to Eqn.(5.22). The quality of approximation using classical gate-charge modulation degrades for larger χ_m. This figure is reproduced from reference [85].

At $n = 100$ phonons, this corresponds to a $\sim 2\%$ asymmetry between sideband rates and a $\sim 1\%$ deviation from the classical case. Indeed a negligible amount compared to the measurement noise in the qubit spectrum.

Going beyond the intuition, a more rigorous numerical comparison can be made between the transition rates under classical and quantum modulation using Eqn.(5.4) and Eqn.(2.78). To perform this comparison, I first calibrate the charge modulation amplitude to units of motional quanta such that they shift the qubit-frequency by the same amount ($\omega_{\mathrm{q}}^{|n\rangle} = \omega_{\mathrm{q}}^{x}(n_x)$),

$$n + \frac{1}{2} = \frac{(4E_c)^2}{2\chi_{\mathrm{m}} E_J} n_x^2, \tag{5.22}$$

where n is the motional quanta, and n_x is the modulation amplitude of gate-charge. In this equation, the 1/2 term on the left-hand side corresponds to the qubit lamb-shift [133] induced by the mechanical vacuum state, but is absent from the right-hand side because the classical gate-charge modulation is performed when the qubit is decoupled from the mechanical oscillator. Fig. 5.6 shows numerical comparisons of the transition rates under classical and quantum theory. Although different for large ratios of $\chi_{\mathrm{m}}/\omega_{\mathrm{m}}$ (Fig. 5.6(b)), for this work with $\chi_{\mathrm{m}}/\omega_{\mathrm{m}} \approx 0.01$, Fig. 5.6(a) demonstrates the simulation with classical modulation to be a good approximation for qubit response to quantized motion in the mechanical oscillator.

5.2.4 Effects of charge noise

So far, the discussion assumes the qubit is always operated at the charge degeneracy point. However, this is not always possible in the presence of charge noise, which causes deviation δn_g in the gate-charge away from the degeneracy point. Indeed, in Fig. 5.1, I observe sideband transition peaks separated by frequency ω_{m} instead of $2\omega_{\mathrm{m}}$, suggesting deviation from the sweet-spot. In this section, I explore the effects of a $1/f$ charge noise on the qubit spectrum, and show the classical gate-modulation remains a faithful simulation of quantized mechanical motion in this experiment (Sec.5.2.4.2). Using the asymmetry in the qubit spectrum at $V_{\mathrm{dc}} = 0$ V and $n_x = 0$, I extract a charge noise intensity consistent with typically reported values in Sec.5.2.4.1. Based on

this intensity, I theoretically calculate the qubit spectrum in Sec.5.2.4.3 for arbitrary modulation amplitudes n_x. The good correspondence between this calculation and the measured qubit response demonstrates that the odd order sideband transitions observed in Fig. 5.1 are indeed caused by charge-noise.

In this section, I model charge noise as a sum of sinusoidal signals at equally-spaced frequencies ω_i with random phases ϕ_i uniformly distributed within range $[0, 2\pi]$ [134],

$$\sum_i n_e(\omega_i) \cos(\omega_i t + \phi_i). \tag{5.23}$$

The noise amplitude $n_e(\omega_i)$ is found by integrating the single-sided noise-power spectral density $S_{2e}(\omega)$ over a frequency range centered at ω_i,

$$n_e(\omega_i) = \int_{\omega_i - \delta\omega}^{\omega_i + \delta\omega} d\omega \sqrt{2 S_{2e}(\omega)}, \tag{5.24}$$

where $2\delta\omega = \omega_{i+1} - \omega_i$. Assuming a $1/f$ noise distribution,

$$S_{2e}(\omega) = \zeta^2 \frac{2\pi \times 10}{\omega}, \tag{5.25}$$

where ζ is the noise intensity at 10 Hz in units of Cooper-pairs ($2e/\sqrt{\text{Hz}}$). Thus, the overall time dependence of the gate-charge centered around the degeneracy point is

$$n_g(t) = \frac{1}{2} + n_x \cos(\omega_{\text{m}} t) + \sum_i n_e(\omega_i) \cos(\omega_i t + \phi_i). \tag{5.26}$$

5.2.4.1 Asymmetric lineshape and charge noise intensity

To explore the effect of this charge noise, I start by finding the noise intensity ζ. This can be achieved by looking at the qubit lineshape at $n_x = 0$. Because charge noise is dominated by components at low frequencies and the qubit spectrum is averaged over many experimental realizations, charge noise result in an asymmetric qubit lineshape (Fig. 5.7). This phenomenon is best understood phenomenologically by treating the incoherent charge noise of Eqn.(5.23) as a set of stationary charge offsets $\{\delta n_g\}$ away from $n_g = 1/2$. Assuming a Gaussian process for this offset with mean $\langle \delta n_g \rangle = 0$ and standard deviation σ_c, the averaged qubit spectrum with $n_x = 0$ is a sum

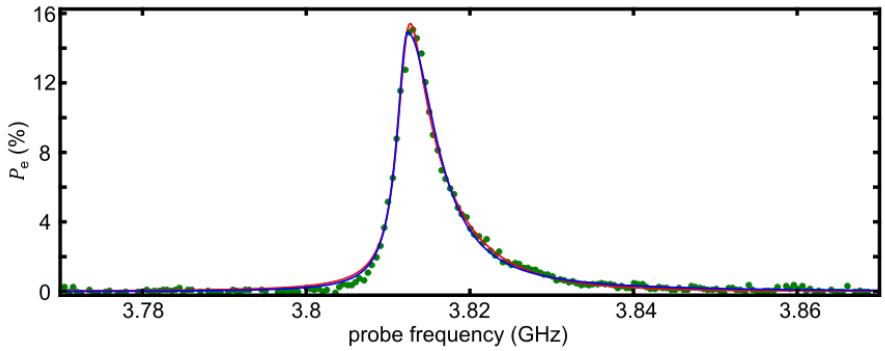

Figure 5.7: Noise-induced asymmetric qubit lineshape
Using Eqn.(4.4), I convert the phase response at $n_x = 0$ in Fig.5.1 to a qubit spectrum (green dots). Because of the highly averaged measurement protocol, the $1/f$ charge noise manifests as an asymmetric qubit lineshape. Modelling the charge noise as a Gaussian random variable, I fit (red) the qubit lineshape with Eqn.(5.27) to find the standard deviation in gate-charge, $\sigma_c = 0.0071$ $(2e)$. Alternatively, I fit the qubit lineshape with skewed Lorentzians (blue) without assumptions of charge noise distribution according to Eqn.(5.41). I use this skewed Lorentzian fit to process the measured qubit response in Sec.5.2.5. This figure is reproduced from reference [85].

of Lorentzians weighted by the corresponding offset probability,

$$P_e(\omega) = \int_{d\delta n_g} \frac{1}{\sqrt{2\pi\sigma_c^2}} \exp\Big(-\frac{\delta n_g^2}{2\sigma_c^2}\Big) \left[\frac{(A\Gamma_{\rm ncn}/2)^2}{\big(\omega - \omega_{\rm q}^b(\delta n_g)\big)^2 + (\Gamma_{\rm ncn}/2)^2(1+A^2)}\right] d\delta n_g, \tag{5.27}$$

where $\Gamma_{\rm ncn}/2$ is the qubit dephasing rate without charge noise, $A = \Omega_R\sqrt{2/\big(\Gamma_1\Gamma_{\rm ncn}\big)}$ is the unitless parameter describing the transition rate, and $\omega_{\rm q}^b(\delta n_g) = \sqrt{E_J^2 + (8E_c\delta n_g)^2}$ is the bare qubit resonance given an offset δn_g.

Using the above equation, I fit the qubit lineshape in Fig. 5.7 with A, E_J and σ_c being free parameters to find a charge-offset uncertainty $\sigma_c = 0.0071(2e)$. Given the measurement protocol, this σ_c value corresponds to [135, 134] a $1/f$ charge noise intensity of $\zeta/2 \approx 1.03\times10^{-3}e/\sqrt{\rm Hz}$ at 10 Hz, consistent with the typical charge noise intensity of $10^{-3} - 10^{-4}\ e/\sqrt{\rm Hz}$ at 10 Hz [125].

5.2.4.2 Classical gate-charge modulation with charge noise

This charge noise has two effects on the qubit spectrum when the gate-charge is classically modulated: while charge noise with frequency components much less than $\omega_{\rm m}$ contributes to an asymmetric qubit lineshape and cause sideband peaks at odd-orders of $\omega_{\rm m}$, charge noise at $\omega_{\rm m}$ cause the classical modulation to become noisy. Nevertheless, the classical gate-charge modulation remains a faithful simulation of quantized mechanical motion in the presence of these effects.

To see this, I start by writing the overall time dependence of the gate-charge. Instead of Eqn.(5.26), I phenomenologically treat the charge noise with frequency components much less than $\omega_{\rm m}$ as a noisy offset charge δn_g. Keeping only the charge noise at frequency $\omega_{\rm m}$, the time dependence of the modulated gate-charge is,

$$\begin{aligned} n_g(t) &= \frac{1}{2} + \delta n_g + n_x\cos\omega_{\rm m}t + n_{\rm m}\cos\left(\omega_{\rm m}t + \phi_{\rm m}\right) \\ &= \frac{1}{2} + \delta n_g + n_n\cos\left(\omega_m t - \phi_n\right), \end{aligned} \tag{5.28}$$

where $n_{\rm m} = n_e(\omega_{\rm m})$ and the noisy phase $\phi_{\rm m}$ is uniformly distributed within range $[0, 2\pi]$. This charge noise at $\omega_{\rm m}$ thus transforms the noiseless n_x modulation into a modulation with a noisy amplitude

$$n_n = \sqrt{n_x^2 + n_{\rm m}^2 + 2n_x n_{\rm m}\cos\phi_{\rm m}}, \tag{5.29}$$

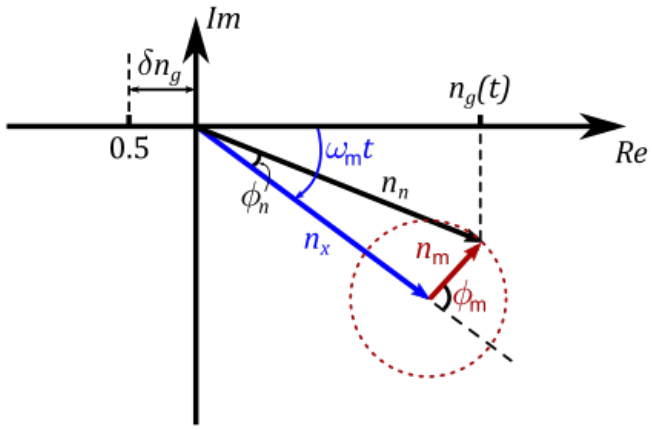

Figure 5.8: A noisy gate-charge modulation
To clarify Eqn.(5.28), I plot the phase-space picture of the gate-charge modulation. The projection on the Re-axis is the instantaneous gate-charge value $n_g(t)$. Charge noise with frequency components much lower than ω_m result in a offset gate charge δn_g. The noiseless modulation (blue) of amplitude n_x rotates around $n_g = 0.5 + \delta n_g$ at frequency ω_m. The charge noise at frequency $\omega_t extm$ (red) has noise amplitude n_m, and is offset from the noiseless modulation at a noisy angle ϕ_m uniformly distributed between $[0, 2\pi]$ (red dashed circle). The net result is therefore an overall modulation (black) with noisy amplitude n_n, and a noisy offset angle $-\phi_n$.

and a noisy phase

$$\phi_n = \arctan\frac{n_{\rm m}\sin\phi_{\rm m}}{n_x + n_{\rm m}\cos\phi_{\rm m}}, \tag{5.30}$$

as shown in Fig. 5.8. Thus, n_n and ϕ_n are random variables found by treating $\phi_{\rm m}$ as a random variable distributed uniformly within $[0, 2\pi]$.

Similar to Sec.5.2.1, the gate-charge modulation of Eqn.(5.28) causes the qubit frequency to shift by an amount proportional to the modulation power n_n^2,

$$\delta\omega_{\rm q}^x(n_n, \delta n_g) = \frac{\left(4E_cE_J/\hbar^2\right)^2}{\left(\omega_{\rm q}^b(\delta n_g)\right)^3} n_n^2, \tag{5.31}$$

where

$$\omega_{\rm q}^b(\delta n_g) = \frac{1}{\hbar}\sqrt{E_J^2 + (8E_c\delta n_g)^2} \tag{5.32}$$

is the bare qubit frequency. Additionally, for a particular $\delta n_g \neq 0$, the gate-charge modulation is not symmetric around the charge degeneracy point. Consequently, sideband transitions appear at odd intervals of $\omega_{\rm m}$,

$$\omega_{x,l}(n_n, \delta n_g) = \omega_{\rm q}^b(\delta n_g) + \delta\omega_{\rm q}^x(n_n, \delta n_g) + l\omega_{\rm m} \qquad (l \in \mathbb{Z}), \tag{5.33}$$

consistent with what I observe in Fig. 5.1. A resonant qubit drive of strength Ω_R at frequency $\omega_{x,l}$ will drive the corresponding transition at rate

$$\Omega_{x,l} = \Omega_R \sum_{2a+b=l} J_a\left[\frac{\delta\omega_{\rm q}^x(\delta n_g, n_n)}{2\omega_{\rm m}}\right] J_b\left[\frac{(8E_c/\hbar)^2}{\omega_{\rm m}\omega_{\rm q}^b(\delta n_g)} n_n\delta n_g\right]. \tag{5.34}$$

To show the classical gate-charge modulation remains a faithful simulation of quantized mechanical motion in the presence of charge noise, I first show the relative uncertainty in the modulation amplitude of Eqn.(5.29) to be negligible. Using the charge noise intensity ζ found above, I integrate $S_{2e}(\omega)$ over frequency range $[\omega_{\rm m} - \gamma_{\rm m}/2, \omega_{\rm m} + \gamma_{\rm m}/2]$ to find $n_{\rm m} \approx 4.02\times10^{-6}(2e)$. For a sense of scale, this noise amplitude can be compared to the modulation amplitude $n_x^0 \approx 2.7\times10^{-3}(2e)$ corresponding to the mechanical zero-point motion, found by requiring $\omega_{\rm q}^x(n_x) = \omega_{\rm q}^{|0\rangle}$ according to Eqn.(5.22). Indeed, $n_{\rm m}$ is much less than the amplitude of any meaningful gate-charge

modulation. Expanding Eqn.(5.29) to first order in n_{m},

$$n_n = n_x + n_{\mathrm{m}} \cos\phi_{\mathrm{m}} + \mathcal{O}(n_{\mathrm{m}}^2), \tag{5.35}$$

I find a relative uncertainty in the modulation amplitude

$$\frac{\sqrt{\mathrm{var}(n_n)}}{\langle n_n \rangle} = \frac{n_n \sqrt{\mathrm{var}\left(\cos\phi_{\mathrm{m}}\right)}}{n_x} \leq 0.001. \tag{5.36}$$

Finally, I compare Eqn.(5.34) to the transition rates $\Omega_{n,l}$ identified in Sec.2.3.5 under the same gate-charge offset and the same static qubit frequency. A similar analysis has been employed in the previous section (Sec.5.2.3) to demonstrate that, when $\chi_{\mathrm{m}} \ll \omega_{\mathrm{m}}$, the classical gate-charge modulation is a good approximation to the quantized motion at $\delta n_g = 0$. The same is also true for reasonable values of $\delta n_g \neq 0$: neglecting the noise in the modulation amplitude $n_n = n_x$ and using the parameter of this work $\chi_{\mathrm{m}}/\omega_{\mathrm{m}} \approx 0.01$, I find the transition rates well approximate each other for values of δn_g within $\pm 3\sigma_c \approx \pm 0.02$ $(2e)$ around zero. I thus conclude the classical gate-charge modulation to remain a good approximation to the quantized motion for this experiment even in the presence of charge noise.

5.2.4.3 Expected qubit spectrum due to charge noise

To attribute the appearance of odd-order sideband transitions in Fig. 5.1 to charge noise, I provide a model that predicts the overall qubit spectrum under the influence of charge noise. This is given by a convolution between the probability of finding a particular charge offset δn_g and its corresponding qubit spectrum $P_e^{\delta n_g}(n_x, \omega)$,

$$P_e(n_x, \omega) = \int_{d\delta n_g} \frac{1}{\sqrt{2\pi\sigma_c^2}} \exp\left(-\frac{{\delta n_g}^2}{2\sigma_c^2}\right) P_e^{\delta n_g}(n_x, \omega) d\delta n_g. \tag{5.37}$$

In turn, the qubit spectrum under a specific δn_g is given by a sum of Lorentzians,

$$P_e^{\delta n_g}(n_x, \omega) = \sum_l \frac{1}{2} \frac{(A_{x,l}\Gamma_{\mathrm{ncn}}/2)^2}{(\omega - \omega_{x,l})^2 + (\Gamma_{\mathrm{ncn}}/2)^2(1 + A_{x,l}^2)}, \tag{5.38}$$

each located at frequencies $\omega_{x,l}$ given by Eqn.(5.33), and driven at a rate that corresponds to,

$$\begin{aligned} A_{x,l} &= \Omega_{x,l}\sqrt{\frac{2}{\Gamma_1\Gamma_{\mathrm{ncn}}}} \\ &= \Omega_R\sqrt{\frac{2}{\Gamma_1\Gamma_{\mathrm{ncn}}}}\sum_{2a+b=l} J_a\left[\frac{\delta\omega_{\mathrm{q}}^x(\delta n_g, n_x)}{2\omega_{\mathrm{m}}}\right] J_b\left[\frac{(8E_c/\hbar)^2}{\omega_{\mathrm{m}}\omega_{\mathrm{q}}^b(\delta n_g)} n_x \delta n_g\right]. \end{aligned} \tag{5.39}$$

Because the qubit drive is applied through the readout cavity at a constant amplitude ϵ_d, the Rabi rate is also dependent on the spectroscopic frequency ω

$$\Omega_R(\omega) = 2\frac{g_c}{\omega - \omega_c}\epsilon_d, \tag{5.40}$$

where g_c is the qubit-cavity coupling rate and ω_c is the cavity frequency. Using the extracted values of Γ_{ncn} and σ_c from Fig. 5.7, I plot the numerical result of Eqn.(5.37) in Fig. 5.9(c). In this figure, only ϵ_d is left free to match the maximum peak-height in the map of Fig. 5.9(b). The good agreement between the experiment (b) and theory (c) confirms the odd-order sideband peaks I observe in Fig. 5.1 can be explained by $1/f$ charge noise.

5.2.5 Finding the qubit spectrum for phonon Fock states

Having established the qubit spectrum under a classical modulation to be in close correspondence with the qubit spectrum for phonon Fock states, I now convert the experimentally measured qubit response under classical modulation (Fig. 5.1, reproduced in Fig. 5.9(a)) to the PSF map $P_e^{|n\rangle}(\omega)$ in two steps:

(1) I connect the measured cavity transmission phase to qubit excitation probability $P_e(\omega)$ using Eqn.4.4. Instead of directly using the measured phase which contains statistical noise, I instead fit the measured spectrum using a sum of skewed Lorentzians where each Lorentzian describes one sideband peak or the center qubit peak:

$$\varphi_c(\omega) = \sum_l \frac{1}{2}\frac{(A_l\Gamma_l/2)^2}{\left(\frac{\omega-\omega_l}{1+L\cdot\mathrm{Sgn}(\omega-\omega_l)}\right)^2 + (\Gamma_l/2)^2\left(1+A_l^2\right)}, \tag{5.41}$$

where ω_l is the resonances of the system under the spectroscopic drive, A_l describes the corresponding transition rate $|\Omega_{x,l}|^2$, and L captures the asymmetry due to charge noise. In this fit,

we also remove the background phase present in Fig. 5.9(a), which increases at larger modulation amplitude. This background phase arises from time-averaging the cavity phase response of Fig. 4.1 to a classical gate-charge modulation around $n_g = 1/2$ (see Sec.4.2.2).

(2) I find the qubit spectrum at integer phonon numbers by interpolating the fit parameters extracted from step (1).

I thus create a new map, as shown in Fig. 5.9(b), which I take as the qubit response to mechanical Fock states. In the rest of this chapter, I demonstrate how to use this map in performing deconvolution procedures and extracting phonon distributions from measured qubit spectra.

Finally, two details need to be considered to properly use this extracted $P_e^{|n\rangle}(\omega)$. First, because the qubit lineshape is strongly dependent on the qubit-drive power (Sec.2.3.4.3), I ensure this power to remain constant for all measurements. Second, I observe the bare qubit frequency to vary over time ($\delta\omega_{\mathrm{q}}^b \sim 2\pi \times 1$ MHz) and between experiments performed at $V_{\mathrm{dc}} = 0$ V and $V_{\mathrm{dc}} = 6$ V ($\delta\omega_{\mathrm{q}}^b \sim 2\pi \times 3$ MHz)). I attribute this to a combination of change in the local flux and change in the qubit's charging energy (when V_{dc} is changed). To correct for this error, I extract the bare qubit frequency by measuring the qubit spectrum with the mechanical oscillator in thermal states before each experiment of interest, and performing a least-squares fit (see Sec.5.4).

5.3 The reconstruction procedure

Having determined $P_e^{|n\rangle}(\omega)$, I now discuss the reconstruction procedure of extracting the phonon distribution from measured qubit spectrum. This is achieved using the Lucy-Richardson deconvolution algorithm [136, 137] discussed in Sec.5.3.1. One way to characterize the uncertainty in the extracted phonon distribution is by using a bootstrapping method, described in Sec.5.3.2.

5.3.1 Reconstruction using Lucy-Richardson deconvolution

The Lucy-Richardson algorithm is an iterative, Bayesian-based deconvolution algorithm. Often used in astronomy, the algorithm is originally aimed at reconstructing images degraded by optical aberrations, which spreads a point-source over a wide space according to a point-spread

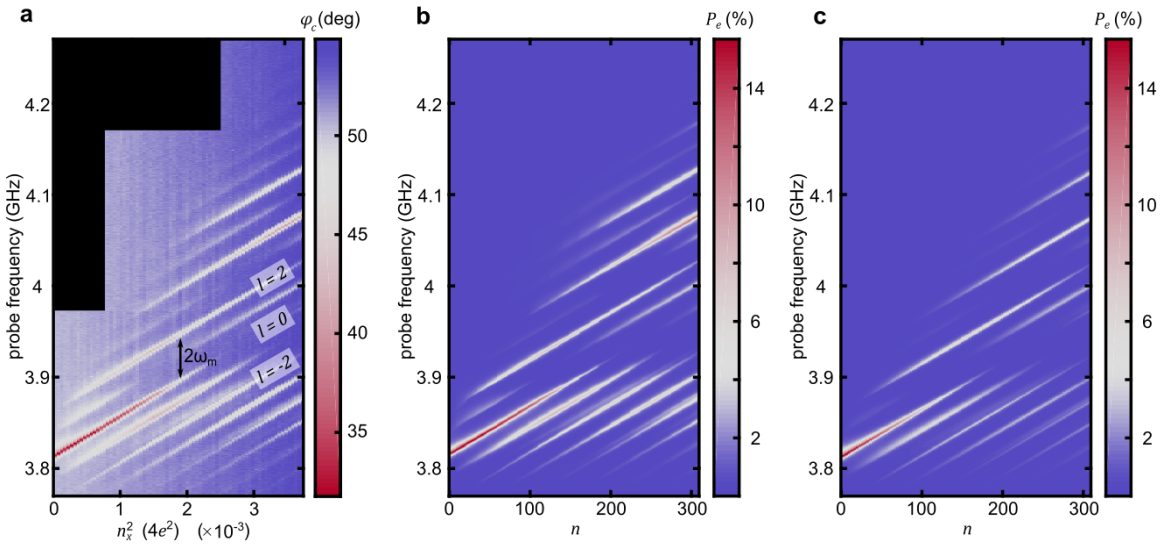

Figure 5.9: Finding $P_e^{|n\rangle}(\omega)$
a, This is identical to Fig. 5.1, reproduced here for easy comparison. **b,** I convert the measured phase response in **a** to the qubit spectra (color-scale vs. y-axis) at particular mechanical Fock states (x-axis) and find $P_e^{|n\rangle}(\omega)$. The cavity transmission phase is fitted (Eqn.5.41), converted to the probability of exciting the qubit, and interpolated at appropriate qubit Stark shifts (Eqn.2.56). I use this map to extract phonon distributions. **c,** Using Eqn.(5.37), I calculate the expected qubit spectra (color-scale vs. y-axis) under a classical gate-charge modulation. The extracted phonon number n (x-axis) is related to the classical modulation amplitude n_x according to Eqn.(5.22). To model the charge-noise, a Gaussian distribution with mean $\langle \delta n_g \rangle = 0$ and standard deviation $\sigma_c = 0.0071(2e)$ is used. The drive strength of the spectroscopic-signal ϵ_d is a free parameter to make the maximum P_e found in this calculation to be equal to the maximum P_e found experimentally in **b**. The good agreement between **b** and **c** confirms the charge-noise as the main source of offset charge. This figure is reproduced from reference [85].

function (PSF). Analogously in this work, detecting a phonon Fock state $|n\rangle$ (point-source) with the qubit results in an image $P_e^{|n\rangle}(\omega)$ spread over a wide range of frequencies. Thus, the PSF is given by the experimentally determined $P_e^{|n\rangle}(\omega)$.

To invert Eqn.(5.1), I use the Lucy-Richardson recurrence formula,

$$P_{i+1}(n) = P_i(n) \sum_{\omega} P_e^{|n\rangle}(\omega) \frac{P_e(\omega)}{\sum_{n'} P_i(n') P_e^{|n'\rangle}(\omega)}, \tag{5.42}$$

where $P_i(n)$ is the deconvolution result after i number of iterations. This process requires an initial guess for the phonon distribution $P_0(n)$, which, for most of this work[10] , is chosen as $P_0(n) = 1/N$ where $N = 200$ is the maximum phonon number at which point the Fock space is truncated. This choice is identical to a Bayes's postulate [137].

The quality of the deconvolution is strongly influenced by the total number of iterations. In general, a larger iteration number i means the algorithm will capture finer details in the measured qubit spectrum. For a noiseless measurement, the extracted phonon distribution will converge to the true phonon distribution at large i. However, in the presence of measurement noise, capturing too many details in the qubit spectrum could mean interpreting measurement noise as actual phonon distribution (i.e., over fitting). To show this, I simulate an experiment (Fig. 5.10) and find the noisy qubit spectrum from a thermal mechanical state with $n_{\text{th}} = 20$ by first using Eqn.(5.1) to find the noiseless qubit spectrum, and then adding noise (see Sec.7.1.3). Terminating the deconvolution procedure at different iteration numbers, I confirm the dependence of its quality on the iteration number. While at small i, the procedure hasn't been repeated enough to deviate far from the initial guess; at large i, it attempts to capture the measurement noise by introducing noise in the extracted phonon distribution. Because I know the exact phonon distribution in this case, I can quantify the deconvolution quality using the rms-error ($\text{RMSE}_{\text{theory}}$) between its result and the true phonon distribution,

$$\text{RMSE}_{\text{theory}}(i) = \sqrt{\frac{1}{N} \sum_{n} [P_i(n) - P_{\text{th}}(n_{\text{th}}, n)]^2}, \tag{5.43}$$

[10] see Sec.7.1.2 for the discussion about the special case where an initial guess of Poissonian distribution is used

where $P_{\text{th}}(n_{\text{th}}, n)$ is the mechanical thermal distribution given by Eqn.(2.9) and $n_{\text{th}} = 20$. As shown in Fig. 5.11(a), the quality of the deconvolution is optimal when $\text{RMSE}_{\text{theory}}$ is minimized at the optimal iteration number $i_{\text{opt}} = 13$. However, i_{opt} cannot be determined universally because it is different for different phonon distributions or for different noise realizations in the qubit spectrum. Instead, I need to find a consistent protocol to determine a suitable iteration number i_{term} to terminate the deconvolution procedure without prior knowledge of the true phonon distribution.

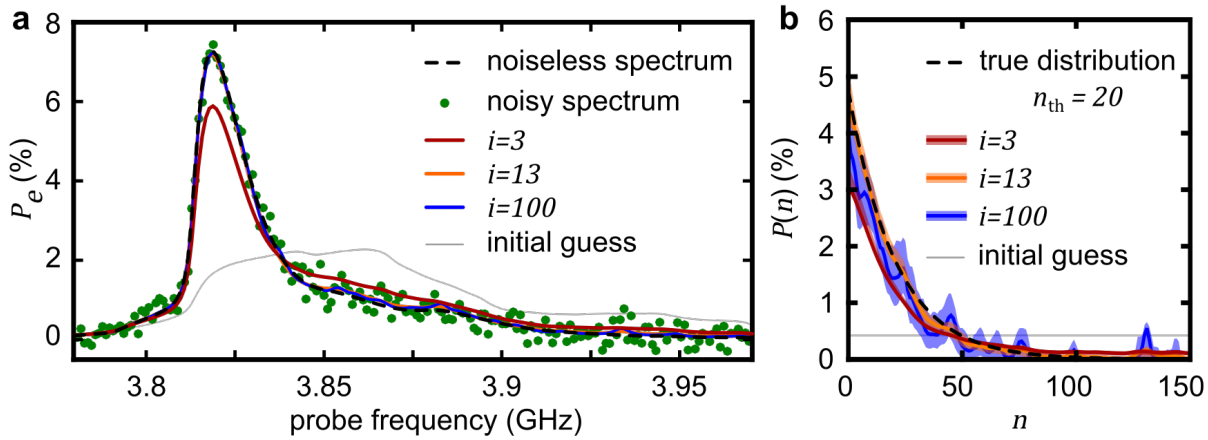

Figure 5.10: Reconstruction vs. iteration number
Assuming a thermal mechanical state (**b**, dashed black line), I synthesize its qubit spectrum (**a**, green dots) by adding noise to the expected (Eqn.(5.1)) noiseless qubit spectrum (black dashed line). Running the Lucy-Richardson algorithm for i iterations, I extract the phonon distribution (**b**, solid line) and find its 90% confidence interval (shaded) using non-parametric bootstrapping. The expected qubit spectra (solid lines) from the extracted phonon distributions are plotted in **a** for comparison. Also plotted is the initial guess (grey) which is a uniform distribution between 0 and 200 phonons.

To this end, I look at the algorithm's rate of update. First, I look at the rate of update between adjacent iterations, which I quantify using

$$\text{RMSE}_{\text{next}}(i) = \sqrt{\frac{1}{N}\sum_{n}\left[P_{i+1}(n) - P_i(n)\right]^2}. \tag{5.44}$$

As shown in Fig. 5.11(a), after a period of rapid change, the rate of update slows down significantly around $i \sim i_{\text{opt}}$. Thus, the rate of update can be a good proxy for determining i_{term}. Additionally, because the rate of update is small around i_{opt}, a small deviation in i_{term} from the optimal point will

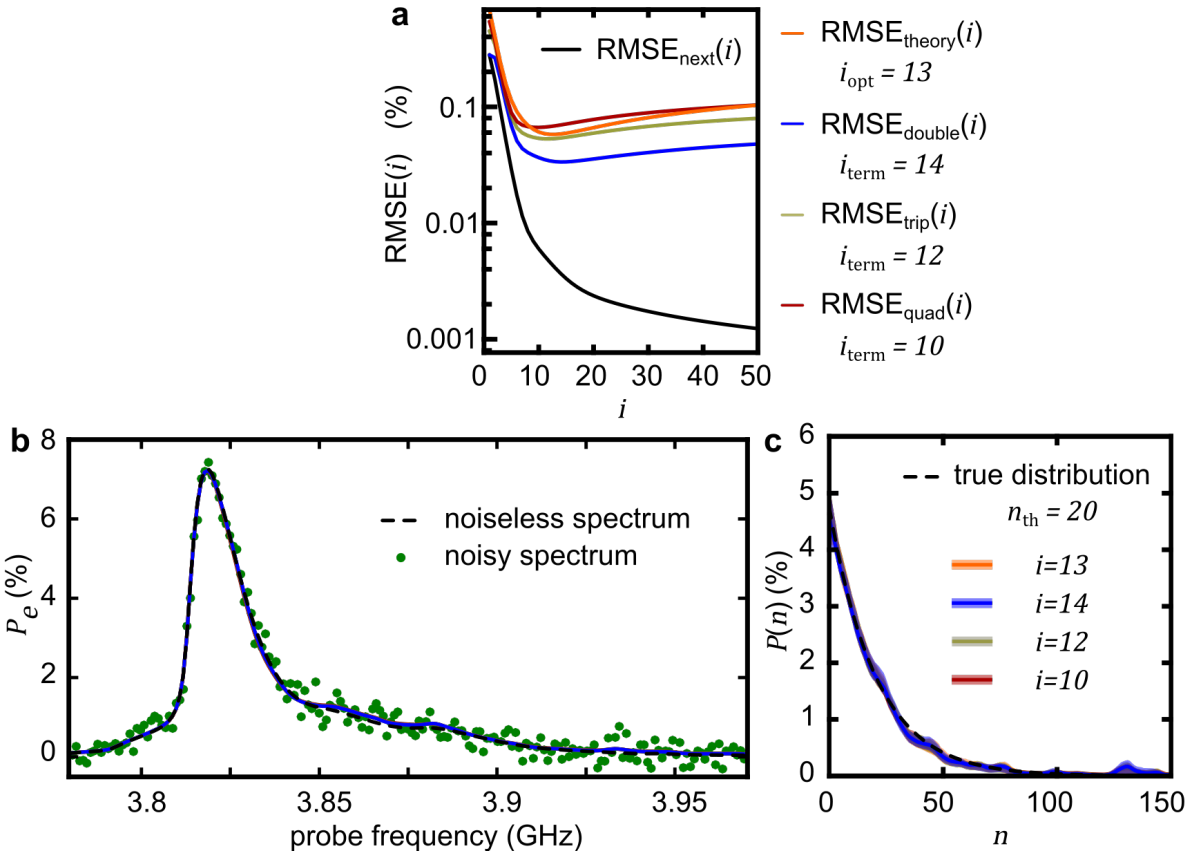

Figure 5.11: Finding i_{term}
a, Using the same synthesized data shown in Fig. 5.10 and the known thermal distribution with $n_{\text{th}} = 20$, I determine $i_{\text{opt}} = 13$ by finding the minimum of $\text{RMSE}_{\text{theory}}(i)$ (orange). I find the rate of update $\text{RMSE}_{\text{next}}(i)$ (black) strongly depends on the iteration number i, and quickly diminishes when $i \sim i_{\text{opt}}$. By minimizing the function $\text{RMSE}_{\text{double}}(i)$ (blue), I determine the iteration number $i_{\text{term}} = 14$ with which I should terminate the reconstruction. Similarly, I can find $i_{\text{term}} = 12$ by minimizing $\text{RMSE}_{\text{triple}}(i)$ (mustard), and $i_{\text{term}} = 10$ by minimizing $\text{RMSE}_{\text{quadruple}}(i)$ (red). **b, c,** With the i_{term} and i_{opt} determined in **a**, I compare their effects on the reconstructed phonon distributions (**c**) and the corresponding expected qubit spectra (**b**). Indeed, because the rate of update is small at these iterations numbers, the small deviations among them only cause negligible changes in the extracted phonon distribution.

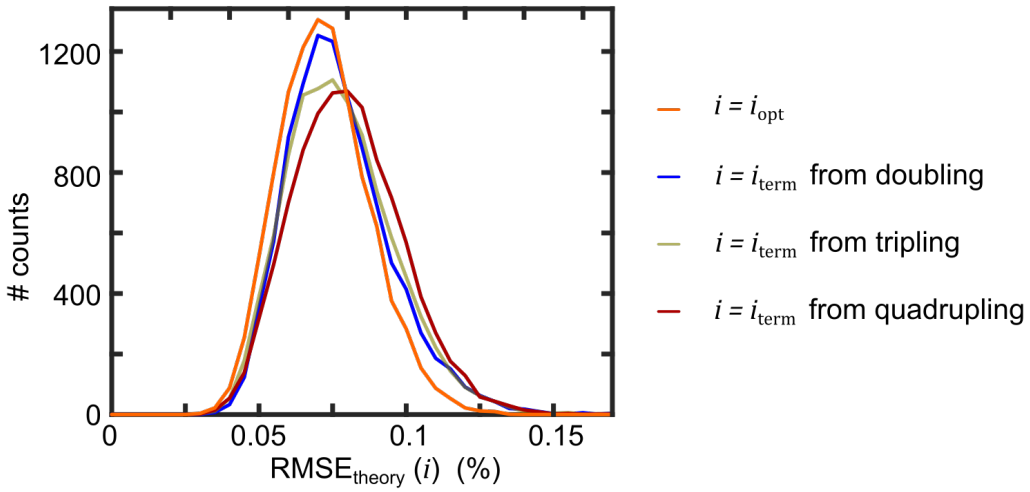

Figure 5.12: Histogram of $\text{RSME}_{\text{theory}}$
Using a thermal mechanical distribution with $n_{\text{th}} = 20$, I create 10^5 different synthesized qubit spectra with different noise realizations. On each synthesized qubit spectrum, I find i_{term} by minimizing $\text{RMSE}_{\text{double}}(i)$. Using this i_{term}, I then extract the phonon distribution and compute its rms-error $\text{RSME}_{\text{theory}}(i_{\text{term}})$ with respect to the true distribution. From its histogram (blue), which largely overlaps with the histogram of the best achievable rms-error $\text{RSME}_{\text{theory}}(i_{\text{opt}})$ (orange), I confirm this method of extracting i_{term} results in extracted phonon distributions close to the truth. Different ways of finding i_{term} such as minimizing $\text{RMSE}_{\text{trip}}(i)$ (mustard) or $\text{RMSE}_{\text{quad}}(i)$ (red) also extract phonon distributions only slightly worse than what can be optimally extracted.

not significantly alter the extracted phonon distribution. Because $\mathrm{RMSE}_{\mathrm{next}}(i)$ decreases monotonically, I instead determine i_{term} by finding the minimum of the rate of update when doubling the iteration number

$$\mathrm{RMSE}_{\mathrm{double}}(i) = \sqrt{\frac{1}{N}\sum_{n}\left[P_{2i}(n) - P_i(n)\right]^2}. \tag{5.45}$$

Although a similar method can be employed by tripling ($\mathrm{RMSE}_{\mathrm{trip}}(i)$) or quadrupling ($\mathrm{RMSE}_{\mathrm{quad}}(i)$) the iteration number to find a slightly different i_{term}, the small rate of update $\mathrm{RMSE}_{\mathrm{next}}(i)$ around these positions means the small deviation in i_{term} will only incur a negligible amount of change in the extracted phonon distribution, as shown in Fig. 5.11. To validate this method, I repeat it on the same thermal phonon distribution with 10^5 different noise realizations for the qubit spectrum, find the rms-error between the extracted phonon distribution at i_{term} and the true distribution $\mathrm{RMSE}_{\mathrm{theory}}(i_{\mathrm{term}})$, and plot its histogram in Fig. 5.12. Compared to the histogram of the best achievable rms-error $\mathrm{RMSE}_{\mathrm{theory}}(i_{\mathrm{opt}})$, the largely overlapped histograms demonstrate that these methods of extracting i_{term} are indeed capable of extracting phonon distributions close to what can be optimally achieved. Thus, for all deconvolutions in this work, I determine i_{term} by finding the minimum of $\mathrm{RMSE}_{\mathrm{double}}(i)$.

5.3.2 Bootstrapping

Although a suitable i_{term} balances between interpreting too few and too many details in the qubit spectrum as actual phonon distribution, it cannot differentiate measurement noise from phonon-induced qubit response. Indeed, despite i_{term}, variations in the noise realization can still alter the extracted phonon distribution. To quantify this effect, I use non-parametric bootstrapping [138]. As discussed in Sec.4.1.1, all qubit spectra I show in this work are the result of averaging many $(100 - 1000)$ individually acquired traces. Take for example the synthesized data of Fig. 5.10(a), the noisy qubit spectrum is the result of averaging 916 independent noise realizations. To create a bootstrap sample, I re-sample randomly among these noise realizations with replacement to find a new set of 916 traces, and then average. Repeating this process for 1000 times, and performing the deconvolution algorithm on those bootstrap samples, I find a histogram

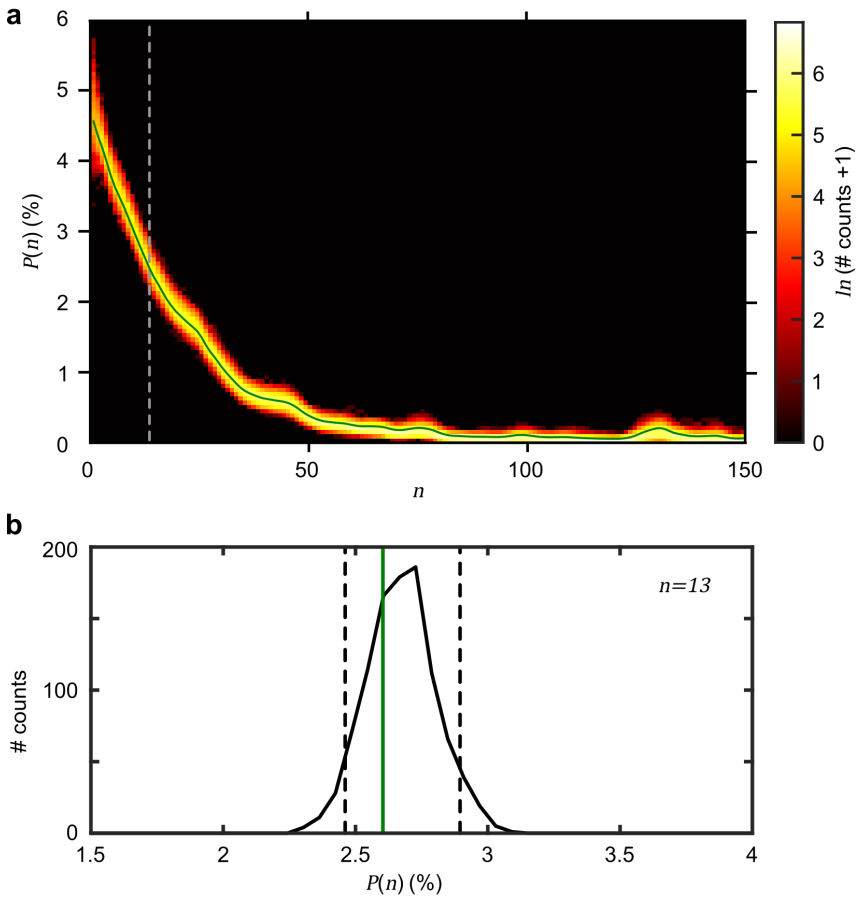

Figure 5.13: Reconstruction bootstrapping and confidence interval
a, Using the synthesized data of Fig. 5.10(a), I create 1000 bootstrap samples and reconstruct their phonon distributions using the deconvolution algorithm. I plot the histogram of finding $P(n)$ (color-scale vs. y-axis) at particular phonon numbers n (x-axis). The solid green line corresponds to the reconstructed phonon distribution using the original mean qubit spectrum. **b,** At a randomly picked value of $n = 13$ (grey dashed line in **a**), I plot the histogram for $P(13)$. From this distribution, I find the 90% confidence interval for $P(13)$ to be within the range $[2.46, 2.90]\%$ (dashed black lines).

of the reconstructed phonon distributions as shown in Fig. 5.13(a). Based on this histogram, I compute the so-called basic bootstrap 90% confidence intervals for each phonon number, as shown in Fig. 5.13(b). These confidence intervals are always shown as the shaded region around the extracted $P(n)$ corresponding to the original mean qubit spectrum. Thus, a smaller shaded region means the reconstructed distribution is less susceptible to measurement noise. In general, I find the reconstructed $P(n)$ from the original mean qubit spectrum lies within its 90% confidence interval.

5.4 Thermal and displaced thermal states

To validate both the deconvolution procedure and the experimentally simulated PSF map, I demonstrate the reconstruction of phonon distribution on thermal and displaced-thermal mechanical states. These experiments are performed at $V_{\mathrm{dc}} = 6$ V. This section follows closely to publication [85].

First, I measure the qubit spectrum when the mechanical oscillator is in thermal equilibrium with the dilution fridge as shown in Fig. 5.14(a). Running the deconvolution procedure with the PSF map found in Sec.5.2, I extract the phonon distribution and its 90% confidence interval. Because the mechanical oscillator is known to be described by the thermal distribution given by Eqn.(2.9), I can also perform a least-squares fit on the measured qubit spectrum by replacing $P(n)$ with $P_{\mathrm{th}}(n_{\mathrm{th}}, n)$ in Eqn.(5.1). In this least-squares fit, the only free parameters are the mechanical thermal population $n_{\mathrm{th}} = 17.7$, and the bare qubit frequency (see Sec.5.2.5).

Additional to the thermal state, I can coherently displace the mechanical oscillator by driving it with the product of V_{dc} and a resonant ac-signal of amplitude V_{coh} applied on the same electrode. Because the mechanical oscillator starts in a thermal state, this driving procedure prepares it in a displaced-thermal state characterized by distribution [139],

$$P(n_{\mathrm{th}}, n_{\mathrm{disp}}, n) = \sum_{m=0}^{\infty} \frac{n_{\mathrm{th}}^m}{(1+n_{\mathrm{th}})^{m+1}} e^{-n_{\mathrm{disp}}} \frac{\min\{m,n\}!}{\max\{m,n\}!} n_{\mathrm{disp}}^{|n-m|} \left[L_{\min\{m,n\}}^{|n-m|}(n_{\mathrm{disp}})\right]^2, \tag{5.46}$$

where $L_n^l(x)$ is the associated Laguerre polynomial, n_{th} is the initial thermal population, and $n_{\mathrm{disp}} = |\alpha|^2 \propto V_{\mathrm{coh}}^2$ is the mean phonon displacement due to the coherent drive. As shown in

Fig. 5.14(b-f), I measure the qubit spectra at different V_{coh} and extract the phonon distributions. Using Eqn.(5.46) and keeping $n_{\mathrm{th}} = 17.7$ constant, I fit the qubit spectra with n_{disp} being the only free parameter. In Fig. 5.14(g), I verify the coherent displacement by plotting the extracted n_{disp} as a function of V_{coh}^2. The linear fit (dashed line) goes through the origin. The 90% confidence interval error bars are found from distributions of n_{disp}, which are extracted by performing the least-squares fit on non-parametric bootstrap samples.

In Fig. 5.14(a-f), the good agreement between the phonon distributions as well as the associated qubit spectra substantiates the deconvolution procedure and the PSF map. In these dressed qubit spectra, individual sideband peaks cannot be identified because these features are smeared by the broad phonon distribution associated with the large thermal occupation. Nevertheless, failure to properly account for the sidebands would have led to substantial errors in the extracted phonon distribution when sideband-induced qubit excitations are erroneously attributed to phonon populations.

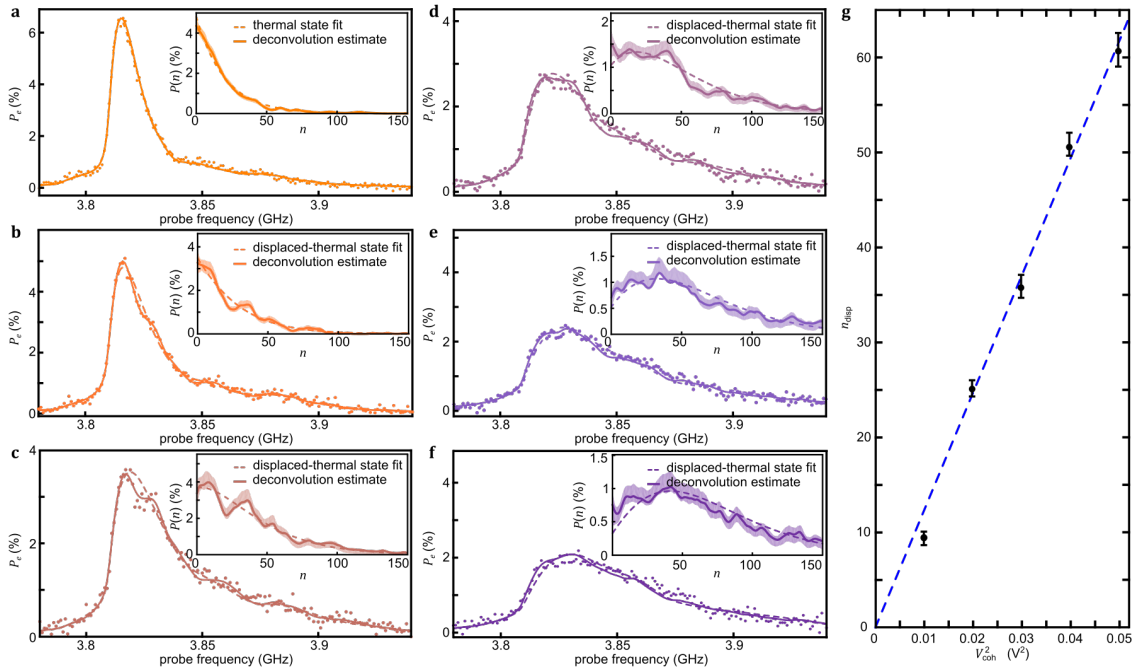

Figure 5.14: Thermal and displaced-thermal mechanical state
For different V_{coh}, I measure the qubit spectrum (dots) and extract the mechanical phonon distribution (inset). Phonon distributions extracted from deconvolution (solid) and their 90% confidence interval (shaded) are plotted alongside the result of least-squares fit (dashed). **a,** With $V_{\mathrm{coh}} = 0$ V, the mechanical oscillator is in a thermal state. A least-squares fit to the thermal distribution finds $n_{\mathrm{th}} = 17.7$. **b-f,** By applying an ac-drive with 25 MHz frequency and amplitude V_{coh} (specified at the generator output), I coherently displace the thermal mechanical state by a mean phonon displacement of n_{disp}. Keeping the extracted n_{th} from **a** constant, I perform least-squares fits assuming displaced thermal distributions to extract n_{disp}. The extracted parameters are: **b,** $V_{\mathrm{coh}} = 100.5$ mV and $n_{\mathrm{dsip}} = 8.0$; **c,** $V_{\mathrm{coh}} = 142$ mV and $n_{\mathrm{dsip}} = 20.0$; **d,** $V_{\mathrm{coh}} = 174$ mV and $n_{\mathrm{dsip}} = 30.6$; **e,** $V_{\mathrm{coh}} = 201$ mV and $n_{\mathrm{dsip}} = 53.5$; and **f,** $V_{\mathrm{coh}} = 225$ mV and $n_{\mathrm{dsip}} = 51.9$. **g,** I plot the extracted n_{dsip} as a function of V_{coh}^2. The error bars correspond to 90% confidence intervals of n_{dsip} are found using non-parametric bootstrapping. Dashed blue line is a linear fit that goes through the origin. This figure is reproduced from reference [85].

Chapter 6

Manipulating the phonon distribution using sideband transitions

With the ability to extract the phonon distribution, I now manipulate it using sideband transitions that simultaneously alter the qubit state and the phonon population. In order to access sideband transitions that add or remove only one phonon at a time (single-phonon sideband transitions), I adopt the technique of driving the ac-dither sideband transitions [140], as described in Sec.6.1. In contrast to that in conventional linear electromechanics [19], the sideband transitions in this work are crucially different in their phonon-number-sensitivity: they only address a small section of the phonon population with a characteristic width of $W \approx 7.1$ phonons [86]. I experimentally demonstrate this property in Sec.6.2. Using these phonon-number-sensitive motional sidebands, I demonstrate in Sec.6.3 an adiabatic energy squeezing technique [85] where, by trapping the oscillator's phonon population in between phonon-creating (blue) and phonon-annihilating (red) sideband transitions, I reduce its uncertainty in number space. This technique enables the preparation of nonclassical mechanical states in Chapter 7.

6.1 Ac-dither sideband transitions

At the charge degeneracy point ($n_g = 1/2$) of the CPB qubit, the symmetry of the Hamiltonian means that single-phonon sideband transitions $|g, n\rangle \leftrightarrow |e, n \pm 1\rangle$ are forbidden to microwave drives applied at frequencies $\omega_d = \omega_{\mathrm{q}}^{|n\rangle} \pm \omega_{\mathrm{m}}$. Although these transitions are clearly observed in the qubit spectrum (see for example, Fig. 7.3), they arise only when charge noise causes n_g to deviate from the degeneracy point, and are thus unreliable resources.

Instead, to reliably access these single-phonon sideband transitions, I adopt the technique of driving ac-dither sidebands. Proposed in reference [140] for a CPB qubit, this technique drives sideband transitions by a combination of two microwave signals: one low frequency ac-dither signal is applied to controllably modulate the CPB gate-charge according to

$$n_g(t) = n_g^0 + n_g^{\text{dither}} \cos\left(\omega_{\text{dither}} t\right). \tag{6.1}$$

This modulation introduces a dynamical $\hat{\sigma}_z$ coupling, which, as discussed in Sec.2.3.5, allows for the creation and annihilation of odd number of phonons. Consequently, a second microwave signal (sideband drive) applied at frequencies,

$$\begin{aligned} \omega_{\text{B}}(n) &= \omega_{\text{q}}^{|n\rangle} + \omega_{\text{m}} \pm \omega_{\text{dither}}, \\ \omega_{\text{R}}(n) &= \omega_{\text{q}}^{|n\rangle} - \omega_{\text{m}} \pm \omega_{\text{dither}}, \end{aligned} \tag{6.2}$$

can drive single-phonon blue or red sideband transitions $|g, n\rangle \leftrightarrow |e, n \pm 1\rangle$ at respective rates

$$\begin{aligned} \Omega_{\text{B}}^{|n\rangle} &= \sqrt{n+1}\Omega_{\text{B},0}, \\ \Omega_{\text{R}}^{|n\rangle} &= \sqrt{n}\Omega_{\text{R},0}. \end{aligned} \tag{6.3}$$

where, for the small dither amplitude $n_g^{\text{dither}} \approx 0.05$ used in this work,

$$\Omega_{\text{B(R)},0} = g_{\text{m}} \frac{\Omega_R}{2\left(\omega_d - \omega_q\right)} J_1\left(\frac{8E_c n_g^{\text{dither}}}{E_J}\right) \tag{6.4}$$

is the bare sideband rate, Ω_R and ω_d are the Rabi rate and frequency of the sideband drive, and $J_1(z)$ is the 1st order Bessel function of the first kind.

Fig. 6.1 shows a full measured qubit spectrum under an ac-dither at frequency $\omega_{\text{dither}} = 2\pi \times 260$ MHz with a large spectroscopic power. The center qubit transition is power broadened and saturated (see Sec.2.3.4.3), with $P_e \approx 0.5$ on resonance. Two groups of three satellite peaks are visible on either side of the main qubit peak, detuned by ω_{dither}. Within each group, I can identify the single-phonon red and blue sideband transitions. Unless specifically noted, I use the set of sideband transitions below the center qubit transition with $\omega_{\text{dither}} = 2\pi \times 257$ MHz for the rest of this thesis.

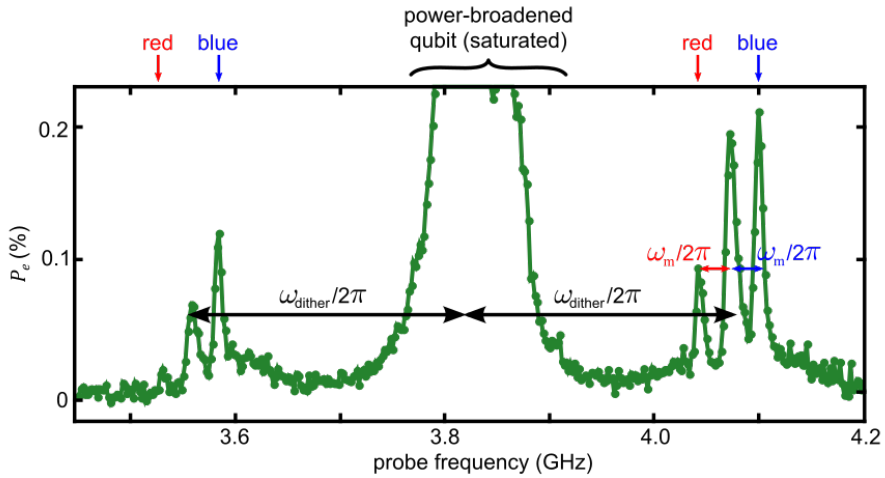

Figure 6.1: Ac-dither sideband spectrum
Ac-dither sideband transitions can be observed in the qubit spectrum, measured at $V_{\mathrm{dc}} = 6$ V with a large qubit probe power. The lower (left) set of red and blue sideband transitions are used to manipulate the phonon populations in this work. This figure is reproduced from reference [86].

6.2 Sideband transition's phonon number sensitivity

In contrast to motional sideband transitions in conventional linear electromechanics that address all phonon numbers simultaneously [19], the sideband transitions in this work are phonon-number-sensitive, addressing only a small section of the phonon population [86]. Because each phonon number Stark shifts the qubit frequency $\omega_q^{|n\rangle}$ by $2\chi_m$, the sideband frequencies in Eqn.(6.2) are changed accordingly. Consequently, as discussed in Sec.5.2.2, a sideband drive resonant with transition $|g, n_{SB}\rangle \leftrightarrow |e, n_{SB} \pm 1\rangle$ is only effective over a characteristic width $W = \Gamma_2/2\chi_m \approx 7.1$ phonons centered about n_{SB}.

To gain an intuitive picture for the effect of driving these phonon-number-sensitive transitions, consider the simplified dynamics of the qubit-mechanical system sketched in Fig. 6.2(a), where the qubit decays are assumed to always conserve phonon numbers. Starting from a thermal state, because the sidebands in this work are always driven incoherently on a time scale much longer than the qubit lifetime and dephasing time ($T_1 \approx 260$ ns, $T_2 \approx 80$ ns), the resulting mechanical state contains no quantum coherence and is fully described by the diagonal elements of its density matrix. A blue sideband drive applied at frequency $\omega_B(n_B)$ drives the transition $|g, n_B\rangle \leftrightarrow |e, n_B + 1\rangle$ resonantly at an effective rate $\Gamma_B^{|n_B\rangle} = \left(\Omega_B^{|n_B\rangle}\right)^2/\Gamma_2$, but also drives its neighboring transition $|g, n\rangle \leftrightarrow |e, n + 1\rangle$ at a reduced effective rate $\Gamma_B^{|n\rangle}$, dependent on the ratio of $(n - n_B)/W$ (Fig. 6.2(b), see also Sec.6.3.1). Because the qubit decay is the dominant relaxation process ($\Gamma_1 \gg \gamma_m$), populations in an initial state of $|g, n\rangle$ is first driven to state $|e, n + 1\rangle$ by the sideband, and then relaxes to state $|g, n + 1\rangle$, resulting in an overall addition of one phonon. If the sideband drive is applied continuously, phonons are repeatedly added until the oscillator reaches a phonon number m so far from n_B that the corresponding sideband rate $\Gamma_B^{|m\rangle}$ is smaller than the thermal decoherence rate $n_{th}\gamma_m$. At a time scale $n_B/\Gamma_B^{|n_B\rangle}$, this process creates a distortion in the phonon distribution around n_B with a characteristic width of W, while leaving populations far away undisturbed, as depicted in Fig. 6.2(c).

Such distortions in the phonon distribution are observed in Fig. 6.3. After driving the ac-

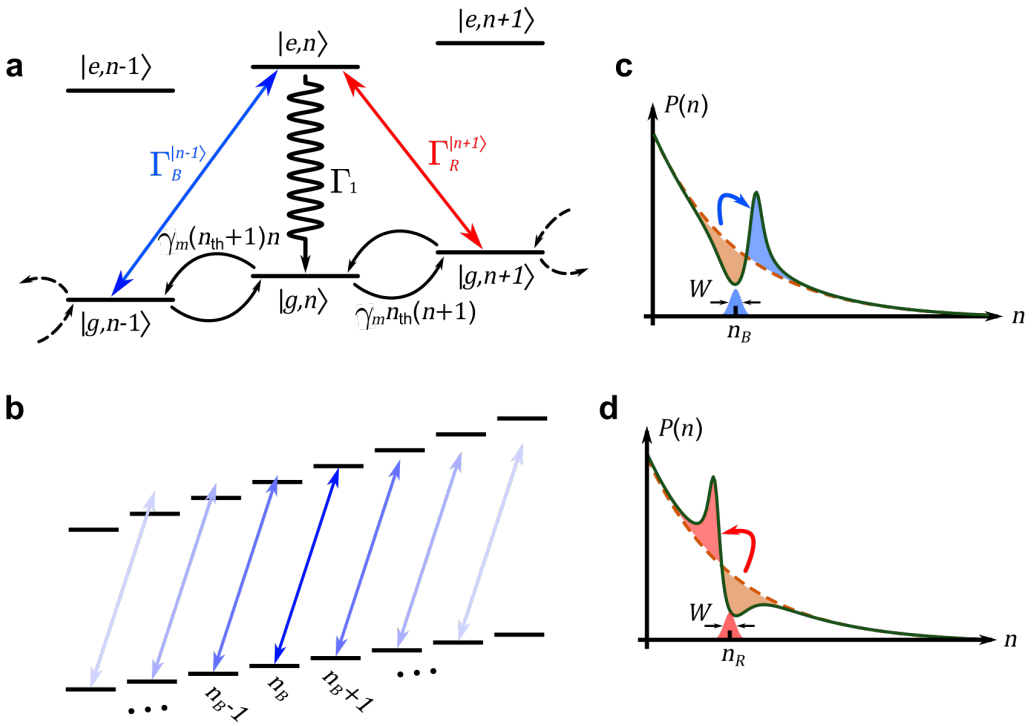

Figure 6.2: Phonon-number-sensitive sideband transitions
a, In the simplified dynamics of the qubit-mechanics system, a qubit decay always preserves the phonon number. Starting from an initial state $|g, n-1\rangle$, a blue sideband drive excites the transition $|g, n-1\rangle \leftrightarrow |e, n\rangle$ at an effective rate $\Gamma_{\mathrm{B}}^{|n-1\rangle}$. Because $\Gamma_1 \gg \gamma_{\mathrm{m}}$, the population in state $|e, n\rangle$ predominantly relaxes to $|g, n\rangle$. Overall, this process adds one phonon to the oscillator. Similarly, the red sideband drive combined with the relaxation process removes one phonon from the oscillator. **b**, Because $W = \Gamma_2/2\chi_{\mathrm{m}} \approx 7.1$ phonons, a sideband drive is phonon-number-sensitive. For example, a blue sideband drive resonant with transition $|g, n_{\mathrm{B}}\rangle \leftrightarrow |e, n_{\mathrm{B}}+1\rangle$ also drives the neighboring transitions at reduced rates. **c,** At a time scale $n_{\mathrm{B}}/\Gamma_{\mathrm{B}}^{|n_{\mathrm{B}}\rangle}$, the phonon-number-sensitive blue sideband drive applied on an initial thermal state (dashed orange) creates a distortion in the phonon distribution (solid green), pushing up a section of the phonon population around n_{B} of characteristic width W while leaving phonons far away unaffected. **d,** Conversely, at a time scale $n_{\mathrm{R}}/\Gamma_{\mathrm{R}}^{|n_{\mathrm{R}}\rangle}$, a red sideband drive creates a similar distortion in the phonon population, removing a section of the population around n_{R} to lower phonon numbers.

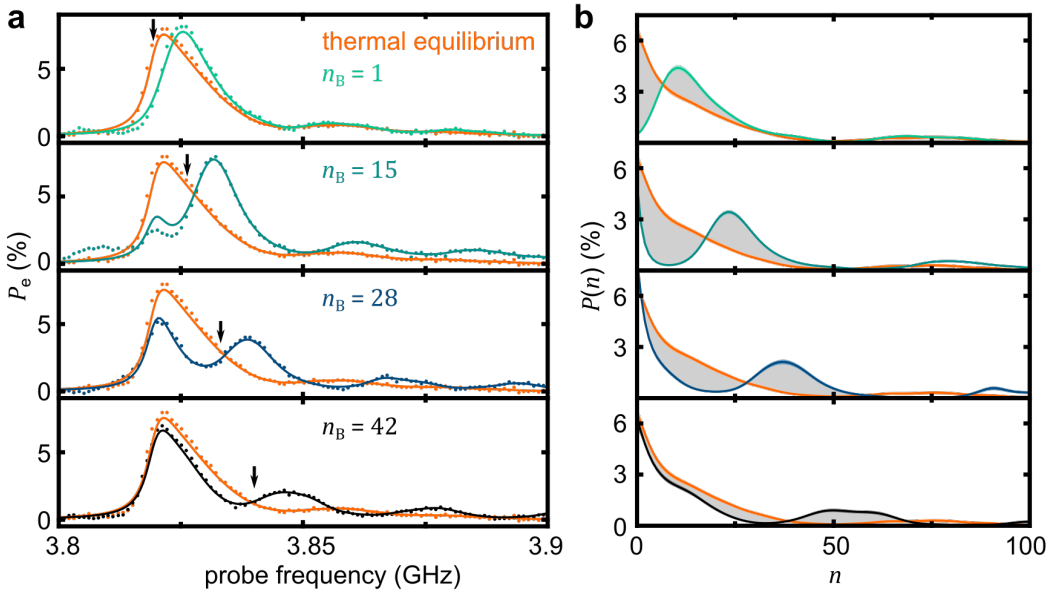

Figure 6.3: Demonstrating the phonon-number-sensitivity of a blue sideband drive
a, Starting from an initial thermal state (orange dots), I drive the blue sideband at different values of n_B and measure the qubit spectrum (dots). Vertical arrows corresponds to the position of n_B mapped to the Stark shifted qubit frequency (that is: $\omega = \omega_q^{|n_B\rangle}$). **b**, Using the deconvolution procedure, I extract the corresponding phonon number distributions (solid lines) and their 90% confidence intervals (shade). The associated qubit spectra (solid lines) are also plotted in **a**. Compared to extracted initial distribution (orange), it is clear that changing the value of n_B addresses different sections of the phonon population (grey shaded region), demonstrating the phonon-number-sensitivity of the blue sideband drive.

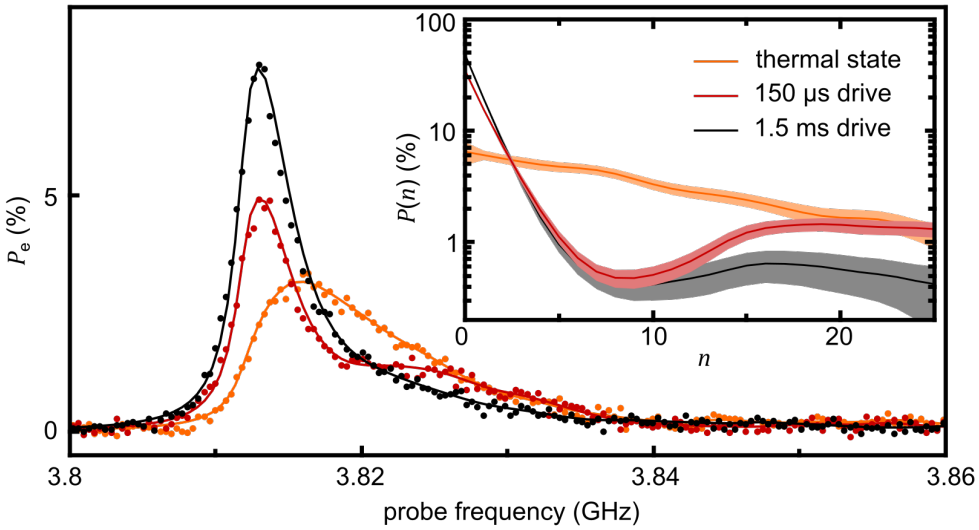

Figure 6.4: Demonstrating the phonon-number-sensitivity of a red sideband drive
Starting from a thermal state (orange), I measure the qubit spectra (dots) after applying a red sideband drive with $n_{\mathrm{R}} \approx 8$ for a duration of 150 μs (red) and 1.5 ms (black). Inset: The phonon distribution (solid line) and its 90% confidence interval (shaded) are extracted using the deconvolution procedure. While the red sideband drive removes the phonon population around n_{R} to below $n = 2$ at short time, phonons far away from n_{R} are only affected at a larger time because of thermal equilibration. This figure is reproduced from reference [86].

dither blue sideband transitions at different frequencies, corresponding to n_{B} ranging from 1 to 41, I measure the qubit spectra and extract the underlying phonon distributions[11] using a deconvolution procedure. Indeed, depending on the value of n_{B}, different parts of the original thermal distribution is altered. As highlighted by the shaded areas, the blue sideband drive takes a small region of the phonon populations around n_{B} and transfers them to higher numbers.

This phonon-number-sensitivity can also be demonstrated with red sideband transitions, but in the time-domain. In Fig. 6.4, I measure the qubit spectrum after applying an ac-dither red-sideband drive at a frequency corresponding to $n_{\mathrm{R}} \approx 8$. When the red-sideband drive is applied for a relatively short time of 150 μs ($\sim n_{\mathrm{R}}/\Gamma_{\mathrm{R}}^{|n_{\mathrm{R}}\rangle} \ll 1/\gamma_{\mathrm{m}}$, red), the phonon populations around $n = 8$ are emptied and transferred to Fock numbers $n \leq 2$. Meanwhile, populations at higher n are not affected because they are outside the number-sensitive region of the sideband drive. However, if the red sideband drive were left on for a much longer time of about 1.5 ms ($\sim 1/\gamma_{\mathrm{m}}$, black), these higher number populations would slowly decay down into the region over which the red sideband drive is effective and get pushed to even lower n. A similar long-time effect is also observed in Fig. 6.3(b): because the blue sideband drive is applied for a long effective time[12] , populations far below n_{B} are affected because they could be thermally excited to the region close to n_{B}.

6.3 Dissipatively squeezing the oscillator's energy

These phonon-number-sensitive sideband transitions enable a dissipative stabilization technique that can simultaneously add energy to and extract entropy from the oscillator [85]. This technique can be intuitively understood with the sketches of Fig. 6.5. To add energy to the oscillator, I slowly increase the blue sideband drive frequency ω_{B} (chirping). This adiabatically moves the center of the addressed transitions n_{B} up in phonon space and creates a steady-state phonon distribution that contains no population below the final value of n_{B} (Fig. 6.5(a)). To extract entropy from

[11] The phonon distributions presented in this section are all reconstructed using the approximate PSF discussed in Appendix.C

[12] Instead of letting the mechanical oscillator relax back to a thermal state after each experiment, I pulse on the blue sideband drive for 10 μs every 25 μs, and repeat this sequence for about one minute before resetting n_g.

the oscillator, I then turn on a red sideband drive centered on the transition $|g, n_{\mathrm{R}}\rangle \leftrightarrow |e, n_{\mathrm{R}} - 1\rangle$, with n_{R} close to but greater than the maximum value of n_{B} (Fig. 6.5(b)). A Fock state $|n\rangle$ will be cooled to a lower occupancy if the effective blue sideband transition rate $\Gamma_{\mathrm{B}}^{|n\rangle}$ is slower than the effective red sideband transition rate $\Gamma_{\mathrm{R}}^{|n\rangle}$, and vice versa. Thus, under conditions $\Gamma_{\mathrm{B}}^{|n_{\mathrm{B}}\rangle} > \Gamma_{\mathrm{R}}^{|n_{\mathrm{B}}\rangle}$ and $\Gamma_{\mathrm{B}}^{|n_{\mathrm{R}}\rangle} < \Gamma_{\mathrm{R}}^{|n_{\mathrm{R}}\rangle}$, the steady state phonon population becomes trapped in between the two-sideband drives.

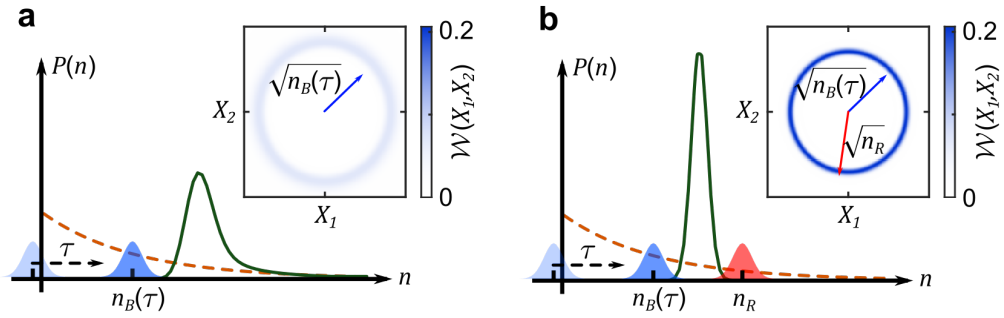

Figure 6.5: Energy squeezing: idea
a, Adiabatically increasing the blue sideband drive frequency (chirping) as a function of time τ changes the center of the addressed sidebands n_{B}. Starting from an initial thermal distribution, this chirping should empty all phonon population below the value of n_{B}, adding energy to the oscillator. The inset show that the resulting state's Wigner function[13] $\mathcal{W}(X_1, X_2)$ is a narrow ring around the (X_1,X_2) quadrature space origin with an inner-radius approximately given by $\sqrt{n_{\mathrm{B}}(\tau)}$. **b**, When the blue sideband drive is chirped toward a static red sideband drive centered at n_{R}, the phonon population should be trapped in between, and become squeezed in energy. Inset: The Wigner function of the resulting energy squeezed state is non-Gaussian and radially symmetric about the quadrature space origin, quite distinct from a quadrature squeezed state.

Fig. 6.6 shows an experimental demonstration of this technique. Starting from a thermal state, I chirp the blue sideband drive for different times τ, corresponding to different values of $n_{\mathrm{B}}(\tau)$, and measure the qubit spectrum. Indeed, at any time τ, the extracted phonon distribution in Fig. 6.6(a) contains no population below $n_{\mathrm{B}}(\tau)$. In Fig. 6.6(b), I demonstrate energy squeezing by repeating the same experiment, but with a red sideband drive parked at $n_{\mathrm{R}} = 44$. Trapped between n_{R} and $n_{\mathrm{B}}(\tau)$, the phonon population becomes increasingly localized in Fock space (smaller

[13] See Sec.7.1.4 for detailed discussion on Wigner function

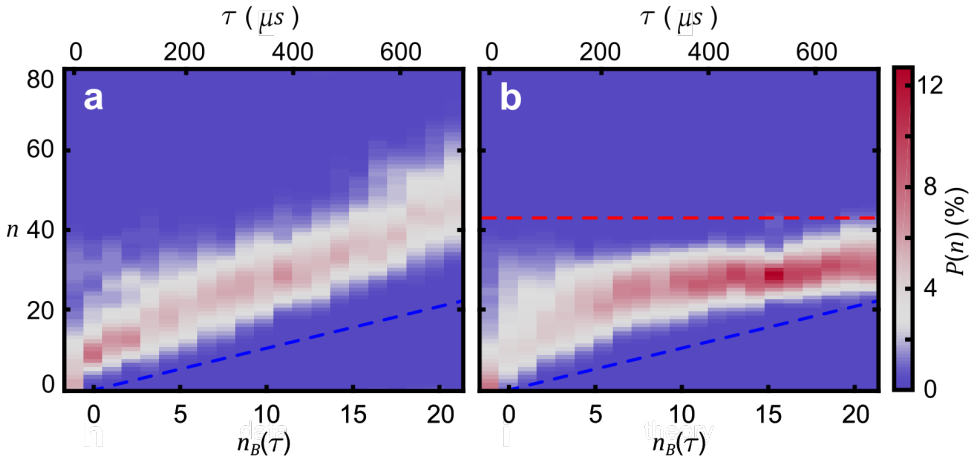

Figure 6.6: Energy squeezing: experiment
a, Chirping the blue sideband drive to a final position of $n_{\mathrm{B}}(\tau)$ (bottom-axis) by stopping the chirp at time τ (top-axis), I measure the qubit spectrum (see Fig. 6.8) and extract its phonon distribution (y-axis vs. colorscale) using deconvolution. At any time, the population is empty below the line $n = n_{\mathrm{B}}(\tau)$ (dashed blue), confirming the idea explained in Fig.6.5(a). **b**, Turning on a red sideband drive parked at n_{R} (dashed red), I repeat the above experiment to observe the phonon population is indeed trapped between the two sideband drives and become squeezed in energy as n_{B} is chirped toward n_{R}.

uncertainty in phonon number) as $n_{\mathrm{B}}(\tau)$ is brought closer to n_{R}. Clearly, these experiments support the intuitive understanding discussed above.

6.3.1 Modelling the time evolution of the hybrid system under sideband drives

To go beyond the intuition and make realistic predictions, I write down the time evolution of the qubit-mechanics system. This section follows closely to reference [85] Because the sidebands are driven on a time scale much longer than the qubit T_1 and T_2, the resulting state of the system is described by the diagonal elements of its density matrix, $P_g^{|n\rangle}$ and $P_e^{|n\rangle}$. Consequently, the time evolutionary of the qubit-mechanics system is well approximated by a set of classical master equations, similar to the classical laser rate equations. In general, these master equations are given by a combination of system dynamics due to sideband drives and decay,

$$\frac{d}{dt}P_{g(e)}^{|n\rangle} = \frac{d}{dt}P_{g(e)}^{|n\rangle}\bigg|_{\mathrm{drive}} + \frac{d}{dt}P_{g(e)}^{|n\rangle}\bigg|_{\mathrm{decay}}. \tag{6.5}$$

The first term in Eqn.(6.5) describes the dynamics due to sideband driving

$$\begin{aligned}
\frac{d}{dt}P_g^{|n\rangle}\bigg|_{\mathrm{drive}} &= -\Big(\Gamma_{\mathrm{B}}^{|n\rangle}(n_{\mathrm{B}}) + \Gamma_{\mathrm{R}}^{|n\rangle}(n_{\mathrm{R}})\Big)P_g^{|n\rangle} \\
&\quad + \Gamma_{\mathrm{R}}^{|n\rangle}(n_{\mathrm{R}})P_e^{|n-1\rangle} + \Gamma_{\mathrm{B}}^{|n\rangle}(n_{\mathrm{B}})P_e^{|n+1\rangle}, \\
\frac{d}{dt}P_e^{|n\rangle}\bigg|_{\mathrm{drive}} &= -\Big(\Gamma_{\mathrm{B}}^{|n\rangle}(n_{\mathrm{B}}) + \Gamma_{\mathrm{R}}^{|n\rangle}(n_{\mathrm{R}})\Big)P_e^{|n\rangle} \\
&\quad + \Gamma_{\mathrm{R}}^{|n\rangle}(n_{\mathrm{R}})P_e^{|n+1\rangle} + \Gamma_{\mathrm{B}}^{|n\rangle}(n_{\mathrm{B}})P_e^{|n-1\rangle},
\end{aligned} \tag{6.6}$$

where $P_{g(e)}^{|n\rangle}$ is the instantaneous population in the qubit ground (excited) state with n phonons. $\Gamma_B^{|n\rangle}$ is the effective blue sideband transition rate between states $|g,n\rangle \leftrightarrow |e,n+1\rangle$, and is related to its quantum counterpart $\Omega_{\mathrm{B}}^{|n\rangle}$ according to

$$\Gamma_{\mathrm{B}}^{|n\rangle} = \frac{\left(\Omega_{\mathrm{B}}^{|n\rangle}\right)^2}{\Gamma_2}. \tag{6.7}$$

For an ac-dither blue sideband drive of bare sideband rates $\Omega_{\mathrm{B(R)},0}$ (Eqn.(6.4)) applied on resonance with transition $|g,n_B\rangle \leftrightarrow |e,n_B+1\rangle$, the effective transition rate $\Gamma_{\mathrm{B}}^{|n\rangle}$ is function of n_{B}, maximized

at $n = n_{\mathrm{B}}$ but reduced for the other transitions by the frequency detuning $2\chi_{\mathrm{m}}(n - n_{\mathrm{B}})$ between their resonances and the sideband drive,

$$\Gamma_{\mathrm{B}}^{|n\rangle}(n_{\mathrm{B}}) = \frac{(n+1)\Omega_{\mathrm{B},0}^2}{\Gamma_2} \frac{1}{1 + \left(\frac{n-n_{\mathrm{B}}}{W/2}\right)^2}, \tag{6.8}$$

where $W = \Gamma_2/2\chi_{\mathrm{m}}$ is the characteristic width of the phonon-number-sensitivity. For a chirped blue sideband drive, n_{B} is a function of time. The effective red sideband rate is governed by a similar equation,

$$\Gamma_{\mathrm{R}}^{|n\rangle}(n_{\mathrm{R}}) = \frac{n\Omega_{\mathrm{R},0}^2}{\Gamma_2} \frac{1}{1 + \left(\frac{n-n_{\mathrm{R}}}{W/2}\right)^2}. \tag{6.9}$$

Next, I write down the master equations due to qubit and mechanical decay, which corresponds to the second term in Eqn.(6.5). In contrast to the intuitive picture discussed above (Fig. 6.2(a)), the qubit decay in general doesn't preserve the phonon number. Following the detailed discussion in Sec.2.3.4.1, I write down the following master equations:

$$\begin{aligned}
\frac{d}{dt}P_g^{|n\rangle}\bigg|_{\mathrm{decay}} &= e^{2r}\gamma_m\Big\{n_{\mathrm{th}}nP_g^{|n-1\rangle} + (1+n_{\mathrm{th}})(1+n)P_g^{|n+1\rangle} - \Big[(1+n)n_{\mathrm{th}} + (1+n_{\mathrm{th}})n\Big]P_g^{|n\rangle}\Big\} \\
&\quad + \Gamma_1 \sum_m |\alpha_{mn}|^2 P_e^{|m\rangle} \\
\frac{d}{dt}P_e^{|n\rangle}\bigg|_{\mathrm{decay}} &= e^{-2r}\gamma_m\Big\{n_{\mathrm{th}}nP_e^{|n-1\rangle} + (1+n_{\mathrm{th}})(1+n)P_e^{|n+1\rangle} - \Big[(1+n)n_{\mathrm{th}} + (1+n_{\mathrm{th}})n\Big]P_e^{|n\rangle}\Big\} \\
&\quad - \Gamma_1 P_e^{|n\rangle}
\end{aligned}, \tag{6.10}$$

where $r = \chi_{\mathrm{m}}/2\omega_{\mathrm{m}} \approx 0.005$, and $\alpha_{mn} = {}_b\langle m|\hat{S}(-2r)\,|n\rangle_b$ is the overlap between different motional states under a qubit flip. In these equations, I ignore the relaxation process where the mechanical oscillator losses many phonons to excite the qubit ($|g,n\rangle \mapsto |e,m\rangle$). Because of the large difference between qubit and mechanical frequency, such process requires the loss of more than 152 phonons ($\omega_{\mathrm{q}}/\omega_{\mathrm{m}} \approx 152$), and is highly unlikely.

Using the classical master equation of Eqn.(6.5), numerical simulations can be performed to predict the effects of driving the sideband transitions. To perform these simulations, the mechanical phonon space is truncated at $n_{\max} = 200$. At every time step in the simulation, the conservation

of probability $\sum_{n=0}^{n_{\max}} \left(P_g^{|n\rangle} + P_e^{|n\rangle}\right) = 1$ is enforced by setting $P_e^{|n_{\max}\rangle} = 0$ and $P_g^{|n_{\max}\rangle} = 1 - \sum_{n=0}^{n_{\max}-1} \left(P_g^{|n\rangle} + P_e^{|n\rangle}\right)$.

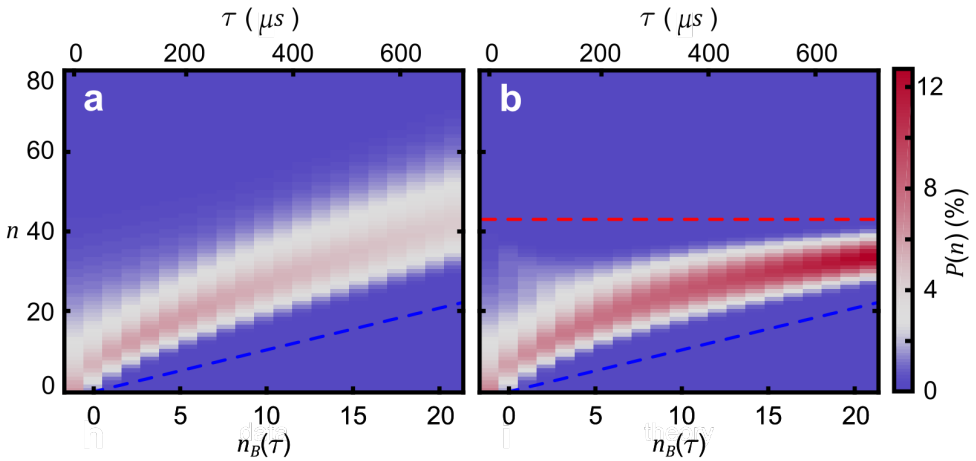

Figure 6.7: Energy squeezing: theory
Using the classical master equations, numerical simulations are performed with the same parameters used in the experiment of Fig.6.6, demonstrating a good agreement between theory and experiment.

Fig. 6.7 displays the results of numerical simulations performed using the experimental parameters found in Fig. 6.6, demonstrating a good agreement between theory and experiment. These parameters are extracted by performing least-squares fits to the measured qubit spectra, similar to Sec.5.4. Specifically:

(1) I first find n_{th} of the initial distribution by fitting the qubit spectrum at $\tau = 0$ to thermal distributions.

(2) Next, I generate a look-up table of phonon distributions with different sideband driving parameters by numerically solving the classical master equation. Through a convolution with the PSF map (Sec.5.2.5), this table is converted into a look-up table of expected qubit spectra.

(3) Using the look-up table, I jointly fit all qubit spectra with only a blue sideband drive but chirped for different τ in Fig. 6.8(a). Because the chirp rate $dn_{\text{B}}/d\tau \approx 38.5$ phonons/ms is

determined experimentally, the only two free parameters are the bare blue sideband rate $\Omega_{\mathrm{B},0} = 2\pi \times 170$ kHz, and the starting position of the chirp $n_{\mathrm{B}}(0) = -1.3$.

(4) Finally, I jointly fit all qubit spectra with both blue and red sideband drives in Fig. 6.8(b). Because I use the same blue sideband drive protocol, I keep the fit results from step (3) as constants. The center of transition for the red sideband drive $n_{\mathrm{R}} = 44$ is determined by the fit result of $n_{\mathrm{B}}(0)$ and the frequency detuning between the initial blue and red sideband drives. A joint least-squares fit to the look-up table finds the only free parameter $\Omega_{\mathrm{R},0} = 2\pi \times 122$ kHz.

It may seem surprising that the sideband drives can move phonon populations so efficiently given the effective sideband rate $\Omega_{\mathrm{B},0}^2/\Gamma_2 \approx 2\pi \times 7.8$ kHz is rather comparable to the mechanical thermal decoherence rate $n_{\mathrm{th}}\gamma_{\mathrm{m}} \approx 2\pi \times 1.4$ kHz. Indeed, this surprising phonon transfer efficiency comes from the fact that a sideband drive simultaneously drives many transitions [86]. To understand this, consider for instance a two-level system $\{|0\rangle, |1\rangle\}$, which is coupled with a hot bath at rate γ such that $P(0) = P(1) = 1/2$ at thermal equilibrium. Turning on a drive takes the population in $|0\rangle$ to $|1\rangle$ at a reduced rate $\Gamma = \gamma$. The steady state populations will be $P(0) = 1/3$ and $P(1) = 2/3$, demonstrating a very inefficient population transfer. However, the same drive will already look more efficient if it address a three level system $\{|0\rangle, |1\rangle, |2\rangle\}$. At equilibrium with the thermal bath, the populations are given by $P(0) = P(1) = P(2) = 1/3$. When the drive is on, the steady state populations are given by $P(0) = 1/7$, $P(1) = 2/7$ and $P(2) = 4/7$. The same goes for even higher level systems.

In the driven dynamics of Eqn.(6.6), I consider only the effects from the intentionally excited ac-dither sideband transitions. However, as I discussed in Sec.7.3, the ac-dither sideband drive can also excites other unintentional sideband transitions, complicating the master equations. Although these unintentional sideband transitions have only negligible effects when the blue sideband drive is located at small values of n_{B}, they will cause an observable spurious cooling for $n_{\mathrm{B}} > 50$. To account for these effects, corrections to the classical master equations will be discussed in Sec.7.3.

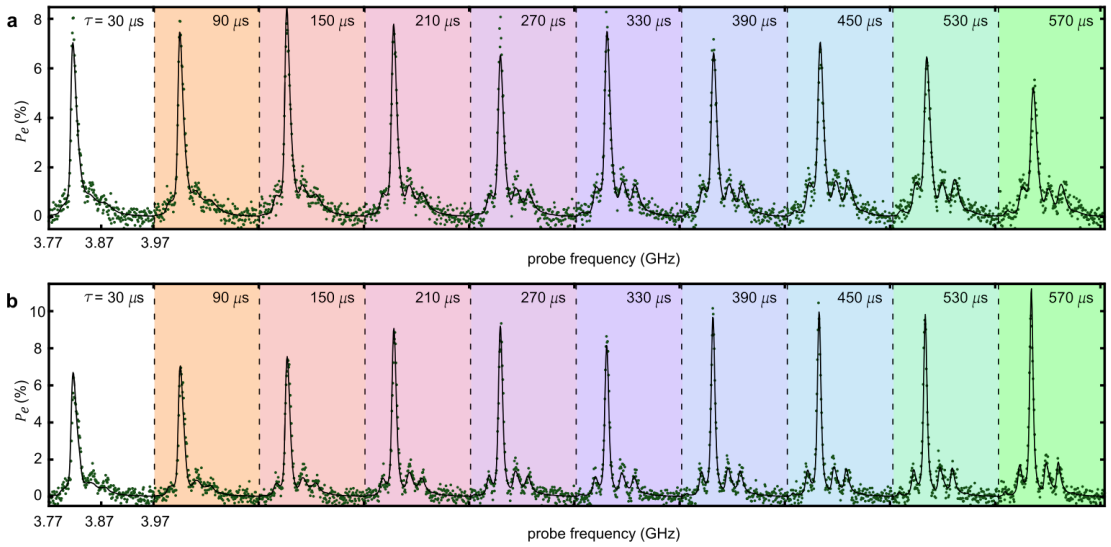

Figure 6.8: Finding the sideband driving parameters
a, Each panel (with the same frequency axis) shows one qubit spectrum (green dots) measured after chirping the blue sideband drive for a time τ. The extracted phonon distributions from these qubit spectra are plotted in Fig. 6.6(a). A joint least-squares fit of these qubit spectra to numerical simulations reveals the blue sideband driving parameters $n_{\mathrm{B}} = -1.5$ and $\Omega_{\mathrm{B},0} = 2\pi \times 170$ kHz. **b**, Similar to **a**, each panel shows the qubit spectrum after chirping the blue sideband drive for time τ, but with the red sideband drive on. These qubit spectra corresponds to the phonon distribution shown in Fig.6.6(b). Keeping the same blue sideband driving parameters, a joint least-squares fit to numerical simulations reveals the red sideband drive strength $\Omega_{\mathrm{R},0} = 2\pi \times 122$ kHz. This figure is reproduced from reference [85].

Chapter 7

Energy squeezing below the classical limit

Finally, I use the energy-squeezing technique to prepare the oscillator in a non-Gaussian nonclassical state of motion [85]. Specifically, I prepare the oscillator in a sub-Poissonian state, where its energy fluctuation is blow the classical limit [87]. In Sec.7.1, I demonstrate the preparation of such a state, with a large mean phonon number $\langle n \rangle = 43$ and a sub-Poissonian number fluctuation of approximately 3. In preparing this energy-squeezed state, I clearly resolve the sideband transitions in the qubit spectrum that were previously obscured by the broad phonon distribution associated with the large thermal occupation in Sec.5.4. In Sec.7.2, I provide a simple physical explanation for these prominent sideband peaks using the Frank-Condon principle [111, 112], and discuss their implications for a quantum non-demolition (QND) measurement of phonons. Finally, in Sec.7.3, I discuss the factor that limits the nonclassicality achieved in this work: a spurious cooling effect mentioned in Sec.6.3.1. This chapter closely follows publication [85].

7.1 Preparation and measurement of a nonclassical state of motion

After optimizing the energy-squeezing protocol discussed in Sec.6.3, I prepare the oscillator in a nonclassical state of motion described by a sub-Poissonian phonon distribution. To demonstrate this, I infer the phonon distribution from the qubit spectrum. However, as I discuss in Sec.7.1.1, this inference requires care because measuring the qubit spectrum can alter the phonon distribution. In Sec.7.1.2, I extract the phonon distribution from the measured qubit spectrum using the deconvolution procedure. Narrower than a coherent state of the same mean phonon number, this ex-

tracted phonon distribution is indeed nonclassical, with a Fano factor $F = \mathrm{var(n)}/\langle n \rangle = 0.257^{+0.002}_{-0.001}$ smaller than the classical limit of $F = 1$ [87]. In Sec.7.1.3, I investigate the statistical significance of this extracted Fano factor, and determine with 99% confidence that this nonclassical mechanical state has a true Fano factor $F_{\mathrm{true}} \leq 0.30$. Finally, in Sec.7.1.4, I relate the Fano factor to other measurements of nonclassicality, such as the negativity in a Wigner function.

7.1.1 Measuring the qubit spectrum

As discussed theoretically in Sec.5.2.2, the sideband peaks observed in a qubit spectrum correspond to the creation or annihilation of phonons. Consequently, to ensure an accurate inference of the phonon distribution, I need to limit the measurement-induced changes in phonon distribution to a negligible amount. This can be achieved by only driving the qubit probe signal for a short 8 μs duration.

To demonstrate this, I measure the qubit spectrum for different duration T_{spec} after preparing the mechanical oscillator in a sub-Poissonian state using the energy-squeezing protocol. The pulsing sequence for this measurement is sketched in Fig. 7.1. Indeed, as Fig. 7.2 shows, when T_{spec} is increased beyond 8 μs[14], changes in the qubit spectrum associated with changing phonon distributions can be observed.

7.1.2 Extracting the nonclassical phonon distribution

To extract the phonon distribution from the measured qubit spectrum, I use the same deconvolution procedure discussed in Sec.5.3, but with one modification: the initial guess for the phonon distribution P_0, instead of a uniform distribution, is assumed as a Poisson distribution. Fig. 7.3(b) shows the phonon distribution extracted using an uniform initial guess. It reveals the

[14] Note that $T_{\mathrm{spec}} = 8$ μs is not a universal condition for avoiding this measurement induced change in phonon distribution. Instead, it is influenced by both measurement noise and the phonon distribution being measured. Unless specifically noted, phonon distributions measured in previous chapters are all performed with the sequence of Fig. 7.1 but a longer $T_{\mathrm{spec}} = 100$ μs. In those experiments, the phonon distribution is already broad because of the large n_{th}, and I'm only interested in detecting how the distribution changes as function of other parameters. Thus for those experiments, I choose to improve the duty cycle of measurements, which use 8 ms repetition rates to allow for the mechanical oscillator to re-equilibrate, at the cost of a small reduction in the fidelity of the extracted phonon distributions.

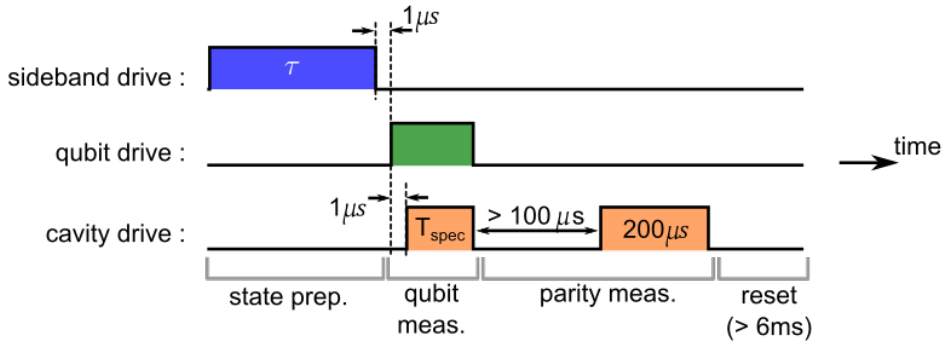

Figure 7.1: Measurement sequence
The pulse sequence (not to scale) used to measure the sub-Poissonian state is sketched. The sequence starts with the preparation of the desired mechanical state by driving the sidebands for a duration $\tau \approx 1$ ms (blue). As discussed in Chapter 4, after waiting for the qubit to decay back to the ground state, I probe the qubit state by simultaneously driving the qubit (green) and measuring the cavity (orange) phase φ_c for duration T_{spec}. To ensure the steady-state qubit spectrum is measured, the qubit drive is applied 1 μs before the start of the phase measurement. After the qubit has relaxed back to its ground state, I again measure φ_c to readout the qubit parity. Finally, I wait for more than 6 ms for the mechanical oscillator to thermalize back to its environment before starting the next measurement cycle.

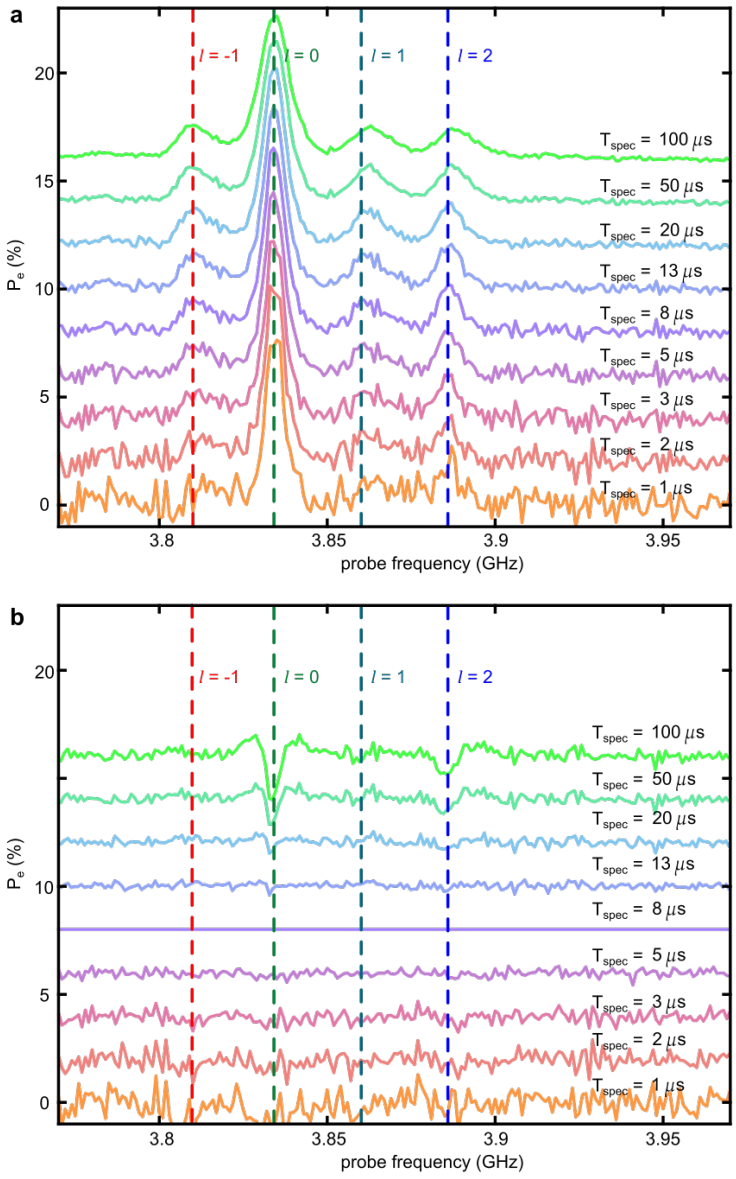

Figure 7.2: Measurement-induced changes in phonon distribution
a, After preparing the desired mechanical state using the energy-squeezing protocol, I measure the qubit spectrum with different qubit probe duration T_{spec}. An incremental offset of 2% is added for each trace. The vertical dashed lines correspond to the positions of the qubit excitation peaks at $T_{\text{spec}} = 8$ μs. With increasing T_{spec}, the $l = -1$ peak shifts toward a lower frequency because of sideband cooling, and the $l = \{1, 2\}$ peaks shift toward higher frequencies because of sideband heating, demonstrating measurement-induced changes in the phonon distribution. With increasing T_{spec}, I also observe a broadening of the center qubit peak caused by the damping of the mechanical oscillator during measurement. **b,** I subtract the $T_{\text{spec}} = 8$ μs qubit spectrum from each qubit spectrum in **a**. Structure can be observed in the traces with $T_{\text{spec}} \geqslant 13$ μs at the positions of the dashed lines. This figure is reproduced from reference [85].

expected energy-squeezed phonon distribution around $\langle n \rangle = 43$, but also finds a small, nonphysical phonon peak around $n = 180$. Initial assigned by the uniform guess, these nonphysical population requires many iterations of the deconvolution procedure to remove. Before this happens, however, the reconstruction starts to over fit in other parts of the phonon distribution (see Sec.5.3.1). Consequently, at the optimal iteration number, some nonphysical populations are left behind. Indeed, I confirm this nonphysical feature to be an artifact of the imperfect reconstruction procedure not only because it disagrees with the physical understanding achieved in Sec.6.3, but also because I observe similar artifacts when the same reconstruction is performed on simulated experiments with known phonon distributions (see Sec.7.1.3). Although these artifacts do not obscure the energy-squeezed phonon distribution, they could lead to a greatly underestimated nonclassicality. In this context, I remove them by providing a better initial guess — a Poisson distribution.

Fig. 7.3(c) shows the phonon distribution extracted with an Poisson initial guess of mean phonon number $\langle n \rangle = 43$. Narrower than a Poisson distribution of the same mean phonon number, the mechanical state prepared using the energy-squeezing protocol is indeed nonclassical [87], with an energy fluctuation below the classical limit. I characterize this nonclassical nature with the Fano factor $F = \mathrm{var}(n)/\langle n \rangle$. For a Poisson distributed state, $F = 1$, and for a Fock state, $F = 0$. When $F < 1$, the phonon distribution is nonclassical, energy squeezed, and Fock-like. For the phonon distribution extracted in Fig. 7.3(c), I find $F = 0.257^{+0.002}_{-0.001}$, where the bound is determined by the uncertainty in the bare qubit frequency (see Sec.5.2.5). To determine the statistical significance of this extracted Fano factor, one option is to use the non-parametric bootstrapping (see Sec.5.3.2) to investigate the effect of measurement noise. However, such an investigation is unable to reveal any systematic bias introduced by the deconvolution procedure.

7.1.3 Bounding the Fano factor

Instead, I quantify the confidence in the extracted Fano factor by performing repeated reconstruction procedures on simulated experiments with known phonon distributions. This way, I reveal simultaneously the effect of measurement noise and any systematic bias from the deconvolution.

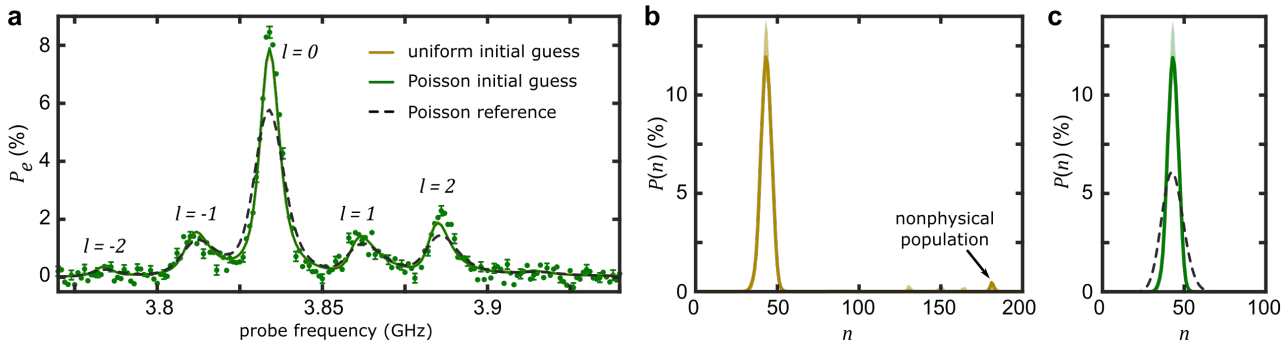

Figure 7.3: Extracting the nonclassical phonon distribution
a, Using $T_{\text{spec}} = 8$ μs, I measure the qubit spectrum (dots) associated with the energy-squeezed phonon distribution. The standard error of the mean (SEM) are extracted individually for each frequency point (see Sec7.1.3), and plotted as error-bars for every fourth point. **b**, Using the deconvolution procedure discussed in Sec.5.3, I extract the phonon distribution (solid line) and its 90% confidence interval (shaded) starting from an uniform initial guess, but find nonphysical population around $n = 180$. **c**, Starting from a Poisson initial guess instead, I remove these artifacts arising from measurement noise to find a sub-Poissonian phonon distribution (green) characterized by $F = \text{var}/\langle n \rangle = 0.257 < 1$, narrower than that of a coherent state (dashed black). For comparison, the associated qubit spectra are plotted in **a**, where the sub-Poissonian nature of the mechanical state is evident in its narrower lineshape. The peaks visible in the qubit spectrum are separated by ω_{m}, and corresponds to transitions $|g, n\rangle \leftrightarrow |e, n + l\rangle$.

Specifically, this study is performed following a four step procedure:

(1) I create a Gaussian distributed phonon distribution characterized by a mean phonon number $\langle n \rangle = 43$ and a Fano factor F_{true}.

(2) This phonon distribution is converted into a noiseless qubit spectrum by convolving it with the PSF map found in Sec.5.2.5.

(3) I simulate an experimental realization by adding the appropriate amount of noise and averaging for the same number of times as the actual experiment (916 times for the data in Fig. 7.3(a)).

(4) The same reconstruction procedure is performed on the simulated experiment to extract a phonon distribution and F_{extract}.

Correctly simulating the experiment in step (3) requires an accurate understanding of the measurement noise. I achieve this understanding by looking at the measurement data corresponding to Fig. 7.3(a). From the 916 individual recorded qubit traces, I find the standard deviation of the measurement signal at each frequency point. At each frequency point, the extracted measurement standard deviation σ_P (green dot) is plotted in Fig. 7.4(a), and arranged according to the mean signal at that frequency. I model the dependence of noise on signal amplitude with a second order polynomial function (black dashed line).

The four-step procedure is repeated many times for different noise realizations and F_{true} to build statistics. Fig. 7.4(b) depicts the result of this statistical study. For each F_{true}, I perform 3000 simulated experiments, each with 916 averages. The extracted F_{extract} are binned into steps of $\delta_F = 0.01$, and the resulting histogram is plotted. The grey solid line corresponds to $F_{\text{extract}} = F_{\text{true}}$, and demonstrates a systematic bias of the deconvolution that generally finds $F_{\text{extract}} > F_{\text{true}}$. For the 1216 simulations that resulted in an F_{extract} within the interval $[0.255, 0.265]$ (black dashed line), the cumulative distribution function (CDF) of F_{true} is plotted in Fig. 7.4(c). Because the experimentally determined $F = 0.257^{+0.002}_{-0.001}$ lies within this range, I thus find $F_{\text{true}} \leq 0.28$ with 95%

confidence and $F_{\text{true}} \leq 0.30$ with 99% confidence for the sub-Poissonian state prepared in Fig. 7.3.

7.1.4 Relating the Fano factor to other measurements of nonclassicality

The Fano factor is but one measurement that can be used to characterize the nonclassicality of this mechanical state. Indeed, it can be related to other commonly used criteria for describing nonclassical states, such as the g_2 correlation function [141],

$$g_2(0) = 1 + \frac{\text{Var}(n) - \langle n \rangle}{\langle n \rangle^2} = 1 + \frac{F-1}{\langle n \rangle}, \tag{7.1}$$

where $g_2(0) < 1$ signifies a nonclassical state. Clearly, this condition is automatically fulfilled by $F < 1$. However, because the mechanical state resides in a single mode of the oscillator, the condition $g_2(0) < 1$ does not imply phonon anti-bunching [142, 141], but only reveals the sub-Poissonian nature of the phonon distribution. In this context, the $g_2(0)$ function contains the same information as F, but unhelpfully compresses the nonclassicality of large mean phonon states into a tiny region of possible values between 1 and $1 - 1/\langle n \rangle$. For example, a pure 50 phonon Fock state with $g_2(0) = 0.98$ is barely distinguishable from a coherent state with $g_2(0) = 1$!

Another common measurement of nonclassicality is the negativity in the Wigner function $\mathcal{W}$ [141]. Because any state prepared using the energy-squeezing protocol will contain only diagonal elements (see Sec.6.3), I can easily compute the Wigner function from the extracted phonon distribution. Doing so with the sub-Poissonian state in Fig. 7.3, I observe a small region of negativity in the Wigner function but with high statistical significance. Unfortunately, the bare qubit frequency is a kind of nuisance parameter whose uncertainty yields systematic uncertainty in the average phonon number $\langle n \rangle$. Although this uncertainty has little effect on F, it causes uncertainty in the location of the Wigner negativity. If I average over all of the possible Wigner functions consistent with the possible bare qubit frequencies, the negativity is diminished such that it has marginal statistical significance.

Instead of further analyzing the data and risk introducing bias, I can relate the extracted Fano factor to a negativity in the Wigner function under the assumption of a Gaussian number

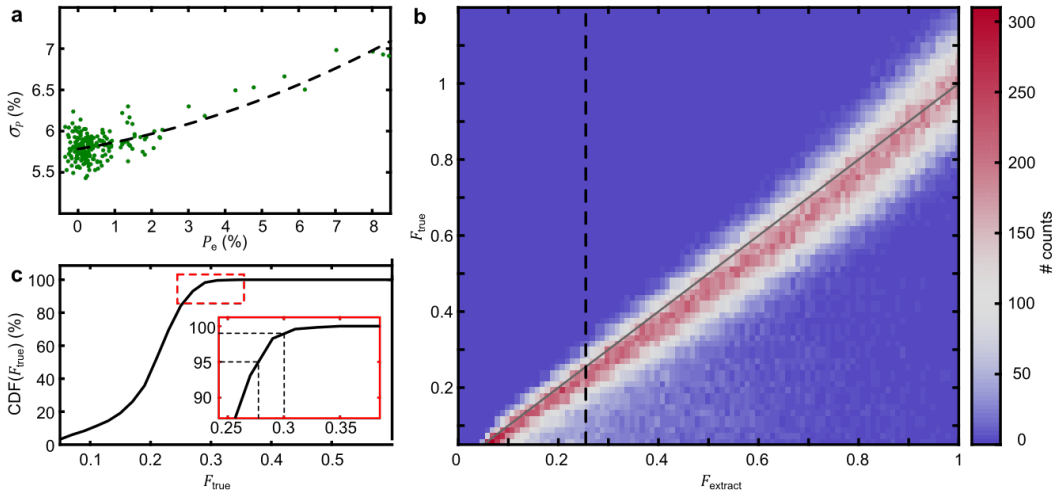

Figure 7.4: Bounding the Fano factor
a, The measurement noise σ_P is plotted as a function of the mean measured signal. The dashed black line is a second order polynomial fit, used to model the noise dependence on signal amplitude. **b,** I plot the histogram of F_{extract} (color-scale vs. x-axis) for different F_{true}. Each F_{true} consists of 3000 different simulated experiments. The solid grey line corresponds to $F_{\text{extract}} = F_{\text{true}}$, and shows that F_{extract} in general overestimates the Fano factor. **c,** Using the CDF of F_{true} for $F_{\text{extract}} \in [0.255, 0.256]$ (dashed black line in **b**), I find with 95% confidence that $F_{\text{true}} \leq 0.28$ and with 99% confidence that $F_{\text{true}} \leq 0.30$. This figure is reproduced from reference [85].

fluctuations, according to reference [143]. In this reference, the authors find that for a Gaussian-distributed sub-Poissonian state, the maximal negativity in the Wigner $\mathcal{W}$ function, defined as the ratio of $\min(\mathcal{W})/\max(\mathcal{W})$, is related to its motional amplitude $r_0 = \sqrt{\langle n \rangle}$ and Fano factor F according to Fig. 6 of the reference, reproduced in Fig. 7.5. In comparison, the sub-Poissonian state prepare in this work is approximately Gaussian-distributed around its mean phonon number $\langle n \rangle = 43$, and has a Fano factor $F \leq 0.28$ with 95% confidence. Under the assumption of a Gaussian number fluctuation, these values place the sub-Poissonian state at the red-stared position in this figure, and indicate a small negativity in its Wigner function.

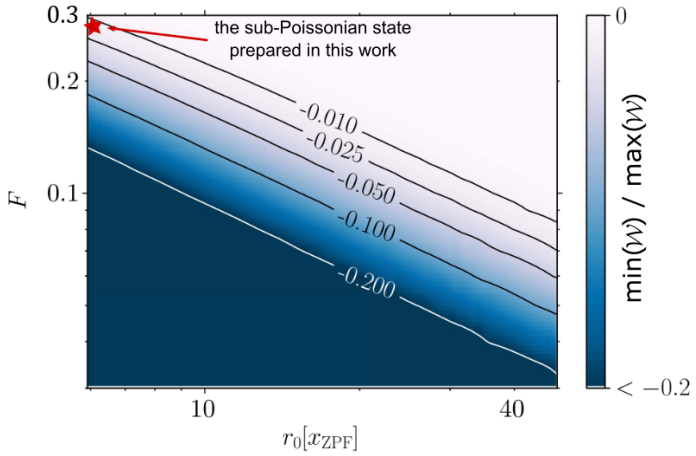

Figure 7.5: Relating the Fano factor to negativity in the Wigner function
For a Gaussian-distributed sub-Poissonian state, the maximal negativity in the Wigner function (color-axis) can be related to its motional amplitude r_0 (x-axis) and Fano factor (y-axis). In comparison, assuming a Gaussian number fluctuation, the sub-Poissonian state prepared in Fig. 7.3 ($r_0 = \sqrt{43}$ and $F \leq 0.28$ with 95% confidence) is located in this figure at the red-stared position, indicating a small negativity in its Wigner function. This figure by Lörch *et al.* [143] is reproduced under CC BY 3.0 license. I have added the red star, its associated labels, and the color-axis label "$\min(\mathcal{W})/\max(\mathcal{W})$".

7.2 Mechanical recoil caused by qubit transitions

In creating the energy-squeezed state, I can now resolve the sideband transitions that were previously obscured by the broad phonon distribution associated with the large thermal occupation in Sec.5.4. The center peak in the qubit spectroscopy ($l = 0$ peak in Fig. 7.3(a)) corresponds to

the qubit transition that conserves phonon number, where as the satellite peaks at $\pm 2\omega_{\mathrm{m}}$ ($l = \pm 2$) are associated with qubit transitions that create and annihilate pairs of phonons. As discussed in Sec.2.3.3.1, these sideband transitions arise because the mechanical spring suddenly stiffens under a qubit excitation, causing overlaps between the mechanical spatial wavefunctions that would be otherwise orthogonal. Indeed, these transitions are highly analogous to the vibronic transitions in molecules, where a fast electronic (qubit) transition connects different slow mechanical states. When the qubit is located at the charge degeneracy point, the symmetry of the mechanical potential prohibits the creation and annihilation of odd number of phonons. However, because charge noise creates a small random bias away from degeneracy, a qubit excitation also exerts a force on the oscillator, as discussed in Sec.2.3.5, displacing it along its position-axis. Consequently, I also observe peaks at $\pm\omega_{\mathrm{m}}$ associated with single-phonon sideband transitions.

In contrast to the sidebands observed in reference [82] at $\langle n \rangle \sim 10^4$ phonons, these peaks are easily resolved at the relatively small phonon number $\langle n \rangle = 43$ because $\chi_{\mathrm{m}}/\omega_{\mathrm{m}}$ is much larger (see Sec.2.3.3). Consequently, they can substantially alter the oscillator's phonon distribution, as evident from the measured-induced change in phonon distribution already discussed in Sec.7.1.1.

The prominence of these sideband peaks also signifies the entry into a regime where the qubit's spontaneous decay can detectably alter the phonon distribution (see Sec.2.2.3). In Fig. 7.3(a), I measure the probability of exciting the qubit when driving at a particular frequency, but each peak must also correspond to a qubit decay process, driven by the quantum noise in the environment. From the ratio of the area underneath the $l = 0$ peak to the total area under all the peaks, I estimate that a qubit decaying from an initial state of $|e, 43\rangle$ will only preserve the phonon number with 63% probability! This probability will further diminish if χ_{m} were increased to better resolve individual phonon numbers.

7.3 Limitations on the achieved nonclassicality

According to Sec.6.3, the energy-squeezing protocol can in principle be performed at arbitrarily large $\langle n \rangle$ to create phonon distributions with minimum widths roughly given by the phonon-

number-sensitivity, $W \approx 7.1$ phonons. Consequently, it is possible to achieve a smaller F, and therefore a higher nonclassicality, by squeezing at a higher $\langle n \rangle$.

However, in this work, I only demonstrate the preparation of a nonclassical mechanical state at a moderate $\langle n \rangle = 43$, because driving the ac-dither sideband[15]introduces an additional unwanted cooling process (spurious cooling) that significantly alters the phonon population at large phonon number $n > 50$. Although this unwanted process does not prevent, but rather helps, achieving a narrow phonon distribution, as I will demonstrate shortly, I instead operated at a point where its effect is negligible to best demonstrate the energy-squeezing protocol's ability of preparing nonclassical states. Moreover, if I were to tolerate this spurious cooling effect, the maximum $\langle n \rangle$ achievable is eventually limited by the inaccuracies in the PSF map experimentally extracted in Sec.5.2.5, causing nonphysical features in the reconstructed phonon distribution when the sub-Poissonian state is prepared at $\langle n \rangle > 80$.

The spurious cooling effect arises because when a blue sideband drive is chirped for time τ to position $n_{\mathrm{B}}(\tau)$ to empty all phonon populations below, it simultaneously cools the populations at larger phonon numbers. This additional unwanted cooling process is conceptually illustrated in Fig. 7.6(a). As mentioned in Sec.6.1, I use the set of ac-dither sidebands below the qubit resonance, $\omega_{\mathrm{B}}(n) = \omega_{\mathrm{q}}^{|n\rangle} \pm \omega_{\mathrm{m}} - \omega_{\mathrm{dither}}$. Meanwhile, the l-th order sideband transition is located at $\omega_l(n) = \omega_{\mathrm{q}}^{|n\rangle} + l\omega_{\mathrm{m}}$. Thus, an ac-dither blue sideband drive centered on transition $|g, n\rangle \leftrightarrow |e, n+1\rangle$ can be close to resonance with the 10-th order red sideband transition $|g, n+35\rangle \leftrightarrow |e, n+25\rangle$, creating an additional cooling effect at larger phonon numbers.

Although the resonant 10-th order red sideband transition provides an easy conceptual understanding to this unwanted effect, it is a subdominant effect. Instead, the spurious cooling effect is dominated by other lower order red sideband transitions excited off-resonantly by the ac-dither blue sideband drive. To understand this, I write the reduced l-th order sideband rate for transition

[15] For all theory and experiments in this section, $\omega_{\mathrm{dither}} = 260$ MHz.

$|g,n\rangle \leftrightarrow |e,n+l\rangle$ due to an ac-dither sideband drive at ω_d (see Sec.6.3.1),

$$\begin{aligned}\Gamma_l^{|n\rangle}(\omega_d) &= \frac{\left|\Omega_n^l\right|^2}{\Gamma_2}\frac{1}{1+\left(\frac{\omega_d-\omega_l(n)}{\Gamma_2/2}\right)^2} \\ &= \frac{\Omega_R^2}{\Gamma_2}\left|\alpha_{n+l,n}^{\text{rsd}}\right|^2\frac{1}{1+\left(\frac{\omega_d-\omega_l(n)}{\Gamma_2/2}\right)^2},\end{aligned} \tag{7.2}$$

where Ω_R is the Rabi rate of the sideband drive, and $\alpha_{n+l,n}^{\text{rsd}}$ is the overlap given by Eqn.(2.93). At smaller l, the increased overlap $\left|\alpha_{n+l,n}^{\text{rsd}}\right|^2$ more than makes up the larger detuning. Moreover, the larger detuning at smaller l also creates a more uniform sideband rate $\Gamma_l^{|n\rangle}(\omega_d)$ as a function of n, resulting in a more efficient manipulation of phonons (see Sec.6.3.1).

In Fig. 7.6(d), I numerically demonstrate the effect of this spurious cooling process. I use the calculated qubit spectrum of Fig. 5.9(c) to find $\left|\alpha_{n+l,n}^{\text{rsd}}\right|^2$. With the driving parameters extracted from Sec.6.3.1, I incorporate up to the 10-th order red sideband transitions into the master equation of Eqn.(6.6) and predict the phonon distribution under a chirped ac-dither blue sideband drive. Compared to Fig. 7.6(c) where the red sideband transitions are ignored, the effect of the spurious cooling is clear. Indeed, as Fig. 7.7 shows, I am able to experimentally prepare a sub-Poissonian state with $\langle n\rangle \approx 77$ with only the chirped blue sideband drive and its associated spurious cooling effects.

Conversely when driving the ac-dither sideband above the qubit, a spurious heating effect appears. To demonstrate this effect, I apply an ac-dither red sideband drive above the qubit frequency at approximately $n_{\text{R}} \approx 10$ and measure the qubit spectrum. As illustrated in Fig. 7.8(a), this ac-dither red sideband drive is close in resonance with the 9-th order blue sideband transition $|g,39\rangle \leftrightarrow |e,n+48\rangle$. This causes the phonon population to bifurcate: for populations close to $n = 10$, they are cooled to lower occupations, while phonons further above are pushed by the unwanted blue sideband transitions to even higher numbers. Consequently, the mechanical state can be regarded as a mixture of two mechanical states, one with a large motion, while the other has a small motion. Fig.7.8(b) shows that these two states can be differentiated by looking at the cavity phase φ_c when the qubit is in the ground state (i.e., parity measurement), because their different

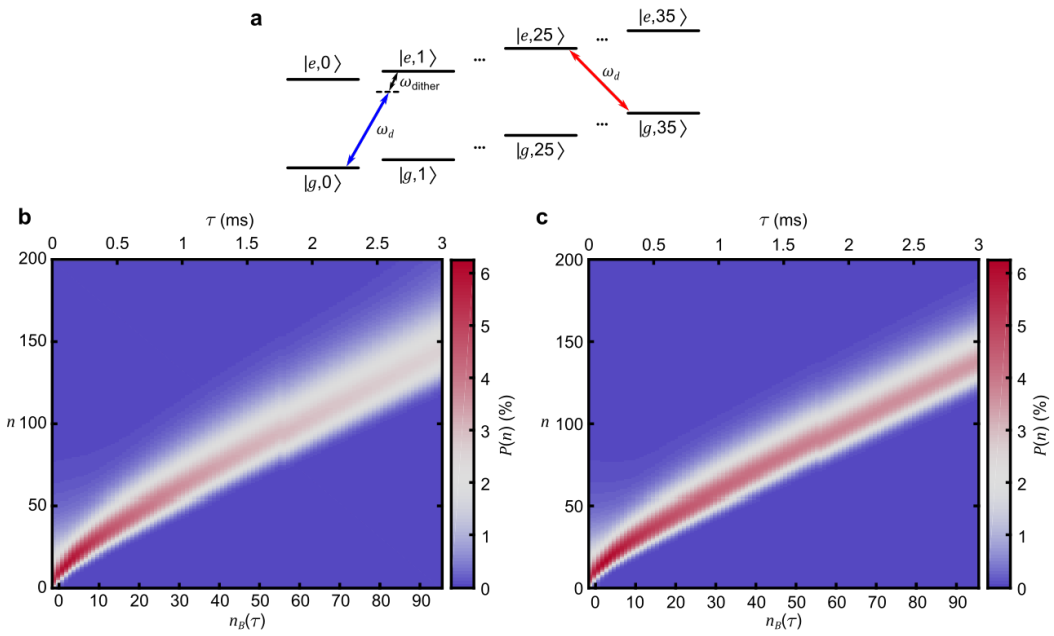

Figure 7.6: A spurious cooling effect from driving ac-dither sideband below the qubit: theory
a, A sideband drive at frequency $\omega_d = \omega_{\mathrm{q}}^{|0\rangle} - \omega_{\mathrm{dither}} + \omega_{\mathrm{m}}$ is simultaneously resonant with the ac-dither blue sideband transition of $|g,0\rangle \leftrightarrow |e,1\rangle$ and the 10-th order red sideband transition of $|g,35\rangle \leftrightarrow |e,25\rangle$. Thus, using this ac-dither blue sideband drive to add phonons to the mechanical oscillator will cause unwanted cooling at larger phonon number. **b**, **c**, I use the master equations and the extracted driving parameters found in Sec.6.3.1 to calculate the phonon distribution (color-scale vs. y-axis) after chirping the ac-dither blue sideband drive for time τ (top-axis). This process should empty all phonon populations below the center of the blue sideband drive $n_B(\tau)$ (bottom-axis). The spurious cooling process is not considered in **b**, but it is modeled in **c**. The unwanted cooling is visible at $n_B(\tau) > 50$.

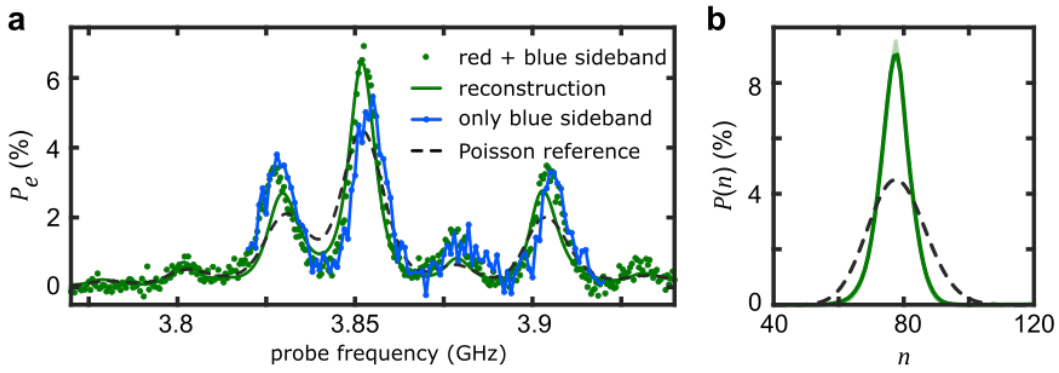

Figure 7.7: A spurious cooling effect from driving ac-dither sideband below the qubit: experiment Chirping a blue sideband drive toward a stationary red sideband drive with $n_{\mathrm{R}} \approx 82$, I energy-squeeze the oscillator's motion and measure the corresponding qubit spectrum (**a**, green dots). Its extracted phonon distribution (**b**, green solid line) and 90% confidence interval (shade) reveals the the oscillator's motion is described by a sub-Poissonian distribution with $\langle n \rangle \approx 77$. Performing the same experiment but now with the red sideband drive off, I measure a similar qubit spectrum (**a**, blue dots with line), also visibly narrower than the expected qubit spectrum from a coherent state (dashed black line). Consistent with the theory prediction in Fig. 7.6, this demonstrates that, at large $\langle n \rangle$, the spurious cooling effect is so strong that a sub-Poissonian state can be prepared solely with a chirped blue sideband drive.

motional amplitudes rectify φ_c by different amounts (see Sec.4.2.2). Selecting on this phase, I can separate the overall measured qubit spectrum into two different spectra, each corresponding to a large-motion state or a small-motion state (Fig.7.8(c)). Indeed, while the small-motion state is consistent with driving ac-dither red sideband transitions, the large-motion state is consistent with driving the spurious blue sideband transitions.

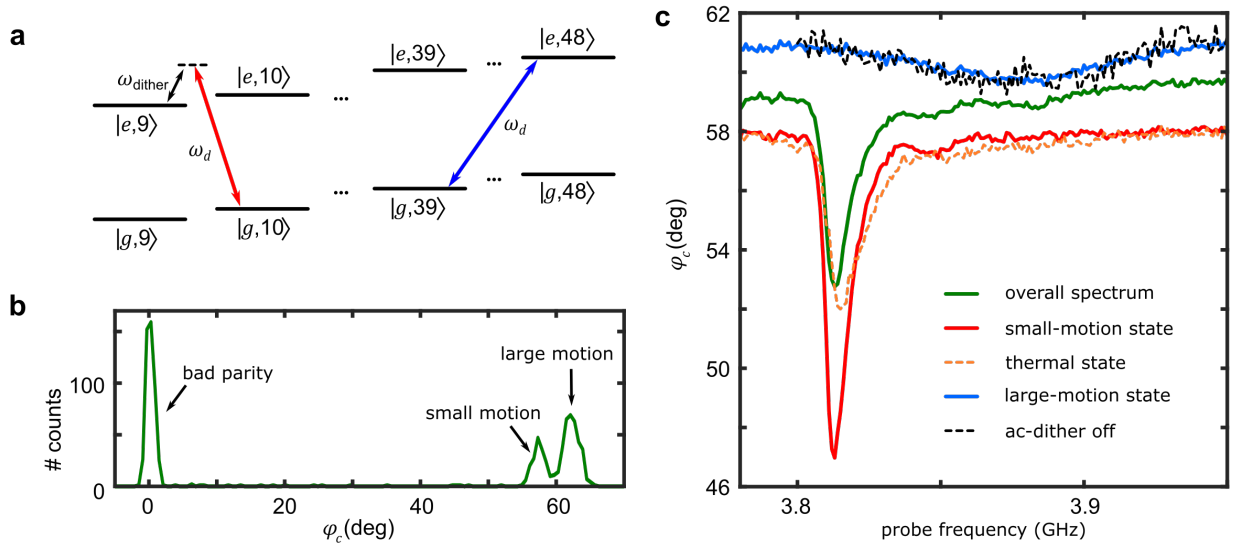

Figure 7.8: A spurious heating effect from driving ac-dither sideband above the qubit
a, An ac-dither red sideband drive is applied at frequency $\omega_d = \omega_{\text{q}}^{|10\rangle} + \omega_{\text{dither}} - \omega_{\text{m}}$. This drive simultaneously resonates with the ac-dither red sideband transition $|g, 10\rangle \leftrightarrow |e, 9\rangle$ and the 9-th order blue sideband transition $|g, 39\rangle \leftrightarrow |e, 48\rangle$. Starting from a thermal state, this will cool phonons around $n = 10$ to smaller occupations, while heating populations above to even higher numbers. **b**, This bifurcation of the oscillator's motional amplitude is revealed by a histogram of the cavity phase φ_c with the qubit in ground state. Indeed, at the good qubit parity position (around $\varphi_c \sim 60$ deg, see Sec.4.1.3), the histogram shows two separate peaks: because different motional amplitudes rectify φ_c by different amounts (see Sec.4.2.2), the lower peak corresponds to the mechanical state with small motion, while the higher peak corresponds to the state with large motion. **c**, Selecting on this phase, I separate the overall qubit spectrum (green) into two different spectra, corresponding to the small-motion (red) and large-motion (blue) states respectively. Compared to the initial thermal state (dashed orange), the spectrum of the small-motion state demonstrates the cooling effect of the ac-dither red sideband transitions. Finally, I perform the same experiment but turn off the ac-dither signal. The resulting qubit spectrum (dashed black) agrees well with the spectrum of the large-motion state, demonstrating the spurious heating effect does not depend on the ac-dither.

Chapter 8

Conclusion

In this thesis, I demonstrated the preparation of a non-Gaussian nonclassical state of motion in a macroscopic mechanical oscillator with a sub-Poissonian phonon distribution. Indeed, it has been an enduring ambition in the field of opto- and electromechanics to access a broad range of quantum states, not just limited to Gaussian states. In this context, this work, along with other demonstrations of non-Gaussian nonclassical states of motion [25, 45, 36, 75], represents a major step toward this goal.

To create this sub-Poissonian nonclassical state of motion, I developed a dissipative stabilization technique that can simultaneously add energy to and extract entropy from a massive mechanical oscillator. Requiring neither number-resolution nor coherent manipulation, this technique provides a hardware-efficient and accessible path toward creating highly energized Fock-like states in other cQED experiments. Such states can be valuable resources for quantum metrology: they have been analyzed for their ability to improve the sensitivity of gravitational wave detectors [15, 14] and demonstrated to resolve small forces on trapped ions [144].

In creating the sub-Poissonian state, I also observed strong sideband peaks in the qubit spectrum. These peaks reveal that a spontaneous qubit transition is likely to alter the occupation of the harmonic oscillator, in stark contrast with standard cQED experiments, where a qubit-based photon (or phonon) measurement is regarded as QND in the far dispersive limit [105]. Indeed, this QND-ness is but an approximation under the assumption of a large oscillator frequency compared to the dispersive shift times phonon number ($\omega_{\mathrm{m}} \gg 2\chi_{\mathrm{m}} n$): a condition easily violated in this work

even by the oscillator's thermal distribution, $n_{\mathrm{th}} \sim 15$. Instead, in the new regime achieved by this work with $\omega_{\mathrm{m}} \sim 2\chi_{\mathrm{m}} n$, the qubit-mechanics system becomes closely analogous to other natural molecular systems. This could lead to novel approaches of studying and controlling such artificial systems with methods developed for molecular systems.

Looking forward, a natural next step to this work would be to increase χ_{m} by increasing V_{dc}. As discussed in Sec.4.2.3, this is prevented by a breakdown of the qubit readout beyond $V_{\mathrm{dc}} = 8$ V. A thorough investigation on this breakdown could reveal interesting three-body interactions that may be leveraged to generate mechanical cat states or tripartite entangled states involving the qubit, the mechanical oscillator, and the microwave resonator [74]. Alternatively, solving this problem would, in principle, allow the device to be operated at a much larger $V_{\mathrm{dc}} = 21$ V. With $2\chi_{\mathrm{m}} \approx 2\pi \times 6.4$ MHz larger than the qubit dephasing rate Γ_2, the hybrid system would enter the strong dispersive limit, where arbitrary quantum control over the mechanical oscillator can be achieved.

Bibliography

[1] H. Cavendish, "XXI. Experiments to determine the density of the earth," Philosophical Transactions of the Royal Society of London, vol. 88, pp. 469–526, 12 1798. [Online]. Available: https://royalsocietypublishing.org/doi/10.1098/rstl.1798.0022

[2] J. G. Lee, E. G. Adelberger, T. S. Cook, S. M. Fleischer, and B. R. Heckel, "New Test of the Gravitational 1/r^2 Law at Separations down to 52μm," Physical Review Letters, vol. 124, no. 10, p. 101101, 3 2020. [Online]. Available: https://link.aps.org/doi/10.1103/PhysRevLett.124.101101

[3] B. P. Abbott et al., "Observation of Gravitational Waves from a Binary Black Hole Merger," Physical Review Letters, vol. 116, no. 6, p. 061102, 2 2016. [Online]. Available: https://link.aps.org/doi/10.1103/PhysRevLett.116.061102

[4] W. Heisenberg, "Ueber quantentheoretische Umdeutung kinematischer und mechanischer Beziehungen." Zeitschrift fuer Physik, vol. 33, no. 1, pp. 879–893, 12 1925. [Online]. Available: http://link.springer.com/10.1007/BF01328377

[5] J. Weber, "Detection and Generation of Gravitational Waves," Physical Review, vol. 117, no. 1, pp. 306–313, 1 1960. [Online]. Available: https://link.aps.org/doi/10.1103/PhysRev.117.306

[6] ——, "Observation of the Thermal Fluctuations of a Gravitational-Wave Detector," Physical Review Letters, vol. 17, no. 24, pp. 1228–1230, 12 1966. [Online]. Available: https://link.aps.org/doi/10.1103/PhysRevLett.17.1228

[7] V. Braginsky and V. Rudenko, "Gravitational waves and the detection of gravitational radiation," Physics Reports, vol. 46, no. 5, pp. 165–200, 10 1978. [Online]. Available: https://linkinghub.elsevier.com/retrieve/pii/0370157378901928

[8] P. Rapagnani, "Development and test atT=4.2K of a capacitive resonant transducer for cryogenic gravitational-wave antennas," Il Nuovo Cimento C, vol. 5, no. 4, pp. 385–408, 7 1982. [Online]. Available: http://link.springer.com/10.1007/BF02561646

[9] K. S. Thorne, "Gravitational-wave research: Current status and future prospects," Reviews of Modern Physics, vol. 52, no. 2, pp. 285–297, 4 1980. [Online]. Available: https://link.aps.org/doi/10.1103/RevModPhys.52.285

[10] A. Abramovici et al., "LIGO: The Laser Interferometer Gravitational-Wave Observatory," Science, vol. 256, no. 5055, pp. 325–333, 4 1992. [Online]. Available: https://www.sciencemag.org/lookup/doi/10.1126/science.256.5055.325

[11] M. Blencowe, "Nanoelectromechanical systems," Contemporary Physics, vol. 46, no. 4, pp. 249–264, 7 2005. [Online]. Available: http://www.tandfonline.com/doi/abs/10.1080/00107510500146865

[12] Y. S. Greenberg, Y. A. Pashkin, and E. Il'ichev, "Nanomechanical resonators," Uspekhi Fizicheskih Nauk, vol. 182, no. 4, p. 407, 2012. [Online]. Available: http://ufn.ru/ru/articles/2012/4/c/

[13] M. Aspelmeyer, T. J. Kippenberg, and F. Marquardt, "Cavity optomechanics," Reviews of Modern Physics, vol. 86, no. 4, pp. 1391–1452, 12 2014. [Online]. Available: https://link.aps.org/doi/10.1103/RevModPhys.86.1391

[14] V. B. Braginsky, Y. I. Vorontsov, and K. S. Thorne, "Quantum Nondemolition Measurements," Science, vol. 209, no. 4456, pp. 547–557, 8 1980. [Online]. Available: https://www.sciencemag.org/lookup/doi/10.1126/science.209.4456.547

[15] C. M. Caves, K. S. Thorne, R. W. P. Drever, V. D. Sandberg, and M. Zimmermann, "On the measurement of a weak classical force coupled to a quantum-mechanical oscillator. I. Issues of principle," Reviews of Modern Physics, vol. 52, no. 2, pp. 341–392, 4 1980. [Online]. Available: https://journals.aps.org/rmp/pdf/10.1103/RevModPhys.52.341

[16] V. B. Braginskii, A. B. Manukin, and M. Y. Tikhonov, "INVESTIGATION OF DISSIPATIVE PONDEROMOTIVE EFFECTS OF ELECTROMAGNETIC RADIATION," Sov. Phys. JETP, vol. 31, no. 5, p. 829, 1970.

[17] M. J. Woolley, A. C. Doherty, G. J. Milburn, and K. C. Schwab, "Nanomechanical squeezing with detection via a microwave cavity," Physical Review A, vol. 78, no. 6, p. 062303, 12 2008. [Online]. Available: https://link.aps.org/doi/10.1103/PhysRevA.78.062303

[18] A. Kronwald, F. Marquardt, and A. A. Clerk, "Arbitrarily large steady-state bosonic squeezing via dissipation," Physical Review A, vol. 88, no. 6, p. 063833, 12 2013. [Online]. Available: https://link.aps.org/doi/10.1103/PhysRevA.88.063833

[19] J. D. Teufel, T. Donner, D. Li, J. W. Harlow, M. S. Allman, K. Cicak, A. J. Sirois, J. D. Whittaker, K. W. Lehnert, and R. W. Simmonds, "Sideband cooling of micromechanical motion to the quantum ground state," Nature, vol. 475, no. 7356, pp. 359–363, 7 2011. [Online]. Available: http://www.nature.com/articles/nature10261

[20] J. Chan, T. P. M. Alegre, A. H. Safavi-Naeini, J. T. Hill, A. Krause, S. Gröblacher, M. Aspelmeyer, and O. Painter, "Laser cooling of a nanomechanical oscillator into its quantum ground state," Nature, vol. 478, no. 7367, pp. 89–92, 10 2011. [Online]. Available: http://www.nature.com/articles/nature10461

[21] E. E. Wollman, C. U. Lei, A. J. Weinstein, J. Suh, A. Kronwald, F. Marquardt, A. A. Clerk, and K. C. Schwab, "Quantum squeezing of motion in a mechanical resonator," Science, vol. 349, no. 6251, pp. 952–955, 8 2015. [Online]. Available: www.sciencemag.org/content/349/6251/948/suppl/DC1

[22] J.-M. Pirkkalainen, E. Damskägg, M. Brandt, F. Massel, and M. A. Sillanpää, "Squeezing of Quantum Noise of Motion in a Micromechanical Resonator," Physical Review Letters, vol. 115, no. 24, p. 243601, 12 2015. [Online]. Available: https://link.aps.org/doi/10.1103/PhysRevLett.115.243601

[23] F. Lecocq, J. B. Clark, R. W. Simmonds, J. Aumentado, and J. D. Teufel, "Quantum Nondemolition Measurement of a Nonclassical State of a Massive Object," Physical Review X, vol. 5, no. 4, p. 041037, 12 2015. [Online]. Available: https://link.aps.org/doi/10.1103/PhysRevX.5.041037

[24] T. a. Palomaki, J. D. Teufel, R. W. Simmonds, and K. W. Lehnert, "Entangling mechanical motion with microwave fields." Science (New York, N.Y.), vol. 342, no. 6159, pp. 710–3, 2013. [Online]. Available: http://www.ncbi.nlm.nih.gov/pubmed/24091706

[25] R. Riedinger, S. Hong, R. A. Norte, J. A. Slater, J. Shang, A. G. Krause, V. Anant, M. Aspelmeyer, and S. Gröblacher, "Non-classical correlations between single photons and phonons from a mechanical oscillator," Nature, vol. 530, no. 7590, pp. 313–316, 2016. [Online]. Available: https://www.nature.com/articles/nature16536.pdf

[26] C. F. Ockeloen-Korppi, E. Damskägg, J.-m. Pirkkalainen, M. Asjad, A. A. Clerk, F. Massel, M. J. Woolley, and M. A. Sillanpää, "Stabilized entanglement of massive mechanical oscillators," Nature, vol. 556, no. 7702, pp. 478–482, 4 2018. [Online]. Available: http://www.nature.com/articles/s41586-018-0038-x

[27] R. Riedinger, A. Wallucks, I. Marinković, C. Löschnauer, M. Aspelmeyer, S. Hong, and S. Gröblacher, "Remote quantum entanglement between two micromechanical oscillators," Nature, vol. 556, no. 7702, pp. 473–477, 4 2018. [Online]. Available: http://www.nature.com/articles/s41586-018-0036-z

[28] S. Kotler et al., "Tomography of Entangled Macroscopic Mechanical Objects," 2020. [Online]. Available: http://arxiv.org/abs/2004.05515

[29] M. Tsang and C. M. Caves, "Coherent Quantum-Noise Cancellation for Optomechanical Sensors," Physical Review Letters, vol. 105, no. 12, p. 123601, 9 2010. [Online]. Available: https://link.aps.org/doi/10.1103/PhysRevLett.105.123601

[30] M. J. Woolley and A. A. Clerk, "Two-mode back-action-evading measurements in cavity optomechanics," Physical Review A, vol. 87, no. 6, p. 063846, 6 2013. [Online]. Available: https://link.aps.org/doi/10.1103/PhysRevA.87.063846

[31] C. F. Ockeloen-Korppi, E. Damskägg, J.-M. Pirkkalainen, A. A. Clerk, M. J. Woolley, and M. A. Sillanpää, "Quantum Backaction Evading Measurement of Collective Mechanical Modes," Physical Review Letters, vol. 117, no. 14, p. 140401, 9 2016. [Online]. Available: https://link.aps.org/doi/10.1103/PhysRevLett.117.140401

[32] S. Bose, K. Jacobs, and P. L. Knight, "Scheme to probe the decoherence of a macroscopic object," Physical Review A, vol. 59, no. 5, pp. 3204–3210, 5 1999. [Online]. Available: https://link.aps.org/doi/10.1103/PhysRevA.59.3204

[33] W. Marshall, C. Simon, R. Penrose, and D. Bouwmeester, "Towards Quantum Superpositions of a Mirror," Physical Review Letters, vol. 91, no. 13, p. 130401, 9 2003. [Online]. Available: https://link.aps.org/doi/10.1103/PhysRevLett.91.130401

[34] A. Bassi, K. Lochan, S. Satin, T. P. Singh, and H. Ulbricht, "Models of wave-function collapse, underlying theories, and experimental tests," Reviews of Modern Physics, vol. 85, no. 2, pp. 471–527, 4 2013. [Online]. Available: https://link.aps.org/doi/10.1103/RevModPhys.85.471

[35] T. A. Palomaki, J. W. Harlow, J. D. Teufel, R. W. Simmonds, and K. W. Lehnert, "Coherent state transfer between itinerant microwave fields and a mechanical oscillator." Nature, vol. 495, no. 7440, pp. 210–4, 2013. [Online]. Available: http://www.nature.com/articles/nature11915

[36] Y. Chu, P. Kharel, W. H. Renninger, L. D. Burkhart, L. Frunzio, P. T. Rakich, and R. J. Schoelkopf, "Quantum acoustics with superconducting qubits," Science, vol. 358, no. 6360, pp. 199–202, 10 2017. [Online]. Available: https://www.sciencemag.org/lookup/doi/10.1126/science.aao1511

[37] A. P. Higginbotham, P. S. Burns, M. D. Urmey, R. W. Peterson, N. S. Kampel, B. M. Brubaker, G. Smith, K. W. Lehnert, and C. A. Regal, "Harnessing electro-optic correlations in an efficient mechanical converter," Nature Physics, vol. 14, no. 10, pp. 1038–1042, 10 2018. [Online]. Available: http://www.nature.com/articles/s41567-018-0210-0

[38] R. D. Delaney, A. P. Reed, R. W. Andrews, and K. W. Lehnert, "Measurement of Motion beyond the Quantum Limit by Transient Amplification," Physical Review Letters, vol. 123, no. 18, p. 183603, 10 2019. [Online]. Available: https://link.aps.org/doi/10.1103/PhysRevLett.123.183603

[39] L. S. Braunstein and P. Van Loock, "Quantum information with continuous variables," Reviews of Modern Physics, vol. 77, no. 2, pp. 513–577, 2005. [Online]. Available: https://journals.aps.org/rmp/pdf/10.1103/RevModPhys.77.513

[40] S. D. Bartlett, B. C. Sanders, S. L. Braunstein, and K. Nemoto, "Efficient Classical Simulation of Continuous Variable Quantum Information Processes," Physical Review Letters, vol. 88, no. 9, p. 097904, 2 2002. [Online]. Available: https://link.aps.org/doi/10.1103/PhysRevLett.88.097904

[41] D. Deutsch, A. Ekert, R. Jozsa, C. Macchiavello, S. Popescu, and A. Sanpera, "Quantum privacy amplification and the security of quantum cryptography over noisy channels," Physical Review Letters, vol. 77, no. 13, pp. 2818–2821, 1996.

[42] C. H. Bennett, G. Brassard, S. Popescu, B. Schumacher, J. A. Smolin, and W. K. Wootters, "Purification of Noisy Entanglement and Faithful Teleportation via Noisy Channels," Physical Review Letters, vol. 76, no. 5, pp. 722–725, 1 1996. [Online]. Available: https://link.aps.org/doi/10.1103/PhysRevLett.76.722

[43] N. Kalb, A. A. Reiserer, P. C. Humphreys, J. J. W. Bakermans, S. J. Kamerling, N. H. Nickerson, S. C. Benjamin, D. J. Twitchen, M. Markham, and R. Hanson, "Entanglement distillation between solid-state quantum network nodes," Science, vol. 356, no. 6341, pp. 928–932, 6 2017. [Online]. Available: https://www.sciencemag.org/lookup/doi/10.1126/science.aan0070

[44] P. Shor, "Algorithms for quantum computation: discrete logarithms and factoring," in Proceedings 35th Annual Symposium on Foundations of Computer Science. IEEE Comput. Soc. Press, 1994, pp. 124–134. [Online]. Available: http://ieeexplore.ieee.org/document/365700/

[45] A. P. Reed et al., "Faithful conversion of propagating quantum information to mechanical motion," Nature Physics, vol. 13, no. 12, pp. 1163–1167, 12 2017. [Online]. Available: http://www.nature.com/articles/nphys4251

[46] F. Lecocq, J. D. Teufel, J. Aumentado, and R. W. Simmonds, "Resolving the vacuum fluctuations of an optomechanical system using an artificial atom," Nature Physics, vol. 11, no. 8, pp. 635–639, 8 2015. [Online]. Available: http://www.nature.com/articles/nphys3365

[47] D. I. Schuster et al., "Resolving photon number states in a superconducting circuit," Nature, vol. 445, no. 7127, pp. 515–518, 2 2007. [Online]. Available: http://www.nature.com/articles/nature05461

[48] R. H. Hadfield, "Single-photon detectors for optical quantum information applications," Nature Photonics, vol. 3, no. 12, pp. 696–705, 12 2009. [Online]. Available: http://www.nature.com/articles/nphoton.2009.230

[49] A. Nunnenkamp, K. Børkje, and S. M. Girvin, "Single-Photon Optomechanics," Physical Review Letters, vol. 107, no. 6, p. 063602, 8 2011. [Online]. Available: https://link.aps.org/doi/10.1103/PhysRevLett.107.063602

[50] J. Qian, A. A. Clerk, K. Hammerer, and F. Marquardt, "Quantum Signatures of the Optomechanical Instability," Physical Review Letters, vol. 109, no. 25, p. 253601, 12 2012. [Online]. Available: https://link.aps.org/doi/10.1103/PhysRevLett.109.253601

[51] X.-W. Xu, H. Wang, J. Zhang, and Y.-X. Liu, "Engineering of nonclassical motional states in optomechanical systems," Physical Review A, vol. 88, no. 6, p. 063819, 12 2013. [Online]. Available: https://link.aps.org/doi/10.1103/PhysRevA.88.063819

[52] A. A. Clerk, K. W. Lehnert, P. Bertet, J. R. Petta, and Y. Nakamura, "Hybrid quantum systems with circuit quantum electrodynamics," Nature Physics, vol. 16, no. 3, pp. 257–267, 3 2020. [Online]. Available: http://www.nature.com/articles/s41567-020-0797-9

[53] T. T. Heikkilä, F. Massel, J. Tuorila, R. Khan, and M. A. Sillanpää, "Enhancing Optomechanical Coupling via the Josephson Effect," Physical Review Letters, vol. 112, no. 20, p. 203603, 5 2014. [Online]. Available: https://link.aps.org/doi/10.1103/PhysRevLett.112.203603

[54] J.-M. Pirkkalainen, S. Cho, F. Massel, J. Tuorila, T. Heikkilä, P. Hakonen, and M. Sillanpää, "Cavity optomechanics mediated by a quantum two-level system," Nature Communications, vol. 6, no. 1, p. 6981, 11 2015. [Online]. Available: http://www.nature.com/articles/ncomms7981

[55] J.-Q. Liao, K. Jacobs, F. Nori, and R. W. Simmonds, "Modulated electromechanics: large enhancements of nonlinearities," New Journal of Physics, vol. 16, no. 7, p. 072001, 7 2014. [Online]. Available: https://iopscience.iop.org/article/10.1088/1367-2630/16/7/072001

[56] S. Gröblacher, K. Hammerer, M. R. Vanner, and M. Aspelmeyer, "Observation of strong coupling between a micromechanical resonator and an optical cavity field," Nature, vol. 460, no. 7256, pp. 724–727, 8 2009. [Online]. Available: http://www.nature.com/articles/nature08171

[57] J. D. Teufel, D. Li, M. S. Allman, K. Cicak, A. J. Sirois, J. D. Whittaker, and R. W. Simmonds, "Circuit cavity electromechanics in the strong-coupling regime," Nature, vol. 471, no. 7337, pp. 204–208, 3 2011. [Online]. Available: http://www.nature.com/articles/nature09898

[58] J. D. Thompson, B. M. Zwickl, A. M. Jayich, F. Marquardt, S. M. Girvin, and J. G. E. Harris, "Strong dispersive coupling of a high-finesse cavity to a micromechanical membrane," Nature, vol. 452, no. 7183, pp. 72–75, 3 2008. [Online]. Available: http://www.nature.com/articles/nature06715

[59] A. M. Jayich, J. C. Sankey, B. M. Zwickl, C. Yang, J. D. Thompson, S. M. Girvin, A. A. Clerk, F. Marquardt, and J. G. E. Harris, "Dispersive optomechanics: a membrane inside a cavity," New Journal of Physics, vol. 10, no. 9, p. 095008, 9 2008. [Online]. Available: https://iopscience.iop.org/article/10.1088/1367-2630/10/9/095008

[60] G. A. Brawley, M. R. Vanner, P. E. Larsen, S. Schmid, A. Boisen, and W. P. Bowen, "Nonlinear optomechanical measurement of mechanical motion," Nature Communications, vol. 7, no. 1, p. 10988, 4 2016. [Online]. Available: http://www.nature.com/articles/ncomms10988

[61] H. Miao, S. Danilishin, T. Corbitt, and Y. Chen, "Standard Quantum Limit for Probing Mechanical Energy Quantization," Physical Review Letters, vol. 103, no. 10, p. 100402, 9 2009. [Online]. Available: https://journals.aps.org/prl/pdf/10.1103/PhysRevLett.103.100402

[62] Y. Yanay, J. C. Sankey, and A. A. Clerk, "Quantum backaction and noise interference in asymmetric two-cavity optomechanical systems," Physical Review A, vol. 93, no. 6, p. 063809, 6 2016. [Online]. Available: https://link.aps.org/doi/10.1103/PhysRevA.93.063809

[63] M. Ludwig, A. H. Safavi-Naeini, O. Painter, and F. Marquardt, "Enhanced Quantum Nonlinearities in a Two-Mode Optomechanical System," Physical Review Letters, vol. 109, no. 6, p. 063601, 8 2012. [Online]. Available: https://link.aps.org/doi/10.1103/PhysRevLett.109.063601

[64] Y. Yanay and A. A. Clerk, "Shelving-style QND phonon-number detection in quantum optomechanics," New Journal of Physics, vol. 19, no. 3, p. 033014, 3 2017. [Online]. Available: https://doi.org/10.1088/1367-2630/aa6206

[65] L. Dellantonio, O. Kyriienko, F. Marquardt, and A. S. Sørensen, "Quantum nondemolition measurement of mechanical motion quanta," Nature Communications, vol. 9, no. 1, p. 3621, 12 2018. [Online]. Available: http://www.nature.com/articles/s41467-018-06070-y

[66] M. Hofheinz et al., "Synthesizing arbitrary quantum states in a superconducting resonator," Nature, vol. 459, no. 7246, pp. 546–549, 5 2009. [Online]. Available: http://www.nature.com/articles/nature08005

[67] B. Vlastakis, G. Kirchmair, Z. Leghtas, S. E. Nigg, L. Frunzio, S. M. Girvin, M. Mirrahimi, M. H. Devoret, and R. J. Schoelkopf, "Deterministically Encoding Quantum Information Using 100-Photon Schrodinger Cat States," Science, vol. 342, no. 6158, pp. 607–610, 11 2013. [Online]. Available: https://www.sciencemag.org/lookup/doi/10.1126/science.1243289

[68] A. D. Armour, M. P. Blencowe, and K. C. Schwab, "Entanglement and Decoherence of a Micromechanical Resonator via Coupling to a Cooper-Pair Box," Physical Review Letters, vol. 88, no. 14, p. 148301, 3 2002. [Online]. Available: https://link.aps.org/doi/10.1103/PhysRevLett.88.148301

[69] E. K. Irish and K. Schwab, "Quantum measurement of a coupled nanomechanical resonator–Cooper-pair box system," Physical Review B, vol. 68, no. 15, p. 155311, 10 2003. [Online]. Available: https://link.aps.org/doi/10.1103/PhysRevB.68.155311

[70] I. Martin, A. Shnirman, L. Tian, and P. Zoller, "Ground-state cooling of mechanical resonators," Physical Review B, vol. 69, no. 12, p. 125339, 3 2004. [Online]. Available: https://link.aps.org/doi/10.1103/PhysRevB.69.125339

[71] L. Tian, "Entanglement from a nanomechanical resonator weakly coupled to a single Cooper-pair box," Physical Review B, vol. 72, no. 19, p. 195411, 11 2005. [Online]. Available: https://link.aps.org/doi/10.1103/PhysRevB.72.195411

[72] D. Wahyu Utami and A. A. Clerk, "Entanglement dynamics in a dispersively coupled qubit-oscillator system," Physical Review A, vol. 78, no. 4, p. 042323, 10 2008. [Online]. Available: https://link.aps.org/doi/10.1103/PhysRevA.78.042323

[73] K. Jacobs, L. Tian, and J. Finn, "Engineering Superposition States and Tailored Probes for Nanoresonators via Open-Loop Control," Physical Review Letters, vol. 102, no. 5, p. 057208, 2 2009. [Online]. Available: https://link.aps.org/doi/10.1103/PhysRevLett.102.057208

[74] M. Abdi, M. Pernpeintner, R. Gross, H. Huebl, and M. J. Hartmann, "Quantum State Engineering with Circuit Electromechanical Three-Body Interactions," Physical Review Letters, vol. 114, no. 17, p. 173602, 4 2015. [Online]. Available: https://link.aps.org/doi/10.1103/PhysRevLett.114.173602

[75] K. J. Satzinger et al., "Quantum control of surface acoustic-wave phonons," Nature, vol. 563, no. 7733, pp. 661–665, 11 2018. [Online]. Available: http://www.nature.com/articles/s41586-018-0719-5

[76] L. R. Sletten, B. A. Moores, J. J. Viennot, and K. W. Lehnert, "Resolving Phonon Fock States in a Multimode Cavity with a Double-Slit Qubit," Physical Review X, vol. 9, no. 2, p. 021056, 6 2019. [Online]. Available: https://link.aps.org/doi/10.1103/PhysRevX.9.021056

[77] P. Arrangoiz-Arriola, E. A. Wollack, Z. Wang, M. Pechal, W. Jiang, T. P. McKenna, J. D. Witmer, R. Van Laer, and A. H. Safavi-Naeini, "Resolving the energy levels of a nanomechanical oscillator," Nature, vol. 571, no. 7766, pp. 537–540, 7 2019. [Online]. Available: http://www.nature.com/articles/s41586-019-1386-x

[78] M. J. A. Schuetz, E. M. Kessler, G. Giedke, L. M. K. Vandersypen, M. D. Lukin, and J. I. Cirac, "Universal Quantum Transducers Based on Surface Acoustic Waves," Physical Review X, vol. 5, no. 3, p. 031031, 9 2015. [Online]. Available: https://link.aps.org/doi/10.1103/PhysRevX.5.031031

[79] V. Bouchiat, D. Vion, P. Joyez, D. Esteve, and M. H. Devoret, "Quantum Coherence with a Single Cooper Pair," Physica Scripta, vol. T76, no. 1, p. 165, 1998. [Online]. Available: https://iopscience.iop.org/article/10.1238/Physica.Topical.076a00165

[80] Y. Makhlin, G. Schön, and A. Shnirman, "Quantum-state engineering with Josephson-junction devices," Reviews of Modern Physics, vol. 73, no. 2, pp. 357–400, 5 2001. [Online]. Available: https://link.aps.org/doi/10.1103/RevModPhys.73.357

[81] M. D. LaHaye, J. Suh, P. M. Echternach, K. C. Schwab, and M. L. Roukes, "Nanomechanical measurements of a superconducting qubit," Nature, vol. 459, no. 7249, pp. 960–964, 6 2009. [Online]. Available: http://www.nature.com/articles/nature08093

[82] J.-M. Pirkkalainen, S. U. Cho, J. Li, G. S. Paraoanu, P. J. Hakonen, and M. A. Sillanpää, "Hybrid circuit cavity quantum electrodynamics with a micromechanical resonator," Nature, vol. 494, no. 7436, pp. 211–215, 2 2013. [Online]. Available: http://www.nature.com/articles/nature11821

[83] F. Rouxinol, Y. Hao, F. Brito, A. O. Caldeira, E. K. Irish, and M. D. LaHaye, "Measurements of nanoresonator-qubit interactions in a hybrid quantum electromechanical system," Nanotechnology, vol. 27, no. 36, p. 364003, 9 2016. [Online]. Available: https://iopscience.iop.org/article/10.1088/0957-4484/27/36/364003

[84] J. Koch, T. M. Yu, J. Gambetta, A. A. Houck, D. I. Schuster, J. Majer, A. Blais, M. H. Devoret, S. M. Girvin, and R. J. Schoelkopf, "Charge-insensitive qubit design derived from the Cooper pair box," Physical Review A, vol. 76, no. 4, p. 042319, 10 2007. [Online]. Available: https://link.aps.org/doi/10.1103/PhysRevA.76.042319

[85] X. Ma, J. J. Viennot, S. Kotler, J. D. Teufel, and K. W. Lehnert, "Nonclassical energy squeezing of a macroscopic mechanical oscillator," 5 2020. [Online]. Available: http://arxiv.org/abs/2005.04260

[86] J. J. Viennot, X. Ma, and K. W. Lehnert, "Phonon-Number-Sensitive Electromechanics," Physical Review Letters, vol. 121, no. 18, 2018. [Online]. Available: https://journals.aps.org/prl/pdf/10.1103/PhysRevLett.121.183601

[87] R. Short and L. Mandel, "Observation of Sub-Poissonian Photon Statistics," Physical Review Letters, vol. 51, no. 5, pp. 384–387, 8 1983. [Online]. Available: https://link.aps.org/doi/10.1103/PhysRevLett.51.384

[88] D. Walls and G. Milburn, Quantum Optics. Springer, 2008.

[89] V. Ambegaokar and A. Baratoff, "Tunneling Between Superconductors," Physical Review Letters, vol. 10, no. 11, pp. 486–489, 6 1963. [Online]. Available: https://link.aps.org/doi/10.1103/PhysRevLett.10.486

[90] M. H. Devoret, "Quantum fluctuations in electrical circuits," in Quantum Fluctuations, Les Houches, Sess. LXIII, 1995. [Online]. Available: http://www.physique.usherb.ca/tremblay/cours/PHY-731/Quantum%7B_%7Dcircuit%7B_%7Dtheory-1.pdf

[91] L. S. Bishop, "Circuit Quantum Electrodynamics," Ph.D. dissertation, Yale University, 2010.

[92] R. J. Schoelkopf, A. A. Clerk, S. M. Girvin, K. W. Lehnert, and M. H. Devoret, "Qubits as Spectrometers of Quantum Noise," in Quantum Noise in Mesoscopic Physics. Dordrecht: Springer Netherlands, 2003, pp. 175–203. [Online]. Available: http://link.springer.com/10.1007/978-94-010-0089-5_9

[93] A. A. Houck et al., "Controlling the spontaneous emission of a superconducting transmon qubit," Physical Review Letters, vol. 101, no. 8, pp. 1–4, 2008.

[94] E. M. Purcell, H. C. Torrey, and R. V. Pound, "Resonance Absorption by Nuclear Magnetic Moments in a Solid," Physical Review, vol. 69, no. 1-2, pp. 37–38, 1 1946. [Online]. Available: https://link.aps.org/doi/10.1103/PhysRev.69.37

[95] J. M. Martinis, M. Ansmann, and J. Aumentado, "Energy Decay in Superconducting Josephson-Junction Qubits from Nonequilibrium Quasiparticle Excitations," Physical Review Letters, vol. 103, no. 9, p. 097002, 8 2009. [Online]. Available: http://link.aps.org/doi/10.1103/PhysRevLett.103.097002

[96] U. Vool et al., "Non-Poissonian Quantum Jumps of a Fluxonium Qubit due to Quasiparticle Excitations," Physical Review Letters, vol. 113, no. 24, p. 247001, 12 2014. [Online]. Available: https://link.aps.org/doi/10.1103/PhysRevLett.113.247001

[97] C. Wang et al., "Measurement and control of quasiparticle dynamics in a superconducting qubit," Nature Communications, vol. 5, no. 1, p. 5836, 12 2014. [Online]. Available: http://www.nature.com/articles/ncomms6836

[98] S. Rajauria, L. M. A. Pascal, P. Gandit, F. W. J. Hekking, B. Pannetier, and H. Courtois, "Efficiency of quasiparticle evacuation in superconducting devices," Physical Review B, vol. 85, no. 2, p. 020505, 1 2012. [Online]. Available: https://link.aps.org/doi/10.1103/PhysRevB.85.020505

[99] R.-P. Riwar, A. Hosseinkhani, L. D. Burkhart, Y. Y. Gao, R. J. Schoelkopf, L. I. Glazman, and G. Catelani, "Normal-metal quasiparticle traps for superconducting qubits," Physical Review B, vol. 94, no. 10, p. 104516, 9 2016. [Online]. Available: https://link.aps.org/doi/10.1103/PhysRevB.94.104516

[100] I. Nsanzineza and B. L. T. Plourde, "Trapping a Single Vortex and Reducing Quasiparticles in a Superconducting Resonator," Physical Review Letters, vol. 113, no. 11, p. 117002, 9 2014. [Online]. Available: https://link.aps.org/doi/10.1103/PhysRevLett.113.117002

[101] M. Taupin, I. M. Khaymovich, M. Meschke, A. S. Mel'nikov, and J. P. Pekola, "Tunable quasiparticle trapping in Meissner and vortex states of mesoscopic superconductors," Nature Communications, vol. 7, no. 1, p. 10977, 4 2016. [Online]. Available: http://www.nature.com/articles/ncomms10977

[102] A. Cottet, "Implementation of a quantum bit in a superconducting circuit," Ph.D. dissertation, Universite Paris VI, 2002. [Online]. Available: http://www.phys.ens.fr/~cottet/ACottetThesis.pdf

[103] D. I. Schuster, "Circuit Quantum Electrodynamics," Ph.D. dissertation, Yale University, 2007. [Online]. Available: https://rsl.yale.edu/sites/default/files/files/RSL_Theses/SchusterThesis.pdf

[104] D. Zueco, G. M. Reuther, S. Kohler, and P. Hänggi, "Qubit-oscillator dynamics in the dispersive regime: Analytical theory beyond the rotating-wave approximation," Physical Review A, vol. 80, no. 3, p. 033846, 9 2009. [Online]. Available: https://link.aps.org/doi/10.1103/PhysRevA.80.033846

[105] B. R. Johnson et al., "Quantum non-demolition detection of single microwave photons in a circuit," Nature Physics, vol. 6, no. 9, pp. 663–667, 9 2010. [Online]. Available: http://www.nature.com/articles/nphys1710

[106] L. Sun et al., "Tracking photon jumps with repeated quantum non-demolition parity measurements," Nature, vol. 511, no. 7510, pp. 444–448, 7 2014. [Online]. Available: http://www.nature.com/articles/nature13436

[107] Z. K. Minev, S. O. Mundhada, S. Shankar, P. Reinhold, R. Gutiérrez-Jáuregui, R. J. Schoelkopf, M. Mirrahimi, H. J. Carmichael, and M. H. Devoret, "To catch and reverse a quantum jump mid-flight," Nature, vol. 570, no. 7760, pp. 200–204, 6 2019. [Online]. Available: http://www.nature.com/articles/s41586-019-1287-z

[108] F. Bloch and A. Siegert, "Magnetic Resonance for Nonrotating Fields," Physical Review, vol. 57, no. 6, pp. 522–527, 3 1940. [Online]. Available: https://journals.aps.org/pr/pdf/10.1103/PhysRev.57.522

[109] J. Larson, "Dynamics of the Jaynes–Cummings and Rabi models: old wine in new bottles," Physica Scripta, vol. 76, no. 2, pp. 146–160, 8 2007. [Online]. Available: https://iopscience.iop.org/article/10.1088/0031-8949/76/2/007

[110] R. Shankar, Principles of Quantum Mechanics. Springer, 1994.

[111] J. Franck and E. G. Dymond, "Elementary processes of photochemical reactions," Transactions of the Faraday Society, vol. 21, no. February, p. 536, 1926. [Online]. Available: https://pubs.rsc.org/en/content/articlepdf/1926/tf/tf9262100536

[112] E. Condon, "A Theory of Intensity Distribution in Band Systems," Physical Review, vol. 28, no. 6, pp. 1182–1201, 12 1926. [Online]. Available: https://link.aps.org/doi/10.1103/PhysRev.28.1182

[113] C. Joshi, E. K. Irish, and T. P. Spiller, "Qubit-flip-induced cavity mode squeezing in the strong dispersive regime of the quantum Rabi model," Scientific Reports, vol. 7, no. 1, p. 45587, 5 2017. [Online]. Available: http://www.nature.com/articles/srep45587

[114] J. D. P. Machado, R. J. Slooter, and Y. M. Blanter, "Quantum signatures in quadratic optomechanics," Physical Review A, vol. 99, p. 53801, 2019. [Online]. Available: https://journals.aps.org/pra/pdf/10.1103/PhysRevA.99.053801

[115] F. Beaudoin, J. M. Gambetta, and A. Blais, "Dissipation and ultrastrong coupling in circuit QED," Physical Review A, vol. 84, no. 4, p. 043832, 10 2011. [Online]. Available: https://journals.aps.org/pra/pdf/10.1103/PhysRevA.84.043832

[116] M. F. Gely, G. A. Steele, and D. Bothner, "Nature of the Lamb shift in weakly anharmonic atoms: From normal-mode splitting to quantum fluctuations," Physical Review A, vol. 98, no. 5, p. 053808, 11 2018. [Online]. Available: https://link.aps.org/doi/10.1103/PhysRevA.98.053808

[117] S. E. Nigg, H. Paik, B. Vlastakis, G. Kirchmair, S. Shankar, L. Frunzio, M. H. Devoret, R. J. Schoelkopf, and S. M. Girvin, "Black-Box Superconducting Circuit Quantization," Physical Review Letters, vol. 108, no. 24, p. 240502, 6 2012. [Online]. Available: https://link.aps.org/doi/10.1103/PhysRevLett.108.240502

[118] A. A. Clerk, M. H. Devoret, S. M. Girvin, F. Marquardt, and R. J. Schoelkopf, "Introduction to quantum noise, measurement, and amplification," Reviews of Modern Physics, vol. 82, no. 2, pp. 1155–1208, 4 2010. [Online]. Available: https://link.aps.org/doi/10.1103/RevModPhys.82.1155

[119] S. A. Fedorov, N. J. Engelsen, A. H. Ghadimi, M. J. Bereyhi, R. Schilling, D. J. Wilson, and T. J. Kippenberg, "Generalized dissipation dilution in strained mechanical resonators," Physical Review B, vol. 99, no. 5, p. 054107, 2 2019. [Online]. Available: https://link.aps.org/doi/10.1103/PhysRevB.99.054107

[120] F. B. Hildebrand, Advanced Calculus for Applications. Prentice-Hall, 1976.

[121] M. Göppl, A. Fragner, M. Baur, R. Bianchetti, S. Filipp, J. M. Fink, P. J. Leek, G. Puebla, L. Steffen, and A. Wallraff, "Coplanar waveguide resonators for circuit quantum electrodynamics," Journal of Applied Physics, vol. 104, no. 11, p. 113904, 12 2008. [Online]. Available: https://doi.org/10.1063/1.3010859

[122] J. Gambetta, A. Blais, D. I. Schuster, A. Wallraff, L. Frunzio, J. Majer, M. H. Devoret, S. M. Girvin, and R. J. Schoelkopf, "Qubit-photon interactions in a cavity: Measurement-induced dephasing and number splitting," Physical Review A, vol. 74, no. 4, p. 042318, 10 2006. [Online]. Available: https://link.aps.org/doi/10.1103/PhysRevA.74.042318

[123] U. Leonhardt and H. Paul, "Measuring the quantum state of light," Progress in Quantum Electronics, vol. 19, no. 2, pp. 89–130, 1 1995.

[124] J. M. Sage, V. Bolkhovsky, W. D. Oliver, B. Turek, and P. B. Welander, "Study of loss in superconducting coplanar waveguide resonators," Journal of Applied Physics, vol. 109, no. 6, p. 063915, 3 2011. [Online]. Available: https://doi.org/10.1063/1.3552890

[125] A. B. Zorin, F.-J. Ahlers, J. Niemeyer, T. Weimann, H. Wolf, V. A. Krupenin, and S. V. Lotkhov, "Background charge noise in metallic single-electron tunneling devices," Physical Review B, vol. 53, no. 20, pp. 13 682–13 687, 5 1996. [Online]. Available: https://link.aps.org/doi/10.1103/PhysRevB.53.13682

[126] A. Cleland, "Macroscopic quantum tunneling in Josephson tunnel junctions and Coulomb blockade in single small tunnel junctions," Lawrence Berkeley National Laboratory (LBNL), Berkeley, CA (United States), Tech. Rep., 4 1991. [Online]. Available: http://www.osti.gov/servlets/purl/5511727-Ra4FnT/

[127] H. Casimir, "On the attraction between two perfectly conducting plates," Proc. K. Ned. Akad., vol. 360, pp. 793–795, 1948. [Online]. Available: https://www.dwc.knaw.nl/DL/publications/PU00018547.pdf

[128] J. Viennot, "Charge and spin dynamics in a hybrid circuit quantum electrodynamics architecture," Ph.D. dissertation, École normale supérieure, 2013. [Online]. Available: https://tel.archives-ouvertes.fr/tel-01062841

[129] D. I. Schuster, A. Wallraff, A. Blais, L. Frunzio, R.-S. Huang, J. Majer, S. M. Girvin, and R. J. Schoelkopf, "ac Stark Shift and Dephasing of a Superconducting Qubit Strongly Coupled to a Cavity Field," Physical Review Letters, vol. 94, no. 12, p. 123602, 3 2005. [Online]. Available: https://link.aps.org/doi/10.1103/PhysRevLett.94.123602

[130] D. Ristè, C. C. Bultink, M. J. Tiggelman, R. N. Schouten, K. W. Lehnert, and L. DiCarlo, "Millisecond charge-parity fluctuations and induced decoherence in a superconducting transmon qubit," Nature Communications, vol. 4, no. 1, p. 1913, 10 2013. [Online]. Available: http://www.nature.com/articles/ncomms2936

[131] J. Li et al., "Motional averaging in a superconducting qubit," Nature Communications, vol. 4, no. 1, p. 1420, 6 2013. [Online]. Available: http://www.nature.com/articles/ncomms2383

[132] M. P. Silveri, J. A. Tuorila, E. V. Thuneberg, and G. S. Paraoanu, "Quantum systems under frequency modulation," Reports on Progress in Physics, vol. 80, no. 5, p. 056002, 5 2017. [Online]. Available: https://iopscience.iop.org/article/10.1088/1361-6633/aa5170

[133] A. Fragner, M. Goppl, J. M. Fink, M. Baur, R. Bianchetti, P. J. Leek, A. Blais, and A. Wallraff, "Resolving Vacuum Fluctuations in an Electrical Circuit by Measuring the Lamb Shift," Science, vol. 322, no. 5906, pp. 1357–1360, 11 2008. [Online]. Available: https://www.sciencemag.org/lookup/doi/10.1126/science.1164482

[134] E. J. McDowell, X. Cui, Z. Yaqoob, and C. Yang, "A generalized noise variance analysis model and its application to the characterization of 1/f noise," Optics Express, vol. 15, no. 7, p. 3833, 2007. [Online]. Available: https://www.osapublishing.org/oe/abstract.cfm?uri=oe-15-7-3833

[135] T. G. M. Kleinpenning and A. H. de Kuijper, "Relation between variance and sample duration of 1/ f noise signals," Journal of Applied Physics, vol. 63, no. 1, pp. 43–45, 1 1988. [Online]. Available: https://doi.org/10.1063/1.340460http://aip.scitation.org/doi/10.1063/1.340460

[136] L. B. Lucy, "An iterative technique for the rectification of observed distributions," The Astronomical Journal, vol. 79, no. 6, p. 745, 1974.

[137] W. H. Richardson, "Bayesian-Based Iterative Method of Image Restoration*," Journal of the Optical Society of America, vol. 62, no. 1, p. 55, 1 1972. [Online]. Available: https://www.osapublishing.org/abstract.cfm?URI=josa-62-1-55

[138] B. Efron and R. Tibshirani, An introduction to the bootstrap. Chapman & Hall, 1994.

[139] F. A. M. de Oliveira, M. S. Kim, P. L. Knight, and V. Buek, "Properties of displaced number states," Physical Review A, vol. 41, no. 5, pp. 2645–2652, 3 1990. [Online]. Available: https://link.aps.org/doi/10.1103/PhysRevA.41.2645

[140] A. Blais, J. Gambetta, A. Wallraff, D. I. Schuster, S. M. Girvin, M. H. Devoret, and R. J. Schoelkopf, "Quantum-information processing with circuit quantum electrodynamics," Physical Review A, vol. 75, no. 3, p. 032329, 3 2007. [Online]. Available: https://link.aps.org/doi/10.1103/PhysRevA.75.032329

[141] C. Gerry and P. Knight, Introductory Quantum Optics. Cambridge University Press, 2005.

[142] H. J. Kimble, M. Dagenais, and L. Mandel, "Photon Antibunching in Resonance Fluorescence," Physical Review Letters, vol. 39, no. 11, pp. 691–695, 9 1977. [Online]. Available: https://link.aps.org/doi/10.1103/PhysRevLett.39.691

[143] N. Lörch, J. Qian, A. Clerk, F. Marquardt, and K. Hammerer, "Laser theory for optomechanics: Limit cycles in the quantum regime," Physical Review X, vol. 4, no. 1, p. 011015, 1 2014. [Online]. Available: https://link.aps.org/doi/10.1103/PhysRevX.4.011015

[144] F. Wolf, C. Shi, J. C. Heip, M. Gessner, L. Pezzè, A. Smerzi, M. Schulte, K. Hammerer, and P. O. Schmidt, "Motional Fock states for quantum-enhanced amplitude and phase measurements with trapped ions," Nature Communications, vol. 10, no. 1, p. 2929, 12 2019. [Online]. Available: https://doi.org/10.1038/s41467-019-10576-4http://www.nature.com/articles/s41467-019-10576-4

Appendix A

Device fabrication

The fabrication of the device is performed with several aluminium depositions on sapphire. This process can be categorized into three major steps.

The first step involves the fabrication of the drumhead. This process is similar to the ones used to create the electromechanical devices in reference [57, 46]. First, a layer of 100 nm Al film is sputtered on a sapphire substrate, patterned using optical UV lithography, and etched in a Cl plasma to create the bottom electrodes of the drumhead. Also defined in this layer of Al film is the bottom electrodes of the waffle capacitor, which forms part of the on-chip dc-line filter. Next, a layer of 190 nm silicon nitride is deposited and patterned to allow for the suspension of the drumhead as well as the waffle capacitors on the dc-line filter. Finally, a second layer of 100 nm Al film is sputtered and patterned to create the top plate of the mechanically compliant capacitor. Additionally, this second layer of Al film also creates the CPW-resonator, the ground plane, the arms that connect the Josephson junctions to the bottom drumhead electrodes, and the rest of the dc-line.

The second step in the fabrication process involves the creation of the Josephson junctions. The Josephson junction is first defined using electron-beam lithography. Using the Dolan-bridge technique [cite Dolan 1977], the junction is then created by evaporating two layers of Al at ± 20 degree angles (25 nm thick followed by 75 nm thick), separated by a thin layer of oxide. Afterward, the junction is connected to the rest of the circuit with a bandage technique [cite Dunsworth 2017].

Finally, the drumhead and all other suspended structures, such as the waffle capacitors,

are released with a SF6 plasma etch [57, 46]. Once released, the suspended drumhead is free to deform because of the stress in the Al film and thermal expansion and contraction. At the base temperature of the dilution refrigerator (~ 25 mK), thermal contraction brings the plate separation to approximately $x_0 \approx 50$ nm. The Josephson energy E_J of the junction is not changed significantly during this step.

Appendix B

Measurement setup and filtering

The schematic of the entire measurement setup is sketched in Fig. B.1. The mechanics-qubit-cavity device (blue box) is mounted to the base stage of a dilution refrigerator. This device has three ports. First, the dc-port allows for the application of the external dc-voltage V_{dc}, which sets the qubit-mechanics coupling rate. Additionally, a coherent drive applied on this port at the mechanical frequency can drive coherent motion in the mechanical oscillator. Also applied on this dc-port is the dither signal, which is used to drive sideband transitions. The second port of the device is the input-port to the microwave cavity. In addition to applying all qubit control and readout signals, this port is also used to reset the CPB gate-charge to the sweet spot. Finally, photons in the cavity leaves primarily from the cavity output-port. Carrying information about the state of the device, these signals are amplified by the combination of a Josephson parametric amplifier (JPA) and a high electron mobility transistor (HEMT) amplifier before being routed to and collected at the room temperature.

B.1 Filtering the dc-line

The filtering of the dc-line is relatively demanding. It must provide a cold radiation environment (approximately 25 mK at the base of the fridge) to the mechanical oscillator at 25 MHz, while allowing microwave drives at such frequencies. The home-made filter (orange box) placed at base temperature is designed to achieve those goals. It behaves as a low-pass filter at low frequency with a 500 Hz cutoff. It becomes a capacitive voltage divider at 500 kHz with about 50 dB inser-

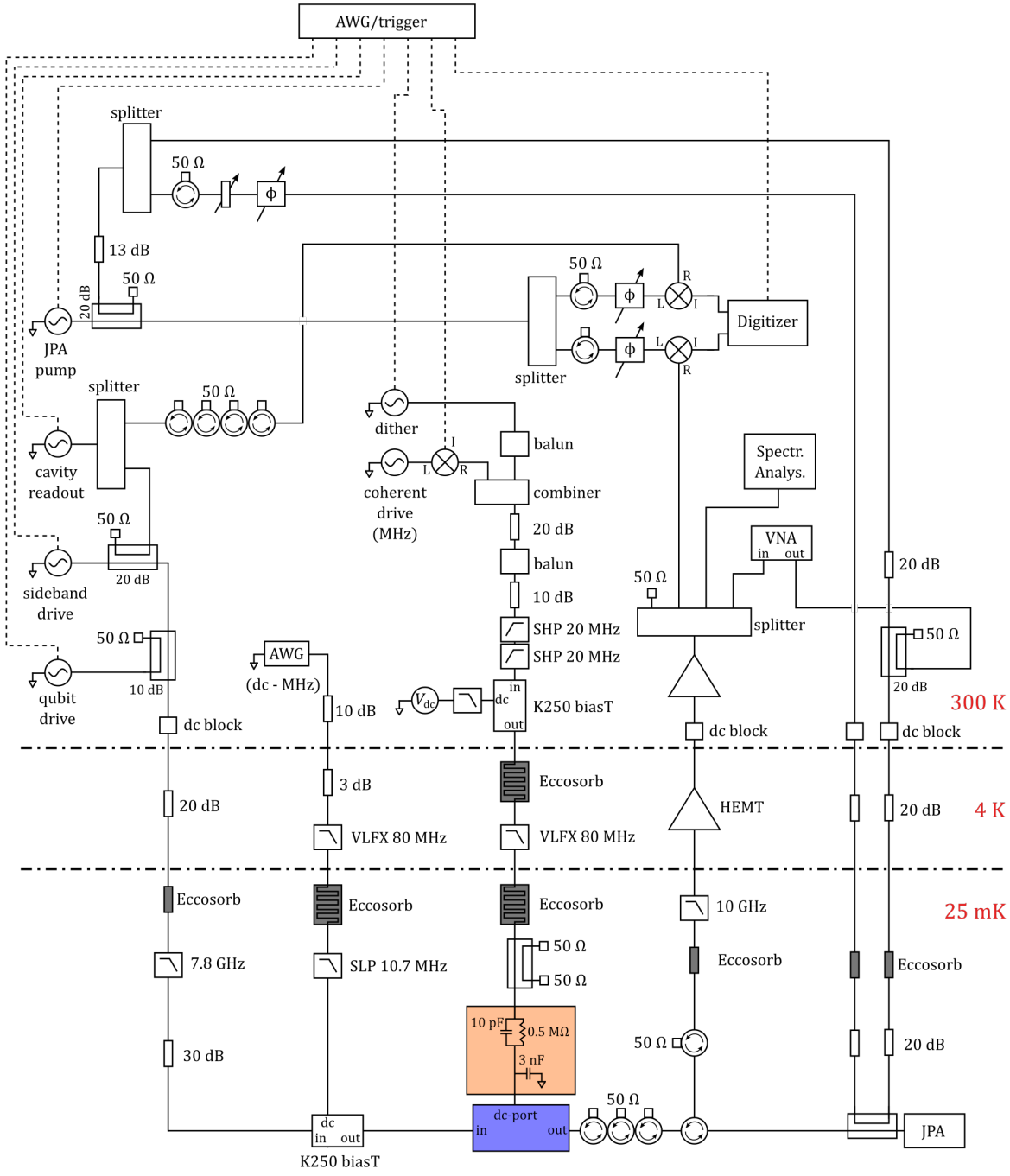

Figure B.1: The full measurement setup
I sketch the full measurement setup used in this work. Pictures of the on-chip device (blue box) can be found in Fig. 3.9.

tion loss up to about 60 MHz, ensuring cold radiation temperature at the mechanical frequency. Behaving as a reflective attenuator at these frequencies, the filter also ensures the microwave drive at ω_m will not create an excessive heat load on the base temperature stage of the fridge. Finally, seen at its output port, the filter also has a small real impedance at the mechanical frequency $\mathrm{Re}\,[Z(\omega_\mathrm{m})] \ll 1\ \Omega$ to avoid damping the mechanical oscillator (see discussion in Sec.3.4).

In addition to these mechanical considerations, I also ensure the dc-line will not cause an increased qubit decay rate (see Sec.2.2.3). This is achieved with a lossless, two-stage on-chip filter. Each stage of this filter is composed of a spiral inductor $L_\mathrm{fil} \approx 20$ nH shorted to ground by a waffle capacitor $C_\mathrm{fil} \approx 25$ pF, as shown in Fig. 3.9(b). Overall, this on-chip filter has a cutoff frequency around 1 GHz and provides 52 dB of isolation at the qubit frequency $\omega_\mathrm{q} \approx 2\pi \times 4$ GHz. To provide an estimate for the rate of qubit decay Γ_1^v caused by voltage noise on this dc-line, I pessimistically assume an input impedance of 50 Ω before the on-chip filter. Using Eqn.(2.30) and assuming $E_c/\hbar \approx 2\pi \times 3.2$ GHz and $C_g \sim 1$ fF, I find a negligible $\Gamma_1^v \ll 1$ Hz.

B.2 The cavity input line

The microwave input line has standard attenuation and filtering. Another dc-line is added to the cavity input at the base temperature with a K250 bias-Tee. This allows for fast control over the CPB gate-voltage with a 10 MHz bandwidth, and is used to set the CPB to its charge degeneracy point (see Sec.4.1.2).

B.3 JPA amplification

The output of the cavity is first amplified by approximately 16 dB by the JPA. The amplifier is pumped at a frequency 4 MHz detuned from the cavity probe signal (at ω_c) to perform heterodyne detection. To ensure very little residual power from the JPA pump would leak into the cavity, the pump is not only detuned many linewidths away from ω_c, but is also actively cancelled with a cancellation signal.

Appendix C

An approximate PSF

For many early experiments in this work, I use an approximate PSF map to process the measured qubit spectra and extract phonon distributions. This is achieved using the same techniques of deconvolution or least-squares fitting discussed in Chapter 5. However, instead of the measured PSF shown in Fig. 5.9(c), I approximate the qubit spectrum $P_e^{|n\rangle}(\omega)$ with exactly $|n\rangle$ phonons as a simple skewed Lorentzian that has been Stark shifted by the phonon number,

$$P_e^{|n\rangle}(\omega) = \frac{1}{2}\frac{(A\Gamma_2/2)^2}{\left[\frac{\omega-\omega_q^{|n\rangle}}{1+L\cdot\mathrm{Sgn}\left(\omega-\omega_q^{|n\rangle}\right)}\right]^2 + (\Gamma_2/2)^2(1+A^2)}, \tag{C.1}$$

where $\omega_q^{|n\rangle}$ is the phonon-number-dependent qubit frequency given by Eqn.(2.56), A is a parameter describing the strength of the qubit drive, $\Gamma_2 \approx 2\pi \times 3.7$ MHz is the FWHM of the qubit lineshape, and L describes the charge-noise-induced asymmetry in this lineshape (see Sec.5.2.4.3). This approximation is valid for very small phonon numbers $n \ll 50$ (because $\omega_m/2\chi_m \approx 50$) as can be observed in Fig. 5.9, but fails at larger phonon number when the sideband peaks become prominent. Consequently, extracting the phonon distribution using this approximate PSF is prone to mistakes, where the deconvolution procedure could erroneously attribute sideband-induced qubit excitations to phonon populations. Indeed, in Fig. [bsb data] where the data is processed using this approximate PSF, the extracted thermal distribution has nonphysical phonon populations around $n \sim 75$ because of the sideband peak ($l = 1$) located at approximately 3.86 GHz. Nevertheless, this approximate deconvolution procedure allowed for a qualitative understanding of the qubit-mechanics

interaction in the early stages of the experiment, allowing, for example, the demonstration of the motional sidebands' phonon-number-sensitivity (see Sec.6.2).

Among all extracted phonon distributions displayed in this thesis, only Fig. , Fig. , and Fig. D.1 are extracted using this approximate PSF. All other distributions are extracted using the more accurate, experimentally determined PSF described in Sec.5.2.

Appendix D

Mechanical damping rate measurement

I measure the damping rate of the mechanical oscillator by driving it out of equilibrium with a red or blue sideband drive and letting it relax to its thermal equilibrium. At different delay times after turning off the sideband drive, I measure the qubit spectrum, extract the phonon distribution using either deconvolution or least-squares fit, and find the mean phonon number $\langle n \rangle$.

Fig. D.1 shows an example of such a measurement after applying a red sideband drive. Performed at an early stage of this work, this experiment is conducted with a much larger $E_J \approx 2\pi \times 4.27$ GHz, quite different from the usual $E_J \approx 2\pi \times 3.8$ GHz used for the majority of this work. Consequently, this data is processed with the approximate PSF discussed in Appendix.C. Because the deconvolution procedure could mistake measurement noise in the qubit spectrum to phonon populations (see for example Sec.7.1.2), it is likely to overestimate $\langle n \rangle$, especially at small delay times when $\langle n \rangle$ is small. Instead, I approximate the phonon distributions as thermal at all delay times, and perform a joint least-squares fit on all qubit spectra at once to find the corresponding phonon distributions. The extracted $\langle n \rangle$ are plotted in the inset, and fits well with a decaying exponential back to the thermal occupancy at equilibrium with the fridge.

Similar measurements are also performed by first driving the blue sideband transitions. Overall, I extract a characteristic mechanical decay time $1/\gamma_{\mathrm{m}} \approx 1.72 \pm 0.32$ ms.

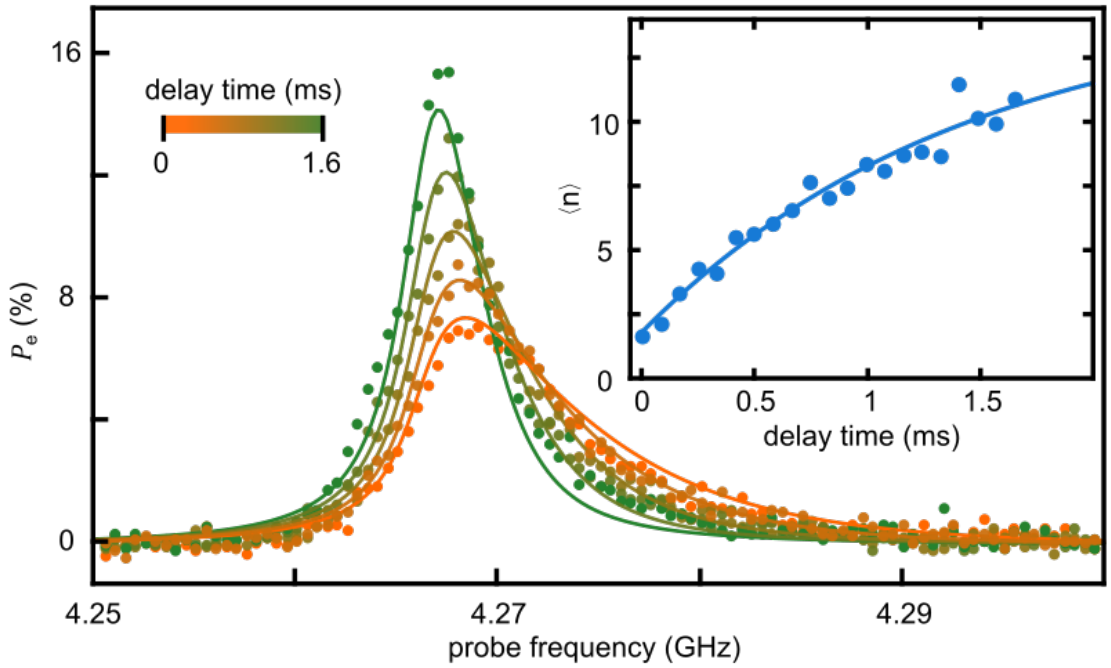

Figure D.1: Measuring γ_m
At $V_{dc} = 6$ V, I measure the qubit spectrum (dots) at different delay times (different colors) after driving a red sideband transition. Assuming the phonon distributions are all described by thermal distributions, I perform a joint least-squares fit (solid lines) simultaneously on all qubit spectra to extract the mean phonon numbers $\langle n \rangle$. Inset: The extracted $\langle n \rangle$ (dots) are plotted as a function of delay times. An exponential fit (solid line) finds a characteristic damping time of 1.5 ms.